OPTICAL AND INFRARED SCATTERING FROM IRREGULARLY-SHAPED PARTICLES SMALL COMPARED TO THE WAVELENGTH

by
Leland Emery Pierce

A dissertation submitted in partial fulfillment
of the requirements for the degree of
Doctor of Philosophy
(Electrical Engineering)
in The University of Michigan
1991

Doctoral Committee:

Professor Emeritus Herschel Weil, Co-chairman
Professor Thomas B. A. Senior, Co-chairman
Associate Professor Robert Ziff
Research Scientist Valdis V. Liepa

To Jan and Debbie

ACKNOWLEDGEMENTS

I would like to thank the members of my committee, in particular professor Herschel Weil for serving as my thesis advisor. Professor Weil was a great help to me in carrying out this investigation and I am grateful to him for his advice, support, and time which he has generously given to me. I would particularly like to thank Prof. Valdis Liepa for finding me some extra money for one of my last semesters of study. Special thanks go to Prof. Charles Yocum of the Dept. of Biological Sciences for his assistance and support with Chapter 5. I would also like to sincerely thank all the faculty and staff at the University of Michigan Radiation Laboratory who have made my five year stay here as a graduate student quite stimulating and enjoyable. I particularly wish to thank my professors and colleagues. Among my fellow graduate students are those that are now PhD's. These include Jianming Jin, Marty Herman, Randy Haupt, Kamal Sarabandi, and Tim Peters. In addition, I would like to mention my fellow graduate students that have yet to finish. Among these are Norm VandenBerg, Kyle McDonald, and Tom Livernois.

Lastly, since many of my figures have been drawn using it, I would like to acknowledge that PostScript® is a registered trademark of Adobe Systems, Incorporated.

PREFACE

This work was performed at the University of Michigan Radiation Laboratory during my graduate studies. The computing facilities available to me at the University of Michigan during this time consisted of a distributed system of Apollo computers administered by the engineering college and a large main frame system, MTS, operated by the University of Michigan Computer Center. I used the Apollo system almost exclusively for the numerical work of this thesis. Although this system was much slower in computational speed than MTS, I was allowed unlimited use of these machines while cpu time on MTS had to be bought. I should also mention that I typeset this thesis on the Apollo network using TEX and the Rackham thesis macro package written by the University of Michigan Computing Center.

I use an $e^{-i\omega t}$ time convention throughout this thesis. The results presented here can always be converted to the $e^{+i\omega t}$ time convention by simply conjugating every complex quantity.

— *Leland Pierce*

TABLE OF CONTENTS

LIST OF FIGURES

Figure

LIST OF TABLES

Table

LIST OF APPENDICES

Appendix

ABSTRACT

OPTICAL AND INFRARED SCATTERING FROM IRREGULARLY-SHAPED PARTICLES SMALL COMPARED TO THE WAVELENGTH

by Leland Emery Pierce

Chairmen: Herschel Weil, Thomas B. A. Senior

Absorption resonances due to shape and material composition are explored in the context of small ($\approx$ 100 nm through 40 μm) naturally-occurring particles. This resonance is very dramatic for small particles that are illuminated at a frequency near the material's bulk absorption band. Here, the dielectric constant has a *negative* real part, thereby allowing the coupling of energy into the resonant modes for this shape, all of which are characterized by negative, real dielectric constants. The extent of this resonant absorption is governed by the spreading of the energy between the modes, and hence by the number of modes and their spacing along the real axis.

This study explored two cases in detail: (1) the enhanced coagulation of two spheres falling in the atmosphere when illuminated near an absorption band, and (2) the absorption of visible light by specialized structures in chloroplasts as the first step in photosynthesis.

The coagulation of two very small dielectric particles is found to be greatly enhanced by the application of an appropriate field, in this case sunlight, during the

process. The forces due to the surrounding atmosphere are also taken into account, but only affect the motion for distant particles, whereas the electromagnetic force dominates for the near interactions at resonance. The simulations also reproduce the known result that small particles tend to coagulate into chains aligned with the applied electric field vector.

Photosynthesis in some plants seems to use this resonant absorption phenomenon as well. The absorbing pigments are distributed on the surface of stacked thin disks in many plants, and it is found that this configuration optimizes their light absorption capability at certain wavelengths. There is also a differential absorption depending on the orientation of the stack to the incident field. It is possible that plants use this phenomenon for regulating the amount of light they absorb.

CHAPTER I

INTRODUCTION

1.1 Motivation

Electromagnetic scattering from particles that are small compared to the incident wavelength has many applications. One of these is the remote sensing of cloud and aerosol properties. Another is the analysis of colloids and other similar chemical and biological systems with light scattering and transmission measurements. Also, Raman scattering and fluorescence from molecules adsorbed at particle surfaces can be better understood with a complete theory of the molecules' interaction with the surface field of the particle.

The major emphasis of this thesis is the study of a class of electromagnetic resonances of these particles in the context of areas in nature where it is operative. These resonances are significant for only certain materials at certain wavelengths. Despite this, they are found to be important in many instances. This is true because when illumination is over a broad spectrum that contains the resonance, the response is often dominated by the resonant response.

Physically, this resonance can be explained as a coupling of electromagnetic energy into an internal, non–electromagnetic vibrational mode of the material: the electromagnetic energy is used to drive the lattice vibrations. This mode occurs in dielectric materials and is called a polariton. Another resonant mode occurs in metals with similar enhanced local fields, however the mechanism is quite different,

where the coupling is to longitudinal plasma waves. This excited mode is called a surface plasmon (see, *e.g.,* Nelson (1979)).

Previous work in the Radiation Laboratory of the EECS Department along lines similar to that used here has been used to analyze the scattering and absorption characteristics of many different shapes (*e.g.,* Czerwinski (1984); Senior and Ahlgren (1972); Weil (1986); Weil, *et al.* (1985); Willis (1982); Senior and Willis (1982)). The present research uses and extends this for two families of shapes: coagulated spheres (not just tangent spheres) and agglomerating spheres as a start to modeling the complex electromagnetic behavior of the many aerosol and colloidal systems that consist of aggregated particles. The work with agglomerating spheres investigates the electric fields in and surrounding a pair of particles as well as the effects of these fields on the agglomeration dynamics and final shapes of such clusters. Another application of the theory is made to the mechanism of photosynthesis in plants.

Our study of the particles consists of a variety of measures of their scattering and absorption characteristics, as well as their near and internal field structures.

1.2 Overview of the Literature

Since the pioneering work of Rayleigh (1897) in small particle scattering, there has been much research in the area. Phillips (1934) formulated the static problem as an integral equation for a general homogeneous dielectric body. Later Stevenson formulated the three lowest-order terms of the expansion in kd (a dimensionless measure of frequency) for a general body (Stevenson (1953a)) and an ellipsoid (Stevenson (1953b)). A good survey book by van de Hulst (1957) helped to unify the notation and gather many important results. Siegel (1959a, 1959b) established some approximate formulas for any body. Later, a series of papers by Kleinman, Senior, and Keller rigorously established many general facts concerning the far field (Kleinman (1967)), induced dipole moments (Keller, *et al.* (1972); Kleinman (1973)), and polarizability tensors (Kleinman (1965); Kleinman and Senior (1972,

1986); Senior (1976, 1980, 1982); Senior and Ahlgren (1972)), all for general homogeneous dielectric bodies, as well as perfect conductors. More specialized studies followed: Herrick and Senior (1972), Weil (1986), Weil, Senior, and Willis (1985), Fuchs (1975, 1978), and Ruppin (1978), as well as more general numerical techniques: Mei and van Bladel (1963); Arvas, Harrington, and Mautz (1986); Sarkar, *et al.* (1981). In addition Ramm (1982) formulated the integral equations in a very rigorous way, without actually implementing them on a computer.

Recently, particle shape came to be recognized as more important than previously thought. Many specific particle shapes have been investigated experimentally, theoretically, and numerically. While nobody has presented analytical closed-form results for the coagulated-sphere shape mentioned previously, there have been results for these shapes in terms of integrals, but only for perfect conductors (Macdonald (1895), Snow (1949)). Nobody has yet investigated the coagulated-sphere shape for dielectric materials and low frequencies, but many authors have studied the two-sphere family of shapes, where the spheres are either separate or touching. Several have looked at the two-sphere problem analytically, as the surfaces are complete spheres. Dielectric sphere pairs were treated by Olaofe (1970), Borghese, *et al.* (1987a, 1987b), Ross (1975, 1976), Goyette and Navon (1976), Ruppin (1982) and, most completely, by Love (1975), although his formulation is not valid if the two spheres are touching. Of course, these treatments are confined to just two separate spheres, and do not do the type of extended analysis included here. Perfectly conducting and touching spheres were treated by: Smith and Barakat (1975); Jeffrey and Onishi (1980); Féat and Levine (1973, 1976a, 1976b); and also O'Meara and Saville (1980), while the problem of nearly-touching perfectly conducting spheres was treated by Jeffrey and van Dyke (1978). Experimental investigations have been done by Wang, *et al.* (1981), with subsequent numerical verification by Kattawar and Dean (1983), and Fuller, *et al.* (1986). These measurements included electri-

cally large- as well as small-particle scattering.

Many other shapes have been treated. Most of the following, however, do not specifically treat or are not limited to electrically small particles. Included among the shapes studied are cubes (Herrick and Senior (1977); Fuchs (1975); Ruppin (1978)), thin disks (Willis (1982); Willis, Weil, and LeVine (1988)), spheres with Chebyshev surface perturbations (Wiscombe and Mugnai (1980); Kiehl, *et al.,* (1980)), as well as others: Embury (1980), Huffman and Bohren (1980), and Kattawar and Humphreys (1980). Experimentally, many irregularly-shaped particles have been treated: Saunders (1970, 1980); Grams (1980); Wang (1980); Zerull, *et al.* (1980, 1984); Bottiger, *et al.* (1980); Srivistava and Brownlee (1980); Bickel and Stafford (1980); Pinnick, *et al.* (1976); Holland and Gagne (1970); and also Fahlen and Bryant (1966). Other studies of a numerical or theoretical nature include Asano and Yamamoto (1975), spheroid theory; Fuchs (1975, 1978), cube theory; and Czerwinski (1984) who numerically investigated the effects of surface roughness on spheroid-like shapes.

Turning now to applications-oriented research, there has been, and still is, a great interest in understanding the light scattering properties of chemical and biological systems. Early on the aim was to understand the brilliant colors of certain colloidal solutions and much effort went into experiments and theory about them. The most famous is the theoretical work of Mie (1908) which models the colloid as a sparse collection of spheres, and presented the so-called Mie theory for scattering by spheres. However, as is well-known today (see fig. 1.1), the small nearly-spherical particles in these colloids tend to cluster together into complex chains. A modern treatment of Mie theory can be found in many references including Bohren and Huffman (1983). Since Mie's time, many investigators have tried to account for the electromagnetic effects due to this clustering in various ways and sometimes with different applications in mind (*e.g.,* Weitz, *et al.* (1986); Berry and Percival (1986)).

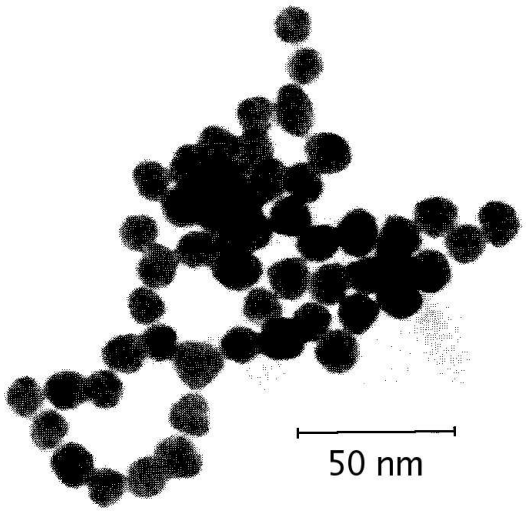

Figure 1.1 — Photo of aggregated gold colloid particles. (From fig. 1 of Weitz, *et al.* (1985))

Hence, there are many applications where light scattering from coagulated particles is of interest. The latter part of this research aims to shed light on this coagulation phenomenon as it relates to light scattering.

The dynamics of the coagulation of small particles has long been of interest. Hocking (1959) presented a simple formulation for the coagulation of two small spherical particles falling in a fluid. Later, Kransogorskaya (1965a, 1965b) extended his work to include the static electromagnetic forces associated with perfectly conducting spheres, using the work of Davis (1962, 1964a, 1964b). The present work extends this to the coagulation of illuminated lossy dielectric spheres, using a static electric field approximation.

1.3 Overview of the thesis

Section 1.4 presents many of the equations governing Rayleigh scattering as derived by Kleinman and Senior over the years, and specialized to scattering by dielectrics. Rayleigh scattering theory is used to approximate the interactions in

this thesis. The particles are electrically small in the sense that their maximum dimensions are small compared to the free space wavelength of the incident field. Note that in Rayleigh scattering the appropriate permittivity is that of the material at the frequency of the incident radiation: $\epsilon(\omega)$ (complex), **not** that at zero frequency: $\epsilon(0)$. This is because the Rayleigh approximation ignores the phase of the incident fields, as in statics, but the material still behaves as if it is in a field of the given frequency.

Chapter 2 presents the basic formulation used throughout the thesis. First the statics problem that is presented in section 1.4 is treated for an arbitrary homogeneous dielectric body using an integral equation method. Next, this solution is specialized to a body with rotational symmetry, and the azimuthal integral carried out. The numerical implementation is presented next, with some comments on the integration procedures following that. Lastly, the accuracy of the programs so developed is verified through a variety of means, both theory and measurement, for some simple shapes.

The next chapter presents the results for the change in absorption characteristics of two spheres when they coagulate. First we present some motivation for the study, followed by the formulation of the absorption cross-section for our system of particles. Next we present our model for the polarizability of non-spherical particles, which is used later. Lastly, we present our results for small gold spheres.

Chapter 4 presents an analysis of the coagulation of two dielectric spheres falling in the atmosphere with an optical or infrared field incident on them. We explore the forces between them and their trajectories when the vibrational aspect of the motion can be neglected. The effects of irradiation at a wavelength near an absorption resonance on the forces and motion is compared and contrasted with the forces and motion when not near a resonance.

Chapter 5 presents a first approximation in applying the resonance concept

to absorption of light in photosynthesis. After the problem is made tractable by appropriate simplifications, the absorption by different geometries that occur in nature are compared to each other. Since chlorophyll appears to have absorption resonances in the visible, and because it often resides in structures that are much smaller than the incident wavelengths, resonant absorption is very probably occurring. This chapter shows some aspects of that absorption, and postulates as to its use in different plants.

Finally, the last chapter gives the conclusions and ideas for possible future extensions to the present work.

1.4 Introduction to Rayleigh Scattering

This section follows Kleinman and Senior (1986). Their presentation is specialized here to dielectric bodies, and sets the stage for the work in Chapter 2. This derivation is the basis for all of the electromagnetic field calculations in this thesis, and as such is included here.

1.4.1 The Scattered Fields

Assume time-harmonic incident fields, $\mathbf{E}^{inc}e^{-i\omega t}$ and $\mathbf{H}^{inc}e^{-i\omega t}$, exterior to a closed finite body with bounding surface S. Hence

$$\nabla \times \mathbf{E}^{inc} = ik_0 Z_0 \mathbf{H}^{inc} \qquad \nabla \times \mathbf{H}^{inc} = -ik_0 Y_0 \mathbf{E}^{inc} \tag{1.1}$$

except at the source. In the above we have:

$$Z_0 = \sqrt{\frac{\mu_0}{\epsilon_0}}; \quad Y_0 = \frac{1}{Z_0}, \text{ and } k_0 = \omega\sqrt{\mu_0\epsilon_0} \tag{1.2}$$

The total field in the exterior region is made up of the incident and scattered fields:

$$\mathbf{E}^t_{ext} = \mathbf{E}^{inc} + \mathbf{E}^s \qquad \mathbf{H}^t_{ext} = \mathbf{H}^{inc} + \mathbf{H}^s \tag{1.3}$$

with $\mathbf{r} \in \text{ext}(S)$, and where the scattered fields satisfy:

$$\nabla \times \mathbf{E}^s = ik_0 Z_0 \mathbf{H}^s \qquad \nabla \times \mathbf{H}^s = -ik_0 Y_0 \mathbf{E}^s \tag{1.4}$$

with $\mathbf{r} \in \text{ext}(S)$ and

$$\lim_{r\to\infty} \mathbf{r} \times (\nabla \times \mathbf{E}^s) + ik_0 r \mathbf{E}^s = \lim_{r\to\infty} \mathbf{r} \times (\nabla \times \mathbf{H}^s) + ik_0 r \mathbf{H}^s = 0 \tag{1.5}$$

where $\mathbf{r}$ is a point in space and r is its magnitude.

The total field in the interior of a lossy dielectric satisfies:

$$\nabla \times \mathbf{E}^t_{int} = i\omega\mu_1 \mathbf{H}^t_{int}\,, \qquad \nabla \times \mathbf{H}^t_{int} = (-i\omega\epsilon_1 + \sigma_1)\mathbf{E}^t_{int} \tag{1.6}$$

where the dielectric is characterized by permittivity ϵ_1, permeability μ_1, and conductivity σ_1. There are also the boundary conditions:

$$\hat{\mathbf{n}} \times \mathbf{E}^t_{int} = \hat{\mathbf{n}} \times \mathbf{E}^t_{ext} \tag{1.7}$$

$$\hat{\mathbf{n}} \times \mathbf{H}^t_{int} = \hat{\mathbf{n}} \times \mathbf{H}^t_{ext} \tag{1.8}$$

$$\hat{\mathbf{n}} \cdot (\epsilon_1 + i\sigma_1/\omega)\mathbf{E}^t_{int} = \hat{\mathbf{n}} \cdot \epsilon_0 \mathbf{E}^t_{ext} \tag{1.9}$$

$$\hat{\mathbf{n}} \cdot \mu_1 \mathbf{H}^t_{int} = \hat{\mathbf{n}} \cdot \mu_0 \mathbf{H}^t_{ext} \tag{1.10}$$

for $\mathbf{r} \in S$ and with $\hat{\mathbf{n}}$ the outward normal to the surface at $\mathbf{r}$.

One can write the representations for these fields as integrals over the surface (the Stratton-Chu equations: see Stratton (1941), p. 466).

$$\alpha(\mathbf{r})\mathbf{E}^s(\mathbf{r}) = \frac{1}{4\pi}\int_S \Big[ik_0 Z_0 \frac{e^{ik_0 R}}{R}\hat{\mathbf{n}}' \times \mathbf{H}^s(\mathbf{r}') + \nabla'\left(\frac{e^{ik_0 R}}{R}\right)\hat{\mathbf{n}}' \cdot \mathbf{E}^s(\mathbf{r}') - \nabla'\left(\frac{e^{ik_0 R}}{R}\right) \times \left(\hat{\mathbf{n}}' \times \mathbf{E}^s(\mathbf{r}')\right)\Big]\, dS' \tag{1.11}$$

$$\alpha(\mathbf{r})\mathbf{H}^s(\mathbf{r}) = \frac{1}{4\pi}\int_S \Big[-ik_0 Y_0 \frac{e^{ik_0 R}}{R}\hat{\mathbf{n}}' \times \mathbf{E}^s(\mathbf{r}') + \nabla'\left(\frac{e^{ik_0 R}}{R}\right)\hat{\mathbf{n}}' \cdot \mathbf{H}^s(\mathbf{r}') - \nabla'\left(\frac{e^{ik_0 R}}{R}\right) \times \left(\hat{\mathbf{n}}' \times \mathbf{H}^s(\mathbf{r}')\right)\Big]\, dS' \tag{1.12}$$

$$\mathbf{r} \in S \cup \text{ext}(S)$$

where:

$$\alpha(\mathbf{r}) = \begin{cases} 1, & \mathbf{r} \in \text{ext}(S); \\ \frac{1}{2}, & \mathbf{r} \in S; \\ 0, & \mathbf{r} \in \text{int}(S). \end{cases} \tag{1.13}$$

$$R = |\mathbf{r} - \mathbf{r}'| \tag{1.14}$$

and S is assumed to be smooth (continuous first derivatives).

Similarly for the incident field, since it satisfies Maxwell's equations in the interior region:

$$[\alpha(\mathbf{r})-1]\mathbf{E}^{inc}(\mathbf{r}) = \frac{1}{4\pi}\int_S \Big[ik_0 Z_0 \frac{e^{ik_0R}}{R}\hat{\mathbf{n}}'\times\mathbf{H}^{inc}(\mathbf{r}') + \nabla'\left(\frac{e^{ik_0R}}{R}\right)\hat{\mathbf{n}}'\cdot\mathbf{E}^{inc}(\mathbf{r}') - \nabla'\left(\frac{e^{ik_0R}}{R}\right)\times\Big(\hat{\mathbf{n}}'\times\mathbf{E}^{inc}(\mathbf{r}')\Big)\Big]\,dS' \tag{1.15}$$

$$[\alpha(\mathbf{r})-1]\mathbf{H}^{inc}(\mathbf{r}) = \frac{1}{4\pi}\int_S \Big[-ik_0 Y_0 \frac{e^{ik_0R}}{R}\hat{\mathbf{n}}'\times\mathbf{E}^{inc}(\mathbf{r}') + \nabla'\left(\frac{e^{ik_0R}}{R}\right)\hat{\mathbf{n}}'\cdot\mathbf{H}^{inc}(\mathbf{r}') - \nabla'\left(\frac{e^{ik_0R}}{R}\right)\times\Big(\hat{\mathbf{n}}'\times\mathbf{H}^{inc}(\mathbf{r}')\Big)\Big]\,dS' \tag{1.16}$$

$\mathbf{r}\notin$ Source

Combining these two sets of equations in the exterior region:

$$\mathbf{E}^{s}(\mathbf{r}) = \frac{1}{4\pi}\int_S \Big[ik_0 Z_0 \frac{e^{ik_0R}}{R}\hat{\mathbf{n}}'\times\mathbf{H}^{t}_{ext}(\mathbf{r}') + \nabla'\left(\frac{e^{ik_0R}}{R}\right)\hat{\mathbf{n}}'\cdot\mathbf{E}^{t}_{ext}(\mathbf{r}') - \nabla'\left(\frac{e^{ik_0R}}{R}\right)\times\Big(\hat{\mathbf{n}}'\times\mathbf{E}^{t}_{ext}(\mathbf{r}')\Big)\Big]\,dS' \tag{1.17}$$

$$\mathbf{H}^{s}(\mathbf{r}) = \frac{1}{4\pi}\int_S \Big[-ik_0 Y_0 \frac{e^{ik_0R}}{R}\hat{\mathbf{n}}'\times\mathbf{E}^{t}_{ext}(\mathbf{r}') + \nabla'\left(\frac{e^{ik_0R}}{R}\right)\hat{\mathbf{n}}'\cdot\mathbf{H}^{t}_{ext}(\mathbf{r}') - \nabla'\left(\frac{e^{ik_0R}}{R}\right)\times\Big(\hat{\mathbf{n}}'\times\mathbf{H}^{t}_{ext}(\mathbf{r}')\Big)\Big]\,dS' \tag{1.18}$$

$\mathbf{r}\in \mathrm{ext}(S)$

1.4.2 Far field

The far field is important for understanding the absorption characteristics of small particles. Using the approximations

$$\frac{e^{ik_0R}}{R} = \frac{e^{(ik_0r - ik_0\hat{\mathbf{r}}\cdot\mathbf{r}')}}{r} \tag{1.19}$$

$$\nabla\times\left(\frac{e^{ik_0R}}{R}\right)\hat{\mathbf{n}}' = \frac{ik_0}{r}(\mathbf{r}\times\hat{\mathbf{n}}')e^{(ik_0r - ik_0\hat{\mathbf{r}}\cdot\mathbf{r}')} \tag{1.20}$$

the fields become

$$\mathbf{E}^s(\mathbf{r}') = \frac{e^{ik_0 r}}{4\pi r} ik_0 \Big[\hat{\mathbf{r}} \times \int_S \hat{\mathbf{n}}' \times \mathbf{E}^t_{ext}(\mathbf{r}') e^{-ik_0 \hat{\mathbf{r}}\cdot\mathbf{r}'}\, dS' - Z_0 \hat{\mathbf{r}} \times \hat{\mathbf{r}} \times \int_S \hat{\mathbf{n}}' \times \mathbf{H}^t_{ext}(\mathbf{r}') e^{-ik_0 \hat{\mathbf{r}}\cdot\mathbf{r}'}\, dS' \Big] \tag{1.21}$$

$$\mathbf{H}^s(\mathbf{r}) = Y_0 \hat{\mathbf{r}} \times \mathbf{E}^s(\mathbf{r}) \tag{1.22}$$

$\mathbf{r}$ far from S

From Kleinman (1967):

$$\int_S \hat{\mathbf{n}}' \times \mathbf{F}\, dS' = \int_S \mathbf{r}' \hat{\mathbf{n}}' \cdot \nabla' \times \mathbf{F}\, dS' \tag{1.23}$$

Applying this identity to the above equations for the far field gives:

$$\int_S \hat{\mathbf{n}}' \times \mathbf{E}^t_{ext}(\mathbf{r}') e^{-ik_0 \hat{\mathbf{r}}\cdot\mathbf{r}'}\, dS' = \int_S \mathbf{r}' \hat{\mathbf{n}}' \cdot \nabla' \times \left[\mathbf{E}^t_{ext}(\mathbf{r}') e^{-ik_0 \hat{\mathbf{r}}\cdot\mathbf{r}'}\right] dS' \tag{1.24}$$

and now:

$$\nabla' \times \left[\mathbf{E}^t_{ext}(\mathbf{r}') e^{-ik_0 \hat{\mathbf{r}}\cdot\mathbf{r}'}\right] = \nabla'\left(e^{-ik_0 \hat{\mathbf{r}}\cdot\mathbf{r}'}\right) \times \mathbf{E}^t_{ext}(\mathbf{r}') + e^{-ik_0 \hat{\mathbf{r}}\cdot\mathbf{r}'} \nabla' \times \mathbf{E}^t_{ext}(\mathbf{r}') \tag{1.25}$$

$$= -ik_0 e^{-ik_0 \hat{\mathbf{r}}\cdot\mathbf{r}'} \hat{\mathbf{r}} \times \mathbf{E}^t_{ext}(\mathbf{r}') + e^{-ik_0 \hat{\mathbf{r}}\cdot\mathbf{r}'} \nabla' \times \mathbf{E}^t_{ext}(\mathbf{r}') \tag{1.26}$$

and using Maxwell's equations gives:

$$\nabla' \times \left[\mathbf{E}^t_{ext}(\mathbf{r}') e^{-ik_0 \hat{\mathbf{r}}\cdot\mathbf{r}'}\right] = \left[-ik_0 \hat{\mathbf{r}} \times \mathbf{E}^t_{ext}(\mathbf{r}') + ik_0 Z_0 \mathbf{H}^t_{ext}(\mathbf{r}')\right] e^{-ik_0 \hat{\mathbf{r}}\cdot\mathbf{r}'} \tag{1.27}$$

Similarly:

$$\int_S \hat{\mathbf{n}}' \times \mathbf{H}^t_{ext}(\mathbf{r}') e^{-ik_0 \hat{\mathbf{r}}\cdot\mathbf{r}'}\, dS' = \int_S \mathbf{r}' \hat{\mathbf{n}}' \cdot \nabla' \times \left[\mathbf{H}^t_{ext}(\mathbf{r}') e^{-ik_0 \hat{\mathbf{r}}\cdot\mathbf{r}'}\right] dS' \tag{1.28}$$

$$\nabla' \times \left[\mathbf{H}^t_{ext}(\mathbf{r}') e^{-ik_0 \hat{\mathbf{r}}\cdot\mathbf{r}'}\right] = -ik_0 e^{-ik_0 \hat{\mathbf{r}}\cdot\mathbf{r}'} \hat{\mathbf{r}} \times \mathbf{H}^t_{ext}(\mathbf{r}') + e^{-ik_0 \hat{\mathbf{r}}\cdot\mathbf{r}'} \nabla' \times \mathbf{H}^t_{ext}(\mathbf{r}') \tag{1.29}$$

$$= \left[-ik_0 \hat{\mathbf{r}} \times \mathbf{H}^t_{ext}(\mathbf{r}') - ik_0 Y_0 \mathbf{E}^t_{ext}(\mathbf{r}')\right] e^{-ik_0 \hat{\mathbf{r}}\cdot\mathbf{r}'} \tag{1.30}$$

This gives:

$$\mathbf{E}^s(\mathbf{r}) = \frac{e^{ik_0 r}}{4\pi r} k_0^2 \Big[\hat{\mathbf{r}} \times \hat{\mathbf{r}} \times \int_S \mathbf{r}' \Big[Z_0 \hat{\mathbf{r}} \cdot \hat{\mathbf{n}}' \times \mathbf{H}^t_{ext}(\mathbf{r}') - \hat{\mathbf{n}}' \cdot \mathbf{E}^t_{ext}(\mathbf{r}')\Big] e^{-ik_0 \hat{\mathbf{r}}\cdot\mathbf{r}'}\, dS' - \hat{\mathbf{r}} \times \int_S \mathbf{r}' \Big[\hat{\mathbf{r}} \cdot \hat{\mathbf{n}}' \times \mathbf{E}^t_{ext}(\mathbf{r}') + Z_0 \hat{\mathbf{n}}' \cdot \mathbf{H}^t_{ext}(\mathbf{r}')\Big] e^{-ik_0 \hat{\mathbf{r}}\cdot\mathbf{r}'}\, dS' \Big] \tag{1.31}$$

$$\equiv \frac{e^{ik_0 r}}{4\pi r} \mathbf{S}(\hat{\mathbf{r}}) \tag{1.32}$$

$\mathbf{r} \in$ far field

1.4.3 Plane Wave Incidence

Assume a linearly-polarized, unit-amplitude plane wave incident on the body:

$$\mathbf{E}^{inc}(\mathbf{r}) = \hat{\mathbf{a}} e^{ik_0 \hat{\mathbf{k}}_0 \cdot \mathbf{r}} \qquad \mathbf{H}^{inc}(\mathbf{r}) = Y_0 \hat{\mathbf{b}} e^{ik_0 \hat{\mathbf{k}}_0 \cdot \mathbf{r}} \tag{1.33}$$

where $\hat{\mathbf{b}} = \hat{\mathbf{k}}_0 \times \hat{\mathbf{a}}, \quad \hat{\mathbf{a}} \cdot \hat{\mathbf{k}}_0 = 0; \quad$ *i.e.,* $\hat{\mathbf{a}}, \hat{\mathbf{b}}, \hat{\mathbf{k}}_0$ are mutually orthogonal.

For completeness some well-known cross-sections are defined next.

Radar Cross-Section:

$$\sigma(\hat{\mathbf{r}}) = \lim_{r \to \infty} 4\pi r^2 \frac{|\mathbf{E}^s|^2}{|\mathbf{E}^{inc}|^2} = \frac{1}{4\pi} \left| \mathbf{S}(\hat{\mathbf{r}}, \hat{\mathbf{k}}_0, \hat{\mathbf{a}}) \right|^2 \tag{1.34}$$

where $\hat{\mathbf{k}}_0$ is the incident field direction and $\hat{\mathbf{a}}$ is its polarization, as in (1.33).

Total Scattering Cross-Section:

$$\sigma_T = \frac{1}{4\pi} \int_\Omega \sigma(\hat{\mathbf{r}})\, d\Omega = \int_{B_\infty} |\mathbf{E}^s|^2 dS \tag{1.35}$$

$$= Z_0 Re \int_{B_\infty} \hat{\mathbf{n}} \cdot \mathbf{E}^s \times \mathbf{H}^{s*}\, dS \tag{1.36}$$

where Ω is a unit sphere, B_∞ is a sphere of radius ∞, and $(\ )^*$ denotes the complex conjugate.

Absorption Cross-Section:

$$\sigma_A = Z_0 Re \int_S \hat{\mathbf{n}} \cdot \mathbf{H}^t_{ext} \times (\mathbf{E}^t_{ext})^*\, dS' \tag{1.37}$$

Extinction Cross-Section:

$$\sigma_{ext} = \sigma_T + \sigma_A \tag{1.38}$$

but also from the forward scattering theorem (e.g., see van de Hulst (1957), pp. 30–31, or Born and Wolf (1980), p. 657):

$$\sigma_{ext} = \frac{1}{k_0} Im\{\hat{\mathbf{a}} \cdot \mathbf{S}(\hat{\mathbf{k}}_0, \hat{\mathbf{k}}_0, \hat{\mathbf{a}})\} \tag{1.39}$$

1.4.4 Rayleigh Scattering of Plane Waves

Expand the incident and scattered fields in powers of (ik_0):

$$\mathbf{E}^{inc}(\mathbf{r}) = \sum_{n=0}^{\infty} (ik_0)^n \mathbf{E}_n^{inc}(\mathbf{r}) \qquad \mathbf{E}_n^{inc}(\mathbf{r}) = \hat{\mathbf{a}} \frac{(\hat{\mathbf{k}}_0 \cdot \mathbf{r})^n}{n!} \tag{1.40}$$

$$\mathbf{H}^{inc}(\mathbf{r}) = \sum_{n=0}^{\infty} (ik_0)^n \mathbf{H}_n^{inc}(\mathbf{r}) \qquad \mathbf{H}_n^{inc}(\mathbf{r}) = Y_0 \hat{\mathbf{a}} \frac{(\hat{\mathbf{k}}_0 \cdot \mathbf{r})^n}{n!} \tag{1.41}$$

for all $k_0 r$, and similarly:

$$\mathbf{E}^{s}(\mathbf{r}) = \sum_{n=0}^{\infty} (ik_0)^n \mathbf{E}_n^{s}(\mathbf{r}) \qquad \mathbf{H}^{s}(\mathbf{r}) = \sum_{n=0}^{\infty} (ik_0)^n \mathbf{H}_n^{s}(\mathbf{r}) \tag{1.42}$$

for small $k_0 r$ and $k_0 X$ only, where X is a characteristic dimension of the body. The coefficients of $(ik_0)^n$ do not depend on k_0, of course.

That the permittivity is not expanded in a series as well may be of some concern. This is especially true when ϵ varies rapidly as a function of frequency. However, because of the assumption of plane-wave incidence at some fixed frequency, one would intuitively think that the material will behave with the ϵ at the incident frequency. The verification section (2.5) will show this to be true for the cases studied here.

Returning now to the series expressions, apply Maxwell's equations to the series for the scattered fields:

$$\nabla \times \mathbf{E}^s = ik_0 Z_0 \mathbf{H}^s \qquad \nabla \times \mathbf{H}^s = -ik_0 Y_0 \mathbf{E}^s \tag{1.43}$$

This gives the two series expressions

$$\sum_{n=0}^{\infty} (ik_0)^n \nabla \times \mathbf{E}_n^s(\mathbf{r}) = ik_0 Z_0 \sum_{n=0}^{\infty} (ik_0)^n \mathbf{H}_n^s(\mathbf{r}) \tag{1.44}$$

$$\sum_{n=0}^{\infty} (ik_0)^n \nabla \times \mathbf{H}_n^s(\mathbf{r}) = -ik_0 Y_0 \sum_{n=0}^{\infty} (ik_0)^n \mathbf{E}_n^s(\mathbf{r}). \tag{1.45}$$

These can be simplified to

$$\sum_{n=0}^{\infty} (ik_0)^n \nabla \times \mathbf{E}_n^s(\mathbf{r}) = Z_0 \sum_{n=0}^{\infty} (ik_0)^{n+1} \mathbf{H}_n^s(\mathbf{r}) \tag{1.46}$$

$$\sum_{n=0}^{\infty} (ik_0)^n \nabla \times \mathbf{H}_n^s(\mathbf{r}) = -Y_0 \sum_{n=0}^{\infty} (ik_0)^{n+1} \mathbf{E}_n^s(\mathbf{r}), \tag{1.47}$$

giving for $\mathbf{E}^s$

$$\nabla\times\mathbf{E}_0^s(\mathbf{r})+(ik_0)\nabla\times\mathbf{E}_1^s(\mathbf{r})+(ik_0)^2\nabla\times\mathbf{E}_2^s(\mathbf{r})+\cdots=Z_0\Big[(ik_0)\mathbf{H}_0^s(\mathbf{r})+(ik_0)^2\mathbf{H}_1^s(\mathbf{r})+\cdots\Big] \tag{1.48}$$

Hence, the 0^{th}-order term gives $\nabla\times\mathbf{E}_0^s(\mathbf{r})=0$. Similarly for $\mathbf{H}^s$: $\nabla\times\mathbf{H}_0^s(\mathbf{r})=0$.

So the determination of the 0^{th}-order scattered fields simplifies to the determination of the solution to two Laplacians:

$$\mathbf{E}_0^s(\mathbf{r})=-\nabla\Phi_0^s(\mathbf{r}) \qquad \nabla^2\Phi_0^s(\mathbf{r})=0 \tag{1.49}$$

$$\mathbf{H}_0^s(\mathbf{r})=-Y_0\nabla\Psi_0^s(\mathbf{r}) \qquad \nabla^2\Psi_0^s(\mathbf{r})=0. \tag{1.50}$$

$$\mathbf{r}\in\mathrm{ext}(S)$$

Since the total field in the exterior is the sum of the incident and scattered fields: $\mathbf{E}_{ext,n}^t=\mathbf{E}_n^s+\mathbf{E}_n^{inc}$ and $\mathbf{H}_{ext,n}^t=\mathbf{H}_n^s+\mathbf{H}_n^{inc}$, the total fields are given by

$$\mathbf{E}_{ext,0}^t(\mathbf{r})=-\nabla\Phi_0^t(\mathbf{r}) \qquad \mathbf{H}_{ext,0}^t(\mathbf{r})=-Y_0\nabla\Psi_0^t(\mathbf{r}). \tag{1.51}$$

Because the incident fields can be expressed as

$$\Phi_0^{inc}(\mathbf{r})=-(\hat{\mathbf{a}}\cdot\mathbf{r}+c) \tag{1.52}$$

$$\Psi_0^{inc}(\mathbf{r})=-(\hat{\mathbf{b}}\cdot\mathbf{r}+c_1) \tag{1.53}$$

the total potentials are given by

$$\Phi_0^t(\mathbf{r})=\Phi_0^s(\mathbf{r})-\hat{\mathbf{a}}\cdot\mathbf{r}-c \tag{1.54}$$

$$\Psi_0^t(\mathbf{r})=\Psi_0^s(\mathbf{r})-\hat{\mathbf{b}}\cdot\mathbf{r}-c_1, \tag{1.55}$$

and so the total exterior potentials also satisfy the Laplacian: $\nabla^2\Phi_0^t(\mathbf{r})=0$ and $\nabla^2\Psi_0^t(\mathbf{r})=0$ for $\mathbf{r}\in\mathrm{ext}(S)$.

Hence, to find the 0^{th} order fields one solves the above statics problem.

1.4.5 Boundary Conditions

The 0^{th}-order boundary conditions are those of the statics problem. Restating those here, in the present notation, where $\epsilon = \epsilon_1 + i\sigma_1/\omega$ is the complex permittivity, gives the following. From the continuity of the total potential

$$\Phi^s_{ext,0} = \Phi^t_{int,0} + \hat{\mathbf{a}} \cdot \mathbf{r} + c, \tag{1.56}$$

and from the continuity of the normal component of $\mathbf{D}$

$$\frac{\partial}{\partial n}\Phi^s_{ext,0} = \frac{\epsilon}{\epsilon_0}\frac{\partial}{\partial n}\Phi^t_{int,0} + \hat{\mathbf{n}} \cdot \hat{\mathbf{a}}. \tag{1.57}$$

1.4.6 Far Field of Dipole

The following derivation follows that of Kleinman (1973). The scattered field satisfies Maxwell's equations in the region exterior to the body:

$$\nabla \times \mathbf{E}^s = ik_0 Z_0 \mathbf{H}^s \qquad \nabla \times \mathbf{H}^s = -ik_0 Y_0 \mathbf{E}^s \tag{1.58}$$

and satisfies the radiation condition (1.5).

From (1.31), because the incident field has no contribution:

$$\mathbf{E}^s = \frac{e^{ik_0 r}}{4\pi r} k_0^2 \hat{\mathbf{r}} \times \int_S \Big\{ (\hat{\mathbf{r}} \times \mathbf{r}')(\hat{\mathbf{r}} \cdot \hat{\mathbf{n}}' \times Z_0 \mathbf{H}^s_0 - \hat{\mathbf{n}}' \cdot \mathbf{E}^s_0) - \mathbf{r}'(\hat{\mathbf{r}} \cdot \hat{\mathbf{n}}' \times \mathbf{E}^s_0 + Z_0 \hat{\mathbf{n}}' \cdot \mathbf{H}^s_0) \Big\}\, dS' \tag{1.59}$$

where:

$$\mathbf{E}^s_0 = \lim_{k_0 \to 0} \mathbf{E}^s, \text{ etc.} \tag{1.60}$$

and $Z_0 \mathbf{H}^s = \hat{\mathbf{r}} \times \mathbf{E}^s$ in the far field.

Kleinman (1973) shows that:

$$\int (\hat{\mathbf{r}} \cdot \hat{\mathbf{n}}' \times \mathbf{F}) \mathbf{r}'\, dS' = \frac{\hat{\mathbf{r}}}{2} \times \int \mathbf{r}' \times (\hat{\mathbf{n}}' \times \mathbf{F})\, dS' \tag{1.61}$$

If one uses $\mathbf{F} = \mathbf{E}^s_0$ and $\mathbf{F} = \mathbf{H}^s_0$ separately, then (1.61) becomes:

$$\begin{aligned} \mathbf{E}^s = -\frac{e^{ik_0 r}}{4\pi r} k_0^2 \Big\{ \hat{\mathbf{r}} \times \hat{\mathbf{r}} \times \int_S \Big[\mathbf{r}'(\hat{\mathbf{n}}' \cdot \mathbf{E}^s_0) + \frac{1}{2}\mathbf{r}' \times (\hat{\mathbf{n}}' \times \mathbf{E}^s_0) \Big]\, dS' \\ + \hat{\mathbf{r}} \times \int_S \Big[\mathbf{r}' Z_0 \hat{\mathbf{n}}' \cdot \mathbf{H}^s_0 + \frac{1}{2}\mathbf{r}' Z_0 \times (\hat{\mathbf{n}}' \times \mathbf{H}^s_0) \Big]\, dS' \Big\} \end{aligned} \tag{1.62}$$

Form an alternate expression for (1.62) using the potentials that define the static fields:

$$\mathbf{E}_0^s = -\nabla\Phi_0^s\,, \qquad\qquad \mathbf{H}_0^s = -Y_0\nabla\Psi_0^s \tag{1.63}$$

Comparing this with (1.62) it is clear that we will need to simplify the following expression:

$$\int \mathbf{r}' \times (\hat{\mathbf{n}}' \times \nabla' f)\, dS' = \int \Big(\sum_{i=1}^{3} \hat{\mathbf{x}}_i x_i'\Big) \times (\hat{\mathbf{n}}' \times \nabla' f)\, dS' \tag{1.64}$$

$$= \sum_{i=1}^{3} \int \hat{\mathbf{x}}_i \times [(\hat{\mathbf{n}}' \times \nabla' f) x_i']\, dS' \tag{1.65}$$

Kleinman (1973) does this and gets:

$$\int \mathbf{r}' \times (\hat{\mathbf{n}}' \times \nabla' f)\, dS' = -2 \int f \hat{\mathbf{n}}'\, dS' \tag{1.66}$$

Using this identity, (1.62) is finally transformed into:

$$\mathbf{E}^s = -\frac{e^{ik_0 r}}{4\pi r} k_0^2 \Big\{ \hat{\mathbf{r}} \times \hat{\mathbf{r}} \times \int_S \Big[-\mathbf{r}' \frac{\partial}{\partial n'} \Phi_0^s + \hat{\mathbf{n}}' \Phi_0^s \Big]\, dS' + \hat{\mathbf{r}} \times \int_S \Big[-\mathbf{r}' \frac{\partial}{\partial n'} \Psi_0^s + \hat{\mathbf{n}}' \Psi_0^s \Big]\, dS' \Big\} \tag{1.67}$$

1.4.7 Equivalent Dipole Moments

For dipoles ($\mathbf{p}$, $\mathbf{m}$) located at the origin the far field is (*e.g.,* Senior and Kleinman (1986); Jones (1964), p. 532):

$$\mathbf{E}^s = -\frac{e^{ik_0 r}}{4\pi r} k_0^2 \Big\{ \frac{1}{\epsilon_0} \hat{\mathbf{r}} \times \hat{\mathbf{r}} \times \mathbf{p} + Z_0 \hat{\mathbf{r}} \times \mathbf{m} \Big\}. \tag{1.68}$$

Hence, equating with (1.67):

$$\mathbf{p} = \epsilon_0 \int \Big(\hat{\mathbf{n}}' \Phi_0^s - \mathbf{r}' \frac{\partial}{\partial n'} \Phi_0^s \Big)\, dS' \tag{1.69}$$

$$\mathbf{m} = Y_0 \int \Big(\hat{\mathbf{n}}' \Psi_0^s - \mathbf{r}' \frac{\partial}{\partial n'} \Psi_0^s \Big)\, dS', \tag{1.70}$$

and equating with (1.62):

$$\mathbf{p} = \int \Big[\mathbf{r}' (\hat{\mathbf{n}}' \cdot \mathbf{E}_0^s) + \frac{1}{2} \mathbf{r}' \times (\hat{\mathbf{n}}' \times \mathbf{E}_0^s) \Big]\, dS' \tag{1.71}$$

$$\mathbf{m} = \int \Big[\mathbf{r}' (\hat{\mathbf{n}}' \cdot \mathbf{H}_0^s) + \frac{1}{2} \mathbf{r}' \times (\hat{\mathbf{n}}' \times \mathbf{H}_0^s) \Big]\, . dS' \tag{1.72}$$

1.4.8 Polarizability Tensor

In accord with the work in sec. 1.4.4, let:

$$\Phi^s = \sum_{i=1}^{3} (\hat{\mathbf{a}} \cdot \hat{\mathbf{x}}_i)\Phi_i^s \qquad \Psi^s = \sum_{i=1}^{3} (\hat{\mathbf{b}} \cdot \hat{\mathbf{x}}_i)\Psi_i^s \tag{1.73}$$

$$\Phi^{inc} = -\hat{\mathbf{a}} \cdot \mathbf{r} \qquad (\mathbf{E}_0^{inc} = \hat{\mathbf{a}}) \tag{1.74}$$

$$\Psi^{inc} = -\hat{\mathbf{b}} \cdot \mathbf{r} \qquad (\mathbf{H}_0^{inc} = Y_0\hat{\mathbf{b}}) \tag{1.75}$$

and let $\mathbf{p} = \epsilon_0 \overline{\overline{P}} \cdot \hat{\mathbf{a}}$, where $\overline{\overline{P}}$ is the polarizability tensor, whose elements are defined as:

$$P_{ij} = \int_S \left(\hat{\mathbf{n}}' \cdot \hat{\mathbf{x}}_i \Phi_j^s - x_i' \frac{\partial}{\partial n'} \Phi_j^s \right) dS' \tag{1.76}$$

The boundary conditions (1.56) and (1.57) become:

$$\Phi_j^s = \Phi_j + x_j \tag{1.77}$$

$$\frac{\partial}{\partial n}\Phi_j^s = \epsilon_r \frac{\partial}{\partial n}\Phi_j + \hat{\mathbf{n}} \cdot \hat{\mathbf{x}}_j \tag{1.78}$$

both when $\mathbf{r} \in S$. Since

$$\int x_i' \frac{\partial}{\partial n'} \Phi_j^s \, dS' = \epsilon_r \int \nabla' \cdot (x_i' \nabla' \Phi_j) \, dV' + \int \nabla' \cdot (x_i' \cdot \hat{\mathbf{x}}_j) dV' \tag{1.79}$$

$$= \epsilon_r \int (\nabla' \Phi_j) \cdot \hat{\mathbf{x}}_i \, dV' + \int \delta_{ij} \, dV' \tag{1.80}$$

$$= \epsilon_r \int (\hat{\mathbf{x}}_i \cdot \hat{\mathbf{n}}') \Phi_j \, dS' + V\delta_{ij} \tag{1.81}$$

where V is the volume of the body, use the boundary conditions to get:

$$\int x_i' \frac{\partial}{\partial n'} \Phi_j^s \, dS' = \epsilon_r \int (\hat{\mathbf{x}}_i \cdot \hat{\mathbf{n}}') \Phi_j^s \, dS' - \epsilon_r \int (\hat{\mathbf{x}}_i \cdot \hat{\mathbf{n}}') x_j' \, dS' + V\delta_{ij} \tag{1.82}$$

Substitution into (1.76) gives

$$P_{ij} = \int \left[\hat{\mathbf{n}}' \cdot \hat{\mathbf{x}}_i \Phi_j^s - x_i' \frac{\partial}{\partial n'} \Phi_j^s \right] dS' \tag{1.83}$$

$$= \int \hat{\mathbf{n}}' \cdot \hat{\mathbf{x}}_i \Phi_j^s \, dS' - \epsilon_r \int \hat{\mathbf{n}}' \cdot \hat{\mathbf{x}}_i \Phi_j^s \, dS' + \epsilon_r \int (\hat{\mathbf{x}}_i \cdot \hat{\mathbf{n}}') x_j' \, dS' - V\delta_{ij} \tag{1.84}$$

$$= (1 - \epsilon_r) \int \hat{\mathbf{n}}' \cdot \hat{\mathbf{x}}_i \Phi_j^s \, dS' + \epsilon_r \int (\hat{\mathbf{x}}_i \cdot \hat{\mathbf{n}}') x_j' \, dS' - V\delta_{ij} \tag{1.85}$$

and since $\Phi_j^t = \Phi_j^s - x_j$, we have

$$P_{ij} = (1-\epsilon_r)\int \hat{\mathbf{n}}' \cdot \hat{\mathbf{x}}_i \Phi_j^t \, dS' + (1-\epsilon_r)\int (\hat{\mathbf{n}}' \cdot \hat{\mathbf{x}}_i) x_j' \, dS' + \epsilon_r \int (\hat{\mathbf{n}}' \cdot \hat{\mathbf{x}}_i) x_j' \, dS' - V\delta_{ij} \tag{1.86}$$

$$P_{ij} = (1-\epsilon_r)\int \hat{\mathbf{n}}' \cdot \hat{\mathbf{x}}_i \Phi_j^t \, dS' \tag{1.87}$$

CHAPTER II

THE STATICS PROBLEM

2.1 Integral Equations for the Potentials

This section follows Senior (1976).

Start with the theorem from Kellogg (1953), p. 223:

If U_1 is harmonic and continuously differentiable in a region with bounding surface S, then for $\mathbf{r}$ inside the body bounded by S:

$$U_1(\mathbf{r}) = \frac{1}{4\pi}\iint_S \left[\frac{\partial U_1(\mathbf{r}')}{\partial n'}\frac{1}{R} - U_1(\mathbf{r}')\frac{\partial}{\partial n'}\left(\frac{1}{R}\right)\right] dS' \tag{2.1}$$

and for $\mathbf{r}$ outside the body:

$$0 = \frac{1}{4\pi}\iint_S \left[\frac{\partial U_1(\mathbf{r}')}{\partial n'}\frac{1}{R} - U_1(\mathbf{r}')\frac{\partial}{\partial n'}\left(\frac{1}{R}\right)\right] dS' \tag{2.2}$$

where $\hat{\mathbf{n}}$ is the outward normal of the bounding surface, $R = |\mathbf{r} - \mathbf{r}'|$, and $\mathbf{r}'$ is a point on the surface of the body.

If U_2 is harmonic and continuously differentiable outside a region with bounding surface S, then for $\mathbf{r}$ inside the body:

$$0 = \frac{1}{4\pi}\iint_S \left[-\frac{\partial U_2(\mathbf{r}')}{\partial n'}\frac{1}{R} + U_2(\mathbf{r}')\frac{\partial}{\partial n'}\left(\frac{1}{R}\right)\right] dS' \tag{2.3}$$

and for $\mathbf{r}$ outside the body:

$$U_2(\mathbf{r}) = \frac{1}{4\pi}\iint_S \left[-\frac{\partial U_2(\mathbf{r}')}{\partial n'}\frac{1}{R} + U_2(\mathbf{r}')\frac{\partial}{\partial n'}\left(\frac{1}{R}\right)\right] dS' \tag{2.4}$$

where $\hat{\mathbf{n}}$ is the outward normal of the bounding surface, $R = |\mathbf{r} - \mathbf{r}'|$, and $\mathbf{r}'$ is a point on the surface of the body.

Assume that the total interior potential is U_1, and that the total exterior potential is $U_2 + \Psi$, where Ψ is the potential due to an incident field, so that on the boundary:

$$\epsilon_1 \frac{\partial U_1}{\partial n}\bigg|_S = \epsilon_2 \frac{\partial (U_2 + \Psi)}{\partial n}\bigg|_S \tag{2.5}$$

$$U_1\Big|_S = (U_2 + \Psi)\Big|_S \tag{2.6}$$

See the figure below for a clarification of the geometry.

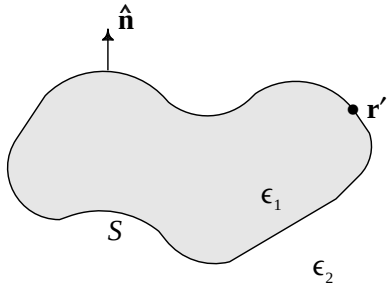

For $\mathbf{r}$ inside the body:

$$U_1 = \frac{1}{4\pi}\iint_S \left[\frac{\partial U_1}{\partial n'}\frac{1}{R} - U_1 \frac{\partial}{\partial n'}\left(\frac{1}{R}\right)\right] dS' \tag{2.7}$$

$$\Psi = \frac{1}{4\pi}\iint_S \left[\frac{\partial \Psi}{\partial n'}\frac{1}{R} - \Psi \frac{\partial}{\partial n'}\left(\frac{1}{R}\right)\right] dS' \tag{2.8}$$

$$0 = \frac{1}{4\pi}\iint_S \left[\frac{-\partial U_2}{\partial n'}\frac{1}{R} + U_2 \frac{\partial}{\partial n'}\left(\frac{1}{R}\right)\right] dS' \tag{2.9}$$

Because of the boundary conditions, form the combination: $\epsilon_1 \times (2.7) + \epsilon_2 \times (2.9)$, to give:

$$\epsilon_1 U_1 = \frac{1}{4\pi}\iint_S \left[\left(\epsilon_2 \frac{\partial \Psi}{\partial n'}\right)\frac{1}{R} - (\epsilon_1 - \epsilon_2) U_1 \frac{\partial}{\partial n'}\left(\frac{1}{R}\right) - \epsilon_2 \Psi \frac{\partial}{\partial n'}\left(\frac{1}{R}\right)\right] dS' \tag{2.10}$$

$$= \frac{\epsilon_2 - \epsilon_1}{4\pi}\iint_S U_1 \frac{\partial}{\partial n'}\left(\frac{1}{R}\right) dS' + \frac{\epsilon_2}{4\pi}\iint_S \left[\frac{\partial \Psi}{\partial n'}\frac{1}{R} - \Psi \frac{\partial}{\partial n'}\left(\frac{1}{R}\right)\right] dS' \tag{2.11}$$

Using (2.8), this gives:

$$\frac{2\epsilon_1}{\epsilon_2 + \epsilon_1} U_1 = \frac{2\epsilon_2}{\epsilon_2 + \epsilon_1}\Psi + \frac{\epsilon_2 - \epsilon_1}{\epsilon_2 + \epsilon_1}\frac{1}{2\pi}\iint_S U_1 \frac{\partial}{\partial n'}\left(\frac{1}{R}\right) dS' \tag{2.12}$$

for the interior potential of a homogeneous dielectric body.

Going through a similar derivation for **r** outside the body:

$$U_2 = \frac{1}{4\pi}\iint_S \left[-\frac{\partial U_2}{\partial n'}\frac{1}{R} + U_2\frac{\partial}{\partial n'}\left(\frac{1}{R}\right)\right] dS' \tag{2.13}$$

$$0 = \frac{1}{4\pi}\iint_S \left[\frac{\partial U_1}{\partial n'}\frac{1}{R} - U_1\frac{\partial}{\partial n'}\left(\frac{1}{R}\right)\right] dS' \tag{2.14}$$

$$0 = \frac{1}{4\pi}\iint_S \left[\frac{\partial \Psi}{\partial n'}\frac{1}{R} - \Psi\frac{\partial}{\partial n'}\left(\frac{1}{R}\right)\right] dS' \tag{2.15}$$

Because of the boundary conditions, form the combination: $\epsilon_2 \times (2.13) + \epsilon_1 \times (2.14)$, to give:

$$\epsilon_2 U_2 = \frac{1}{4\pi}\iint_S \left[\left(\epsilon_1\frac{\partial U_1}{\partial n'} - \epsilon_2\frac{\partial U_2}{\partial n'}\right)\frac{1}{R} - (\epsilon_1 U_1 - \epsilon_2 U_2)\frac{\partial}{\partial n'}\left(\frac{1}{R}\right)\right] dS' \tag{2.16}$$

yielding:

$$\epsilon_2(U_2+\Psi) = \epsilon_2\Psi + \frac{\epsilon_2-\epsilon_1}{4\pi}\iint_S U_1\frac{\partial}{\partial n'}\left(\frac{1}{R}\right) dS' + \frac{\epsilon_2}{4\pi}\iint_S \left[\frac{\partial \Psi}{\partial n'}\frac{1}{R} - \Psi\frac{\partial}{\partial n'}\left(\frac{1}{R}\right)\right] dS' \tag{2.17}$$

and because of (2.15) this gives:

$$\frac{2\epsilon_2}{\epsilon_2+\epsilon_1}(U_2+\Psi) = \frac{2\epsilon_2}{\epsilon_2+\epsilon_1}\Psi + \frac{\epsilon_2-\epsilon_1}{\epsilon_2+\epsilon_1}\frac{1}{2\pi}\iint_S U_1\frac{\partial}{\partial n'}\left(\frac{1}{R}\right) dS' \tag{2.18}$$

for the total exterior field of a dielectric body.

To find an integral equation for the potential **on** the surface, use a limiting process from the inside. For **r** inside the body, use (2.12). To evaluate this in the region of the singularity of the integrand at $R = 0$, let **r** be **on** the boundary and deform the integration surface, as shown in fig. 2.1, with ε representing a small distance, into $S - S_\delta + S_\varepsilon$.

This is done in such a way so that $\lim_{\varepsilon\to 0}(S - S_\delta) + S_\varepsilon = S$, where S is the undeformed surface. So actually evaluate the expression:

$$\frac{2\epsilon_1}{\epsilon_2+\epsilon_1}U_1 = \frac{2\epsilon_2}{\epsilon_2+\epsilon_1}\Psi + \frac{\epsilon_2-\epsilon_1}{\epsilon_2+\epsilon_1}\frac{1}{2\pi}\left[\iint\!\!\!\!\!\!-_S U_1\frac{\partial}{\partial n'}\left(\frac{1}{R}\right) dS' + \lim_{\varepsilon\to 0}\iint_{S_\varepsilon} U_1\frac{\partial}{\partial n'}\left(\frac{1}{R}\right) dS'\right] \tag{2.19}$$

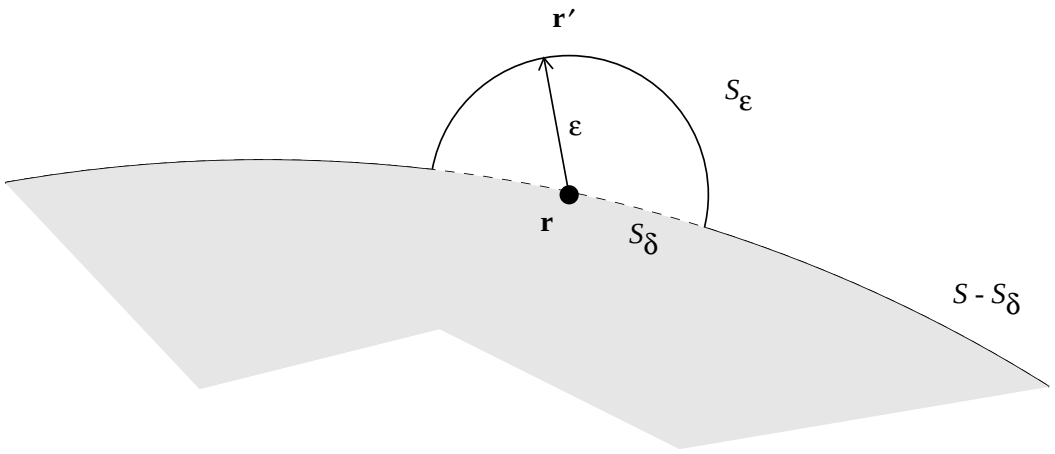

Figure 2.1 — Geometry for Cauchy principal value integral showing hemispherical path, S_ε, around the singular point.

where $⨍_S = \iint_{S-S_\delta}$ defines what is meant by the Cauchy principal value integral; the original integral with a small region surrounding the self-point eliminated from the integral.

It is necessary to evaluate the integral

$$\iint_{S_\varepsilon} U_1 \frac{\partial}{\partial n'}\left(\frac{1}{R}\right)\, dS' \tag{2.20}$$

over S_ε where this is a hemispherical surface centered at $\mathbf{r}$. It is known that for a sphere:

$$\frac{\partial}{\partial n'}\left(\frac{1}{R}\right) = \frac{\partial}{\partial R}\left(\frac{1}{R}\right) = -R^{-2} \qquad \text{and} \qquad dS' = R^2 \sin\theta\, d\theta\, d\phi \tag{2.21}$$

Hence:

$$\iint_{S_\varepsilon} U_1 \frac{\partial}{\partial n'}\left(\frac{1}{R}\right)\, dS' = \int_{\phi=0}^{2\pi}\int_{\theta=0}^{\pi/2}\left(\frac{-U_1}{R^2}\right) R^2 \sin\theta\, d\theta\, d\phi = -2\pi U_1(\mathbf{r}) \tag{2.22}$$

Using this in our original expression gives:

$$\frac{2\epsilon_1}{\epsilon_2+\epsilon_1}U_1(\mathbf{r}) = \frac{2\epsilon_2}{\epsilon_2+\epsilon_1}\Psi(\mathbf{r}) + \frac{\epsilon_2-\epsilon_1}{\epsilon_2+\epsilon_1}\frac{1}{2\pi}\left[⨍_S U_1(\mathbf{r}')\frac{\partial}{\partial n'}\left(\frac{1}{R}\right)\, dS' + \left(-2\pi U_1(\mathbf{r})\right)\right]$$

(2.23)

$$U_1(\mathbf{r}) = \frac{2\epsilon_2}{\epsilon_2+\epsilon_1}\Psi(\mathbf{r}) + \frac{\epsilon_2-\epsilon_1}{\epsilon_2+\epsilon_1}\frac{1}{2\pi}\iint_S U_1(\mathbf{r}')\frac{\partial}{\partial n'}\left(\frac{1}{R}\right)\,dS' \tag{2.24}$$

for $\mathbf{r}$ on the surface of the body.

One could also have found the integral equation for the potential on the surface using a limiting process from the **outside**, with the same result.

2.2 Rotational Symmetry

This section follows Senior and Ahlgren (1972), while filling in some steps. On the surface S of the homogeneous dielectric body, (2.24) is valid:

$$U_{surf}(\mathbf{r}) = \frac{2\epsilon_2}{\epsilon_2+\epsilon_1}\Psi(\mathbf{r}) + \frac{\epsilon_2-\epsilon_1}{\epsilon_2+\epsilon_1}\frac{1}{2\pi}\iint_S U_{surf}(\mathbf{r}')\frac{\partial}{\partial n'}\left(\frac{1}{R(\mathbf{r},\mathbf{r}')}\right)\,dS' \tag{2.25}$$

where

$R(\mathbf{r},\mathbf{r}') = \left|\mathbf{r}-\mathbf{r}'\right|$,

$\Psi(\mathbf{r})$ is the external, 'incident', potential,

U_{surf} is the total potential on the surface S, and

$\hat{\mathbf{n}}'$ is the outward surface normal.

Specializing this formulation to a body of revolution is carried out in what follows. This requires the use of cylindrical coordinates (ρ,ϕ,z), as illustrated in fig. 2.2, and that Ψ is restricted to be only either $-x$ or $-z$. We shall do each of these two cases separately.

2.2.1 $\Psi = -x$

Here use $\Psi(\mathbf{r}) = -x$, or $-\rho\cos\phi$. Since the equation of the body is independent of ϕ, this gives:

$$U_{surf}(\mathbf{r}) = V_1(s)\cos\phi \tag{2.26}$$

where s is a measure of the position on the surface in the $x-z$ plane, *i.e.*, the arc length.

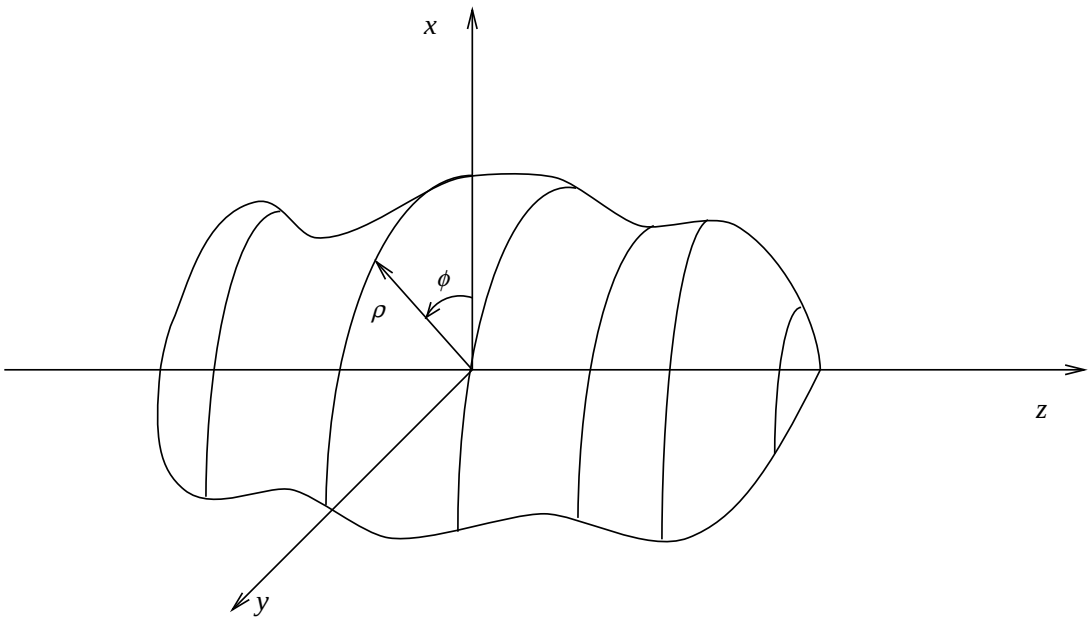

Figure 2.2 — A rotationally-symmetric body in the cartesian and cylindrical coordinate systems.

The integral in this case is rewritten as

$$V_1(s)\cos\phi = \frac{-2\epsilon_2}{\epsilon_2+\epsilon_1}\rho\cos\phi + \frac{\epsilon_2-\epsilon_1}{\epsilon_2+\epsilon_1}\frac{1}{2\pi}\iint_S \left[V_1(s')\cos\phi'\right]\frac{\partial}{\partial n'}\left(\frac{1}{R(\mathbf{r},\mathbf{r}')}\right)dS' \tag{2.27}$$

where:

$$R(\mathbf{r},\mathbf{r}') = \sqrt{(\rho-\rho')^2+(z-z')^2+2\rho\rho'[1-\cos(\phi-\phi')]} \tag{2.28}$$

$$dS' = \rho' d\phi' ds' \tag{2.29}$$

$$\hat{\mathbf{n}}' = \cos\alpha'(\hat{\mathbf{x}}\cos\phi' + \hat{\mathbf{y}}\sin\phi') - \hat{\mathbf{z}}\sin\alpha' \tag{2.30}$$

$$\text{with: } \alpha' = \tan^{-1}\left(\frac{\partial\rho'}{\partial z'}\right) \tag{2.31}$$

Using the above,

$$\frac{\partial}{\partial n'}\left(\frac{1}{R}\right) = \hat{\mathbf{n}}'\cdot\nabla'\left(\frac{1}{R}\right) = -\frac{1}{R^3}\Big\{\cos\alpha'[\rho'-\rho\cos(\phi-\phi')] - \sin\alpha'(z-z')\Big\} \tag{2.32}$$

Hence

$$V_1(s)\cos\phi = \frac{-2\epsilon_2}{\epsilon_2+\epsilon_1}\rho\cos\phi + \frac{\epsilon_2-\epsilon_1}{\epsilon_2+\epsilon_1}\frac{1}{2\pi}\ \mathrm{I}_1 \tag{2.33}$$

where

$$\mathrm{I}_1 = \oint_0^{smax} V_1(s')\rho' \int_0^{2\pi} \cos\phi' \frac{\partial}{\partial n'}\left(\frac{1}{R}\right) d\phi' ds' \tag{2.34}$$

$$= \oint_0^{smax} V_1(s')\rho' \cos\phi \Big[2\Big\{ \rho\cos\alpha'\Omega_2 + [(z'-z)\sin\alpha' - \rho'\cos\alpha']\Omega_1 \Big\}\Big] ds' \tag{2.35}$$

$$\text{with: } \Omega_1 = \int_0^\pi \frac{\cos\gamma}{R^3} d\gamma, \qquad \Omega_2 = \int_0^\pi \frac{\cos^2\gamma}{R^3} d\gamma \tag{2.36}$$

Notice that the $\cos\phi$ term cancels in the equation, giving:

$$V_1(s) = \frac{-2\epsilon_2}{\epsilon_2+\epsilon_1}\rho + \frac{\epsilon_2-\epsilon_1}{\epsilon_2+\epsilon_1}\frac{1}{\pi} \oint_0^{smax} V_1(s')\rho' \Big\{ \rho\cos\alpha'\Omega_2 + [(z'-z)\sin\alpha' - \rho'\cos\alpha']\Omega_1 \Big\} ds' \tag{2.37}$$

for an ambient field (far from the particle) of $\hat{\mathbf{x}}$, or a potential of $-x$.

2.2.2 $\Psi = -z$

In this case Ψ is independent of ϕ. Hence, since the body is independent of ϕ, the surface potential is as well:

$$U_{surf}(\mathbf{r}) = V_3(s) \tag{2.38}$$

This gives:

$$V_3(s) = \frac{-2\epsilon_2}{\epsilon_2+\epsilon_1} z + \frac{\epsilon_2-\epsilon_1}{\epsilon_2+\epsilon_1}\frac{1}{2\pi} \oint_0^{smax} V_3(s')\rho' \int_0^{2\pi} \frac{\partial}{\partial n'}\left(\frac{1}{R}\right) d\phi' ds' \tag{2.39}$$

In a manner similar to that used in sec. 2.2.1, write:

$$\int_0^{2\pi} \frac{\partial}{\partial n'}\left(\frac{1}{R}\right) d\phi' = \int_0^{2\pi} \frac{\partial}{\partial n'}\left(\frac{1}{R}\right) d(\phi-\phi') \tag{2.40}$$

$$= 2\Big\{ \rho\cos\alpha'\Omega_1 + [(z'-z)\sin\alpha' - \rho'\cos\alpha']\Omega_0 \Big\} \tag{2.41}$$

$$\text{with: } \Omega_0 = \int_0^\pi \frac{d\gamma}{R^3} \tag{2.42}$$

which simplifies to

$$V_3(s)=\frac{-2\epsilon_2}{\epsilon_2+\epsilon_1}z+\frac{\epsilon_2-\epsilon_1}{\epsilon_2+\epsilon_1}\frac{1}{\pi}\oint_0^{smax} V_3(s')\rho'\Big\{\rho\cos\alpha'\Omega_1+[(z'-z)\sin\alpha'-\rho'\cos\alpha']\Omega_0\Big\}ds' \tag{2.43}$$

for an ambient field (far from the particle) of $\hat{\mathbf{z}}$, or a potential of $-z$.

Note that because the $\phi-$integral is from 0 to 2π one only need use a collection of line segments and arcs to define the body such that this collection is contained in the first and second quadrants of the $z-x$ plane, *i.e.*, $x \geq 0$, for all z.

Appendix A contains some of the details of this derivation.

2.3 Basic Numerical Implementation

Rewrite the surface integral equations [(2.37) and (2.43)]:

$$V_1(s) = \frac{-2\epsilon_2}{\epsilon_2+\epsilon_1}\rho + \frac{\epsilon_2-\epsilon_1}{\epsilon_2+\epsilon_1}\frac{1}{\pi}\oint_0^{smax} V_1(s')K_1(s,s')\,ds' \tag{2.44}$$

$$V_3(s) = \frac{-2\epsilon_2}{\epsilon_2+\epsilon_1}z + \frac{\epsilon_2-\epsilon_1}{\epsilon_2+\epsilon_1}\frac{1}{\pi}\oint_0^{smax} V_3(s')K_3(s,s')\,ds' \tag{2.45}$$

where the integrals have been simplified by inserting the kernel functions K_1 and K_3.

Discretization of each of these equations is necessary in order to solve them on a computer. Define:

$$\text{rect}\left(\frac{x-x_0}{\Delta x}\right) = \begin{cases} 0; & x < x_0 - \Delta x/2 \\ 1; & x_0 - \Delta x/2 \leq x \leq x_0 + \Delta x/2 \\ 0; & x_0 + \Delta x/2 < x \end{cases} \tag{2.46}$$

which is a rectangular pulse, centered at $x = x_0$ with width Δx and unit height.

Assuming that $V_m(s)$ is adequately represented as a finite sum of these gives

$$V_m(s) = \sum_{i=1}^{N} v_{i,m}\text{rect}\left(\frac{s-s_i}{\Delta s_i}\right) \tag{2.47}$$

with $m = 1, 3$ and where Δs_i depends on i, to allow for variable sampling densities. Putting this into the integral:

$$\oint_0^{smax} V_m(s')K_m(s,s')\,ds' = \oint_0^{smax}\left[\sum_{i=1}^{N} v_{i,m}\text{rect}\left(\frac{s'-s_i}{\Delta s_i}\right)\right]K_m(s,s')\,ds' \tag{2.48}$$

Because both the sum and the integral are finite one can exchange their order:

$$= \sum_{i=1}^{N} v_{i,m} \fint_0^{smax} \text{rect}\left(\frac{s'-s_i}{\Delta s_i}\right) K_m(s,s')\,ds' \quad = \sum_{i=1}^{N} v_{i,m} \fint_{s_i-\Delta s_i/2}^{s_i+\Delta s_i/2} K_m(s,s')\,ds' \tag{2.49}$$

So the integral equation is:

$$\sum_{i=1}^{N} v_{i,m}\text{rect}\left(\frac{s-s_i}{\Delta s_i}\right) = \frac{2\epsilon_2}{\epsilon_2+\epsilon_1}\Psi_m(s) + \frac{\epsilon_2-\epsilon_1}{\epsilon_2+\epsilon_1}\frac{1}{\pi}\sum_{i=1}^{N} v_{i,m} \fint_{s_i-\Delta s_i/2}^{s_i+\Delta s_i/2} K_m(s,s')\,ds' \tag{2.50}$$

where $\Psi_1(s) = -\rho$, and $\Psi_3(s) = -z$, are the ambient static potentials.

Lastly, let $s = s_j$, *i.e.,* enforce this equation at discrete points along the boundary. This gives a set of N simultaneous equations:

$$v_{j,m} = \frac{2\epsilon_2}{\epsilon_2+\epsilon_1}\Psi_m(s_j) + \frac{\epsilon_2-\epsilon_1}{\epsilon_2+\epsilon_1}\frac{1}{\pi}\sum_{i=1}^{N} v_{i,m} \fint_{s_i-\Delta s_i/2}^{s_i+\Delta s_i/2} K_m(s_j,s')\,ds' \tag{2.51}$$

where $j = 1, 2, \cdots, N$.

Figure 2.3 shows what **one** of the N equations represents in graphical form. The integral is over the i-th segement, represented by the arrow with s' near it. The kernel, K_m, is evaluated at s_j, and over the entire i-th segment. Also note that $v_{j,m}$ and $\Psi_m(s_j)$ are evaluated at the point s_j as indicated above.

This yields the value of the potential at s_j: $v_{j,m}$, while using the value of the ambient static potential at s_j: $\Psi_m(s_j)$.

This set of equations is next put into matrix form. The canonical form appears as:

$$[A]\mathbf{x} = \mathbf{b} \tag{2.52}$$

where in this case $\mathbf{x}$ is the unknown column vector: $\mathbf{v}_m = (v_{1,m},\, v_{2,m}, \cdots, v_{N,m})^T$, and $[A]$ is an $N \times N$ matrix.

Putting the present set of equations into this canonical form:

$$v_{j,m} = \frac{2\epsilon_2}{\epsilon_2+\epsilon_1}\Psi_m(s_j) + \frac{\epsilon_2-\epsilon_1}{\epsilon_2+\epsilon_1}\frac{1}{\pi}\sum_{i=1}^{N} v_{i,m} \fint_{s_i-\Delta s_i/2}^{s_i+\Delta s_i/2} K_m(s_j,s')\,ds' \tag{2.53}$$

$$\frac{-2\pi\epsilon_2}{\epsilon_2-\epsilon_1}\Psi_m(s_j) = -\pi\frac{\epsilon_2+\epsilon_1}{\epsilon_2-\epsilon_1}v_{j,m} + \frac{\epsilon_2-\epsilon_1}{\epsilon_2-\epsilon_1}\sum_{i=1}^{N} v_{i,m} \fint_{s_i-\Delta s_i/2}^{s_i+\Delta s_i/2} K_m(s_j,s')\,ds' \tag{2.54}$$

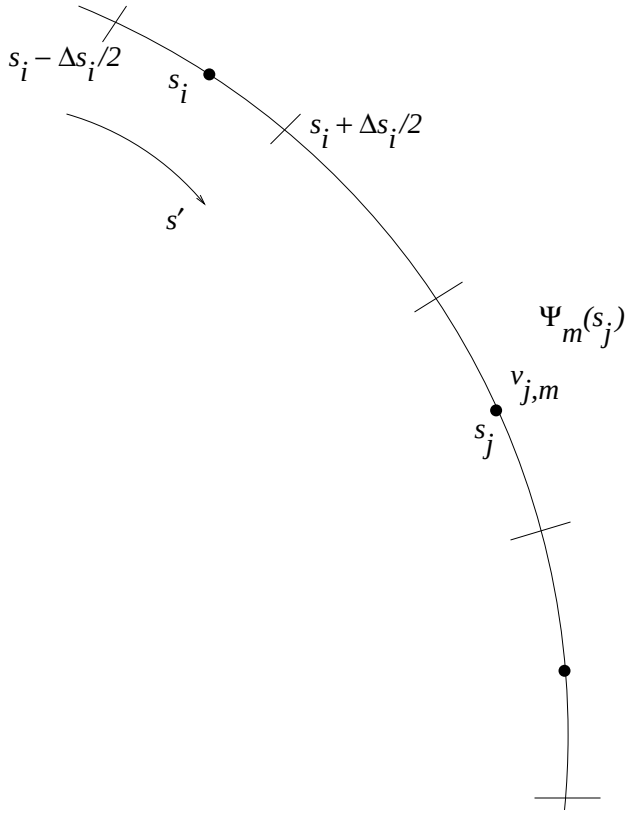

Figure 2.3 — Diagram for the evaluation of one of the N equations.

For convenience of notation, let $v_{j,m} = -\frac{w_{j,m}}{\epsilon_2 - \epsilon_1}$, $\epsilon_2 = 1$, and $\epsilon_1 = \epsilon$. This gives:

$$-\frac{2\pi}{1-\epsilon}\Psi_m(s_j) = \pi\frac{1+\epsilon}{1-\epsilon}\frac{w_{j,m}}{1-\epsilon} + \sum_{i=1}^{N}\frac{-w_{i,m}}{1-\epsilon}\fint_{s_i-\Delta s_i/2}^{s_i+\Delta s_i/2} K_m(s_j, s')\,ds' \qquad (2.55)$$

Hence:

$$-\pi\frac{1+\epsilon}{1-\epsilon}w_{j,m} + \sum_{i=1}^{N} w_{i,m}\fint_{s_i-\Delta s_i/2}^{s_i+\Delta s_i/2} K_m(s_j, s')\,ds' = 2\pi\Psi_m(s_j) \qquad (2.56)$$

for $j = 1, 2, \cdots, N$.

This can be written in matrix form as follows:

$$\begin{bmatrix} -\pi\frac{1+\epsilon}{1-\epsilon}+\fint_{s_1^-}^{s_1^+} K_m(s_1,s')ds' & \cdots & \int_{s_N^-}^{s_N^+} K_m(s_1,s')\,ds' \\ \int_{s_1^-}^{s_1^+} K_m(s_2,s')\,ds' & \cdots & \cdots \\ \vdots & \ddots & \vdots \\ \int_{s_1^-}^{s_1^+} K_m(s_N,s')\,ds' & \cdots & -\pi\frac{1+\epsilon}{1-\epsilon}+\fint_{s_N^-}^{s_N^+} K_m(s_N,s')ds' \end{bmatrix} \begin{bmatrix} w_{1,m} \\ w_{2,m} \\ \vdots \\ w_{N,m} \end{bmatrix} = \begin{bmatrix} 2\pi\Psi_m(s_1) \\ 2\pi\Psi_m(s_2) \\ \vdots \\ 2\pi\Psi_m(s_N) \end{bmatrix} \tag{2.57}$$

where $s_i^- = s_i - \Delta s_i/2$ and $s_i^+ = s_i + \Delta s_i/2$.

Note that the Cauchy principal value only need be considered when evaluating the terms on the diagonal. In all others K_m is not singular because s_j is not between $(s_i - \Delta s_i/2)$ and $(s_i + \Delta s_i/2)$. Also note that ϵ appears only in the term $-\pi\frac{1+\epsilon}{1-\epsilon}$, which is present in the diagonal terms alone. This is helpful later on.

In terms of the variable names used in the computer program:

$$[Ax]\mathbf{W} = \mathbf{B} \tag{2.58}$$

where $[Ax]$ is an $N \times N$ matrix of complex numbers (in general) whose entries are:

$$Ax(i,j) = \int_{s_j-\Delta s_j/2}^{s_j+\Delta s_j/2} K_m(s_i,s')\,ds' \qquad (j \neq i) \tag{2.59}$$

$$Ax(i,i) = -\pi\frac{1+\epsilon}{1-\epsilon} + \fint_{s_i-\Delta s_i/2}^{s_i+\Delta s_i/2} K_m(s_i,s')\,ds' \tag{2.60}$$

and $\mathbf{W}$ and $\mathbf{B}$ are column vectors of length N. The entries of $\mathbf{W}$ are unknown, while the entries of $\mathbf{B}$ are from the 'incident' field:

$$\mathbf{B}(i) = 2\pi\Psi_m(s_i) \tag{2.61}$$

Using the standard LINPACK routines, this matrix equation is readily solved for the unknown vector $\mathbf{W}$.

This is the standard method that is used for solving for the potentials , V_i, given a geometry and material, but one may also solve for the values of ϵ that will cause

the matrix to be singular: they are simple functions of the eigenvalues of a related matrix (one without the $\epsilon-$terms in the diagonal elements).

To see why, rewrite the matrix equation as

$$\{[E] - \lambda[I]\}\,\mathbf{W} = \mathbf{B} \tag{2.62}$$

where in this case $[E]$ is $[Ax]$ without the $\epsilon-$terms in its diagonal, and $[I]$ is the identity matrix. Hence

$$\lambda = \pi\frac{1+\epsilon}{1-\epsilon} \tag{2.63}$$

For the eigenvalue problem one sets the excitation vector equal to zero to get:

$$[E]\mathbf{W} = \lambda\mathbf{W} \tag{2.64}$$

Thus one obtains

$$\epsilon = \frac{\lambda - \pi}{\lambda + \pi} \tag{2.65}$$

as the values for the relative permittivity that cause the matrix problem

$$[Ax]\mathbf{W} = \mathbf{B} \tag{2.66}$$

to be singular. The matrix $[Ax]$ will be singular, or nearly so, corresponding to the physical situation where the 'incident' field (either $\hat{\mathbf{x}}$ or $\hat{\mathbf{z}}$) is at a frequency where the relative permittivity of the material is at or very near one of the values calculated above. Hence, excitation of a 'natural mode' of the object, which causes energy absorption to be very high will occur for these frequencies.

Remember that the set of λ's is the set of eigenvalues of the matrix $[E]$. This matrix is **real**, unlike $[Ax]$ which is complex for some given complex ϵ.

For the potential that is internal or external to the body use the surface potential in (2.12) and (2.18):

$$\frac{2\epsilon}{1+\epsilon}V_m(\mathbf{r}) = \frac{2}{1+\epsilon}\Psi_m(\mathbf{r}) + \frac{1-\epsilon}{1+\epsilon}\frac{1}{2\pi}\iint_S V_m(\mathbf{r}')\frac{\partial}{\partial n'}\left(\frac{1}{R}\right)\,dS' \qquad \mathbf{r} \in int(B) \tag{2.67}$$

$$\frac{2}{1+\epsilon}\Big[V_m(\mathbf{r})+\Psi_m(\mathbf{r})\Big]=\frac{2}{1+\epsilon}\Psi_m(\mathbf{r})+\frac{1-\epsilon}{1+\epsilon}\frac{1}{2\pi}\iint_S V_m(\mathbf{r}')\frac{\partial}{\partial n'}\left(\frac{1}{R}\right)\,dS' \qquad \mathbf{r}\in ext(B) \tag{2.68}$$

with $m=1$ or $m=3$.

Using the expression for the internal potentials, one may solve for V_m in an analogous way to the solution for the surface potentials:

$$\frac{2\epsilon}{1+\epsilon}V_m(\mathbf{r})=\frac{2}{1+\epsilon}\Psi_m(\mathbf{r})+\frac{1-\epsilon}{1+\epsilon}\frac{1}{\pi}\sum_{i=1}^{N}v_{i,m}\fint_{s_i-\Delta s_i/2}^{s_i-\Delta s_i/2}K_m(\mathbf{r},s')\,ds' \tag{2.69}$$

$$V_m(\mathbf{r})=\frac{1}{\epsilon}\Psi_m(\mathbf{r})+\frac{1-\epsilon}{2\epsilon}\frac{1}{\pi}\sum_{i=1}^{N}v_{i,m}\fint_{s_i-\Delta s_i/2}^{s_i-\Delta s_i/2}K_m(\mathbf{r},s')\,ds' \tag{2.70}$$

With $v_{i,m}=-\frac{w_{i,m}}{1-\epsilon}$:

$$V_m(\mathbf{r})=\frac{-1}{2\epsilon}\left[2\begin{pmatrix}\rho\\ z\end{pmatrix}+\frac{1}{\pi}\sum_{i=1}^{N}w_{i,m}\fint_{s_i-\Delta s_i/2}^{s_i-\Delta s_i/2}K_m(\mathbf{r},s')\,ds'\right] \tag{2.71}$$

for $\mathbf{r}$ inside the body.

For $\mathbf{r}$ outside the body, the total external potential is found to be:

$$V_m(\mathbf{r})+\Psi_m(\mathbf{r})=-\frac{1}{2}\left[-2\Psi_m(\mathbf{r})+\frac{1}{\pi}\sum_{i=1}^{N}w_{i,m}\fint_{s_i-\Delta s_i/2}^{s_i-\Delta s_i/2}K_m(\mathbf{r},s')\,ds'\right] \tag{2.72}$$

Note that this is the same equation as for the internal potential, except for a factor of ϵ. This follows from the continuity of $\mathbf{D}$. Hence, calculating all the potentials using the equation for the internal potentials and then multiplying this number by ϵ if $\mathbf{r}$ is external to the body, gives the correct external potential. This is done in the program.

Since the potentials have been determined, the polarizability tensor elements can now be calculated. In the present case of rotational symmetry about the z-axis one only need calculate $P_{11}=P_{22}$ and P_{33}, all others being zero, as shown by Senior (1976). From (1.89):

$$P_{ij}=(1-\epsilon)\int_S \hat{\mathbf{n}}'\cdot\hat{\mathbf{x}}_i\Phi_j^t\,dS' \tag{2.73}$$

As was done previously, the surface integral is transformed to :

$$P_{ij}=(1-\epsilon)\fint_0^{smax}\int_0^{2\pi}\hat{\mathbf{n}}'\cdot\hat{\mathbf{x}}_i\left[\frac{-W_j(s')}{1-\epsilon}\right]\rho'\,d\phi'ds' \tag{2.74}$$

For P_{33} this gives:

$$P_{33} = -\oint_0^{smax} \int_0^{2\pi} (-\sin\alpha') W_3(s') \rho' \, d\phi' ds' \tag{2.75}$$

$$P_{33} = 2\pi \oint_0^{smax} \rho' \sin\alpha' \; W_3(s') \, ds', \tag{2.76}$$

and for P_{11}:

$$P_{11} = -\oint_0^{smax} \int_0^{2\pi} (\cos\alpha' \cos\phi') [W_1(s') \cos\phi'] \rho' \, d\phi' ds' \tag{2.77}$$

$$= -\pi \oint_0^{smax} \rho' \cos\alpha' W_1(s') \, ds'. \tag{2.78}$$

These are the equations used in the program.

2.4 Singularity Extraction and Integration

Senior (1983) and Willis (1984) have outlined procedures for computing the near and internal fields for various special cases which are quite restrictive both in terms of body geometry and field point position. These computations require special effort due to the rapidly-varying integrand when near the surface or near the symmetry axis. In this section the method of Senior and Willis is further generalized while keeping the body axially symmetric, so that now an accurate computation can be performed for any body profile made of circular arcs or straight lines, within the limits of accuracy of the matrix inversion routines.

This enhanced accuracy and functionality of the program is necessary in order to accurately model the geometries of interest in this thesis. The previous code could not handle re-entrant shapes well, and so could not accurately model the fields for the coagulating spheres or for clefts that were at all sharp. Furthermore, this new version of the computational procedures gives accurate values near the symmetry axis which was not possible in the earlier procedure. Without these, the force calculations would be seriously compromised, as the point of closest approach of the two spheres during coagulation is along the axis of symmetry. Also, the field point may now be anywhere, allowing the total internal and external fields to

be calculated at all points of space. This is important both for accurate surface potential values and for complete field plots.

All of these enhancements require the removal and analytical integration of two potentially nearly–singular terms from the numerical integration procedure of the program. This allows the surface integrals to be far more accurate when the field point is extremely close to the surface; much closer than in the previous formulation. This integration procedure is outlined in the remainder of this section.

When a purely numerical integration is used the accuracy is low, especially near the body's surface. The reason is the presence of a singularity stemming from the elliptic integral expressions. Hence, remove a small region around the singularity from the domain of integration and do this integration analytically (although approximately). This analytical term is then added to the numerical result, giving accurate potential values at points which are very near the body's surface. This procedure is summarized below and explained in more detail in Appendix B.

The evaluation of the Ω_i's involves elliptic integrals and their derivatives. (See Appendix 1, especially part 6.) Hence, the integrands of equations 3.1 and 3.2 contain various combinations of these elliptic integrals. Unfortunately, these functions vary rapidly under certain circumstances and hence undermine our attempt at an approximate integral as a small finite sum. One way to get an accurate evaluation of the integral is to increase the number of sampling points, but since the required number becomes intolerably large, the terms in these series expressions that are the major contributors to the rapid variation are removed and the integrations are done analytically. Figure 2.4 shows the elliptic integrals as evaluated by the series expressions. (See Appendix A, especially part 6.)

In particular, the terms removed from these series include a $1/(1-m)$ term and a $\ln|1/(1-m)|$ term. Each of these is plotted in fig. 2.5.

At $\phi = 0$, and $\hat{\mathbf{x}}$-excitation, (2.71) and (2.72) give:

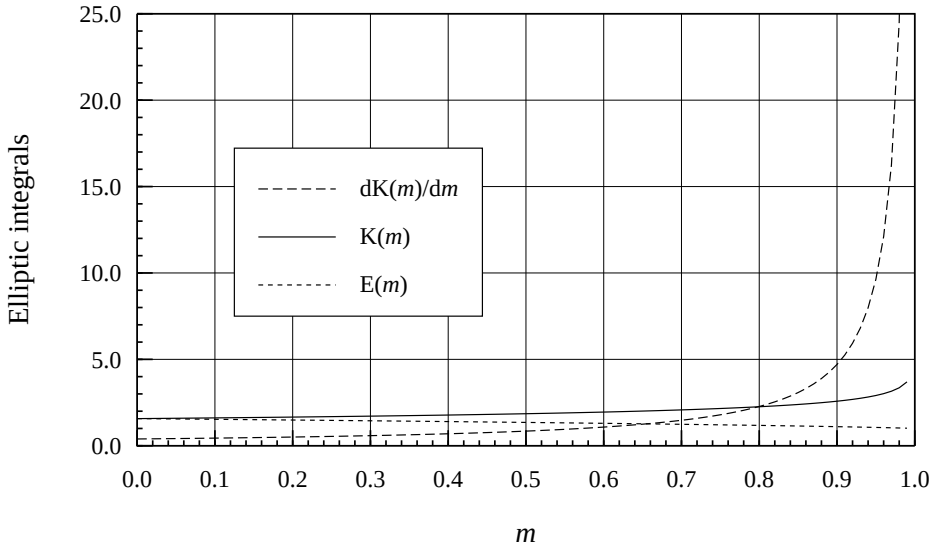

Figure 2.4 — Elliptic integrals as functions of m.

$$\left.\begin{array}{rl} \text{outside:} & -2\Phi_1(\mathbf{r}) \\ \text{bndry:} & -(1+\epsilon)\Phi_1(\mathbf{r}) \\ \text{inside:} & -2\epsilon\Phi_1(\mathbf{r}) \end{array}\right\} = 2\rho + \frac{1}{\pi}\int_S W_1(s')\Big\{\rho\cos\alpha'\,\Omega_2 + [(z'-z)\sin\alpha' - \rho'\cos\alpha']\,\Omega_1\Big\}\rho'\mathrm{d}s' \tag{2.79}$$

with

$$\Phi_1(\mathbf{r}) = -\frac{1}{1-\epsilon}W_1(s)\cos\phi \tag{2.80}$$

and where Ω_1 and Ω_2 are elliptic integrals containing the troublesome singularities. Following Senior (1983), break up the integral into two pieces, one not near the

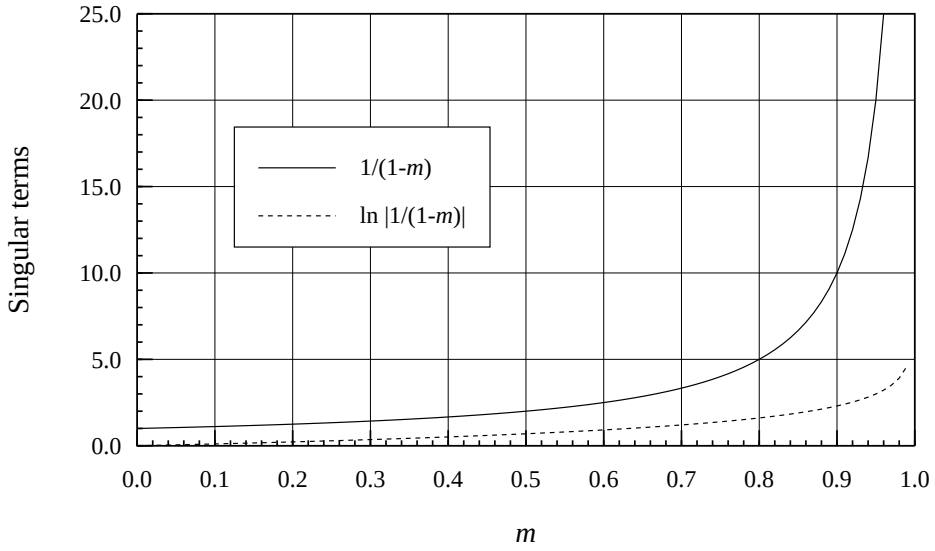

Figure 2.5 — Singular terms as functions of m.

singular point (denote this point by s_0), and one surrounding it very closely (S_1):

$$= 2\rho + \frac{1}{\pi}\int_{S-S_1} W_1(s')K_1(s,s')ds' + \frac{1}{\pi}W_1(s_0)\int_{S_1} K_1(s,s')ds' \tag{2.81}$$

$$= 2\rho + \mathrm{I}_{1A} + W_1(s_0)\mathrm{I}_{1B} \tag{2.82}$$

where K_1 stands for the kernel of (2.79).

The concern here is with the second integral, as the first can be done with good accuracy numerically. Write I_{1B} as a sum of non-singular and singular terms:

$$\mathrm{I}_{1B} = \widetilde{\mathrm{IK}}_1 + \mathrm{IK}_{1\alpha} + \mathrm{IK}_{1\beta} \tag{2.83}$$

where $\widetilde{\mathrm{IK}}_1$ stands for the non-singular part of the integrated kernel, $\mathrm{IK}_{1\alpha}$ stands for the integrated kernel with only the $\frac{1}{m_1}$-singularity terms retained, and $\mathrm{IK}_{1\beta}$ stands for the integrated kernel with only the $\ln\left(\frac{1}{m_1}\right)$-singularity terms retained.

A similar decomposition can be employed for the $\hat{\mathbf{z}}$-incidence case, giving:

$$\mathrm{I}_{3B} = \widetilde{\mathrm{IK}}_3 + \mathrm{IK}_{3\alpha} + \mathrm{IK}_{3\beta} \tag{2.84}$$

where the terms have similar meanings to those in (2.83), but applied to the $\hat{\mathbf{z}}$-incidence kernel function.

The integrals are next simplified by integrating over a flat approximation to the curved boundary, as shown in fig. 2.6. This entails a transfer to the $s-t$ coordinate system Note that this is redefining the s variable from global to local, and from curvilinear to distance on a straight line.

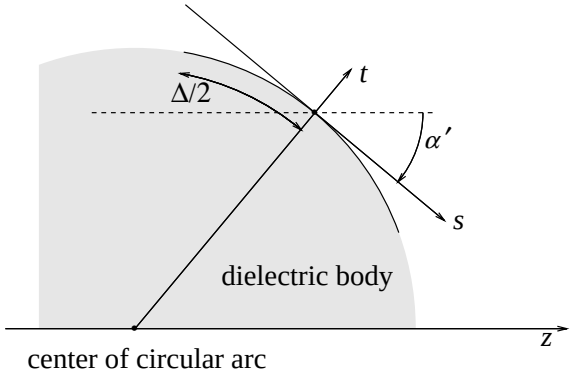

Figure 2.6 — Definition of local *s*-*t* coordinates.

The terms are then of the form:

$$\mathrm{IK}_{1\alpha} = A\int_{-\Delta/2}^{+\Delta/2}\frac{1}{1-m}ds' + B\int_{-\Delta/2}^{+\Delta/2}\frac{s'}{1-m}ds' \tag{2.85}$$

$$\mathrm{IK}_{3\alpha} = C\int_{-\Delta/2}^{+\Delta/2}\frac{1}{1-m}ds' + D\int_{-\Delta/2}^{+\Delta/2}\frac{s'}{1-m}ds' \tag{2.86}$$

$$\mathrm{IK}_{1\beta} = E\int_{-\Delta/2}^{+\Delta/2}\ln\left(\frac{1}{1-m}\right)ds' + F\int_{-\Delta/2}^{+\Delta/2}s'\ln\left(\frac{1}{1-m}\right)ds' \tag{2.87}$$

$$\mathrm{IK}_{3\beta} = G\int_{-\Delta/2}^{+\Delta/2}\ln\left(\frac{1}{1-m}\right)ds' + H\int_{-\Delta/2}^{+\Delta/2}s'\ln\left(\frac{1}{1-m}\right)ds' \tag{2.88}$$

After the integrations are performed and after much tedious algebra the result for the $\frac{1}{m_1}$-singularity terms is

$$\mathrm{IK}_{1\alpha} = \frac{2[s^2+t^2+t'^2+2t'\sin\alpha'(s\cos\alpha'-t\sin\alpha')](s^2+t^2-t'^2)}{\{s^2+(t+t')^2+4t'\sin\alpha'(s\cos\alpha'-t\sin\alpha')\}^{5/2}}\cdot \mathrm{I}_\alpha \tag{2.89}$$

$$\mathrm{IK}_{3\alpha} = \frac{4t'\cos^2\alpha'(s\sin\alpha' + t\cos\alpha')(s^2 + t^2 - t'^2)}{\{s^2 + (t+t')^2 + 4t'\sin\alpha'(s\cos\alpha' - t\sin\alpha')\}^{5/2}} \cdot \mathrm{I}_\alpha \tag{2.90}$$

with

$$\begin{aligned}
\mathrm{I}_\alpha = & \frac{2[s^2 + t^2 + t'^2 + 2t'\sin\alpha'(s\cos\alpha' - t\sin\alpha')](s^2 + t^2 - t'^2)}{\{s^2 + (t+t')^2 + 4t'\sin\alpha'(s\cos\alpha' - t\sin\alpha')\}^{5/2}} \cdot \\
\Big[\Big[& (\cos\alpha' + \frac{4\sin^2\alpha'}{t'}(s\sin\alpha' + t\cos\alpha'))\Delta \\
& + 4\sin\alpha'(s\sin\alpha' + t\cos\alpha')(\cos\alpha' + \frac{s\sin\alpha'}{t'})\ln\left|\frac{\frac{\Delta^2}{4} - s\Delta + s^2 + (t'-t)^2}{\frac{\Delta^2}{4} + s\Delta + s^2 + (t'-t)^2}\right| \\
& + \frac{4(s\sin\alpha' + t\cos\alpha')}{t'-t}[2\sin\alpha'(s\sin\alpha' + t\cos\alpha') + t'(\cos^2\alpha' - \sin^2\alpha') + \frac{\sin^2\alpha'}{t'}(s^2 - t^2)] \\
& \cdot \left[\tan^{-1}\left(\frac{\Delta - 2s}{2(t'-t)}\right) + \tan^{-1}\left(\frac{\Delta + 2s}{2(t'-t)}\right)\right]\Big]\Big]
\end{aligned} \tag{2.91}$$

The result for the $\ln\left(\frac{1}{m_1}\right)$-singularity terms is

$$\mathrm{IK}_{1\beta} = \beta_1[t'\cos\alpha'\mathrm{I}_1 + \sin\alpha'\mathrm{I}_2] \tag{2.92}$$

$$\mathrm{IK}_{3\beta} = \beta_3[t'\cos\alpha'\mathrm{I}_1 + \sin\alpha'\mathrm{I}_2] \tag{2.93}$$

with

$$\begin{aligned}
\beta_1 = & (s\sin\alpha' + t\cos\alpha')\cos\alpha'\frac{8\mathrm{Z}}{\mathrm{X}^2\mathrm{Y}^{3/2}}\left\{\begin{array}{l} 2b_1\mathrm{X}\cdot\mathrm{Z} + \frac{1}{2}\mathrm{Y}\left[s^2 + (t'-t)^2\right. \\ \left. + 6t'\cos\alpha'(s\sin\alpha' + t\cos\alpha')\right] \end{array}\right\} \\
& - \left(s\cos\alpha'\sin\alpha' + (t'-t)\sin^2\alpha' + t'\cos^2\alpha'\right)\frac{1}{\mathrm{Y}^{5/2}}\left\{8b_1\mathrm{Z} + \frac{1}{2}\mathrm{X}\right\}
\end{aligned} \tag{2.94}$$

$$\begin{aligned}
\beta_3 = & (s\sin\alpha' + t\cos\alpha')\cos\alpha'\frac{1}{\mathrm{Y}^{5/2}}\left\{8b_1\mathrm{Z} + \frac{1}{2}\mathrm{X}\right\} \\
& - \left(s\cos\alpha'\sin\alpha' + (t'-t)\sin^2\alpha' + t'\cos^2\alpha'\right)\frac{1}{\mathrm{Y}^{5/2}}\left\{(4b_1 - 1)\mathrm{X} - s^2 - (t-t')^2\right\}
\end{aligned} \tag{2.95}$$

and

$$
\begin{aligned}
\mathrm{I} = & \left[\ln|\eta_1^+| - 2\right]\left(\frac{\Delta}{2} - s\right) - \left[\ln|\eta_1^-| - 2\right]\left(-\frac{\Delta}{2} - s\right) \\
& + 2(t'-t)\left\{\tan^{-1}\left(\frac{\frac{\Delta}{2} - s}{(t'-t)}\right) - \tan^{-1}\left(\frac{-\frac{\Delta}{2} - s}{(t'-t)}\right)\right\} \\
& - \left[\ln|\eta_2^+| - 2\right]\left(s[\sin^2\alpha' - \cos^2\alpha'] + 2t\sin\alpha'\cos\alpha' + \frac{\Delta}{2}\right) \\
& + \left[\ln|\eta_2^-| - 2\right]\left(s[\sin^2\alpha' - \cos^2\alpha'] + 2t\sin\alpha'\cos\alpha' - \frac{\Delta}{2}\right) \\
& - 2[t(\sin^2\alpha' - \cos^2\alpha') - t' - 2s\sin\alpha'\cos\alpha'] \cdot \\
& \left\{\tan^{-1}\left(\frac{s[\sin^2\alpha' - \cos^2\alpha'] + 2t\sin\alpha'\cos\alpha' + \frac{\Delta}{2}}{t(\sin^2\alpha' - \cos^2\alpha') - 2s\sin\alpha'\cos\alpha' - t'}\right)\right. \\
& \left. - \tan^{-1}\left(\frac{s[\sin^2\alpha' - \cos^2\alpha'] + 2t\sin\alpha'\cos\alpha' - \frac{\Delta}{2}}{t(\sin^2\alpha' - \cos^2\alpha') - 2s\sin\alpha'\cos\alpha' - t'}\right)\right\}
\end{aligned} \tag{2.96}
$$

$$
\begin{aligned}
\mathrm{II} = & \frac{1}{2}\left[\frac{\Delta^2}{4} - s^2 + (t'-t)^2\right]\ln\left|\frac{\eta_1^+}{\eta_1^-}\right| - s\Delta \\
& + 2s(t'-t)\left[\tan^{-1}\left(\frac{\frac{\Delta}{2} - s}{(t'-t)}\right) - \tan^{-1}\left(\frac{+\frac{\Delta}{2} + s}{(t'-t)}\right)\right] \\
& - \frac{1}{2}\left\{\begin{array}{l} \dfrac{\Delta^2}{4} - 2\left[s(\sin^2\alpha' - \cos^2\alpha') + 2t\sin\alpha'\cos\alpha'\right]^2 \\ \\ + \left[s^2 + (t'-t)^2 + 4t'\cos\alpha'(s\sin\alpha' + t\cos\alpha')\right] \end{array}\right\}\ln\left|\frac{\eta_2^+}{\eta_2^-}\right| \\
& - \left[s(\sin^2\alpha' - \cos^2\alpha') + 2t\sin\alpha'\cos\alpha'\right]\Delta \\
& + 2\left[s(\sin^2\alpha' - \cos^2\alpha') + 2t\sin\alpha'\cos\alpha'\right]\left[t(\sin^2\alpha' - \cos^2\alpha') - t' - 2s\sin\alpha'\cos\alpha'\right] \\
& \cdot \left[\tan^{-1}\left(\frac{s(\sin^2\alpha' - \cos^2\alpha') + 2t\sin\alpha'\cos\alpha' + \left(\frac{\Delta}{2}\right)}{\left[t(\sin^2\alpha' - \cos^2\alpha') - t' - 2s\sin\alpha'\cos\alpha'\right]}\right)\right. \\
& \left. - \tan^{-1}\left(\frac{s(\sin^2\alpha' - \cos^2\alpha') + 2t\sin\alpha'\cos\alpha' - \left(\frac{\Delta}{2}\right)}{\left[t(\sin^2\alpha' - \cos^2\alpha') - t' - 2s\sin\alpha'\cos\alpha'\right]}\right)\right]
\end{aligned} \tag{2.97}
$$

and

$$
\mathrm{X} = 4t'\cos\alpha'(s\sin\alpha' + t\cos\alpha') \tag{2.98}
$$

$$
\mathrm{Y} = s^2 + (t+t')^2 + 4t'\sin\alpha'(s\cos\alpha' - t\sin\alpha') \tag{2.99}
$$

$$
\mathrm{Z} = s^2 + t^2 + t'^2 + 2t'\sin\alpha'(s\cos\alpha' - t\sin\alpha') \tag{2.100}
$$

This completes the specification of the analytical integration of the nearly-singular terms. As an example of the use of these formulas, the calculated potentials are compared in figure 2.7 to the purely analytical results for a sphere (see eqs. 2.103, 2.104). Note that at the sphere surface $r = 0.5$ and the potential has a lower error than at nearby points. For the non-resonant case (*e.g.*, $\epsilon_r = 2.0 + j0.1$) the worst error is in the exterior, at a distance of 4×10^{-5} from the surface, with a value of 2.2%. For the near-resonant case (*e.g.*, $\epsilon_r = -2.0 + j0.1$) the error at the same distance goes to 6.5%. Closer than this the error increases dramatically, as can be seen by the trend in the plots. Using these plots one can get some idea as to how accurate the near-surface results are for irregularly-shaped bodies.

2.5 Verification

This section presents further verifications of the formulation (secs. 2.1 and 2.2) and the implementation (secs. 2.3 and 2.4). Numerical comparisons are made between the present numerical method and a number of analytic results. The purpose of these comparisons is so that we are confident of the numerical results in later applications where analytic results are not available. For a single sphere and a hollow sphere these include a comparison of the potentials, electric fields, polarizabilities, and resonant dielectric constants. The comparison is very favorable. Next, evaluation using a theoretical formulation (Love (1975)) of the potential and electric field for the two-sphere system is compared with our results. Following this, a comparison is made using two spheres near each other, showing good agreement with the surface intensity, or $|\mathbf{E}|^2$, as computed by the analytical/numerical technique of Aravind, *et al.* (1981) for a variety of separations. Next, very good agreement is obtained with the theoretical resonances obtained numerically (in a similar manner to that of Aravind, *et al.*) by Ruppin (1978) of the two-sphere system as a function of separation. Lastly, good agreement is obtained with the numerical resonances for thin disks obtained numerically by the the method of Chu, Weil, and Willis (Weil

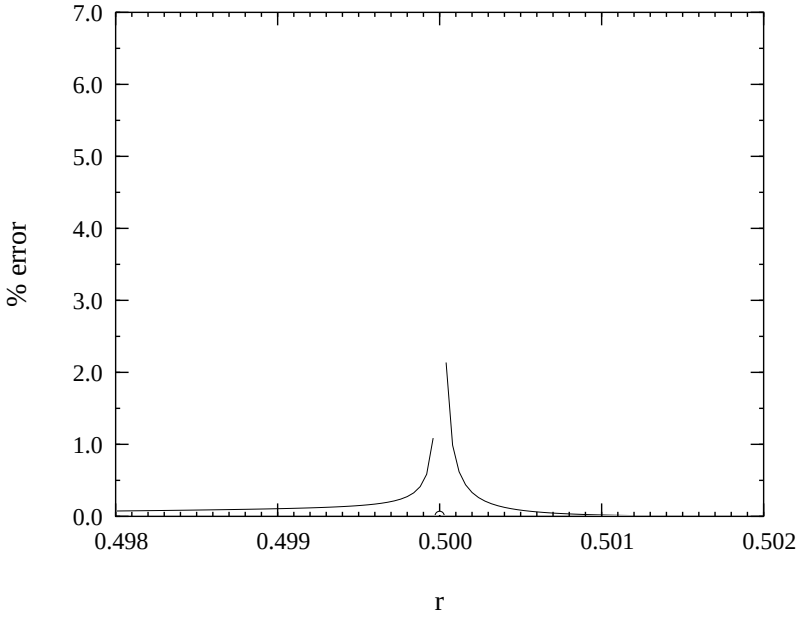

(a)

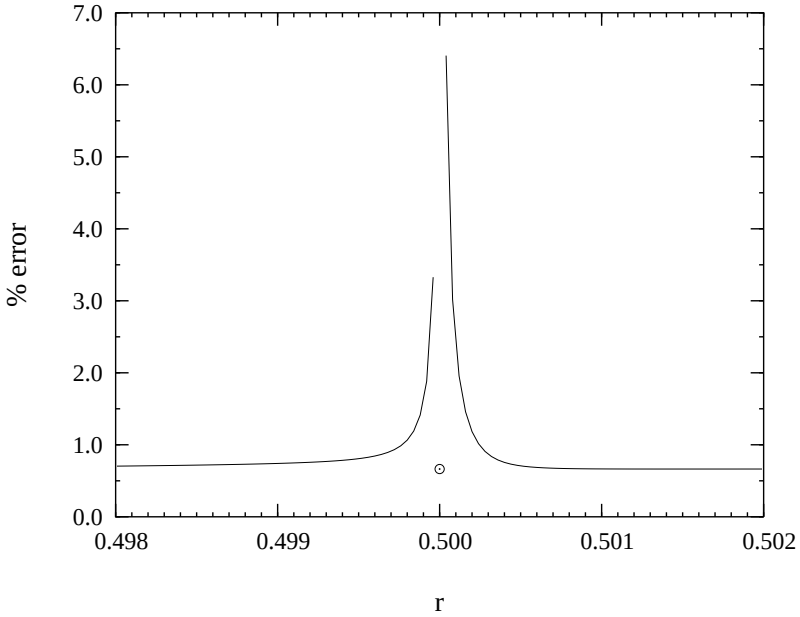

(b)

Figure 2.7 — Near-body accuracy for sphere of radius $r = 0.5$.

$\theta = 30°$. (a) Non-resonant case, $\epsilon_r = 2.0 + j0.1$. (b) Resonant case, $\epsilon_r = -2.0 + j0.1$.

and Willis (1987)).

2.5.1 Sphere

Assume an ambient (static) electric field of unit amplitude in the direction $+\hat{\mathbf{z}}$, the sphere centered at the origin. Figure 2.8 shows the geometry in the plane $\phi = 0$.

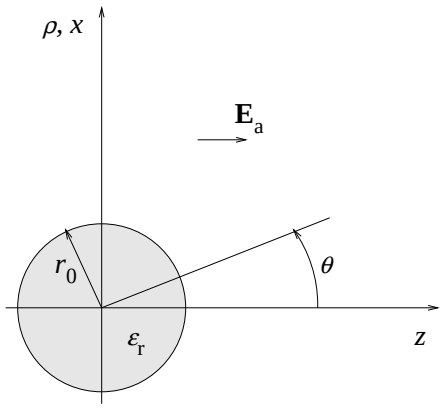

Figure 2.8 — Geometry for single sphere.

The ambient (static) field is

$$\mathbf{E}_a = \hat{\mathbf{z}} = \nabla z = \nabla(r\cos\theta) = \cos\theta\,\hat{\mathbf{r}} - \sin\theta\,\hat{\boldsymbol{\theta}} \tag{2.101}$$

This gives the ambient potential:

$$\Phi_a = -z = -r\cos\theta \tag{2.102}$$

because $\mathbf{E}_a = -\nabla\Phi_a$.

The general solution to the potential problem is

$$\Phi = \begin{cases} C_1\, r\cos\theta & r \le r_0 \\ (-r + C_2/r^2)\cos\theta & r > r_0 \end{cases} \tag{2.103}$$

where:

$$C_1 = \frac{-3}{\epsilon_r + 2} \qquad\qquad C_2 = r_0^3\left(\frac{\epsilon_r - 1}{\epsilon_r + 2}\right) \tag{2.104}$$

This theoretical formulation is now compared to the numerical results. Figure 2.9 shows some typical results for surface potentials of a sphere. In every case the error is less than 0.01%, and this is typical, even near the resonance at $\epsilon_r = -2$. Naturally, there is a region of the complex ϵ_r-plane where ϵ_r will be so close to -2 that the error is very high, but that is expected due to the nature of the numerical solution: the matrix inversion gets less accurate the closer ϵ_r is to the resonance. Despite this, the program is clearly giving a very accurate solution for the sphere in all cases except those where it is too near a resonance.

Figure 2.10 shows some near-field potentials for the spheres, and again the results are excellent.

To find the polarizability of a sphere, start with the expression for a dipole field:

$$\Phi_{dipole} = \frac{p \cos\theta}{4\pi\epsilon_0 r^2} \tag{2.105}$$

where p is the dipole moment, directed along the $\hat{\mathbf{z}}$-direction. The field of the sphere is

$$\Phi = (-r + C_2/r^2)\cos\theta \qquad r > r_2 \tag{2.106}$$

so that the equivalent dipole in the far field is $p = 4\pi\epsilon_0 C_2$, giving a polarizability $\alpha = 4\pi C_2$, and so:

$$\frac{\alpha}{V} = \frac{4\pi C_2}{\frac{4}{3}\pi r_0^3} = 3\left(\frac{\epsilon_r - 1}{\epsilon_r + 2}\right) \tag{2.107}$$

To find the resonant epsilons, one must find the zeroes of the denominator of α. It has but one zero at $\epsilon_r = -2$; this is the one resonant epsilon for the sphere.

Some typical results for the polarizability of a sphere are shown in fig. 2.11. The plots show excellent agreement with theory, even very close to the resonance at $\epsilon_r = -2$. The reason that the polarizability is of interest is that the absorption is proportional its imaginary part, for a particular polarization. This is shown in sec. 3.2.

Lastly, some resonant values calculated by the program are shown in fig. 2.12. As might be expected, the more subsections that are used to divide the surface,

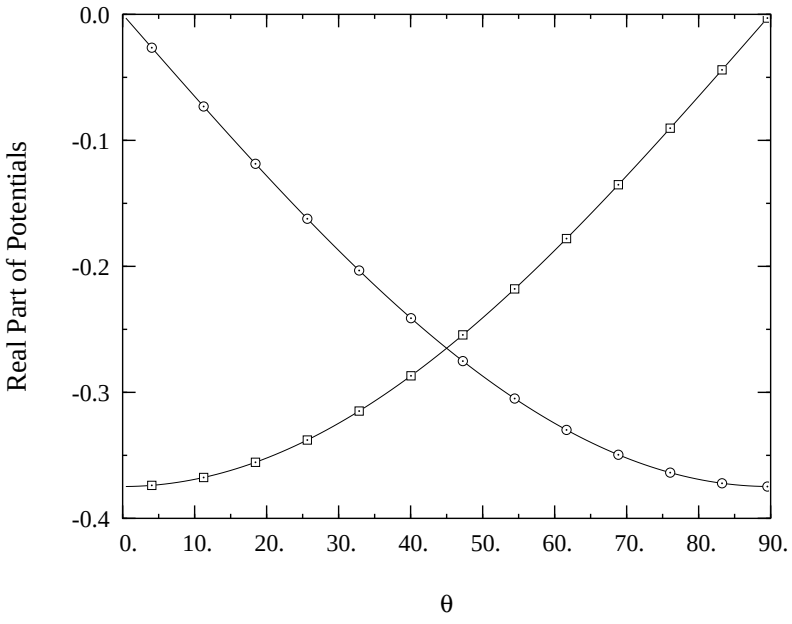

(a)

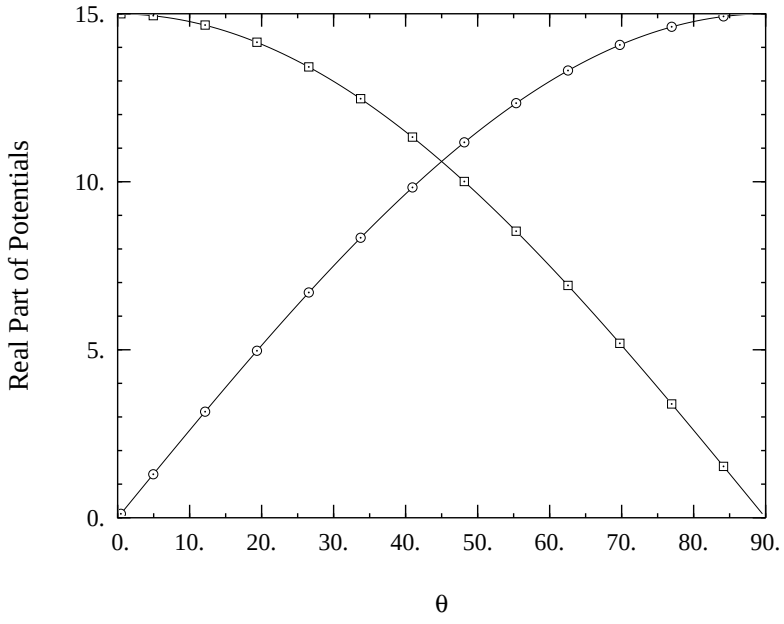

(b)

Figure 2.9 — Surface potentials for sphere.

Sphere radius is 0.5. Real part only. Lines show numerical results, marks show theory: circles, $\hat{\mathbf{x}}$-incidence, squares, $\hat{\mathbf{z}}$-incidence, (a) Non-resonant case, $\epsilon_r = 2.0 + j0.1$. (b) Near-resonant case, $\epsilon_r = -2.0 + j0.1$.

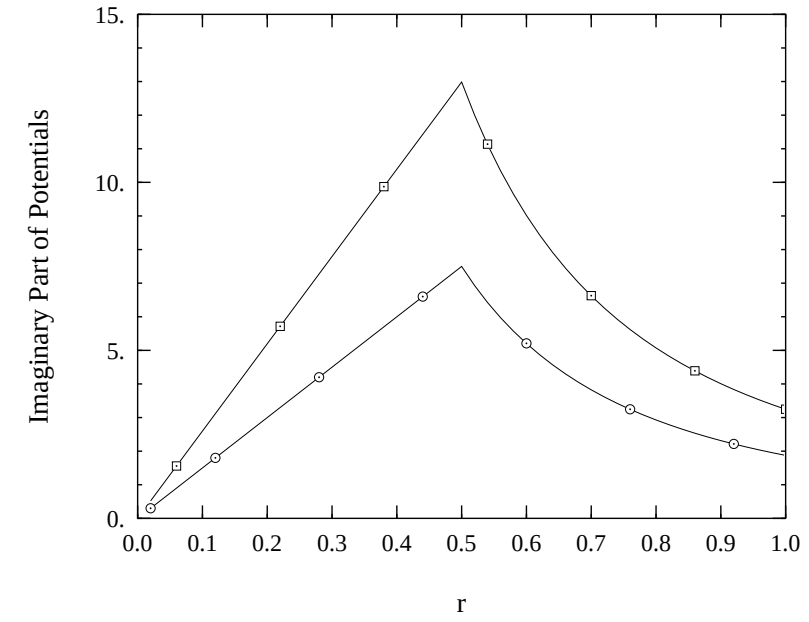

(a)

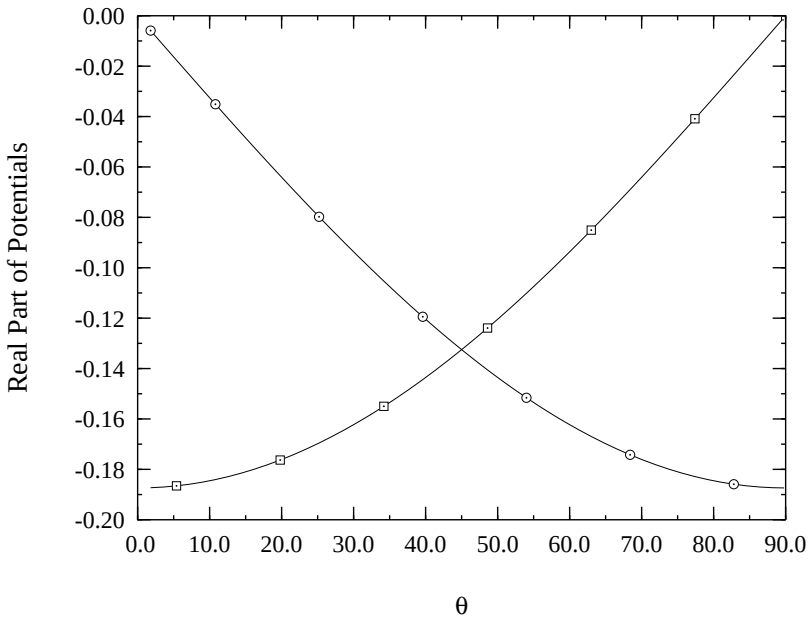

(b)

Figure 2.10 — Near-field potentials for sphere.

Sphere radius is 0.5. Lines show numerical results, marks show theory: circles, $\hat{\mathbf{x}}$-incidence; squares, $\hat{\mathbf{z}}$-incidence, (a) $Im\{\text{potentials}\}$, $\epsilon_r = -2.0 + j0.1$, $\theta = 30°$. (b) $Re\{\text{potentials}\}$, $\epsilon_r = 2.0 + j0.1$, $r = 0.25$.

the closer the resonant values get to theory. After about 50 subsections the values become indistinguishable on this scale.

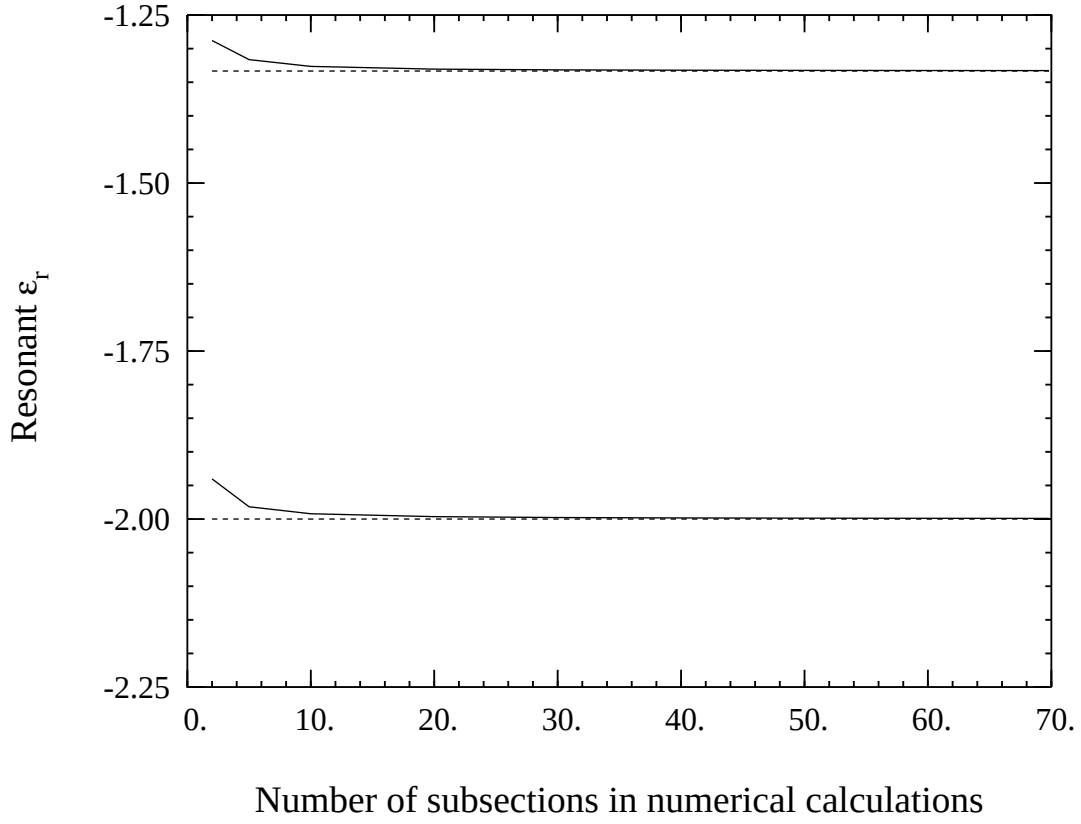

Figure 2.12 — Resonant ϵ_r values for a sphere *vs.* the number of subsections used in surface discretization.

2.5.2 Hollow Sphere

Assume an ambient electric field in the direction $+\hat{\mathbf{z}}$, the spherical dielectric shell centered at the origin. Figure 2.13 shows the geometry in the plane $\phi = 0$.

The ambient (static) field is

$$\mathbf{E}_a = \hat{\mathbf{z}} = \nabla z = \nabla(r\cos\theta) = \cos\theta\,\hat{\mathbf{r}} - \sin\theta\,\hat{\boldsymbol{\theta}} \tag{2.108}$$

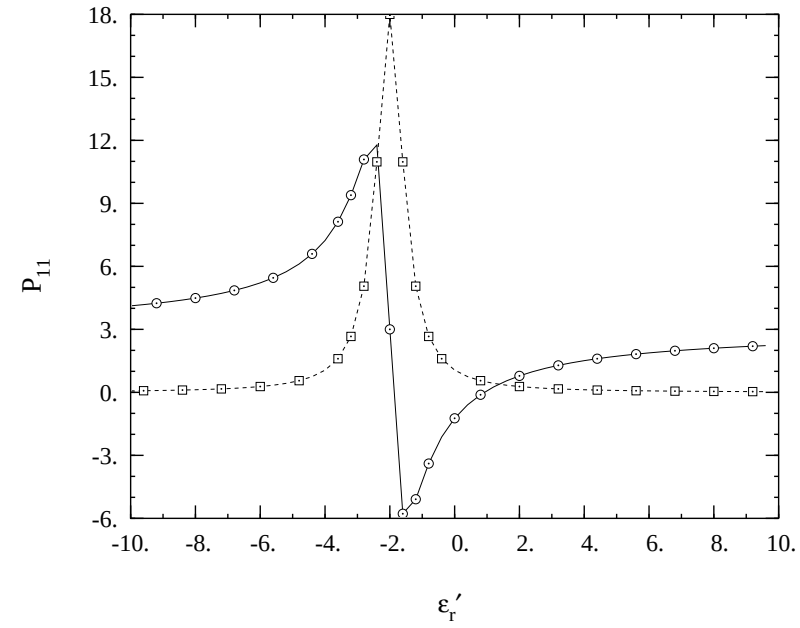

(a)

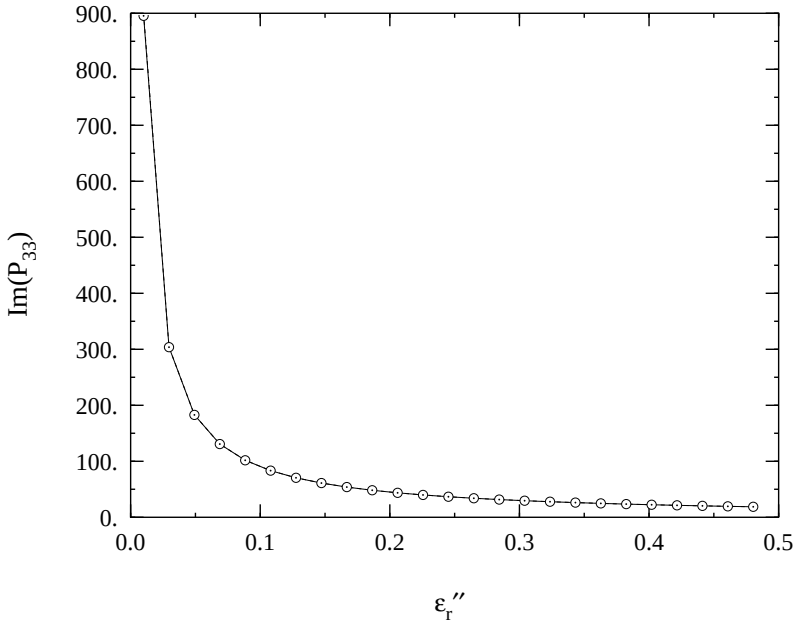

(b)

Figure 2.11 — Polarizabilities for sphere.

Lines show numerical results, marks show theory. (a) P_{11} for $\epsilon_r'' = 0.5$, circles: Real part, squares: Imaginary part. (b) $Im\{P_{33}\}$ for $\epsilon_r'' = -2.0$.

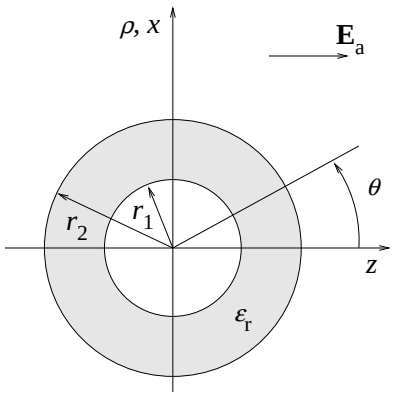

Figure 2.13 — Geometry for single hollow sphere.

This gives the ambient potential:

$$\Phi_a = -z = -r\cos\theta \tag{2.109}$$

because $\mathbf{E}_a = -\nabla\Phi_a$.

The general solution to the potential problem is

$$\Phi = \begin{cases} A_1\, r\cos\theta & r \le r_1 \\ (A_2\, r + B_2/r^2)\cos\theta & r_1 < r \le r_2 \\ (-r + B_3/r^2)\cos\theta & r_2 < r \end{cases} \tag{2.110}$$

where:

$$A_1 = A_2 + B_2/r_1^3 \tag{2.111}$$

$$A_2 = -1 + (B_3 - B_2)/r_2^3 \tag{2.112}$$

$$B_2 = \frac{1}{3\epsilon_r}\left[B_3(2+\epsilon_r) - r_2^3(\epsilon_r - 1)\right] \tag{2.113}$$

$$B_3 = r_2^3 \frac{\left[(2\epsilon_r+1)\left(\frac{r_2}{r_1}\right)^3 - 1 + \epsilon_r\right](\epsilon_r - 1) + 3\epsilon_r(1-\epsilon_r)}{\left[(2\epsilon_r+1)\left(\frac{r_2}{r_1}\right)^3 - 1 + \epsilon_r\right](2+\epsilon_r) + 3\epsilon_r(1-\epsilon_r)} \tag{2.114}$$

This theoretical formulation is now compared to the numerical results. A typical result for the surface potential is shown in fig. 2.14. The angle θ is measured from

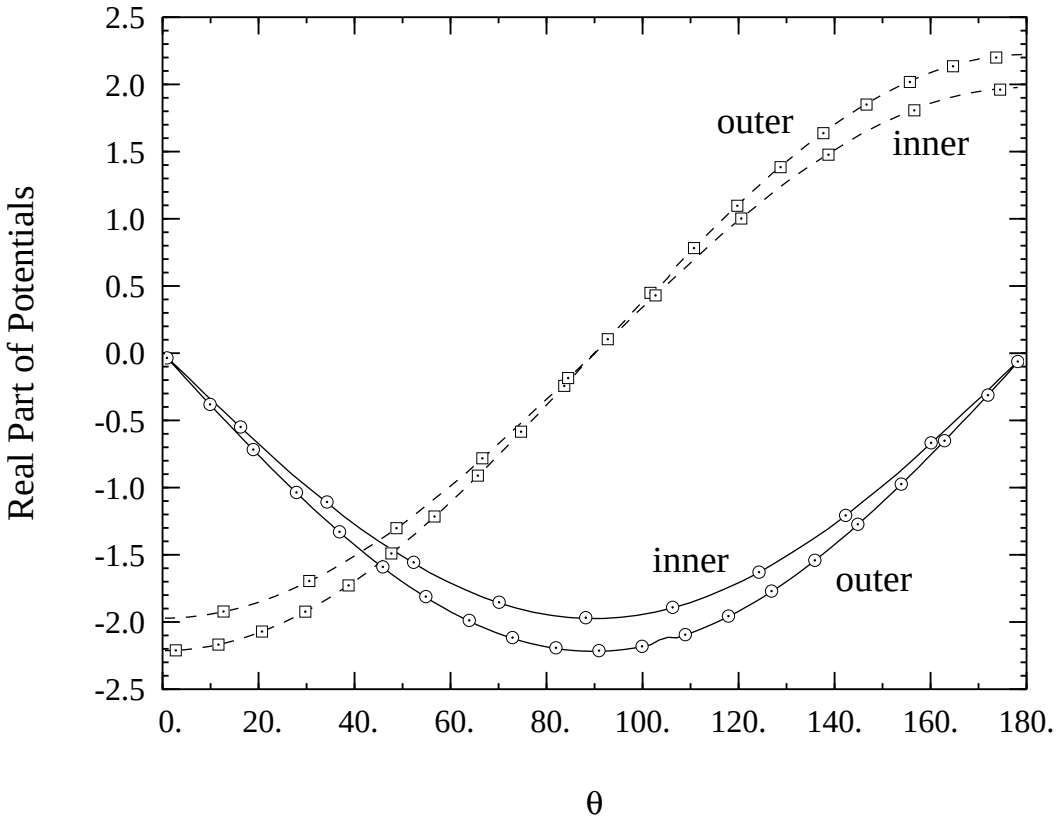

Figure 2.14 — Surface potentials for hollow sphere.

Real parts only, inner radius is half the outer radius. $\epsilon_r = -2.0 + j0.1$. Lines show numerical results, marks show theory. circles: $\hat{\mathbf{x}}$-incidence, squares: $\hat{\mathbf{z}}$-incidence, Outer and inner refer to which of the surfaces the potentials are on.

---

the positive z-axis, and both inside and outside surface potentials are shown. The agreement is excellent.

To find the polarizability of a hollow sphere, start with the expression for a dipole field:

$$\Phi_{dipole} = \frac{p \cos\theta}{4\pi\epsilon_0 r^2} \tag{2.115}$$

where p is the dipole moment, directed along the $\hat{\mathbf{z}}$-direction. The field of the hollow sphere is

$$\Phi = (-r + B_3/r^2)\cos\theta \qquad r > r_2 \tag{2.116}$$

so that the equivalent dipole in the far field is $p = 4\pi\epsilon_0 B_3$, giving a polarizability $\alpha = 4\pi B_3$, and so:

$$\frac{\alpha}{V} = \frac{4\pi B_3}{\frac{4}{3}\pi(r_2^3 - r_1^3)} = \frac{3B_3}{(r_2^3 - r_1^3)} \tag{2.117}$$

The resonant epsilons are given by the zeroes of the denominator of B_3 which are

$$\epsilon_r = \frac{-(5a^3 + 4) \pm 3\sqrt{a^3(a^3 + 8)}}{4(a^3 - 1)} \tag{2.118}$$

These are the two resonant epsilons for the hollow sphere. The largest one (in magnitude) is the one with the negative square-root.

A comparison of the calculated polarizabilities and theory is shown in fig. 2.15. In each case the agreement is excellent even very near the major resonance at $\epsilon_r \approx -2.782$. The worst case out of the many runs made (not all shown here) occurs in the real part near the resonance, where the calculated values are positive and the theoretical values go negative. This only happens in a small region near a resonance.

This small region of error is unimportant in the context of this thesis. However, if one wished to decrease the error, the eigenvalue computation could be done with higher precision. Despite this, no matter how close the computed resonance positions are to the theoretical positions, near the region where they don't agree the error will be high. There is nothing more one can do except shrink this region by using higher-precision calculations.

The computed and theoretical resonance values are compared in fig. 2.16. The agreement is excellent. Note that calculated polarizabilities can be quite inaccurate very near a resonance because of the slight difference between calculated and theoretical resonance values: if the distance in the ϵ_r-plane of ϵ_r (chosen for the calculation of the polarizability) to the two different resonant ϵ_r values is of the same order of magnitude, then the calculated values agree with theory; if not, which is the case when ϵ_r is chosen very near one of the resonance values, then the errors

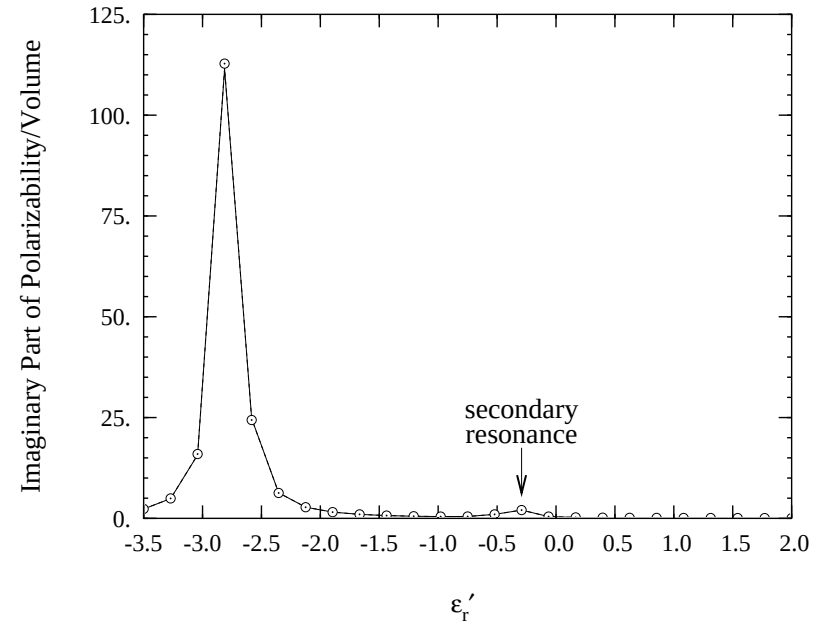

(a)

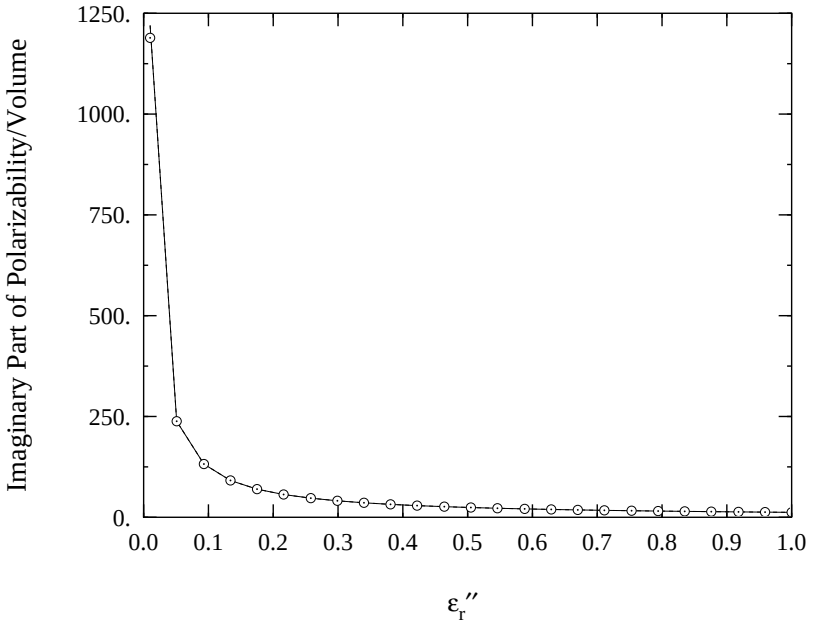

(b)

Figure 2.15 — Polarizability for hollow sphere.

Imaginary part. Inner radius is half the outer radius. Lines show numerical results, circles show theory. (a) $\epsilon_r'' = 0.1$. (b) $\epsilon_r' = -2.782$.

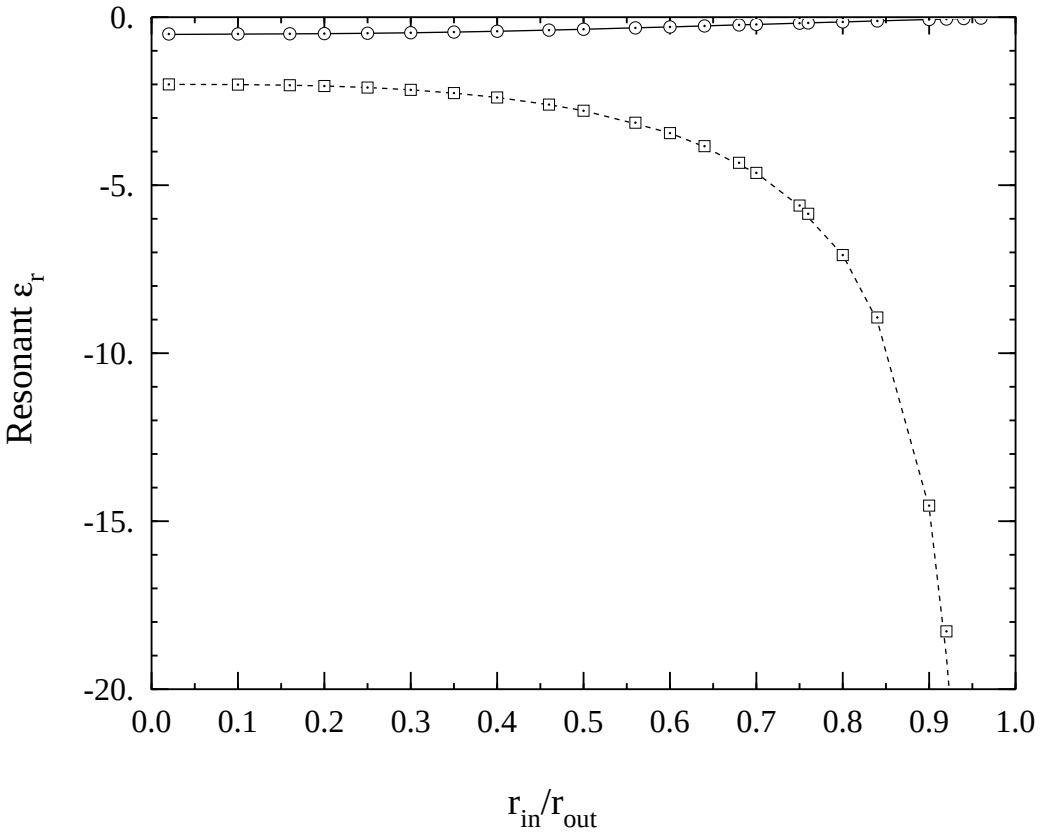

Figure 2.16 — Hollow sphere resonances.

Lines show numerical results, marks show theory. squares: major resonance, circles: minor resonance.

can be tremendous. Except for that situation, the numerical results are quite good. (See the comments at the end of sec. 2.5.2 for a way to minimize this error.)

2.5.3 Fields for Two Separate Spheres

The work of Love (1975) is presented here and compared to the numerical results, while other aspects of the two-sphere problem are investigated in the following sections.

Potentials

For an ambient electric field $E_0\hat{\mathbf{z}}$, and a geometry with two separate spheres, Love obtains the following expressions for the external and internal potentials:

$$\Psi_3^{ext} = -(\cosh\eta - \cos\tau)^{\frac{1}{2}} 2^{\frac{1}{2}} E_0 d \sum_{n=0}^{\infty} P_n(\cos\tau) \left\{ \pm(2n+1) e^{\mp(n+\frac{1}{2})\eta} + 4\Delta_1 \mu_{3n} \sinh\left[(n+\frac{1}{2})\eta\right] \right\} \tag{2.119}$$

$$\Psi_3^{int} = \mp(\cosh\eta - \cos\tau)^{\frac{1}{2}} 2^{\frac{1}{2}} E_0 d \sum_{n=0}^{\infty} P_n(\cos\tau) \left\{ (2n+1) + 2\left(e^{(2n+1)\eta_0} - 1\right)\Delta_1 \mu_{3n} \right\} e^{\mp(n+\frac{1}{2})\eta} \tag{2.120}$$

where η and τ are bispherical coordinates (see fig. 2.17) and:

$$\mu_{3n} = \sum_{N=0}^{\infty} \frac{\left\{N - (N-1)e^{-2\eta_0}\right\} e^{-2N\eta_0}}{\alpha_{3N} q_{3,N-1} - \beta_{3N} + \gamma_{3N} p_{3,N+1}} \cdot \left\{ \delta_{n,N} + H(n-N) \prod_{l=N+1}^{n} p_{3,l} + H(N-n) \prod_{l=n}^{N-1} q_{3,l} \right\} \tag{2.121}$$

$$d = a \sinh\eta_0 \tag{2.122}$$

$$a = \text{ sphere radius} \tag{2.123}$$

$$\text{separation } = 2R = 2a\cosh\eta_0 \tag{2.124}$$

$$\Delta_1 = \frac{\epsilon_r - 1}{\epsilon_r + 1} \tag{2.125}$$

$$P_n \text{ are the Legendre polynomials of the first kind} \tag{2.126}$$

$$H(x) = \begin{cases} 0, & \text{if } x \le 0; \\ 1, & \text{else.} \end{cases} \qquad \delta_{n,N} = \begin{cases} 1, & \text{if } n = N; \\ 0, & \text{else.} \end{cases} \tag{2.127}$$

and where:

$$\alpha_{3,N} = N\left[e^{-\eta_0} - \Delta_1 e^{-2N\eta_0}\right] \tag{2.128}$$

$$\beta_{3,N} = (2N+1)\cosh\eta_0 - \Delta_1 \sinh\eta_0 - N\Delta_1 e^{-2N\eta_0} - (N+1)\Delta_1 e^{-2(N+1)\eta_0} \tag{2.129}$$

$$\gamma_{3,N} = (N+1)\left[e^{\eta_0} - \Delta_1 e^{-2(N+1)\eta_0}\right] \tag{2.130}$$

with the continued fractions:

$$p_{3,n} = \frac{\alpha_{3,n}}{\beta_{3,n} -} \frac{\gamma_{3,n}\alpha_{3,n+1}}{\beta_{3,n+1} -} \frac{\gamma_{3,n+1}\alpha_{3,n+2}}{\beta_{3,n+2} -} \cdots \tag{2.131}$$

$$q_{3,n} = \frac{\gamma_{3,n}}{\beta_{3,n} -} \frac{\alpha_{3,n}\gamma_{3,n-1}}{\beta_{3,n-1} -} \frac{\alpha_{3,n-1}\gamma_{3,n-2}}{\beta_{3,n-2} -} \cdots \frac{\alpha_{3,1}\gamma_{3,0}}{\beta_{3,0}} \tag{2.132}$$

Similarly, for $\hat{\mathbf{x}}$-incidence:

$$\Psi_1^{ext} = +(\cosh\eta - \cos\tau)^{\frac{1}{2}} 2^{\frac{3}{2}} E_0 d \sum_{n=1}^{\infty} P_n^1(\cos\tau)\cos\phi \left\{ e^{\mp(n+\frac{1}{2})\eta} + 2\Delta_1\mu_{1n}\cosh\left[(n+\frac{1}{2})\eta\right]\right\} \tag{2.133}$$

$$\Psi_1^{int} = +(\cosh\eta - \cos\tau)^{\frac{1}{2}} 2^{\frac{3}{2}} E_0 d \sum_{n=1}^{\infty} P_n^1(\cos\tau)\cos\phi \left\{ 1 + \Delta_1\mu_{1n}\left(e^{(2n+1)\eta_0}+1\right)\right\} e^{\mp(n+\frac{1}{2})\eta} \tag{2.134}$$

where:

$$\mu_{1n} = \sum_{N=1}^{\infty} \frac{\left\{1 - e^{-2\eta_0}\right\} e^{-2N\eta_0}}{\alpha_{1N}q_{1,N-1} - \beta_{1N} + \gamma_{1N}p_{1,N+1}} \left\{ \delta_{n,N} + H(n-N)\prod_{l=N+1}^{n} p_{1,l} + H(N-n)\prod_{l=n}^{N-1} q_{1,l}\right\} \tag{2.135}$$

P_n^1 are the associated Legendre functions of order 1

$$\alpha_{1,N} = (N-1)\left[e^{-\eta_0} + \Delta_1 e^{-2N\eta_0}\right] \tag{2.136}$$

$$\beta_{1,N} = (2N+1)\cosh\eta_0 - \Delta_1\sinh\eta_0 + N\Delta_1 e^{-2N\eta_0} + (N+1)\Delta_1 e^{-(2N+2)\eta_0} \tag{2.137}$$

$$\gamma_{1,N} = (N+2)\left[e^{\eta_0} + \Delta_1 e^{-(2N+2)\eta_0}\right] \tag{2.138}$$

with the continued fractions:

$$p_{1,n} = \frac{\alpha_{1,n}}{\beta_{1,n} -} \frac{\gamma_{1,n}\alpha_{1,n+1}}{\beta_{1,n+1} -} \frac{\gamma_{1,n+1}\alpha_{1,n+2}}{\beta_{1,n+2} -} \cdots \tag{2.139}$$

$$q_{1,n} = \frac{\gamma_{1,n}}{\beta_{1,n} -} \frac{\alpha_{1,n}\gamma_{1,n-1}}{\beta_{1,n-1} -} \frac{\alpha_{1,n-1}\gamma_{1,n-2}}{\beta_{1,n-2} -} \cdots \frac{\alpha_{1,1}\gamma_{1,0}}{\beta_{1,0}} \tag{2.140}$$

To relate the bispherical coordinates to the $\rho - z$ coordinates used in the rest of this work, use the relations:

$$\eta = -\ln(PL/PL') \qquad \tau = \text{ the angle } LPL' \tag{2.141}$$

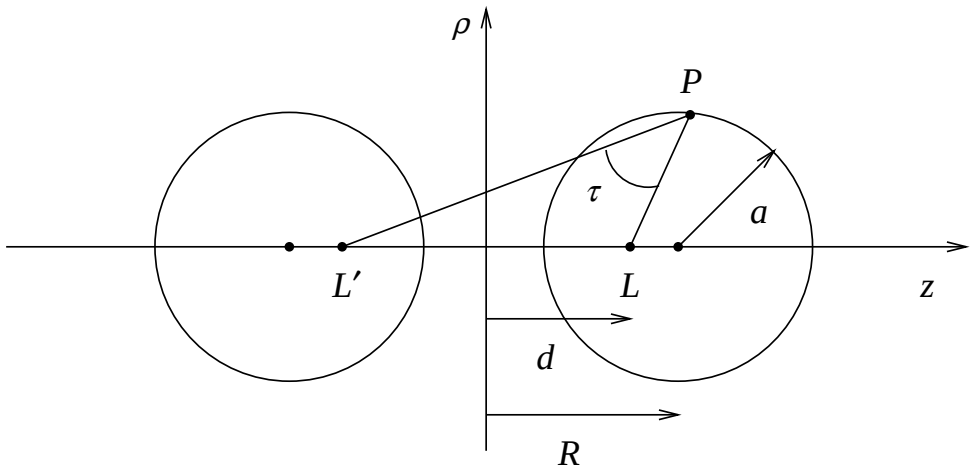

Figure 2.17 — Definitions of η and τ of the bispherical coordinate system.

where the distances and angles are indicated in the figure below:

For $\phi = 0$, these relations give:

$$\eta = -\frac{1}{2}\ln\left(\frac{\rho^2 + (z-d)^2}{\rho^2 + (z+d)^2}\right) \tag{2.142}$$

$$\tau = \tan^{-1}\left(\frac{\rho}{z-d}\right) - \tan^{-1}\left(\frac{\rho}{z+d}\right) \tag{2.143}$$

Also note that given R and a, then d and η_0 are determined:

$$l = 2(R-a) \qquad d = a\sinh\eta_0 \qquad l = 2a(\cosh\eta_0 - 1) \tag{2.144}$$

giving:

$$\eta_0 = \cosh^{-1}\left(\frac{l}{2a} + 1\right) \tag{2.145}$$

$$d = a\sinh\left[\cosh^{-1}\left(\frac{l}{2a} + 1\right)\right] \tag{2.146}$$

Since the only available FORTRAN subroutine calculates P_n, but not P_n^1, an expression for P_n^1 in terms of P_n is needed. From Abramowitz and Stegun (1964):

$$P_\nu^\mu(x) = e^{i\mu\pi}P_\nu^\mu(x + i0) \tag{2.147}$$

$$P_\nu^{\mu+1}(z) = (z^2-1)^{-\frac{1}{2}}\left[(\nu-\mu)zP_\nu^\mu(z) - (\nu+\mu)P_{\nu-1}^\mu(z)\right] \tag{2.148}$$

$$P_{-\nu-1}^\mu(z) = P_\nu^\mu(z) \tag{2.149}$$

with $z = x + iy$, so that

$$P_n^1(\cos\tau) = \begin{cases} \dfrac{-1}{\sin\tau}\left[n\cos\tau P_n(\cos\tau) - nP_{n-1}(\cos\tau)\right] & \text{for } n \geq 1; \\ 0 & \text{for } n = 0; \end{cases} \tag{2.150}$$

This completes the specification of Love's results for the potential.

The surface potentials calculated using the procedures of sec. 2.3 are compared to a computational version of Love's theory in fig. 2.18. Shown is the case for $\phi = 0$, with θ varying over the perimeter of one of the spheres. Various geometries and dielectric constants are shown to validate the numerical methods over a wide range of parameters. It is seen that the agreement is excellent; less than 0.1% error in fact.

Note that all the particular shapes are a function of one parameter: the center-to-center separation, measured in units of particle diameter. Hence a separation of 1 gives the geometry of two whole spheres just touching, a separation of zero gives just one sphere, and a separation of 2 gives two spheres whose surfaces are separated by a length equal to the diameter of one sphere.

Next, figs. 2.19 and 2.20 show off-surface potentials. Figure 2.19 gives the potentials at distances along a radial line from the center of the sphere on the positive z-axis, at an angle of θ with the z-axis. In each case the surface of the sphere is at $r = 0.5$. Again, the agreement is excellent. Figure 2.20 shows the potentials along a line at a fixed distance from the boundary, which is therefore a circular arc either inside or outside the sphere. The angle θ is measured from the positive z-axis toward the positive x-axis. Again, in each case the agreement is excellent.

In general, every case that was tried yielded results with errors less than 0.2%.

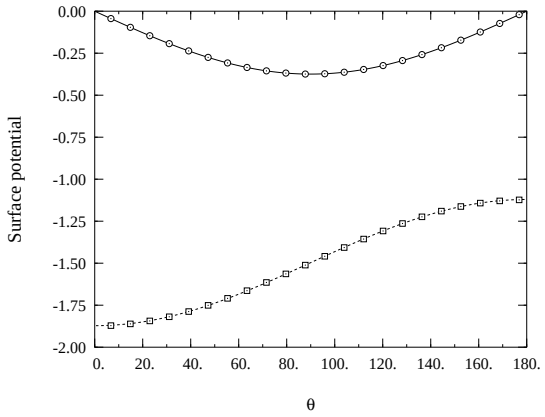

(a)

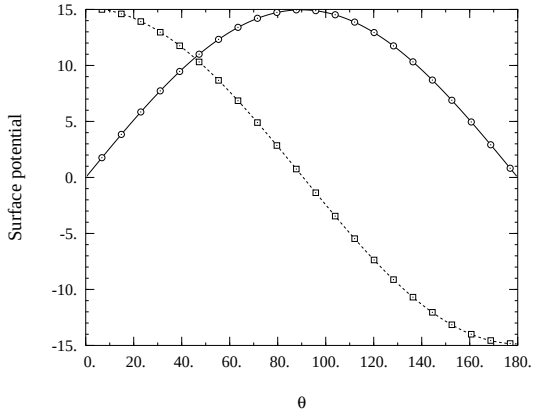

(b)

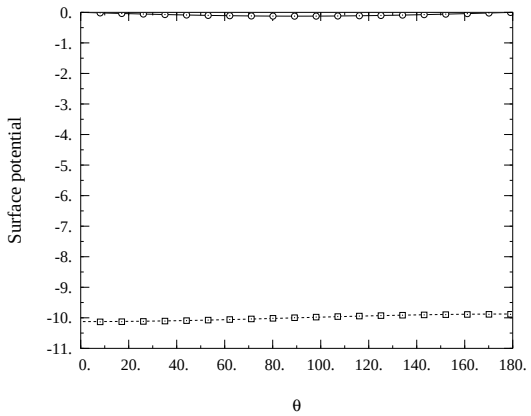

(c)

Figure 2.18 — Surface potentials for 2-sphere.

Lines show numerical results, marks show Love's theory: circles, $\hat{\mathbf{x}}$-incidence; squares, $\hat{\mathbf{z}}$-incidence; (a) Real part, separation = 3, $\epsilon_r = 2.0 + j0.1$. (b) Imaginary part, separation = 5, $\epsilon_r = -2.0 + j0.1$. (c) Real part, separation = 20, $\epsilon_r = 10.0 + j1.0$.

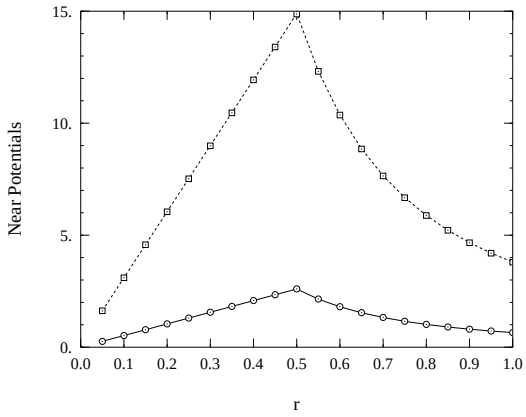

(a)

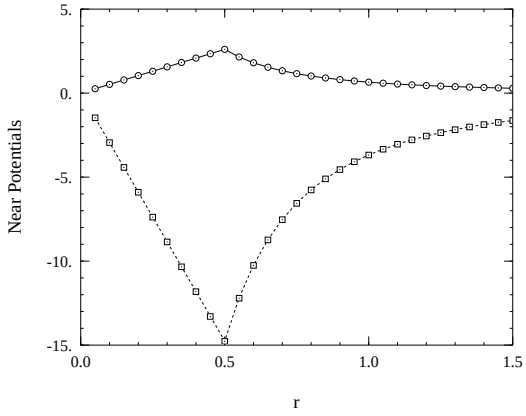

(b)

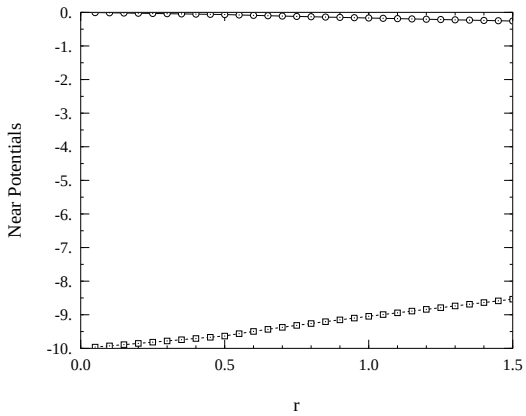

(c)

Figure 2.19 — Near potentials for 2-sphere as function of r.

Lines show numerical results, marks show Love's theory: circles, $\hat{\mathbf{x}}$-incidence; squares, $\hat{\mathbf{z}}$-incidence; (a) Imaginary part, radial line at $\theta = 30°$, separation $= 5$, $\epsilon_r = -2.0 + j0.1$. (b) Imaginary part, radial line at $\theta = 170°$, separation $= 20$, $\epsilon_r = -2.0 + j0.1$. (c) Real part, radial line at $\theta = 170°$, separation $= 20$, $\epsilon_r = +2.0 + j0.1$.

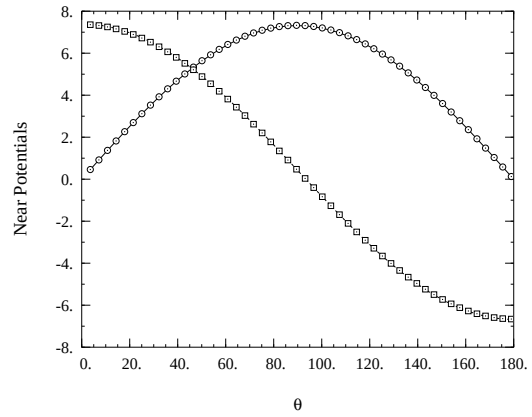

(a)

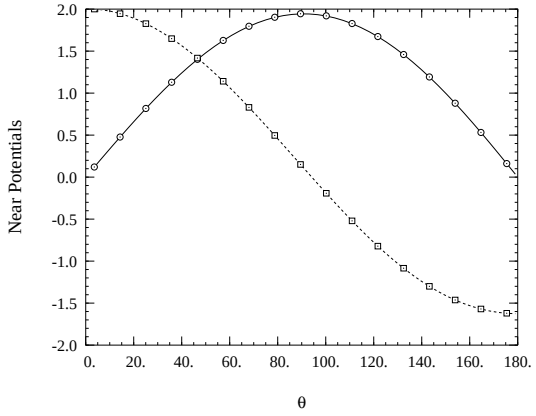

(b)

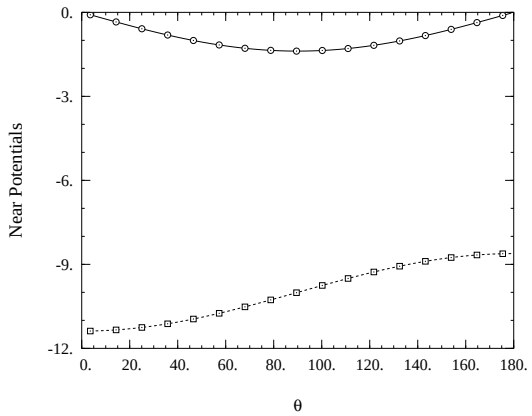

(c)

Figure 2.20 — Near potentials for 2-sphere, as function of θ.

Lines show numerical results, marks show Love's theory: circles, $\hat{\mathbf{x}}$-incidence; squares, $\hat{\mathbf{z}}$-incidence; (a) Imaginary part, inside, $r = 0.25$, separation $= 3$, $\epsilon_r = -2.0 + j0.1$. (b) Imaginary part, outside, $r = 1.4$, separation $= 5$, $\epsilon_r = -2.0 + j0.1$. (c) Real part, outside, $r = 1.4$, separation $= 20$, $\epsilon_r = +2.0 + j0.1$.

Electric Fields

To find the electric field, use the gradient in bispherical coordinates:

$$\mathbf{E} = \frac{-(\cosh\eta - \cos\tau)}{d}\left(\hat{\boldsymbol{\eta}}\frac{\partial}{\partial\eta}\Psi + \hat{\boldsymbol{\tau}}\frac{\partial}{\partial\tau}\Psi + \hat{\boldsymbol{\phi}}\frac{1}{\sin\tau}\frac{\partial}{\partial\phi}\Psi\right) \tag{2.151}$$

Rewriting the external $\hat{\mathbf{z}}$-incident potential:

$$\Psi_3^{ext} = -(\cosh\eta - \cos\tau)^{\frac{1}{2}} A \sum_{n=0}^{\infty} P_n(\cos\tau)\left\{\pm(2n+1)e^{\mp(n+\frac{1}{2})\eta} + B_n \sinh\left[(n+\frac{1}{2})\eta\right]\right\} \tag{2.152}$$

from which we obtain

$$\frac{\partial}{\partial\eta}\Psi_3^{ext} = -A\frac{1}{2}(\cosh\eta - \cos\tau)^{-\frac{1}{2}}\sinh\eta \sum_{n=0}^{\infty} P_n(\cos\tau)\Big\{\pm(2n+1)e^{\mp(n+\frac{1}{2})\eta} + B_n \sinh\left[(n+\frac{1}{2})\eta\right]\Big\} \tag{2.153}$$

$$- A(\cosh\eta - \cos\tau)^{\frac{1}{2}} \sum_{n=0}^{\infty} P_n(\cos\tau)\Big\{\pm(2n+1)[\mp(n+\frac{1}{2})]e^{\mp(n+\frac{1}{2})\eta} + B_n \cosh\left[(n+\frac{1}{2})\eta\right](n+\frac{1}{2})\Big\} \tag{2.154}$$

$$\frac{\partial}{\partial\tau}\Psi_3^{ext} = -A\frac{1}{2}(\cosh\eta - \cos\tau)^{-\frac{1}{2}}\sin\tau \sum_{n=0}^{\infty} P_n(\cos\tau)\Big\{\pm(2n+1)e^{\mp(n+\frac{1}{2})\eta} + B_n \sinh\left[(n+\frac{1}{2})\eta\right]\Big\} \tag{2.155}$$

$$- A(\cosh\eta - \cos\tau)^{\frac{1}{2}} \sum_{n=0}^{\infty} \frac{d}{d\tau}\left[P_n(\cos\tau)\right]\Big\{\pm(2n+1)e^{\mp(n+\frac{1}{2})\eta} + B_n \sinh\left[(n+\frac{1}{2})\eta\right]\Big\} \tag{2.156}$$

$$\frac{\partial}{\partial\phi}\Psi_3^{ext} = 0 \tag{2.157}$$

Rewriting the external $\hat{\mathbf{x}}$-incident potential:

$$\Psi_1^{ext} = 2(\cosh\eta - \cos\tau)^{\frac{1}{2}} A \sum_{n=1}^{\infty} P_n^1(\cos\tau)\cos\phi\left\{e^{\mp(n+\frac{1}{2})\eta} + D_n \cosh\left[(n+\frac{1}{2})\eta\right]\right\} \tag{2.158}$$

which gives:

$$\frac{\partial}{\partial\eta}\Psi_1^{ext} = A(\cosh\eta-\cos\tau)^{-\frac{1}{2}}\sinh\eta\sum_{n=1}^{\infty}P_n^1(\cos\tau)\cos\phi\Big\{e^{\mp(n+\frac{1}{2})\eta} + D_n\cosh\Big[(n+\frac{1}{2})\eta\Big]\Big\} \quad (2.159)$$

$$2A(\cosh\eta-\cos\tau)^{\frac{1}{2}}\sum_{n=1}^{\infty}P_n^1(\cos\tau)\cos\phi\Big\{\mp(n+\frac{1}{2})e^{\mp(n+\frac{1}{2})\eta} + D_n\sinh\Big[(n+\frac{1}{2})\eta\Big](n+\frac{1}{2})\Big\} \quad (2.160)$$

$$\frac{\partial}{\partial\tau}\Psi_1^{ext} = A(\cosh\eta-\cos\tau)^{-\frac{1}{2}}\sin\tau\sum_{n=1}^{\infty}P_n^1(\cos\tau)\cos\phi\Big\{e^{\mp(n+\frac{1}{2})\eta} + D_n\cosh\Big[(n+\frac{1}{2})\eta\Big]\Big\} \quad (2.161)$$

$$2A(\cosh\eta-\cos\tau)^{\frac{1}{2}}\sum_{n=1}^{\infty}\frac{d}{d\tau}\Big[P_n^1(\cos\tau)\Big]\cos\phi\Big\{e^{\mp(n+\frac{1}{2})\eta} + D_n\cosh\Big[(n+\frac{1}{2})\eta\Big]\Big\} \quad (2.162)$$

$$\frac{1}{\sin\tau}\frac{\partial}{\partial\phi}\Psi_1^{ext} = \frac{-2A}{\sin\tau}(\cosh\eta-\cos\tau)^{\frac{1}{2}}\sum_{n=1}^{\infty}P_n^1(\cos\tau)\sin\phi\Big\{e^{\mp(n+\frac{1}{2})\eta}+D_n\cosh\Big[(n+\frac{1}{2})\eta\Big]\Big\} \quad (2.163)$$

In summary:

$$\mathbf{E}_3^{ext} = \hat{\boldsymbol{\eta}}E_{3\eta} + \hat{\boldsymbol{\tau}}E_{3\tau} \quad (2.164)$$

$$\mathbf{E}_1^{ext} = \hat{\boldsymbol{\eta}}E_{1\eta} + \hat{\boldsymbol{\tau}}E_{1\tau} + \hat{\boldsymbol{\phi}}E_{1\phi} \quad (2.165)$$

where:

$$A = \sqrt{2}E_0(\cosh\eta-\cos\tau) \quad (2.166)$$

$$B_n = 4\Delta_1\mu_{3n} \quad (2.167)$$

$$D_n = 2\Delta_1\mu_{1n} \quad (2.168)$$

By evaluating the above formulas, the theory can be compared to the numerical work, but because there is a need in Chapter 5 for only the external surface electric

field, attention will be confined to this. Figure 2.21 shows the normal component of the external surface electric field. In most cases the agreement is excellent. However, at large separations **and** large dielectric constants the agreement for the $\hat{\mathbf{z}}$-incidence cases is poor, and a 25% error is typical. This is mentioned here for completeness only, as the dielectric constants used later are never nearly as high.

The reason for this large error goes back to the crude approximation used to find the electric field: a finite difference of the potentials. As an example, in the case shown here the potentials used in the finite difference had an accuracy of about 0.25%. The Δr necessary for an accurate value of the surface electric field under normal circumstances was found to be 0.01 and this was also used for the large separation, large ϵ cases as well. This meant that the errors were multiplied 100 times, yielding the observed 25% error. Again, this is mentioned for completeness only and does not affect later calculations because the dielectric constants used there are much smaller.

If more accurate electric field values are required, a completely different approach is called for. Returning to the original governing integral equations in terms of the potentials, one could form $\mathbf{E} = -\nabla\Phi$, which would result in integral equations for the components of $\mathbf{E}$ on the surface. This could be solved using a numerical procedure analogous to that used here. The only trouble is that the integrals are more poorly behaved than is the case for the potentials.

Figure 2.22 shows the tangential component of the external surface electric field. Again, in most cases the agreement is excellent. However, in every case with a large dielectric constant the $\hat{\mathbf{z}}$-incident tangential field was inaccurate. The explanation is the same as stated previously, except that the errors are much less dependent on the separation.

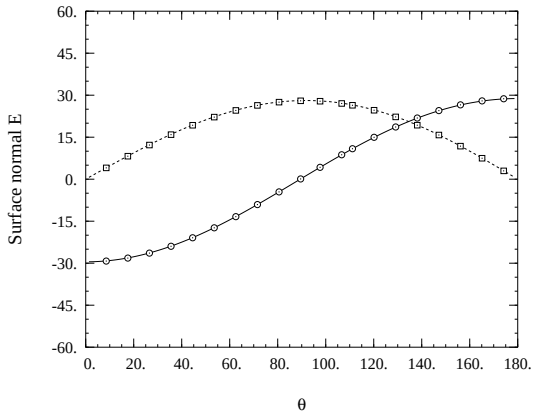

(a)

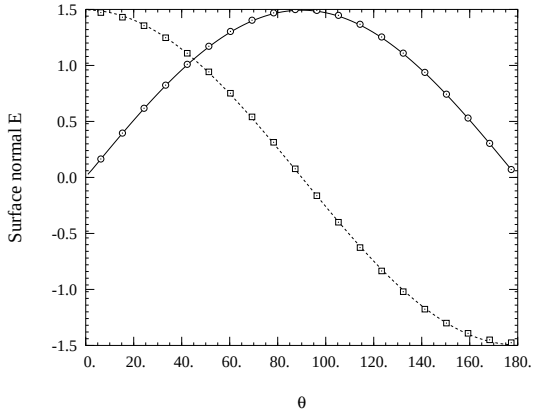

(b)

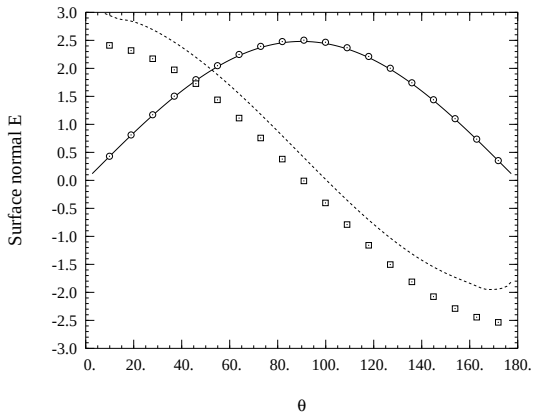

(c)

Figure 2.21 — Surface normal electric field for 2-sphere, as function of θ.

Lines show numerical results, marks show Love's theory: circles, $\hat{\mathbf{x}}$-incidence; squares, $\hat{\mathbf{z}}$-incidence; (a) Imaginary part, separation = 3, $\epsilon_r = -2.0 + j0.1$. (b) Real part, separation = 5, $\epsilon_r = +2.0 + j0.1$. (c) Real part, separation = 20, $\epsilon_r = 10.0 + j1.0$.

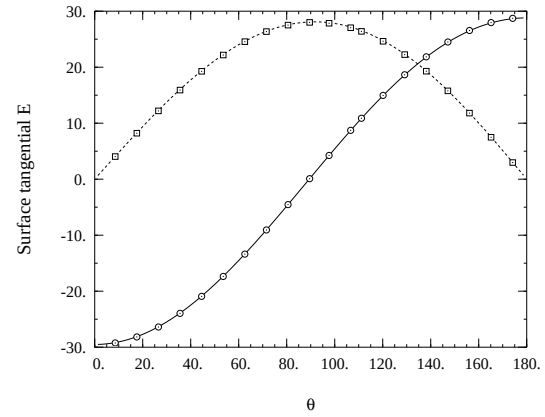

(a)

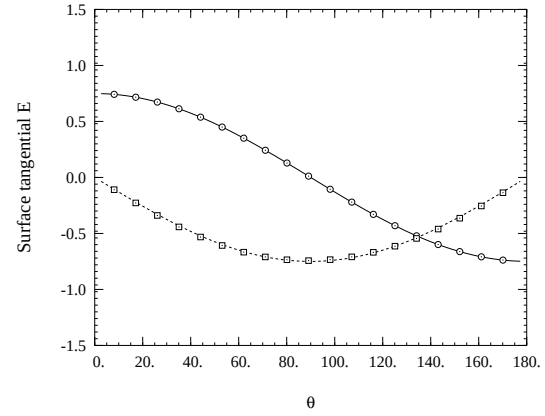

(b)

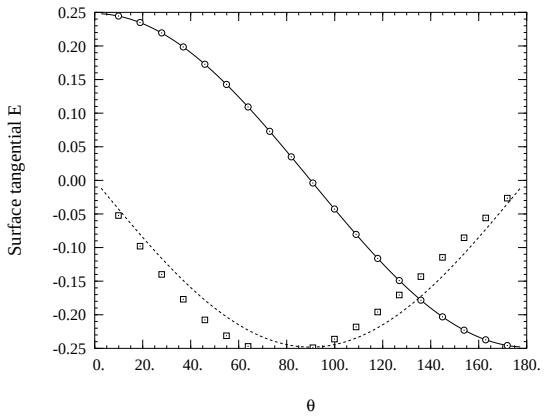

(c)

Figure 2.22 — Surface tangential electric field for 2-sphere, as function of θ.

Lines show numerical results, marks show Love's theory: circles, $\hat{\mathbf{x}}$-incidence; squares, $\hat{\mathbf{z}}$-incidence; (a) Imaginary part, separation = 3, $\epsilon_r = -2.0 + j0.1$. (b) Real part, separation = 5, $\epsilon_r = +2.0 + j0.1$. (c) Real part, separation = 20, $\epsilon_r = 10.0 + j1.0$.

To find the polarizability of the 2-sphere combination, and also the resonances, one can use Love's far-field potentials:

$$\Psi_1 \Big|_{\text{far field}} = -8E_0\Delta_1 a^3 \sinh^3\eta_0 \frac{\sin\theta\cos\phi}{R^2} \sum_{n=1}^{\infty} n(n+1)\mu_{1n} \tag{2.169}$$

$$\Psi_3 \Big|_{\text{far field}} = -8E_0\Delta_1 a^3 \sinh^3\eta_0 \frac{\cos\theta}{R^2} \sum_{n=0}^{\infty} (2n+1)\mu_{3n} \tag{2.170}$$

Comparing these to the far field of a dipole, oriented in either the $\hat{\mathbf{x}}$ or $\hat{\mathbf{z}}$ direction as appropriate, the volume-normalized polarizabilities are found to be:

$$\frac{\alpha_1}{V} = -12E_0\Delta_1 \sinh^3\eta_0 \sum_{n=1}^{\infty} n(n+1)\mu_{1n} \tag{2.171}$$

$$\frac{\alpha_3}{V} = -12E_0\Delta_1 \sinh^3\eta_0 \sum_{n=0}^{\infty} (2n+1)\mu_{3n} \tag{2.172}$$

The values for the resonances can be found by noting the values of the real part of the relative permittivity, ϵ_r, (with the imaginary part zero) which cause the imaginary part of the polarizability to become infinite, or equivalently, where the real part of the polarizability has an abrupt sign change from $+\infty$ to $-\infty$. This is not an easy task as stated. However, if one looks at the reciprocal of the real part, this quantity has a well-behaved sign change, going through zero smoothly at the position of the resonance. This was the idea that was used numerically to find the resonance values. Note that some zeroes are more easily found by the routines than others, and to find a particular one may require a very good initial guess, otherwise a different zero will be found instead.

The polarizabilities are compared in fig. 2.23. The agreement is excellent when not too near a resonance. Near a resonance, *i.e.,* when $|\epsilon_r - \epsilon_{res}| < 0.08$ or so, the error can be quite large, as is seen in part (b) of the figure. There, the $\hat{\mathbf{z}}$-incident polarizability is plotted with the real part of ϵ_r held constant at -2, and the imaginary part allowed to vary from near zero to one. Near zero, the error in the imaginary part is 161 out of 663, for an error of 25%. For the real part the error is much worse: the calculated curve goes positive while the theory goes negative! At

$\epsilon_r'' = 0.01$ the real part should be -396, but is instead 249. While this is bad, it does not reflect poorly on the formulation, but the numerical implementation: as the precision and accuracy of the matrix formation and inversion increase, this error decreases. But note that there will **always** be a small but finite region around each resonance where the agreement is poor. To obtain accurate results **at** the resonance requires a different approach, namely using an appropriate eigenvector expansion, as is developed in sec. 3.3. In summary, the agreement is quite good when at least 0.1 away from a resonance.

2.5.4 Two-Sphere Intensity

Aravind, *et al.* (1981) have carried out a theoretical investigation of the surface and near field intensities for two nearly (but not quite) touching spheres of the same size and material parameters. They solved the static boundary value problem but obtained the expansion coefficients numerically, rather than analytically as Love did. Then they solved for the intensity, $|\mathbf{E}|^2$, for a particular ambient uniform field direction. The particle material they considered was silver (in vacuum). This last point is a bit of a problem: the relative permittivity as a function of frequency, $\epsilon_r(\omega)$, for silver that was used was neither given nor referenced. Comparison with their data was therefore complicated. Despite this, a good approximation to their values was obtained (apparently) for, at least, the frequencies corresponding to $\omega = 3.48\,eV$ and $\omega = 3.21\,eV$, and very approximately elsewhere, by judiciously varying the imaginary part of ϵ_r at these two frequencies until reasonable agreement was obtained. These final values for ϵ_r were well within the limits of the available measured data (Physik Daten (1981)). Hence, the $\epsilon_r(\omega)$ used here was likely somewhat different from that used by Aravind, *et al.,* (1981) except at the two previously-mentioned frequencies.

The plots all show the same physical situation: two silver spheres (in vacuum) at varying separations with a uniform ambient field directed at 45° to their line of

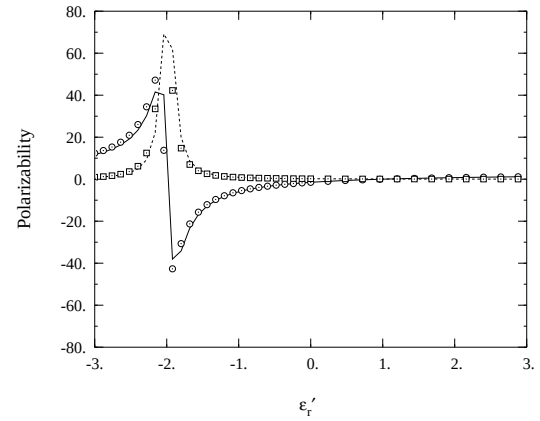

(a)

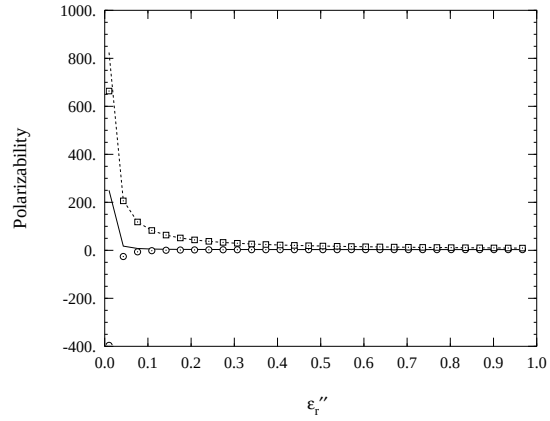

(b)

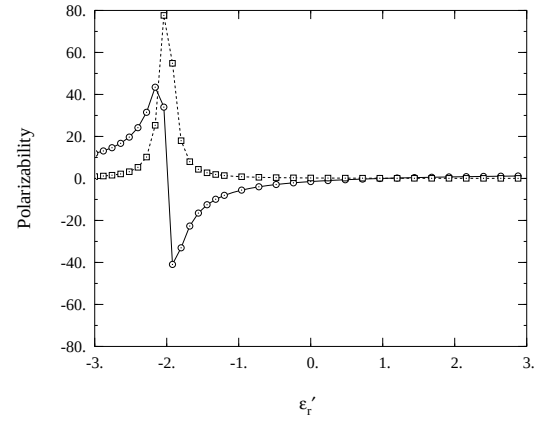

(c)

Figure 2.23 — Polarizability for 2-sphere (ẑ-incidence).

Lines show numerical results, marks show Love's theory: circles, real part; squares, imaginary part; (a) Separation = 3, $\epsilon_r'' = 0.1$. (b) Separation = 5, $\epsilon_r' = -2.0$. (c) Separation = 20, $\epsilon_r'' = 0.1$.

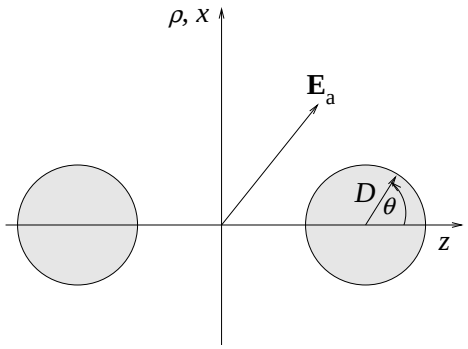

Figure 2.24 — Geometry for two spheres near each other.

centers (see fig. 2.24 below).

Figure 2.25 shows the intensity on the surface of one of the spheres as a function of ω, where ω is the energy of a photon, proportional to its frequency through $\omega = h\nu$, where h is Planck's constant. Here, the differences in $\epsilon_r(\omega)$ show up clearly in the differences between the theoretical solutions for an isolated sphere: small but noticeable differences from $\omega = 2.5\,eV$ through $\omega = 3.5\,eV$. The agreement for two spheres with center-to-center separation of 1.05 is not as good, especially below $3\,eV$ and at $3.5\,eV$, but both methods show the dual maxima quite clearly, with a worst case error of about 7%.

Figures 2.26 and 2.27 show the intensity along the surface of one of the spheres ($sep = 1.05$), as a function of angle, θ, where $\theta = 180°$ is the surface point closest to the other sphere, and $\theta = 45°$ corresponds to the point used in figure 2.25. Figure 2.26 is at $\omega = 3.48\,eV$, the main peak in figure 2.25, while figure 2.27 is at $\omega = 3.21\,eV$, the minor peak in figure 2.25. The agreement is excellent except in figure 2.27 for θ between $-120°$ and $-60°$ where the error is about 10%. Possibly this region is particularly sensitive to the choice of $\epsilon_r(\omega)$.

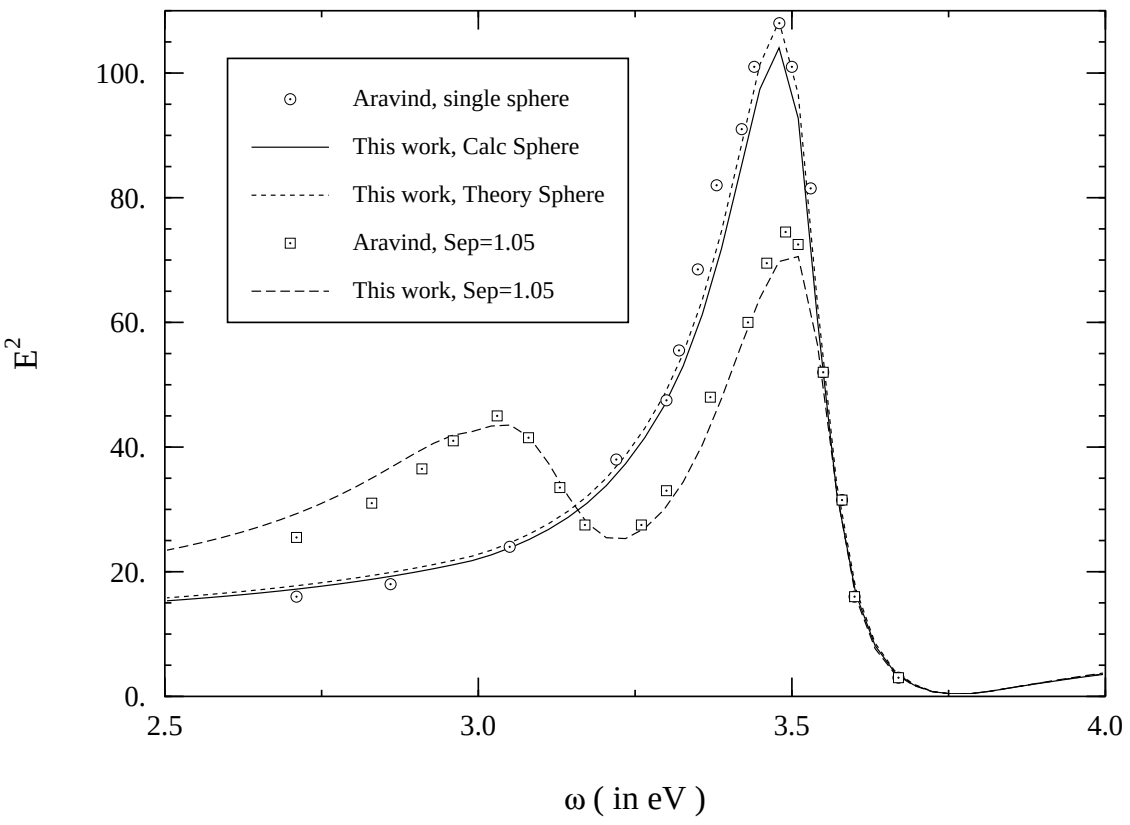

Figure 2.25 — Calculated $|\mathbf{E}|^2$ on sphere surface ($\theta = 45°$) compared with Aravind *et. al. vs.* ω.

Figures 2.28 and 2.29 show the intensity of the field along the line of centers for a separation of 1.05. Hence, the plots are symmetric, with $d/D = 0$ being the surface of one sphere, and $d/D = 1$ being the surface of the other. Here, the points were particularly difficult to accurately interpolate from the plots in Aravind's article due to the low variability (dynamic range) of the curve, and also because of the thickness of the line. Both the present data plot and Aravind's are symmetric (although they may not appear that way). The agreement here is quite good also, about 5% worst case error.

Overall, the agreement with Aravind *et al.* (1981) is very good, despite using only finite-differencing of the potentials.

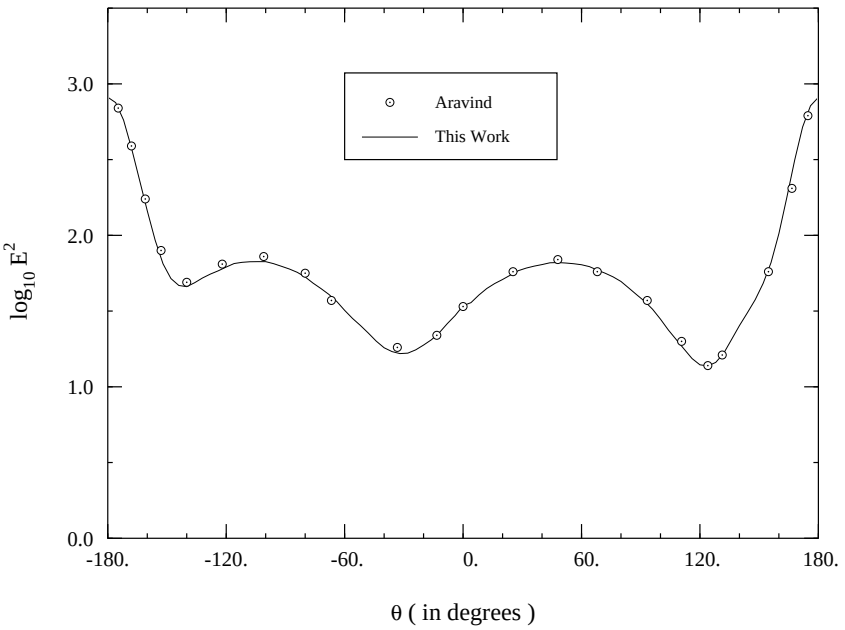

Figure 2.26 — Calculated $|\mathbf{E}|^2$ on sphere surface compared with Aravind *et. al. vs.* θ for $\omega = 3.48\,eV$.

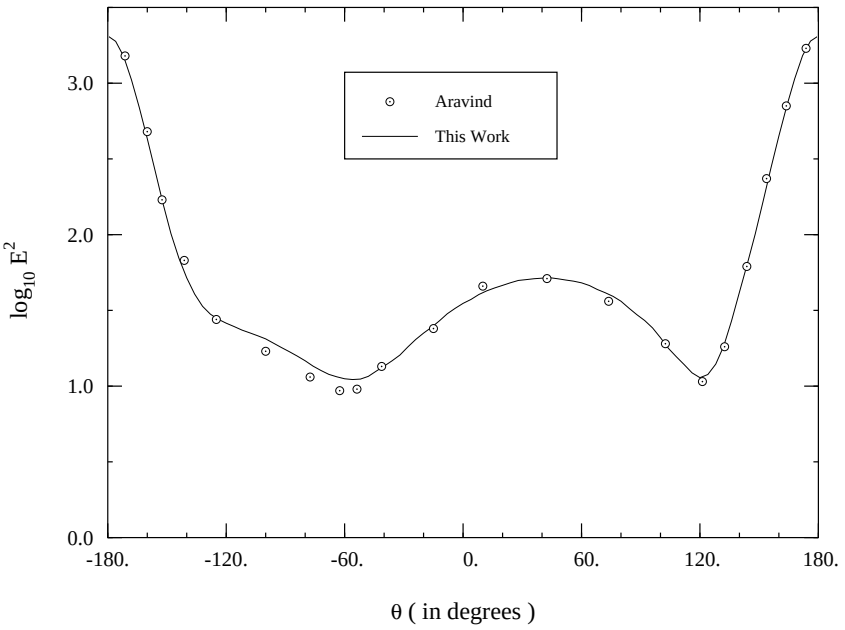

Figure 2.27 — Calculated $|\mathbf{E}|^2$ on sphere surface compared with Aravind *et. al. vs.* θ for $\omega = 3.21\,eV$.

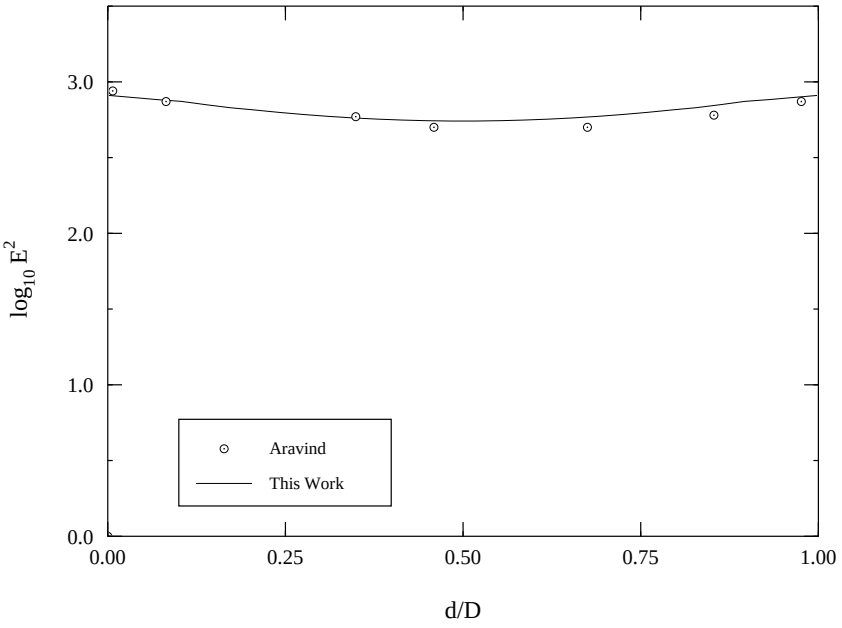

Figure 2.28 — Calculated $|\mathbf{E}|^2$ along line of centers between the two spheres compared with Aravind *et. al.* for $\omega = 3.48\,eV$.

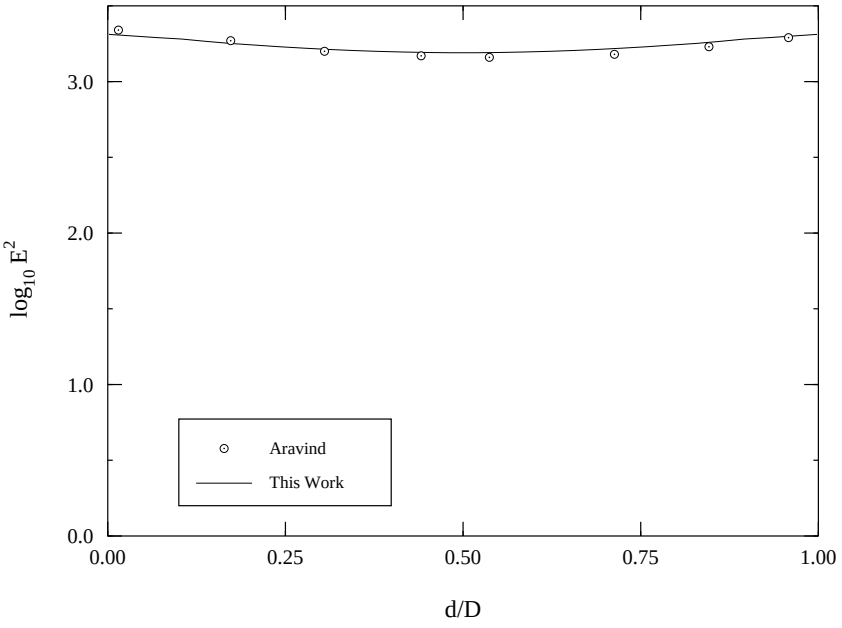

Figure 2.29 — Calculated $|\mathbf{E}|^2$ along line of centers between the two spheres compared with Aravind *et. al.* for $\omega = 3.21\,eV$.

2.5.5 Two-Sphere Resonances

The resonances were also calculated by Ruppin (1975) using a theoretical formulation similar to the one by Love (1975) that was presented earlier, but Ruppin's solution of the difference equation was numerical rather than analytical. Hence, his results, as presented in figures 2.30 and 2.31 are estimated from his published (graphical) results. (Note that the ratio d/R is equivalent to the previously defined center-to-center separation, in units of diameters.) The agreement between his and the present numerical technique is quite good except for slight differences for the the minor resonances for nearly-touching spheres at $\hat{\mathbf{x}}$ incidence.

Next, in fig. 2.32 the formulation of Love is compared to the present numerical technique. The results are even better: excellent agreement everywhere, even where there were discrepancies with Ruppin's work. This implies that Ruppin's numerical solution of the difference equation was not quite good enough at that separation. In summary, the values for the resonant dielectric constants as calculated numerically show excellent agreement with the theory of Love and all three methods are at least in good agreement.

2.5.6 Thin Disk Resonances

The numerical code of Chu, Weil, and Willis (Weil and Willis (1987)) (CWW for short) was available for direct comparison of the resonances for thin disks with flat ends. This section shows a comparison of the results for very thin disks with a diameter-to-thickness ratio of 23:1, which is the ratio used in our Chapter 5, section 5.5, to simulate some apects of photosynthesis. Note, however, that this section gives the comparison for flat-edged disks, while Chapter 5 uses round-end disks. This changes the values of the resonances slightly, but was necessary, as that is all the CWW code is capable of doing. The same code was used for the generation of the resonances in Chapter 5 as was used here, just the input data file was changed to account for the slightly different geometry.

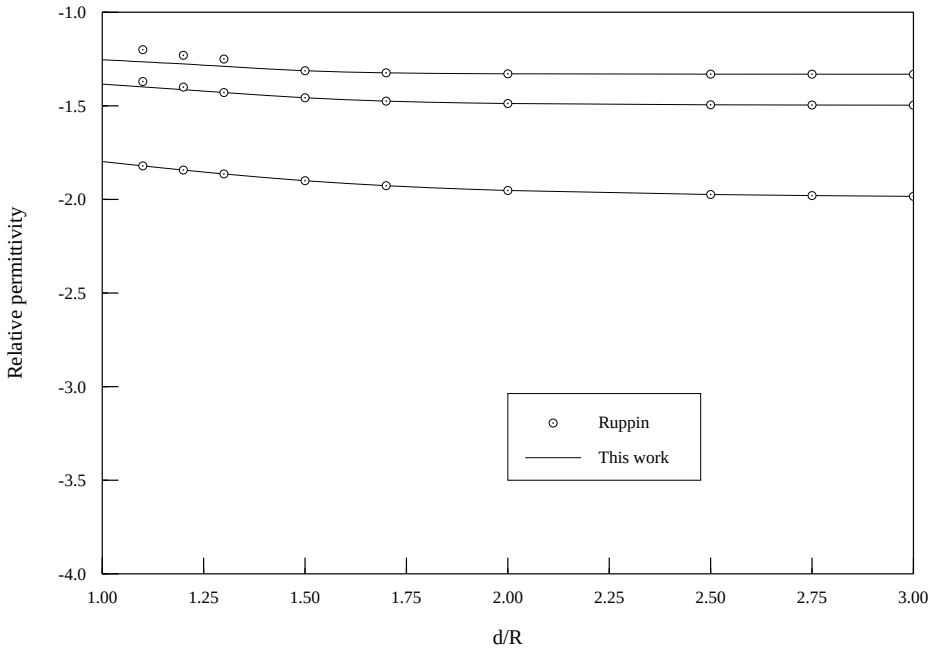

Figure 2.30 — Calculated resonant epsilons as a function of separation compared with Ruppin for $\hat{x}$-incidence.

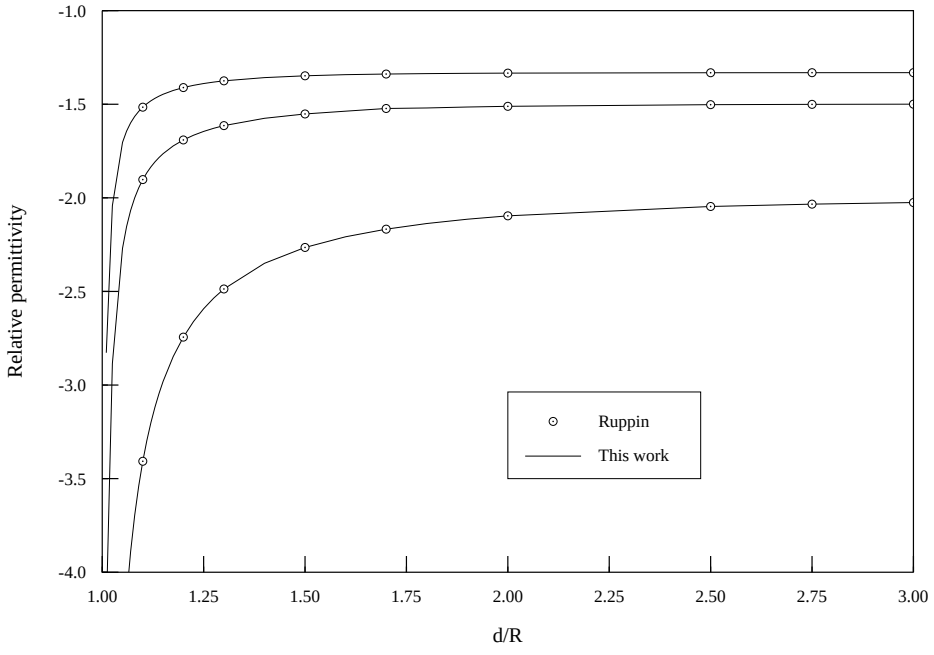

Figure 2.31 — Calculated resonant epsilons as a function of separation compared with Ruppin for $\hat{z}$-incidence.

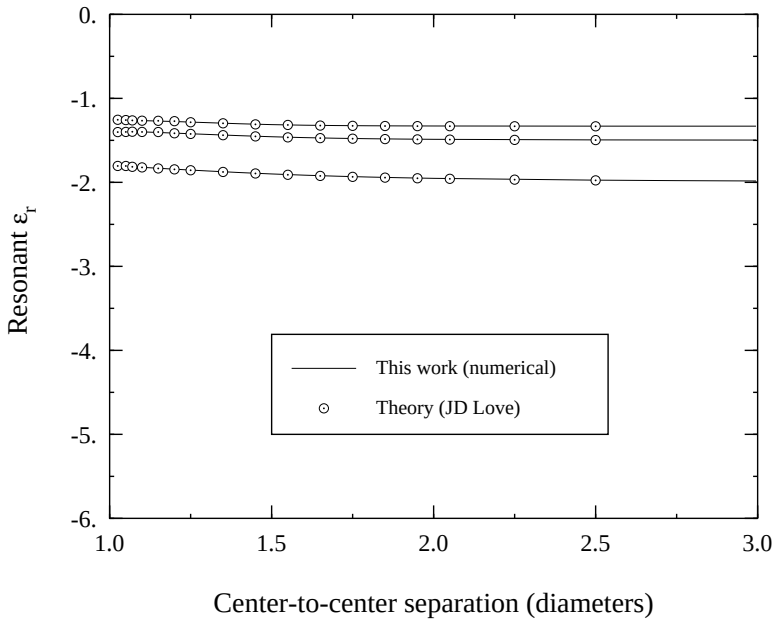

(a)

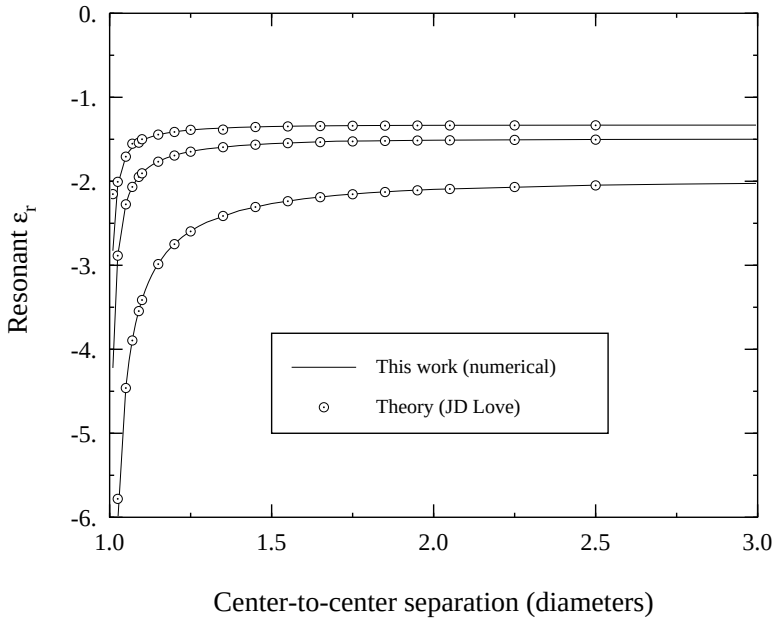

(b)

Figure 2.32 — Resonances for 2-sphere.

The major ones are more negative. Lines show numerical results, circles show theory. (a) $\hat{\mathbf{x}}$-incidence, (b) $\hat{\mathbf{z}}$-incidence.

The table below gives a comparison of the resonance positions obtained using the two different codes. The major and next two largest resonances for each incidence are given. The values do not agree exactly as in the previous sections, but are quite close.

Table 2.1 — Comparison of major resonances for thin disks.

incidence	This Work	CWW
$\hat{\mathbf{x}}$	-2.762	-2.92 $\pm$ 0.08
	-1.491	-1.67 $\pm$ 0.04
	-1.10	-1.08 $\pm$ 0.08
$\hat{\mathbf{z}}$	-2.864	-2.76 $\pm$ 0.08
	-1.510	-1.64 $\pm$ 0.08
	-1.00	-1.16 $\pm$ 0.08

A word about the CWW method is in order here. It is similar to a moment method code, but with a set of functions (defined throughout the whole disk) already assumed for the unknown field quantities. The coefficients of these field quantities are the unknowns. Final output is currents and absorption and extinction cross-sections. Given a plot of the absorption cross-section as a function of the real part of the relative permittivity (negative), with a small imaginary part, one can estimate where the resonances occur by picking out the highest peaks. Although not presented here, that is what was done to obtain the numbers presented here for the CWW code results. This is why the CWW results have the accuracy ranges: the points used to form the plot were at that spacing, and therefore the resonances are unknown to that degree.

In summary though, the agreement is good, and so the resonance positions found in Chapter six are believable.

2.6 Summary

This chapter has presented the analytical and numerical background for the remainder of the thesis. The integral equations were derived, then specialized to the case of rotational symmetry. The numerical implementation was covered in some detail, giving the resultant matrix equation and some of the numerical problems and their solutions. Lastly, exhaustive verification runs were made to be sure that the code was performing accurately for the cases of interest in this thesis. The verification work clearly shows that the numerical code is an accurate model of the electromagnetic interactions in the cases of interest here. With that, the code is next used to understand the coagulation effects on absorption (Chapter 3), the effect of the dielectric constant on the coagulation dynamics of two dielectric spheres (Chapter 4), and finally, the possible uses evolution has made of this phenomenon in the tailoring of the photosynthetic apparatus in some plants (Chapter 5).

CHAPTER III

COAGULATION EFFECTS ON ABSORPTION

3.1 Motivation

The coagulation of particles is ubiquitous in physical science. Some colloidal solutions show dramatic color changes when their constituent particles coagulate. Also, aerosols in the Earth's upper atmosphere are very often made up of many different particles agglomerated together. Understanding the effect this agglomeration has on the electromagnetic absorption is therefore an important issue worthy of study.

Before beginning, however, the topic of modeling the dielectric constant of materials is important. This is particularly true when investigating absorption bands in or near the visible range of electromagnetic radiation for particular materials; these have a real part of ϵ_r that is less than zero in this frequency range. Consequently, the Lorentz model for the permittivity, ϵ, is presented in this section. The presentation follows that given in Bohren and Huffman (1983), pp. 228-231.

The Lorentz model for ϵ is a classical theory based on a classical model of an atom as a mass on a spring: the valence electron being the mass and the spring representing the force field of the remainder of the atom. With a spring constant, K, and damping constant, b, the electron is driven by the local electric field:

$$m\ddot{\mathbf{x}} + b\dot{\mathbf{x}} + K\mathbf{x} = e\mathbf{E} \tag{3.1}$$

with e being the charge of the electron, m its mass, and $\mathbf{x}$ its position relative to the nucleus.

When $\mathbf{E}$ is harmonic in time, with frequency ω, so is $\mathbf{x}$, giving the approximate result:

$$\mathbf{x} = \frac{(e/m)\mathbf{E}}{\omega_0^2 - \omega^2 - i\gamma\omega} \tag{3.2}$$

where $\omega_0^2 = K/m$, and $\gamma = b/m$. The induced dipole moment of this atom is therefore $\mathbf{p} = e\mathbf{x}$. If it is assumed that there are N atoms per unit volume then the dipole moment per unit volume, $\mathbf{P}$, is:

$$\mathbf{P} = \frac{\omega_p^2}{\omega_0^2 - \omega^2 - i\gamma\omega}\epsilon_0\mathbf{E} \tag{3.3}$$

with $\omega_p^2 = Ne^2/(m\epsilon_0)$. By definition, then

$$\epsilon_r = 1 + \frac{\omega_p^2}{\omega_0^2 - \omega^2 - i\gamma\omega} \tag{3.4}$$

and with $\epsilon_r = \epsilon_r' + j\epsilon_r''$:

$$\epsilon_r' = 1 + \frac{\omega_p^2(\omega_0^2 - \omega^2)}{(\omega_0^2 - \omega^2)^2 + \gamma^2\omega^2} \tag{3.5}$$

$$\epsilon_r'' = \frac{\omega_p^2\gamma\omega}{(\omega_0^2 - \omega^2)^2 + \gamma^2\omega^2} \tag{3.6}$$

These functions are plotted in fig. 3.1.

In this thesis the concern is with the IR and optical range of frequencies. In this range it is known that the physical mechanism underlying the dielectric behavior is the relative displacements of different ions from their equilibrium positions (Kittel (1976), pp. 410–411). To obtain a heuristic understanding one can think of the material as being made up of dipoles with some damping mechanism. The strength of each dipole oscillates as $e\mathbf{x}$:

$$\mathbf{p} = \frac{(e^2/m)\mathbf{E}}{\omega_0^2 - \omega^2 - i\gamma\omega} \tag{3.7}$$

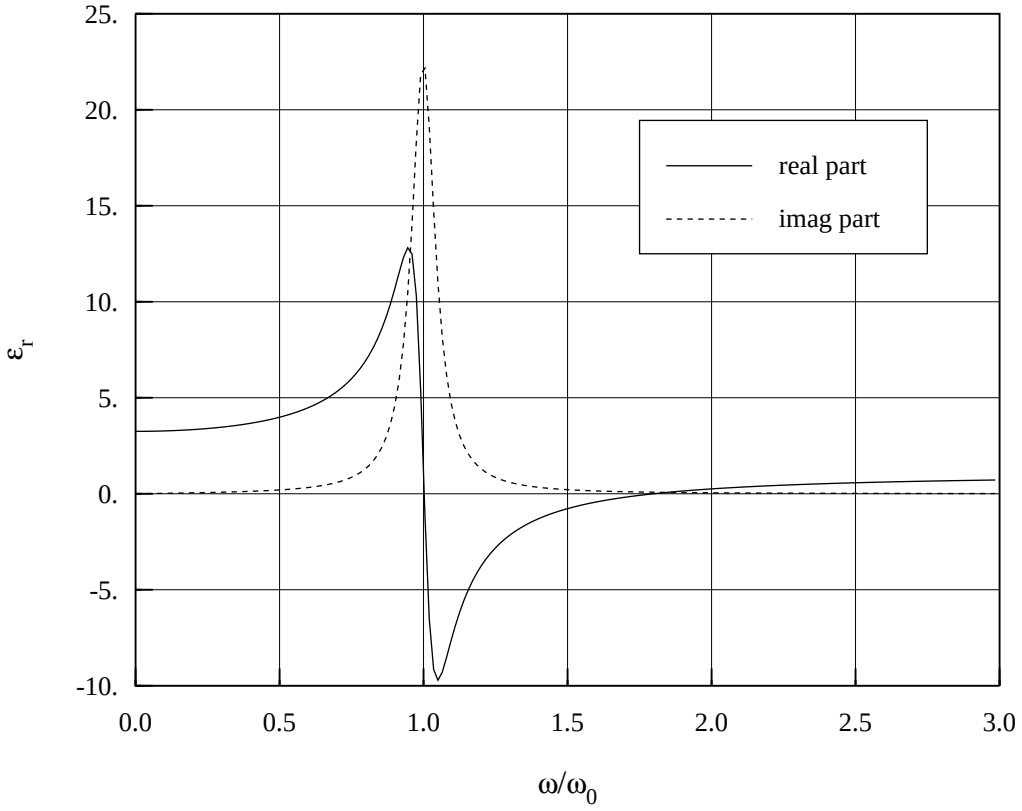

Figure 3.1 — Permittivity as a funtion of ω/ω_0 for the Lorentz model.

or, in terms of the magnitude and phase:

$$|\mathbf{p}| \propto \frac{1}{\sqrt{(\omega_0^2 - \omega^2)^2 + \gamma^2\omega^2}} \tag{3.8}$$

$$arg\,\mathbf{p} \propto \tan^{-1}\left(\frac{\gamma\omega}{\omega_0^2 - \omega^2}\right) \tag{3.9}$$

These functions are plotted in figs. 3.2 and 3.3.

Note that for frequencies below ω_0 the dipole oscillates more-or-less in phase with the excitation, but that above ω_0 the dipole is generally 180° out of phase with the excitation: the dipole opposes the incident field. The magnitude increases dramatically near ω_0 but falls off rapidly away from the resonance. Because ϵ_r has the constant term added to the dipole-like term, the values are shifted, giving ϵ_r a

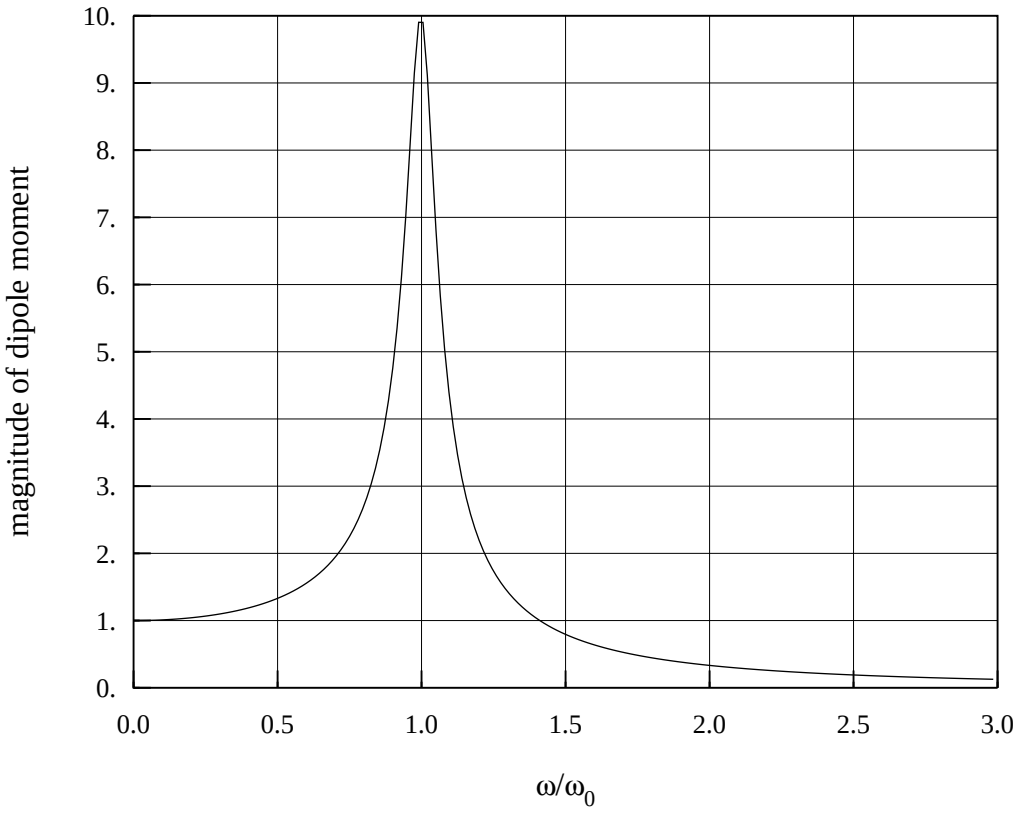

Figure 3.2 — Magnitude of dipole moment as a funtion of ω/ω_0 for the Lorentz model.

negative value only in a finite region above ω_0, by virtue of the large negative dipole moments in the atoms near, but above, resonance at ω_0.

Because the magnitude of the opposing dipole moment falls off for increasing $\omega > \omega_0$, the value of ϵ_r' eventually rises above zero to 1 at $\omega = \infty$.

Although this is a classical explanation and derivation, the formulas arrived at are still valid, but with the symbols reinterpreted for quantum mechanics. See Bohren and Huffman to explore this further.

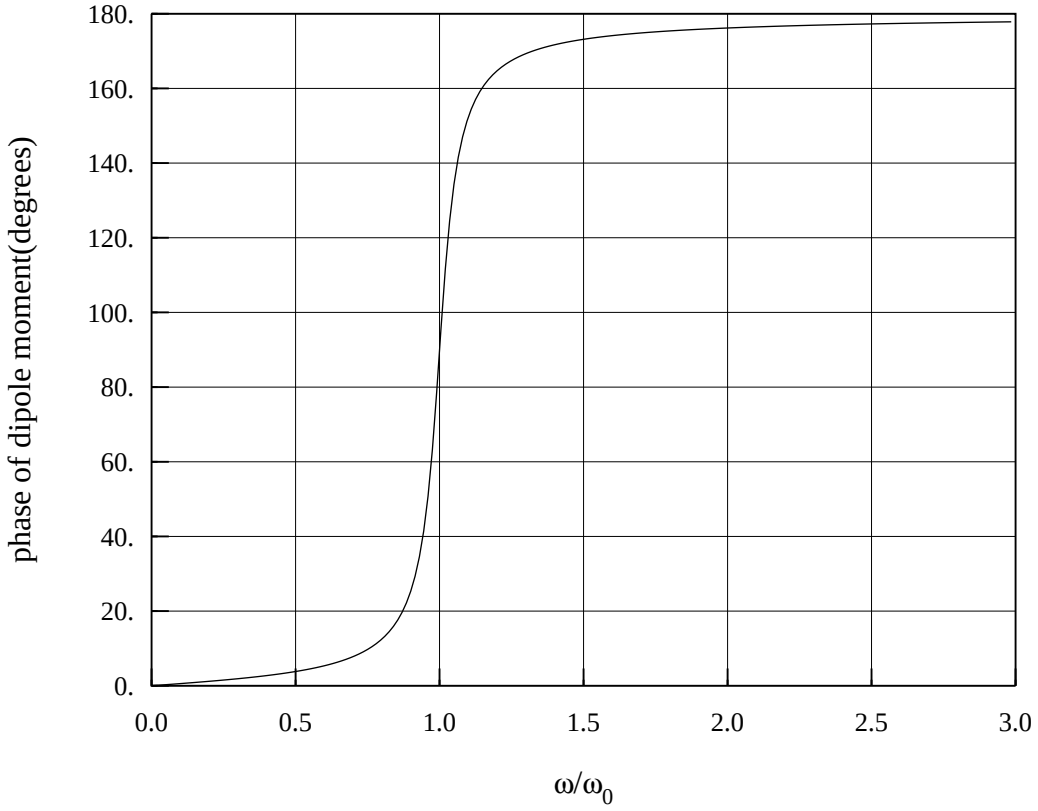

Figure 3.3 — Phase of dipole moment as a funtion of ω/ω_0 for the Lorentz model.

3.2 Formulation

In Kleinman and Senior (1986) the case of cylindrically symmetric particles is treated. There, the polarizability tensor is shown to consist of three terms on the diagonal, all others being zero, with $P_{11} = P_{22}$. The scattering coefficient **S** is shown to be:

$$\mathbf{S}(\hat{\mathbf{r}}, \hat{\mathbf{k}}, \hat{\mathbf{a}}) = -k_0^2 \left[P_{11}\hat{\mathbf{r}}\times(\hat{\mathbf{r}}\times\hat{\mathbf{a}}) + (P_{33} - P_{11})(\hat{\mathbf{a}}\cdot\hat{\mathbf{z}})\hat{\mathbf{r}}\times(\hat{\mathbf{r}}\times\hat{\mathbf{z}})\right] \tag{3.10}$$

which assumes that no magnetic dipole terms are present.

For the case of the electric field polarized in the $\hat{\mathbf{x}}$-direction, we have: $\hat{\mathbf{a}} = -\hat{\mathbf{x}}, \hat{\mathbf{k}} = -\hat{\mathbf{z}}$. Putting this into the forward scattering theorem ($\hat{\mathbf{r}} = -\hat{\mathbf{k}}$) yields:

$$\sigma_{ext} = k_0 Im\{P_{11}\} \tag{3.11}$$

and for an electric field polarized in the $\hat{\mathbf{z}}$-direction,

$$\sigma_{ext} = k_0 Im\{P_{33}\} \tag{3.12}$$

Lastly, the scattering cross-section is shown to approach zero for small scatterers, and so:

$$\sigma_{ext} = \sigma_{abs} \tag{3.13}$$

for Rayleigh scatterers.

This means that the absorption characteristics of a particle are clear from the polarizability tensor elements. Hence, in the following, these elements are the main subject of interest.

3.3 Polarizability Model

A new model for the polarizability of small dielectric particles is now proposed. This model is presented in Pierce and Weil (1990) where its application to coagulating and coagulated spheres is investigated numerically. First, an investigation of the solution of the scattering problem for small particles of general shape is made and the polarizability model is presented in its general form. Then this formulation is specialized to the case of two spheres coagulating and coagulated.

3.3.1 Introduction

The calculation of absorption spectra is useful and desirable by itself, but a more theoretically satisfying calculation that can yield much deeper insight into the absorption spectra of irregularly shaped particles cosiders P_{ii} as a function of ϵ, instead of frequency and material. Cast in this way, there is a direct analogy with the analytical formula for a sphere. For a Rayleigh sphere we have:

$$Im\{\mathrm{P}_{11}\} = \frac{9\epsilon_r''}{(\epsilon_r' + 2)^2 + \epsilon_r''^2} \tag{3.14}$$

where ϵ_r' and ϵ_r'' are the real and imaginary parts, respectively, of the complex relative permittivity of the sphere. This can intuitively be seen as a sharp resonance of

"strength" $9/\epsilon_r''$ at $\epsilon_r' = -2$, which stands out against a more uniform background; see fig. 3.4. Physically, this resonance can be explained as a coupling of electromagnetic energy into an internal, non–electromagnetic vibrational mode of the material: the electromagnetic energy is used to drive the lattice vibrations. In dielectric materials this mode is called a polariton, whereas in metals a similar excited mode is called a surface plasmon (see, *e.g.,* Nelson (1979)).

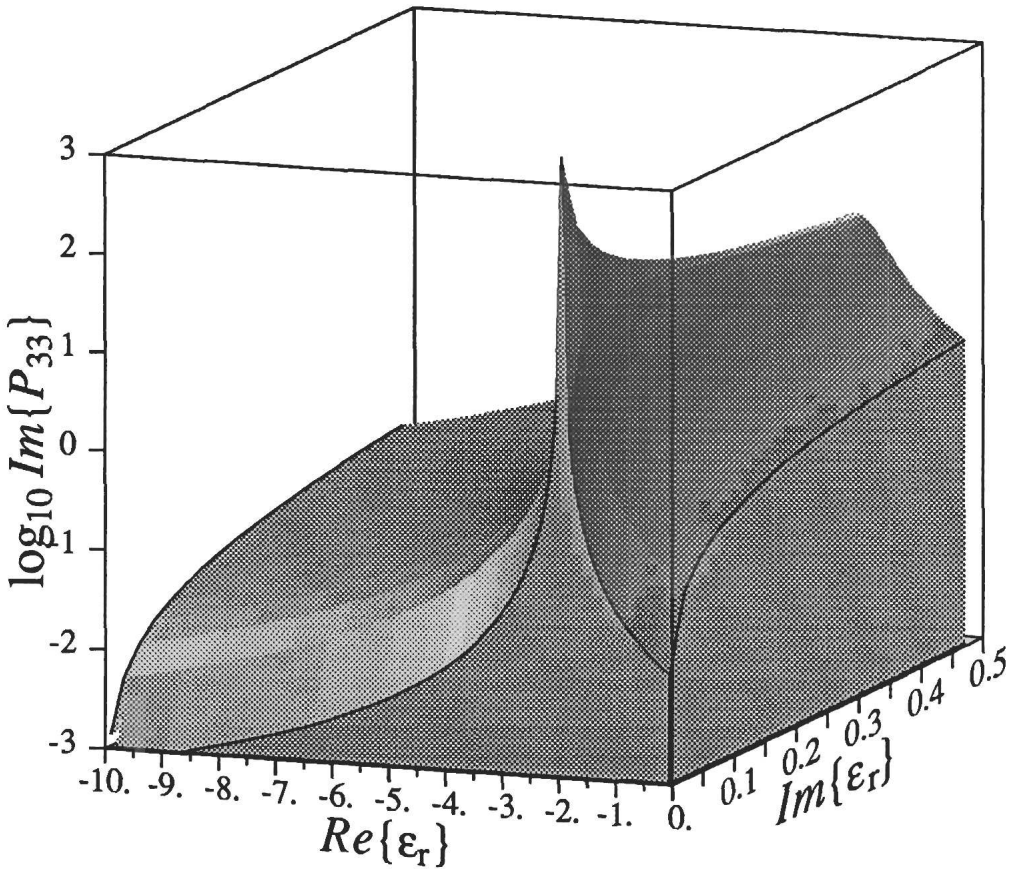

Figure 3.4 — Analytical *Im*{Polarizability} for a sphere.

Expressions similar to those for the sphere can be obtained for ellipsoids (see Bohren and Huffman (1983), p. 350). Using this idea, a reformulation of the numerical procedure yields the eigenvalues of the integral equation. The resonant

positions (ϵ_r' to give infinite absorption when $\epsilon_r'' = 0$) are then simple functions of these eigenvalues. Using these resonant ϵ's and some numerically-generated values of $Im\{\mathrm{P}_{ii}(\epsilon)\}$, the data can be fitted to a generalization of the preceding formula; i.e.:

$$Im\{\mathrm{P}_{ii}(\epsilon)\} = \sum_{k=1}^{N} \frac{\mathrm{A}_k \epsilon_r''}{(\epsilon_r' - \epsilon_{res,k})^2 + \epsilon_r''^2} \tag{3.15}$$

This procedure works quite well. The only problem with it is the chice of N: the discretized version of the integral equation has as many eigenvalues as the size of the matrix we create. Which of these are "real" and not an artifact of the discretization? So far, we have chosen those resonances that are most prominent for large ϵ_r''. Sometimes this leaves out certain resonances that are numerically quite prominent when ϵ_r'' is small, but decay rapidly with increasing ϵ_r''. However, most of the possible resonances corresponding to the eigenvalues don't even get this far: they have no peak near the negative real ϵ axis; hence, they are assumed to be due to the discretization process. So far, the resonances that decay quickly are also thought of as spurious, but more analysis in the future may reveal a different explanation. Illustrations of this for the particular shapes investigated here are included in sections 3.4.2 and 3.4.3.

3.3.2 General Particles

For a homogeneous particle of arbitrary shape, the integral equation for the surface potential, from (2.24), is:

$$\Phi(\mathbf{r}) = \frac{2\epsilon_2}{\epsilon_2 + \epsilon_1}\Psi(\mathbf{r}) + \frac{\epsilon_2 - \epsilon_1}{\epsilon_2 + \epsilon_1}\frac{1}{2\pi} \iint_S \Phi(\mathbf{r}')\frac{\partial}{\partial n'}\left(\frac{1}{R}\right) dS' \tag{3.16}$$

where the integral is taken to be a Cauchy principal value integral, $\Psi(\mathbf{r})$ is the excitation field (static), and $R = |\mathbf{r} - \mathbf{r}'|$, with both $\mathbf{r}$ and $\mathbf{r}'$ on the surface. See Chapter 2 for the other definitions.

For notational convenience let $\Phi(\mathbf{r}) = -W(\mathbf{r})/(\epsilon_2 - \epsilon_1)$, and also let $\Psi = 0$, for

the eigenvalue problem. This yields:

$$\iint_S W(\mathbf{r})K(\mathbf{r},\mathbf{r}')\,dS' = 2\pi\frac{\epsilon_2+\epsilon_1}{\epsilon_2-\epsilon_1}W(\mathbf{r}) \tag{3.17}$$

or, more simply:

$$LW = \lambda W \tag{3.18}$$

See Arfken (1985) for an example. This linear operator equation has a discrete spectrum of infinitely-many eigenvalues, λ_i, all real and negative, and a corresponding orthogonal set of eigenfunctions, W_i.

It is also well-known that one can represent the solution to (3.16) as an expansion in terms of these eigenfunctions,

$$\Phi(\mathbf{r}) = \sum_{i=1}^{\infty}\beta_i\left(\frac{-1}{\epsilon_2-\epsilon_1}\right)W_i(\mathbf{r}) \tag{3.19}$$

where W_i satisfies $LW_i = \lambda_i W_i$, and β_i is some unknown coefficient. Representing Ψ in a similar way gives

$$\Psi(\mathbf{r}) = \sum_{i=1}^{\infty}\alpha_i\left(\frac{-1}{\epsilon_2-\epsilon_1}\right)W_i(\mathbf{r}) \tag{3.20}$$

where in this case, the α_i are known because Ψ is known. Specifically:

$$\alpha_i = \iint_S \Psi(\mathbf{r})W_i(\mathbf{r})\,dS' \equiv \langle\Psi, W_i\rangle \tag{3.21}$$

Hence, (3.16) becomes:

$$\sum_{i=1}^{\infty}\beta_i W_i(\mathbf{r}) = \frac{2\epsilon_2}{\epsilon_2-\epsilon_1}\sum_{i=1}^{\infty}\alpha_i W_i(\mathbf{r}) + \frac{1}{\lambda}\frac{1}{2\pi}\iint_S\left(\sum_{i=1}^{\infty}\beta_i W_i(\mathbf{r})\right)K(\mathbf{r},\mathbf{r}')\,dS' \tag{3.22}$$

since exchanging the order of integration and summation is allowable. After taking the inner product of the whole equation with W_j, an equation for the unknown coefficients is produced:

$$\beta_j = \frac{1-\epsilon_{res,j}}{\epsilon_r-\epsilon_{res,j}}\langle\Psi, W_j\rangle \tag{3.23}$$

where $\epsilon_{res,j}$ is the value of ϵ_r corresponding to the eigenvalue λ_j, where $\epsilon_r = \epsilon_1/\epsilon_2$.

Because the polarizability tensor elements are functions of the total surface potential (1.87):

$$P_{ii} = (1 - \epsilon_r) \iint_S (\hat{\mathbf{n}}' \cdot \hat{\mathbf{x}}_i) \Phi_j(\mathbf{r}') \rho' \, dS' \tag{3.24}$$

with $i, j = 1, 2, 3$, and where $\hat{\mathbf{x}}_i, i = 1, 2, 3$, represents the three orthogonal unit vectors of a cartesian coordinate system, and using the eigenfunction expansion for Φ_j, this gives:

$$P_{ij} = (1 - \epsilon_r) \iint_S (\hat{\mathbf{n}}' \cdot \hat{\mathbf{x}}_i) \sum_{k=1}^{\infty} \beta_k^j W_k^j(\mathbf{r}') \, dS' \tag{3.25}$$

with $i, j = 1, 2, 3$, leading to the model:

$$P_{ij} = V \sum_{k=1}^{N} \frac{A_k^{ij}}{\epsilon_r - \epsilon_{res,k}^j} \tag{3.26}$$

where V is the volume of the body, $\epsilon_{res,k}^j$ is the value of ϵ_r that corresponds to λ_k for z-incidence ($j = 3$), and for x-incidence ($j = 1$), and lastly, A_k^{ij} is the coupling coefficient for that term:

$$A_k^{ij} = \frac{1}{V} \left[(1 - \epsilon_r)(1 - \epsilon_{res,k}^j) \langle \Psi^j, W_k^j \rangle \iint_S (\hat{\mathbf{n}}' \cdot \hat{\mathbf{x}}_i) W_k^j(\mathbf{r}) \, dS' \right] \tag{3.27}$$

The volume is explicitly extracted because it is known that the static polarizability is proportional to the volume. It is also assumed that only a finite number of terms is needed for convergence to within any desired accuracy, for a given ϵ_r. As with Fourier series, the terms with the largest (in magnitude) coupling coeffients, A_k^{ij}, should be used in the summation.

Note that each term in the summation is of the form:

$$\frac{1 - \epsilon_r}{\epsilon_r - \epsilon_{res,k}^j} f \tag{3.28}$$

where f is not a function of ϵ_r. Hence, the variation of each term in the ϵ_r-plane is already known and can be analyzed. Use $P(\epsilon_r)$ as the symbol to represent the coefficient of f:

$$P(\epsilon_r) \equiv \frac{1 - \epsilon_r}{\epsilon_r - \epsilon_{res,k}^j} \tag{3.29}$$

Notice that this term does not depend on i, the observation polarization, but only on j, the excitation polarization, and k, the particular eigenvalue. Hence, the terms in a single column of the tensor all have the same set of eigenvalues and eigenvectors and so the only difference between them must be due to the coupling coefficient term, which expresses the inner product of an eigenfunction, W_i, and the projection of the surface normal along the excitation (i) direction ($\hat{\mathbf{n}}' \cdot \hat{\mathbf{x}}_i$). Hence, the symmetries of $\overline{\overline{P}}$ reflect the symmetries of the body through its excitation eigenvalues and eigenfunctions as well as the excitation polarization.

The variation of the term $P(\epsilon_r)$ is the most critical here. This term exhibits the dramatic resonance effects that are so important under certain circumstances. In fact, near a resonance ($\epsilon_r \approx \epsilon^j_{res,k}$) the field and the polarizability can often be accurately represented by a single term in the series, the k-th term, which nearly blows up. An analysis of a single term near $\epsilon^j_{res,k}$ is therefore in order.

Expressing the real and imaginary parts separately, gives:

$$Re\{P(\epsilon_r)\} = \frac{(\epsilon_r' - 1)(\epsilon_r' - \epsilon_{res,k}) + (\epsilon_r'')^2}{(\epsilon_r' - \epsilon_{res})^2 + (\epsilon_r'')^2} \tag{3.30}$$

$$Im\{P(\epsilon_r)\} = \frac{\epsilon_r''(1 - \epsilon_{res})}{(\epsilon_r' - \epsilon_{res})^2 + (\epsilon_r'')^2} \tag{3.31}$$

where $\epsilon_r = \epsilon_r{}' + i\epsilon_r{}''$. Figure 3.5 shows this function for $\epsilon_{res} = -5$ and three different values for ϵ_r''.

3.3.3 Application to Rotationally Symmetric Bodies

Equation (3.16) can be specialized to a particle or set of particles with rotational symmetry about the z-axis, with the medium being free-space and with uniform static fields as the excitation:

$$V_j(s) = \frac{1}{1+\epsilon_r}(-x_j) + \frac{1-\epsilon_r}{1+\epsilon_r}\frac{1}{2\pi}\oint_s V_j(s')K_j(s,s')\,ds' \qquad ; j = 1,3 \tag{3.32}$$

where $j = 1$ is for an incident field direction $\hat{\mathbf{x}}$, and $j = 3$ is for $\hat{\mathbf{z}}$-incidence We also have $\Phi_1(\mathbf{r}) = V_1(s)\cos\phi$, and $\Phi_3(\mathbf{r}) = V_3(s)$, where s is the distance along

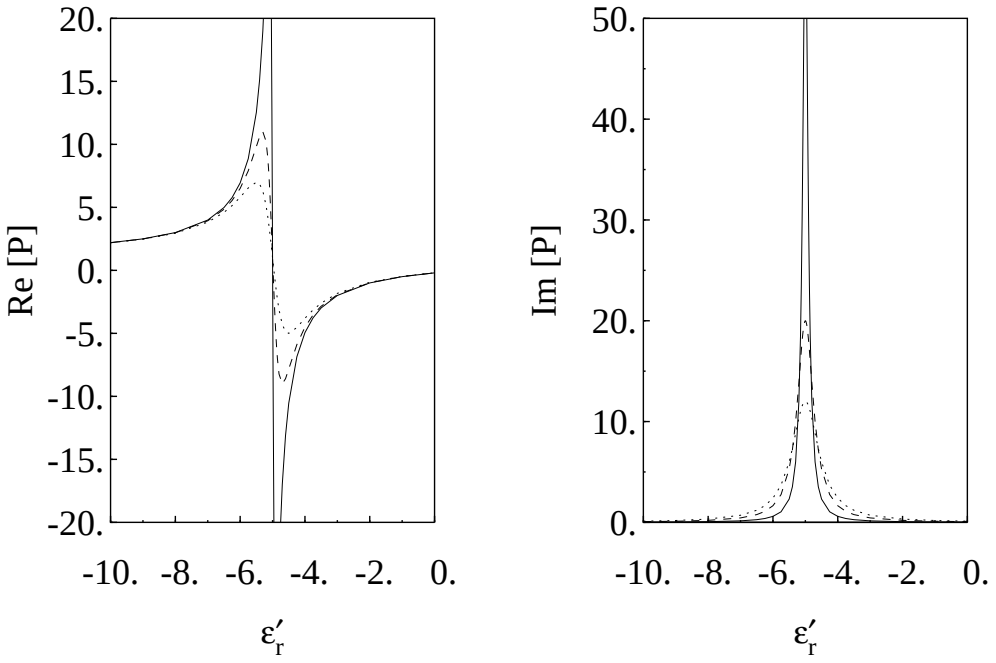

Figure 3.5 — Variation of function P (3.30, 3.31) near a resonance.
For $\epsilon_{res} = -5$, (——), $\epsilon_r{}'' = 0.1$; (– – –), $\epsilon_r{}'' = 0.3$; ($\cdot\ \cdot\ \cdot$), $\epsilon_r{}'' = 0.5$.

---

the perimeter in the x-z plane, $\epsilon_r = \epsilon/\epsilon_0$ is the relative permittivity to that of free space, and K_j is the Green's function for each excitation:

$$K_1(s,s') = \rho' \left\{ \rho \cos\alpha' \Omega_2 + [(z'-z)\sin\alpha' - \rho' \cos\alpha'] \Omega_1 \right\} \tag{3.33}$$

$$K_3(s,s') = \rho' \left\{ \rho \cos\alpha' \Omega_1 + [(z'-z)\sin\alpha' - \rho' \cos\alpha'] \Omega_0 \right\} \tag{3.34}$$

in a cylindrical coordinate system (ρ, ϕ, z), and

$$\Omega_i = \int_0^\pi \frac{\cos^i \gamma}{R^3}\, d\gamma, \tag{3.35}$$

which can be expressed in terms of elliptic integrals and their derivatives.

For a numerical solution we discretize (3.32) with the substitution:

$$V_j(s) = \sum_{i=1}^{N} v_{ij}\, \mathrm{rect}\left(\frac{s - s_i}{\Delta s_i}\right) \tag{3.36}$$

where the rect function is a unit-amplitude rectangular pulse, centered at $s = s_i$ with width Δs_i. This transforms the integral equation into a matrix equation, solvable by standard numerical techniques.

From (1.87):

$$P_{jj} = (1 - \epsilon_r) \oint_s \int_0^{2\pi} (\hat{\mathbf{n}}' \cdot \hat{\mathbf{x}}_j) \Phi_j(r) \rho' \, d\phi' \, ds' \tag{3.37}$$

and using an eigenfunction expansion for Φ_j yields

$$P_{jj} = (1 - \epsilon_r) \int_0^{2\pi} (\hat{\mathbf{n}}' \cdot \hat{\mathbf{x}}_j) \oint_s \sum_{k=1}^{\infty} \beta_k^j \phi_k^j(s') \rho' \, d\phi' \, ds' \tag{3.38}$$

which gives

$$P_{jj} = (1 - \epsilon_r) \sum_{k=1}^{\infty} \frac{A_k^{jj}}{\epsilon_r - \epsilon_{res,k}^j} \quad ; j = 1, 3 \tag{3.39}$$

where $\epsilon_{res,k}^1$ and $\epsilon_{res,k}^3$ are the two sets of eigenvalues for the integral operator, and A_k^{11} and A_k^{33} are the coupling coefficients:

$$A_k^{33} = 2\pi(\epsilon_{res,k}^3 - 1) \frac{\langle z', W_k^3 \rangle \langle \rho' \sin \alpha', W_k^3 \rangle}{\langle W_k^3, W_k^3 \rangle} \tag{3.40}$$

$$A_k^{11} = -\pi(\epsilon_{res,k}^1 - 1) \frac{\langle \rho', W_k^1 \rangle \langle \rho' \cos \alpha', W_k^1 \rangle}{\langle W_k^1, W_k^1 \rangle} \tag{3.41}$$

with the inner product defined here as:

$$\langle a, b \rangle \equiv \oint_s a(s') b(s') \, ds' \tag{3.42}$$

The eigenfunctions, W_k^j, are those of the following integral equation:

$$\oint_s W_k^j(s') K_j(s, s') \, ds' - \pi \left(\frac{1 + \epsilon_r}{1 - \epsilon_r} \right) W_k^j(s) = 2\pi \Psi^j(s) \tag{3.43}$$

where $j = 1, 3;\ k = 1, 2, \ldots \infty$ and with the excitation, Ψ^j, set to zero.

3.4 Results for Coagulated Equal Spheres

3.4.1 Near and Internal Fields, Spectra

Two spheres were simulated, both separate and overlapping. Two examples are shown in fig. 3.6.

Figure 3.6 — Two examples from the family of coagulated spheres.

The center–to–center separation of the two spheres is given in terms of the sphere diameter. For example, the separate spheres shown in fig. 3.6 have a center–to–center separation of about 2, whereas the two overlapping spheres have a center–to–center separation of about 0.8 . This is made more clear in figure 3.7.

The fields were plotted with a variety of separations and also at many different frequencies, ω, using for each frequency the $\epsilon(\omega)$ for gold, as tabulated in Physik Daten (1981). These values are denoted by τ in figures 3.9 through 3.12. Due to symmetry, only a portion of the field structure is shown. That part of the field that intersects the plane through the symmetry axis (see fig. 3.8) and is in the first quadrant (darkened piece of the plane) is displayed in the field plots. The see-thru view shown in fig. 3.8 is meant to represent a particle that is being halved by the

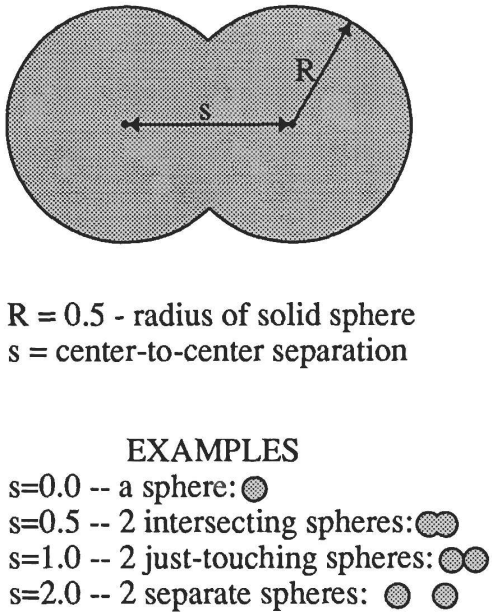

Figure 3.7 — The coagulated sphere geometry.

cutting plane, $y = 0$, with the portion that is darkened being the region of the plane that is displayed in the field plots. In the remaining quadrants the field can then be determined by symmetry.

Typical field plots are shown in figs. 3.9–3.12 for the near–resonance case and for an off–resonance case. Each of the field plots shows the real and imaginary parts of the potential for a particular shape, frequency and electric field direction:

x-directed means $\mathbf{E}^{inc}$ is vertical.

z-directed means $\mathbf{E}^{inc}$ is horizontal.

Each plot has 4–6 equipotential lines, while ΔV (or "spacing in volts" on the plots) between them varies from plot–to–plot. Hence a large value for ΔV means that we have high local **E**-field concentrations.

The dimensionless average absorption cross–section, as described earlier, was plotted for each geometry as a function of the free space wavelength. Typical

spectra are shown in figs. 3.13–3.22.

More detailed and complete results for the coagulated sphere case are provided in Pierce and Weil (1987, 1988).

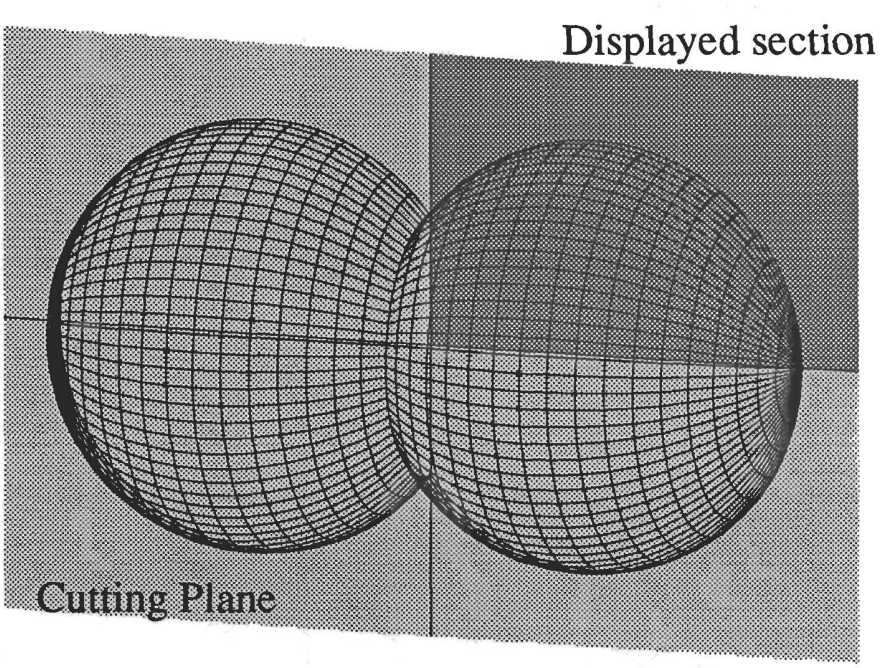

Figure 3.8 — Position of field plots in relation to the particle.

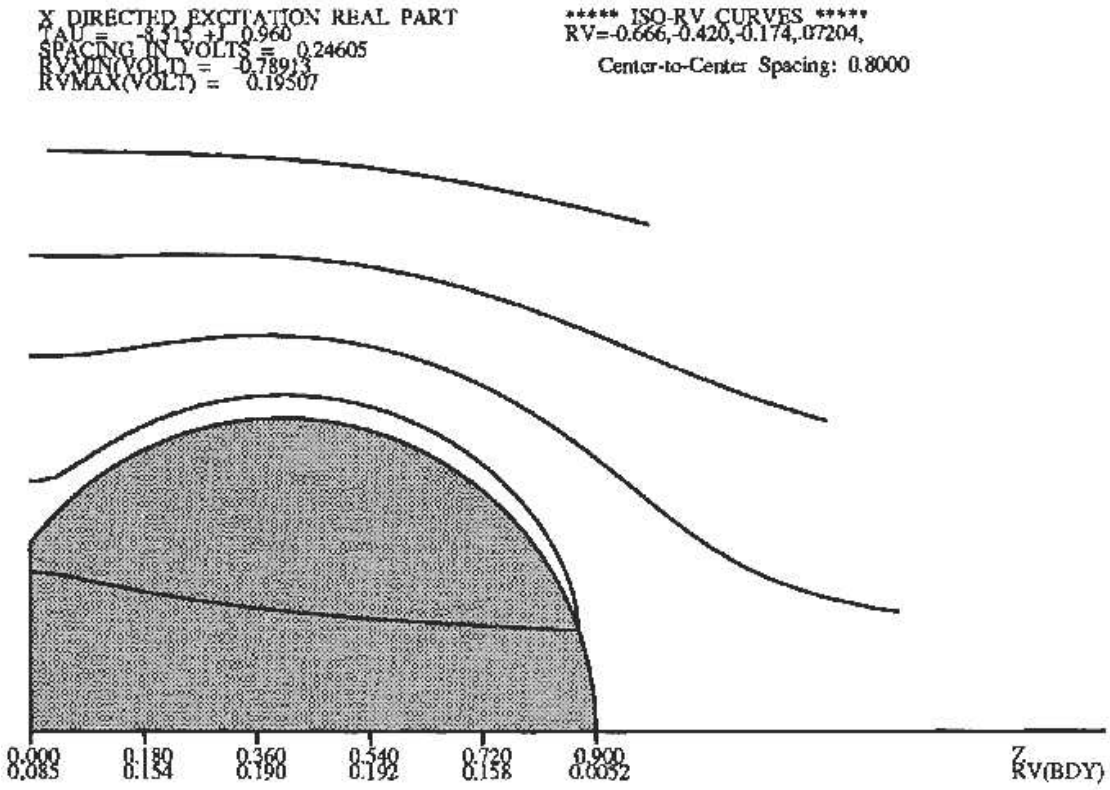

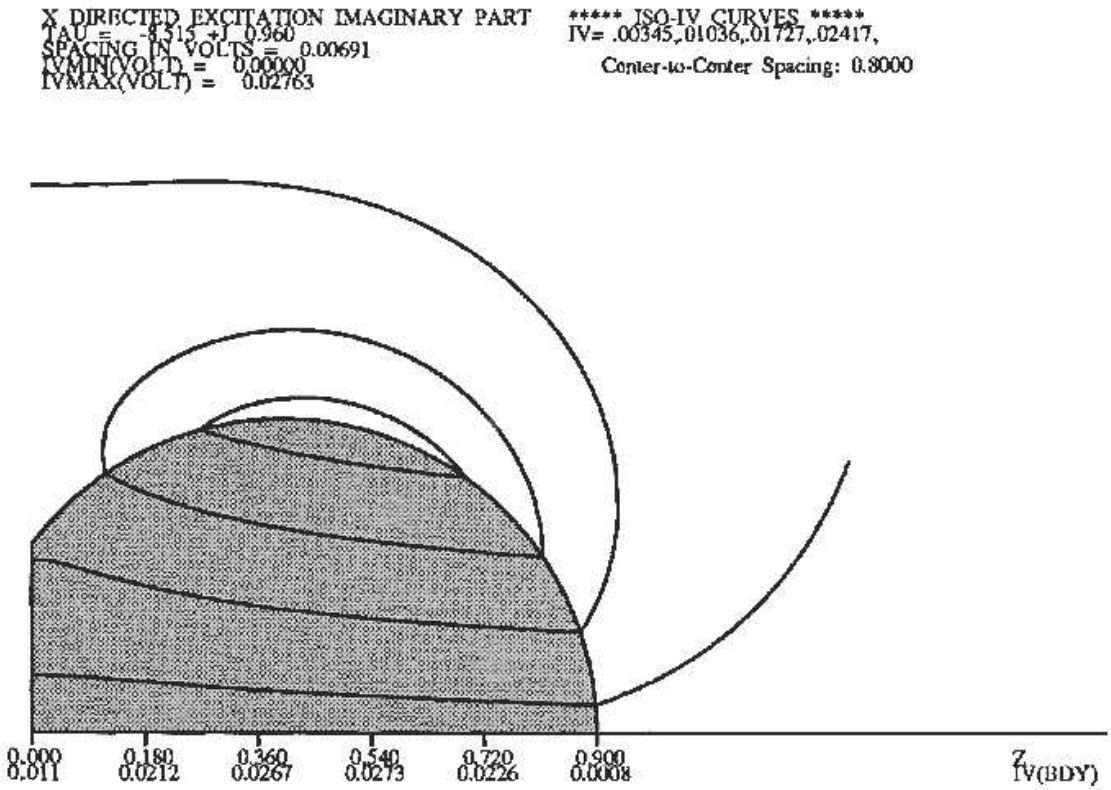

Figure 3.9 — Iso–potential lines for near–resonance case ($\hat{\mathbf{x}}$–inc.)

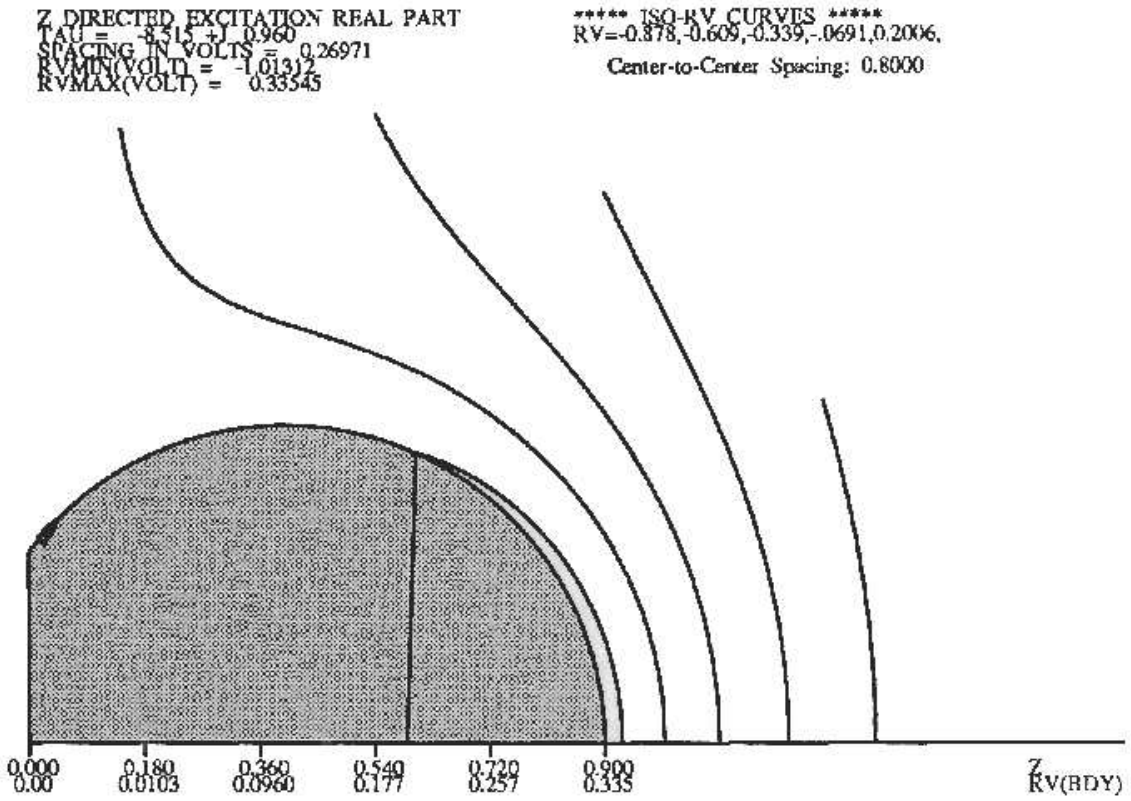

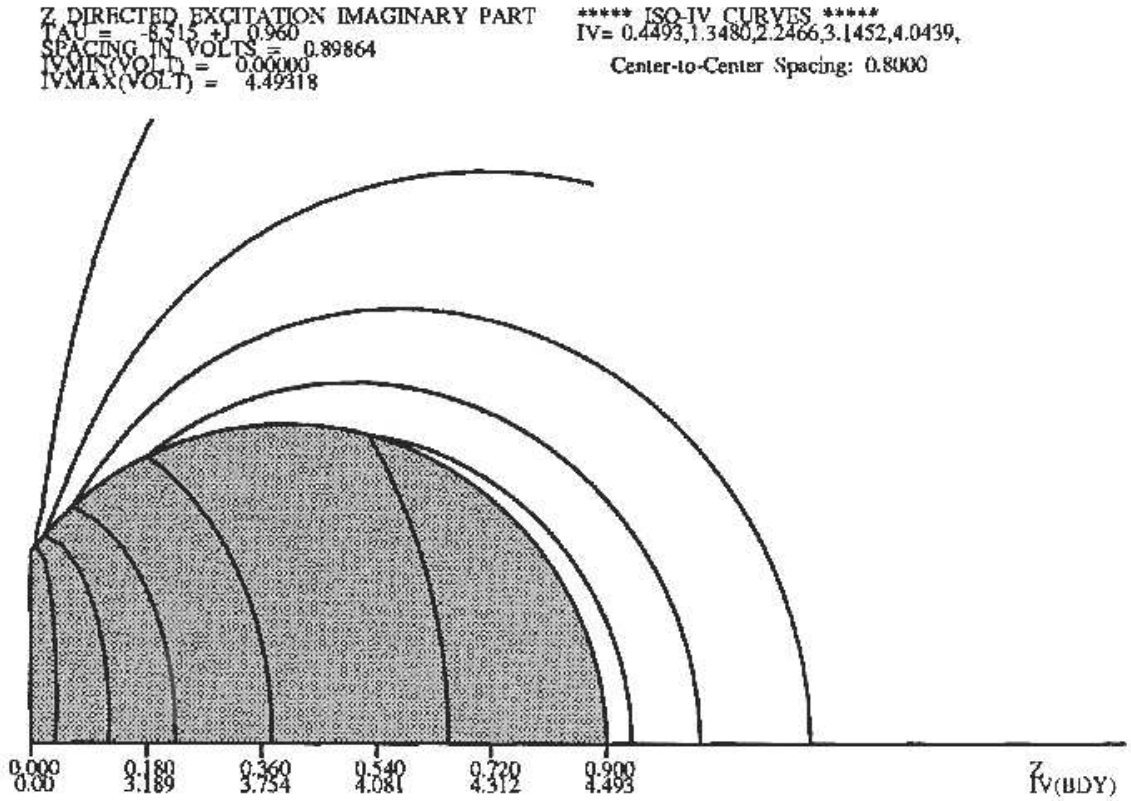

Figure 3.10 — Iso–potential lines for near–resonance case ($\hat{z}$–inc.)

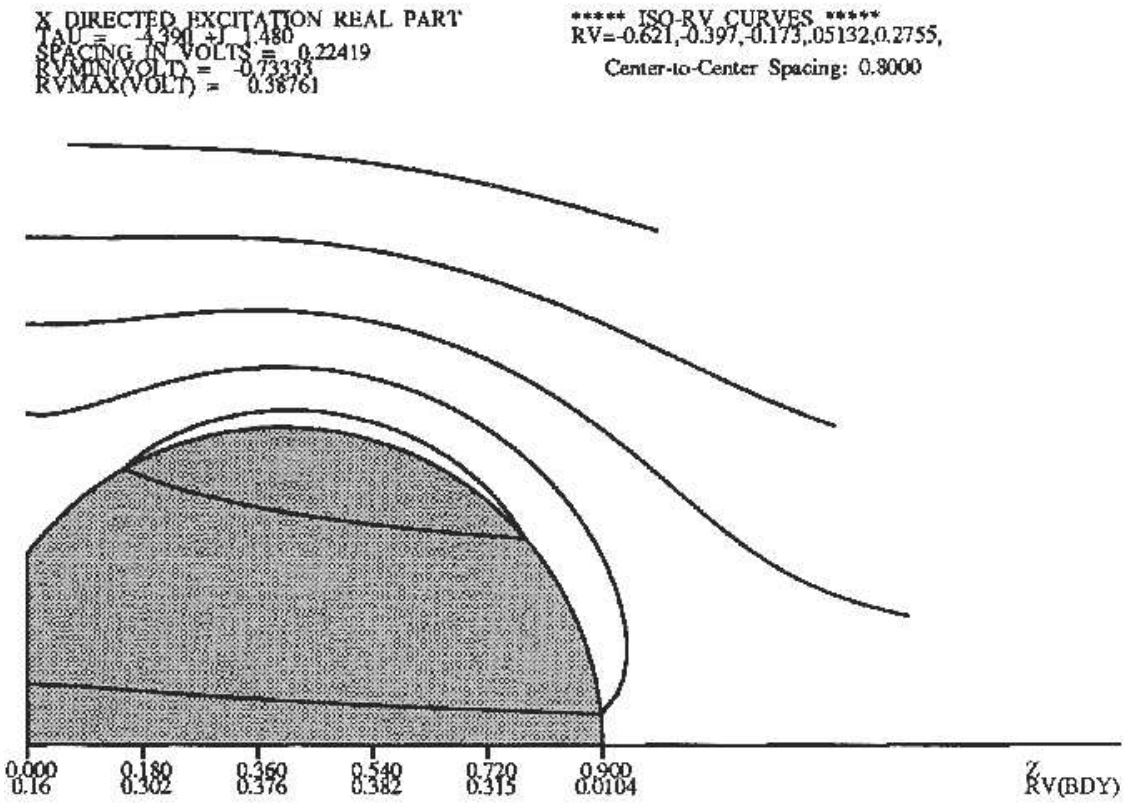

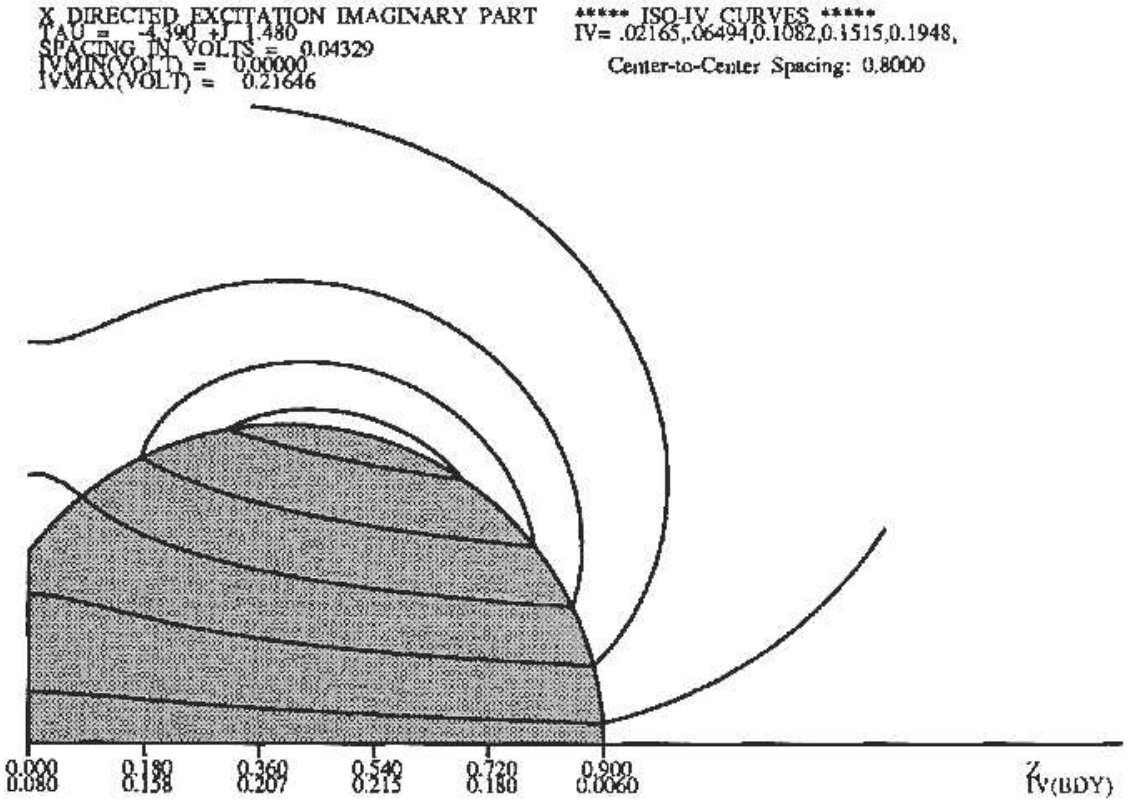

Figure 3.11 — Iso–potential lines for off–resonance case ($\hat{x}$–inc.)

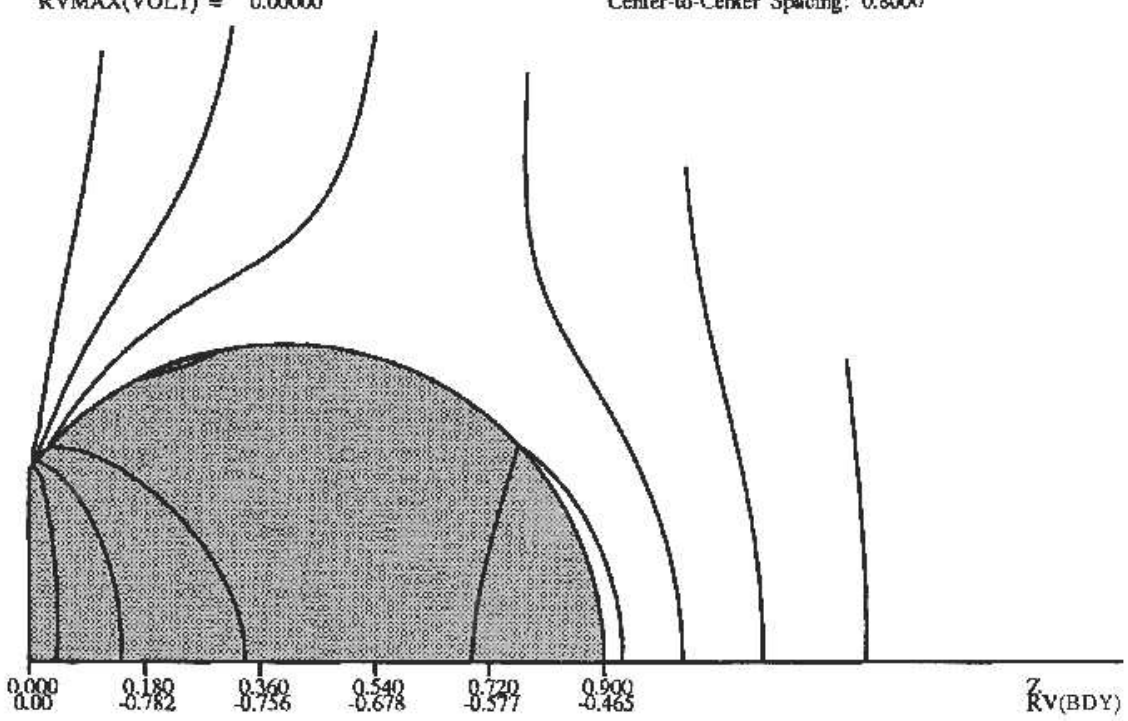

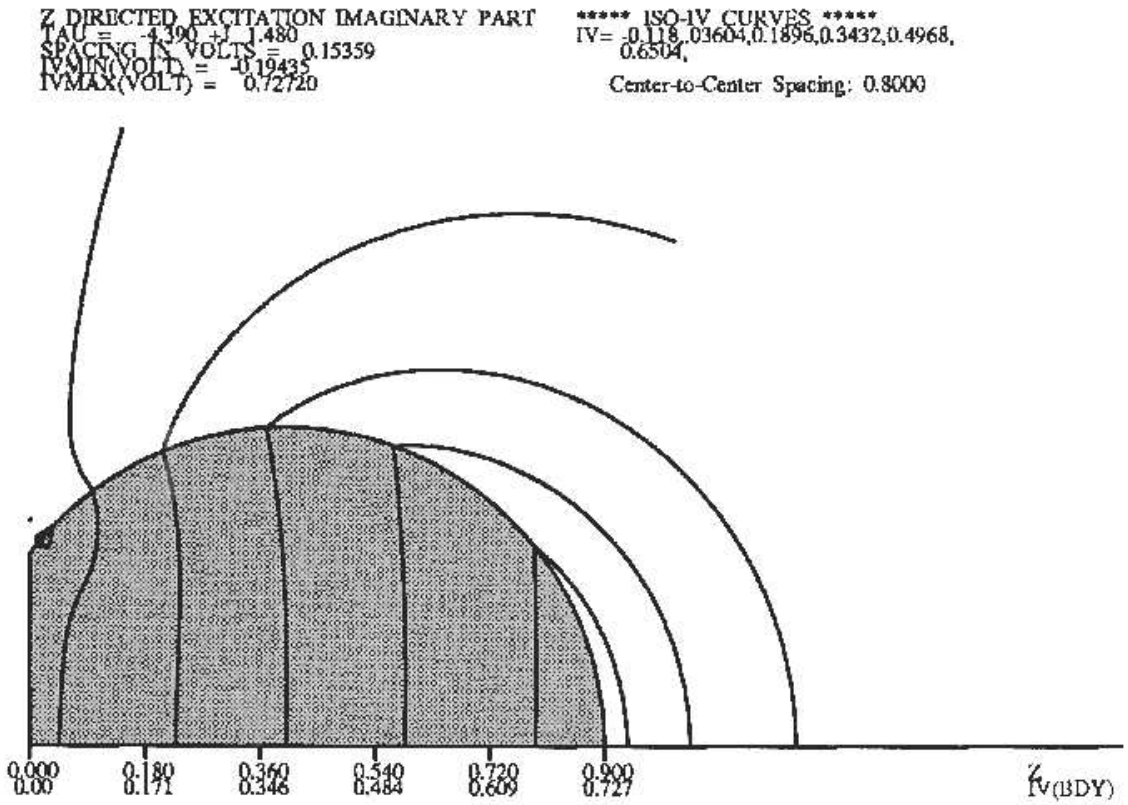

Figure 3.12 — Iso–potential lines for off–resonance case ($\hat{z}$–inc.)

In comparing the near– and off–resonance fields, note that the resonance itself is numerically apparent in the magnitudes of the resonant $\hat{\mathbf{z}}$–directed imaginary part of the potentials: an increase of slightly less than five times. This resonance is for the $\hat{\mathbf{z}}$–directed excitation only. The field structure for the $\hat{\mathbf{x}}$–directed cases changes very little. One notable difference is that the field strength in the imaginary parts ($\hat{\mathbf{x}}$–dir) becomes about ten times smaller as compared to the off–resonance case. This is interesting and deserves further investigation to determine if it is a general feature or just a specific occurrence.

Moving on to a comparison of the $\hat{\mathbf{z}}$–directed field plots, the most striking difference is in the field structure: the resonant field lines are much more curved. A consequence of this is that the near–surface electric field is much stronger and the internal field is much weaker: hence the term "surface mode" for this kind of resonance behavior. There are a number of other distinguishing features of these field plots, but their significance in undetermined at this time: the "chimney" in the real part has moved from an off–center position off–resonance to, apparently, the central position of the particle; the field concentration at the central cusp of the particle has moved from the real part off–resonance to the imaginary part near–resonance.

The following pages show the dimensionless absorption spectrum (Im.P_{ii}) of coagulated gold particles in the frequency range near that of visible light, as calculated by the method outlined in Chapter 2. Note that the vertical scales are different, and that the absorption spectrum for a single sphere is included in each plot for comparison. Recall that 'sep' in these plots stands for the center–to–center separation between the two spherical particles that make up the coagulated particle. A separation of 1.0 indicates that the two spheres are just barely touching one another, while a separation of 0.8 indicates that the two spheres are overlapping and are coagulated. A separation greater than one indicates that the two spheres are near each other but not touching.

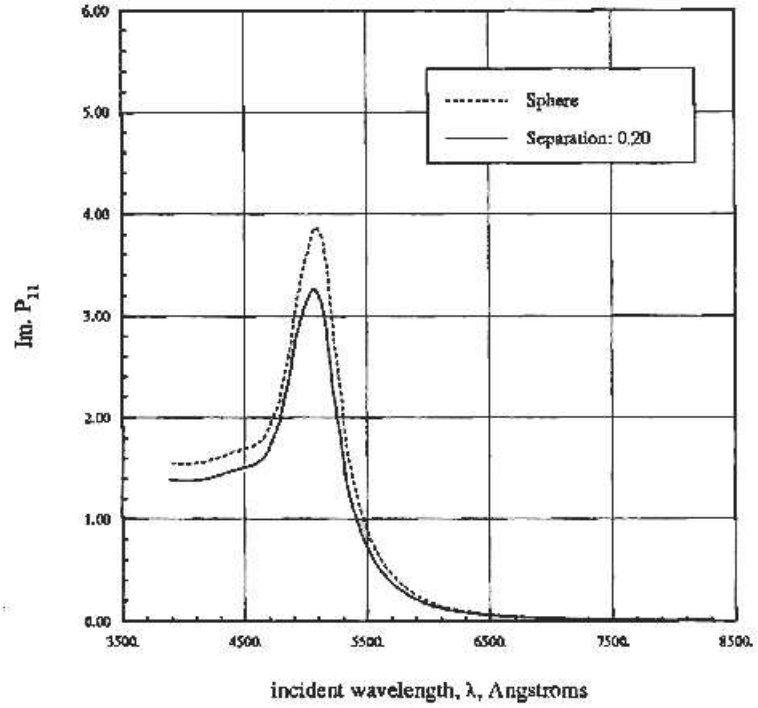

Figure 3.13 — $\hat{x}$–incidence absorption spectrum, sep=0.2

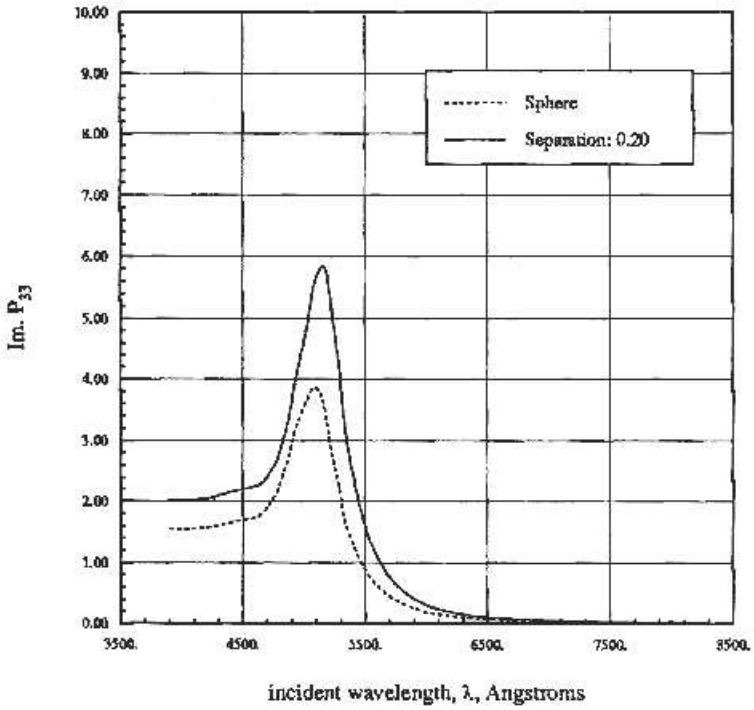

Figure 3.14 — $\hat{z}$–incidence absorption spectrum, sep=0.2

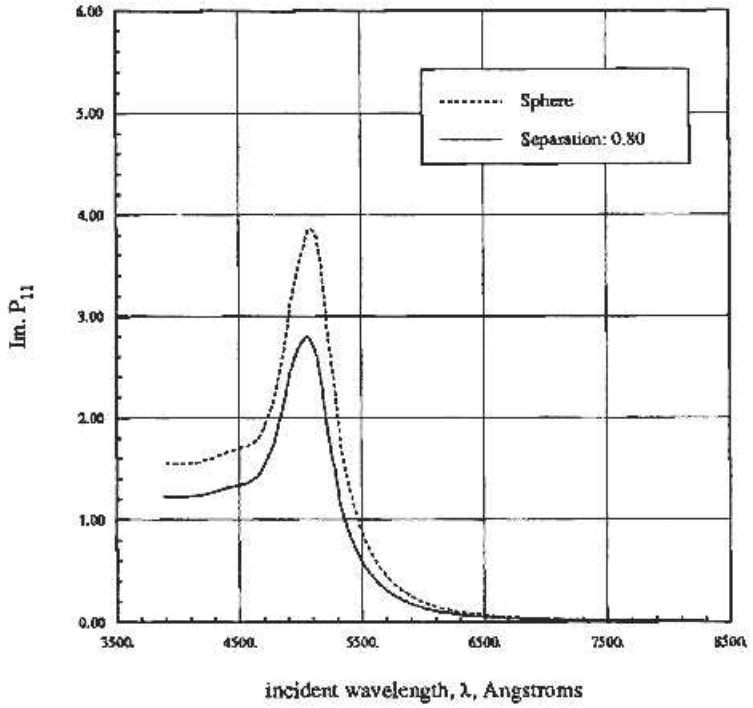

Figure 3.15 — $\hat{x}$–incidence absorption spectrum, sep=0.8

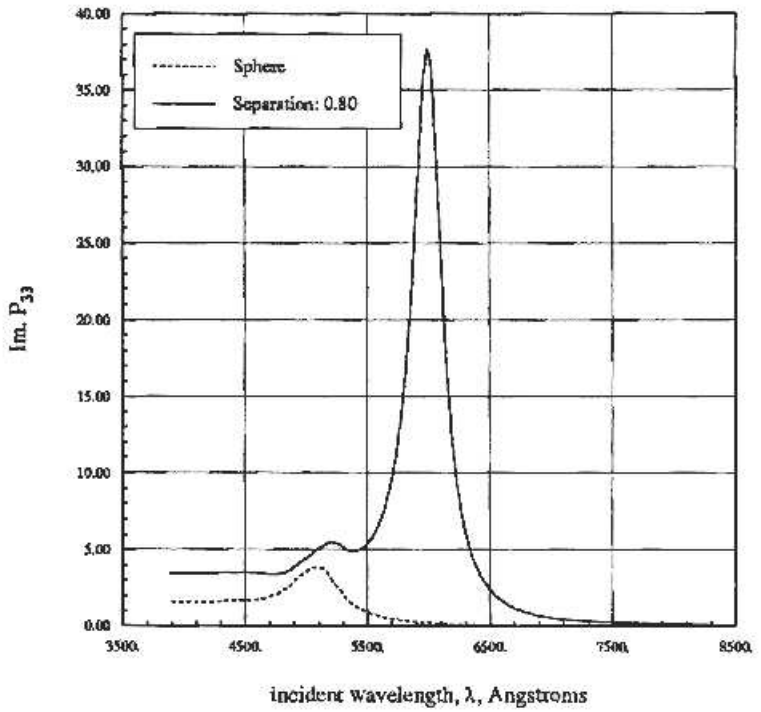

Figure 3.16 — $\hat{z}$–incidence absorption spectrum, sep=0.8

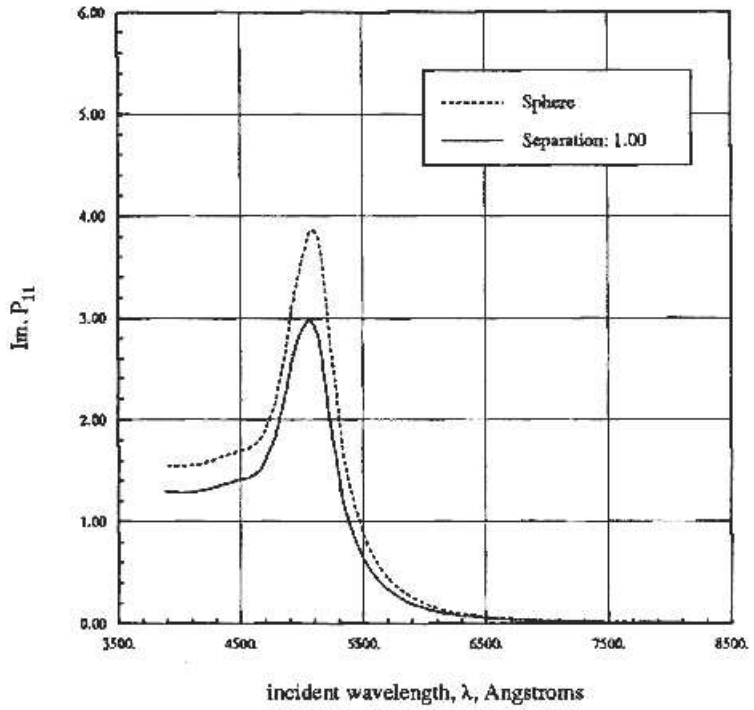

Figure 3.17 — $\hat{x}$–incidence absorption spectrum, sep=1.0

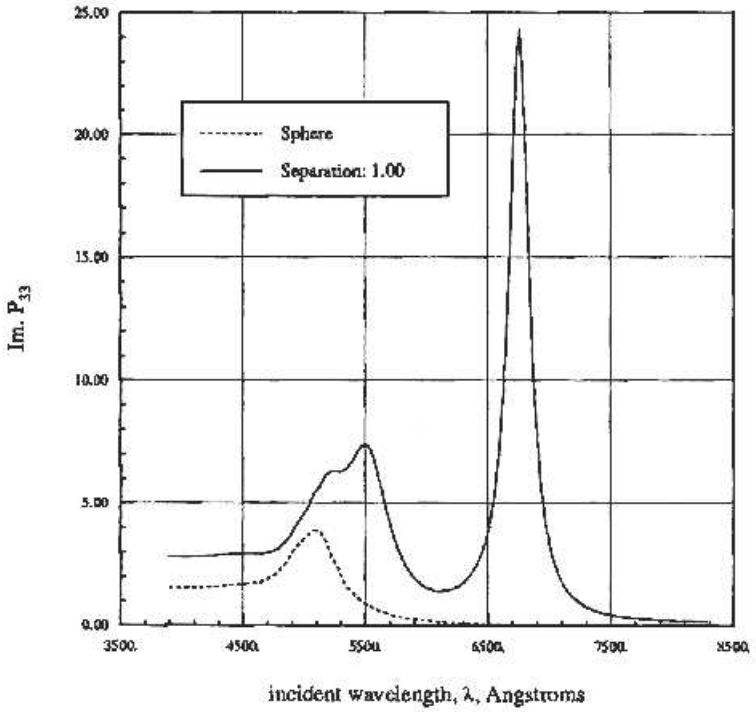

Figure 3.18 — $\hat{z}$–incidence absorption spectrum, sep=1.0

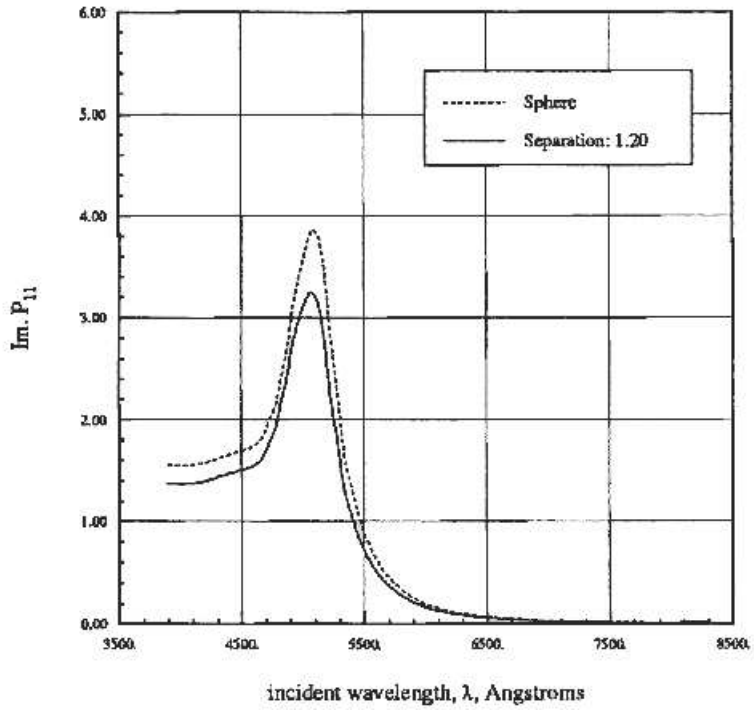

Figure 3.19 — $\hat{x}$–incidence absorption spectrum, sep=1.2

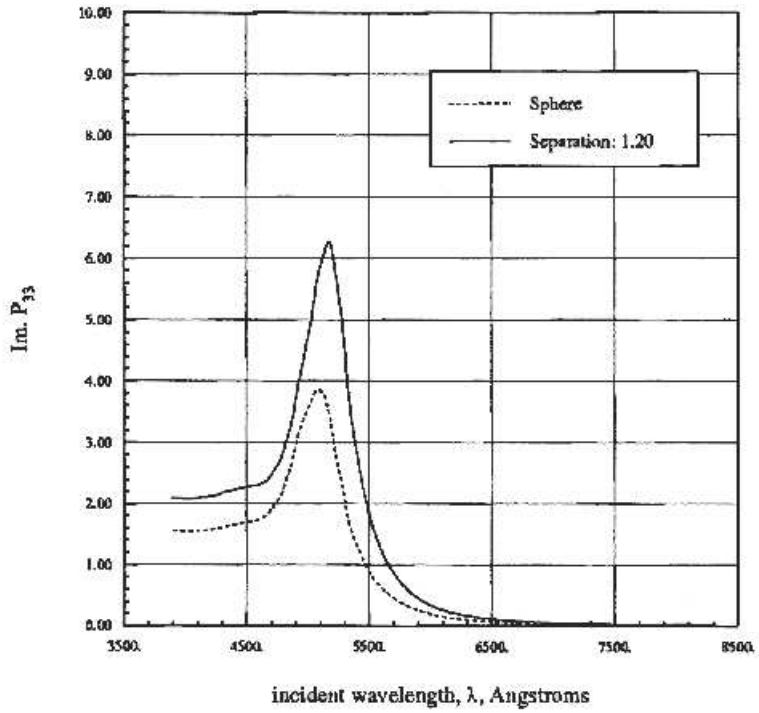

Figure 3.20 — $\hat{z}$–incidence absorption spectrum, sep=1.2

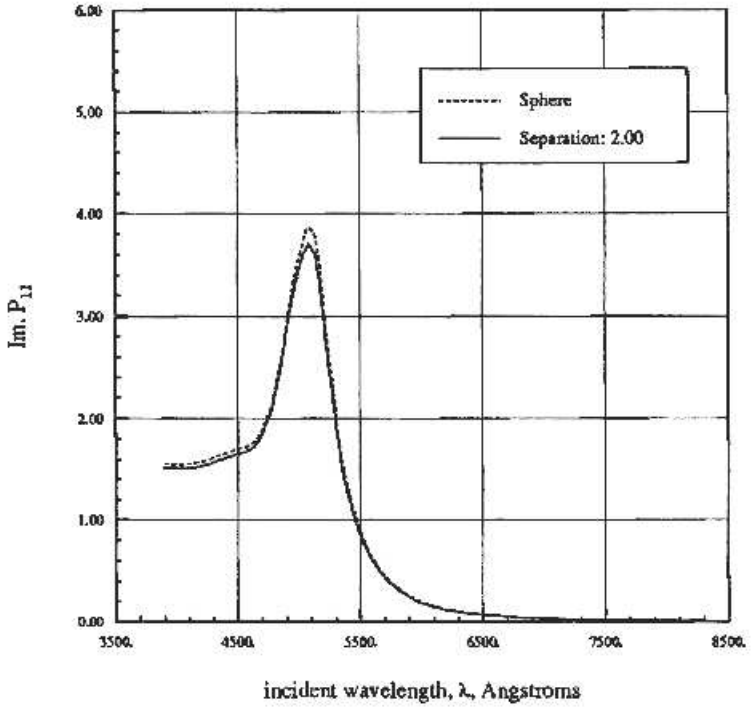

Figure 3.21 — $\hat{x}$–incidence absorption spectrum, sep=2.0

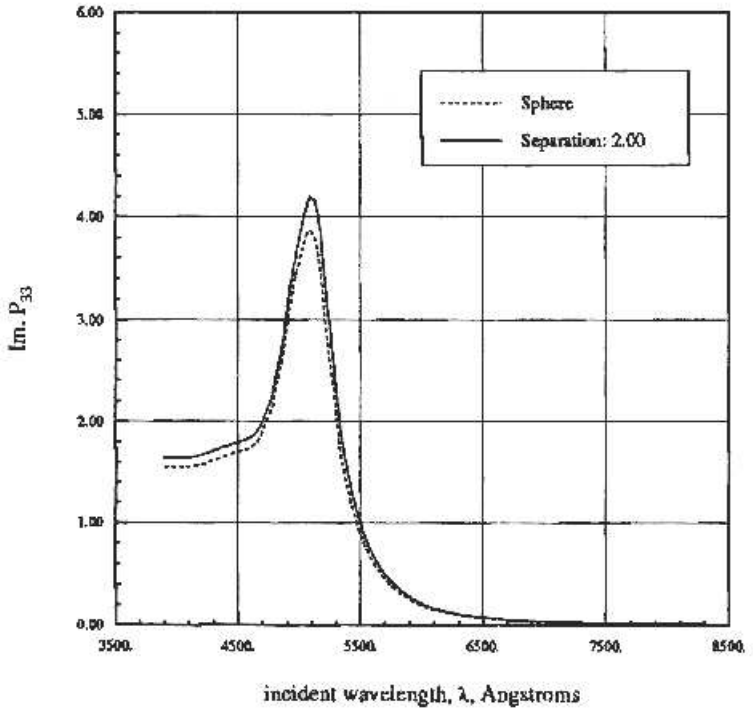

Figure 3.22 — $\hat{z}$–incidence absorption spectrum, sep=2.0

These absorption cross–section plots are done for gold particles at approximately optical wavelengths. The most obvious similarity among these spectra is the smallness of the variation of the $\hat{\mathbf{x}}$–directed absorption: the single absorption peak is retained, with respect to its wavelength of occurrence, over the entire family of geometries. The magnitude of this absorption peak varies between 3 and 6 compared to the sphere's 4.

The variation of the $\hat{\mathbf{z}}$–directed spectra is greater, as one might expect from the previous field comparisons. The single–sphere peak appears to be retained, although it moves slightly (about 200 Angstroms) and its magnitude varies between 4 and 6. The most interesting feature, however, is the appearance of new absorption peaks. These peaks only occur for coagulated spheres that are nearly–whole spheres. In our examples, this is shown for separations of 0.8 and 1.0; *i.e.,* for nearly–whole, but coagulated spheres (0.8), and for whole but touching spheres (1.0). In each case the absorption peak is 6 to 10 times as strong as the single–sphere peak, and both are also shifted to longer wavelengths. The positions and strengths of these absorption peaks are highly dependent on geometry. Also of note, for the just–touching spheres (sep = 1.0), is a more complicated absorption spectrum in the region of the single–sphere peak: there appear to be two overlapping absorption peaks, each at a longer wavelength than the single–sphere peak.

The implications of these spectra for the colors of colloidal gold will be discussed in section 3.4.3.

3.4.2 Polarizability Tensors

The polarizability tensor elements are functions of complex ϵ, and are best displayed as surfaces in three–dimensional space. The following two figures (figs. 3.23 and 3.24) show a numerically–generated surface (using the method and code as described in secs. 2.1–2.4), and the results of applying the model from sec. 3.3.3 using the three major resonances.

A comparison of figures 3.23 and 3.24 shows that the fit (3.27), as far as it goes, does an excellent job. The error in regions not near $Re\{\epsilon_r\} = -1$ is on the order of 1%. This shows that in those regions the simple, intuitive, and physically meaningful model presented earlier is valid. In the region near $Re\{\epsilon_r\} = -1$, however, the fit does not agree well with the numerically–generated data. The major reason for this is that the model chosen used only the three largest resonances. When the other, weaker, resonances are added to the model, the fit, of course, improves in that region.

3.4.3 Resonances

As discussed in section 3.3, the resonances, and associated strengths, for a particle completely determine the behavior of its polarizability tensor elements, as a function of relative permittivity. Hence, the resonances were investigated for the coagulated sphere family of shapes. Figures 3.25 and 3.26 show the behavior of the major resonances: major as determined by their strength. The strength was measured using the absorption cross–section of the particle with a dielectric constant equal to that of the resonant value with 0.1 added to its imaginary part to give some loss. The movement of these resonances in the ϵ–plane can be seen as a possible cause for the variability in the color of a suspension of such particles when observed in white light: different particle shapes (degrees of coagulation) will cause the suspension to appear to have different colors than other shapes would.

These figures present the magnitude and position for the resonances observed in this family of geometries in a very complete way. The positions are clearly shown in fig. 3.25 for both $\hat{\mathbf{x}}$– and $\hat{\mathbf{z}}$–incidence. The relative magnitudes of these resonances are displayed in fig. 3.26.

In these figures one can easily see the movement of the resonances away from that of the sphere (-2), and their eventual return for the case of two separated

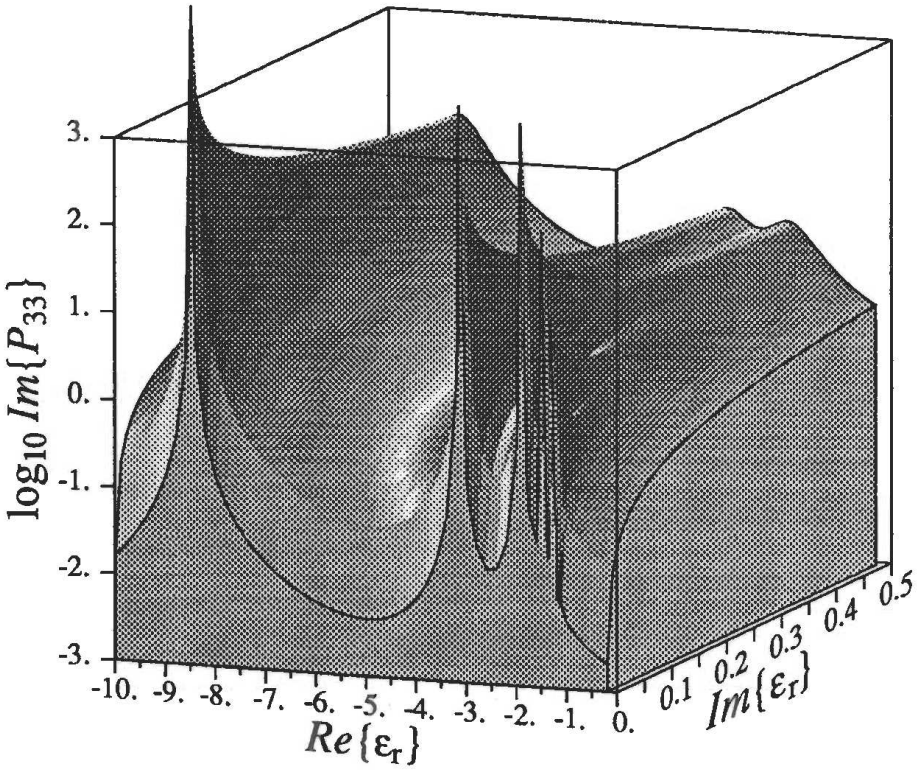

Figure 3.23 — $\hat{z}$–incidence, *Im*{Polarizability}, sep=0.8, numerical.

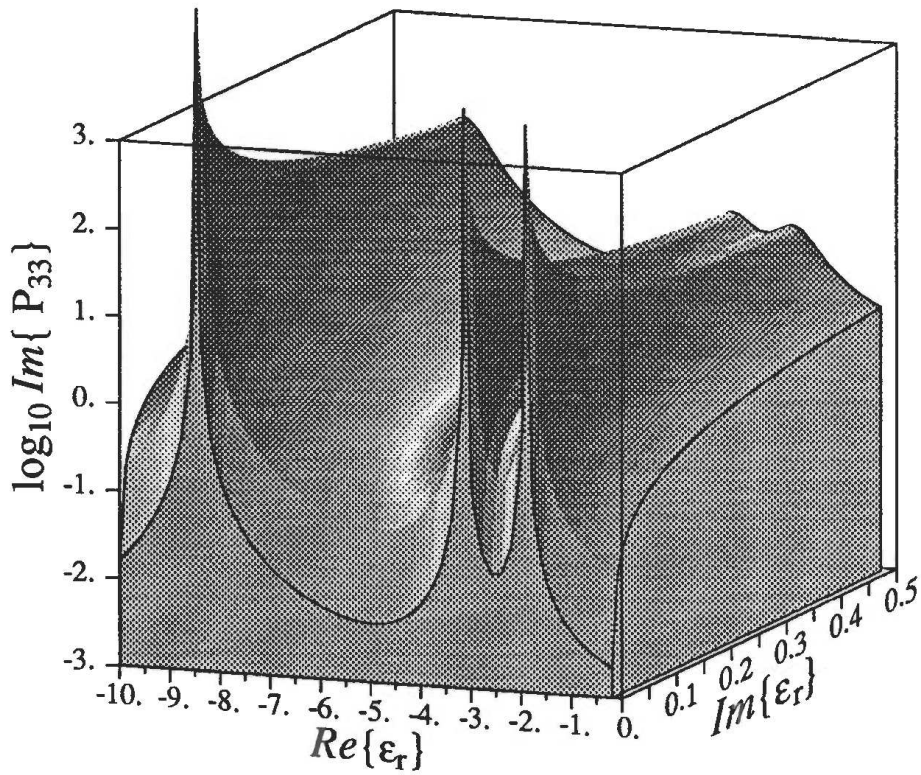

Figure 3.24 — $\hat{z}$–incidence, *Im*{Polarizability}, sep=0.8, model.

spheres. Between these two extremes the behavior is quite different for the $\hat{\mathbf{x}}$– and $\hat{\mathbf{z}}$–directed cases: the $\hat{\mathbf{x}}$–directed resonance remains very close to $\epsilon_r = -2$ and moves closer to $\epsilon_r = 0$ during its deviation while the $\hat{\mathbf{z}}$–directed case spawns many resonances all increasing rapidly as the separation approaches unity (touching whole spheres). The major $\hat{\mathbf{z}}$–directed resonance is also much larger in magnitude than the $\hat{\mathbf{x}}$–directed resonance.

Note that a previous paper (Weil (1986)) gave a plot similar to fig. 3.25 here, but that the lines were drawn in the wrong direction due to insufficient data. That has been corrected here.

An intuitive method for understanding absorption spectra is to use the numerically–generated or modeled polarizability tensor elements and merely superimpose the plot of the relative permittivity on it. This gives a line on the wavy surface which can be visualized as a particular wavy slice through this surface to give rise to an absorption spectrum. This concept is illustrated in figs. 3.27 and 3.28. Figure 3.27 shows the line on the surface of the polarizability tensor, while fig. 3.28 shows the equivalent absorption cross–section, which in this case is the $\mathrm{Im.P}_{33}$.

Looking at fig. 3.27, note that the value of the bulk relative permittivity for gold at about 4000 Angstroms is about $-2 + j6$, and so the spectrum begins in the upper right corner. In comparing these two figures keep in mind that the surface is plotted with a logarithmic vertical scale, while the absorption spectrum uses a linear vertical scale. Despite this, we can still observe the two prominent absorption peaks of fig. 3.28 in fig. 3.27. This is an intuitively pleasing way of thinking about absorption spectra for particular materials and particle shapes.

The model of the polarizability tensor elements can be used to generate a fit to the absorption cross–section as a function of geometry as well as wavelength. This scheme was used to generate figure 3.29, which is in fact a good fit to the available numerical data.

This figure shows the absorption spectrum for the $\hat{\mathbf{z}}$–directed incident electric

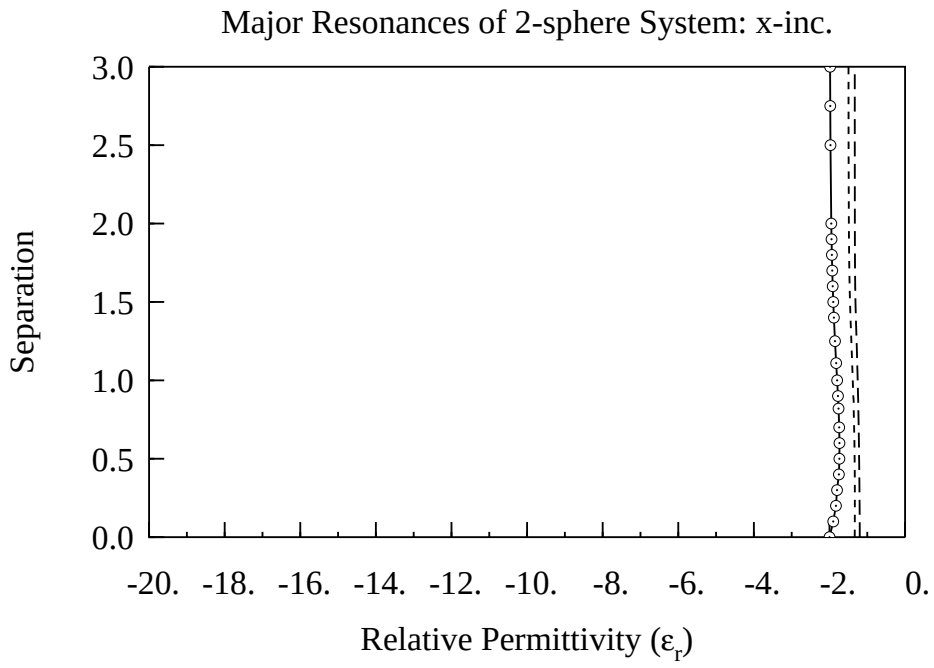

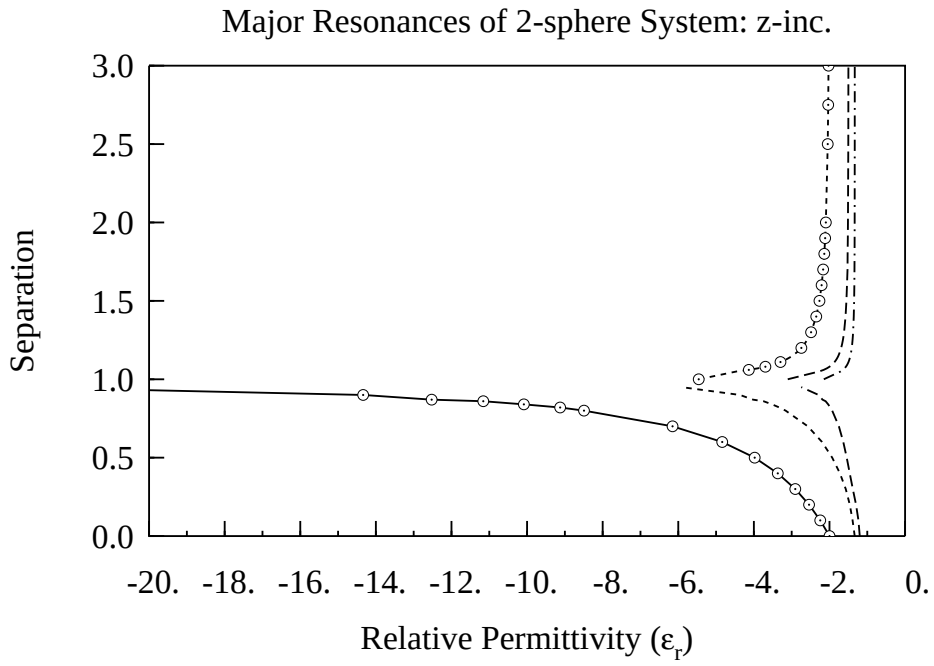

Figure 3.25 — Major resonances for coagulated and coagulating spheres.

The marks indicate the major resonance for a particular separation. Different lines indicate continuity of a particular resonance as the shape changes.

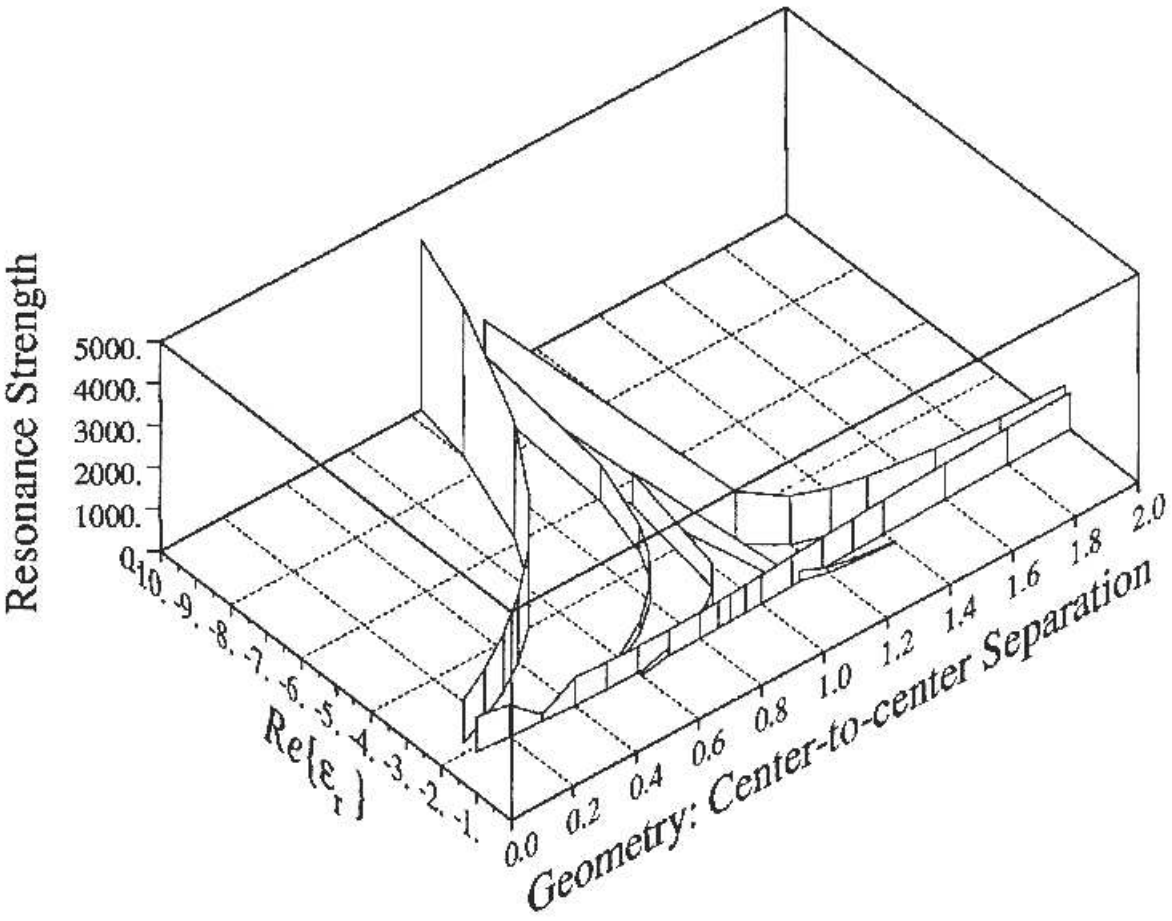

Figure 3.26 — Strengths of major resonances for coagulated and coagulating spheres.

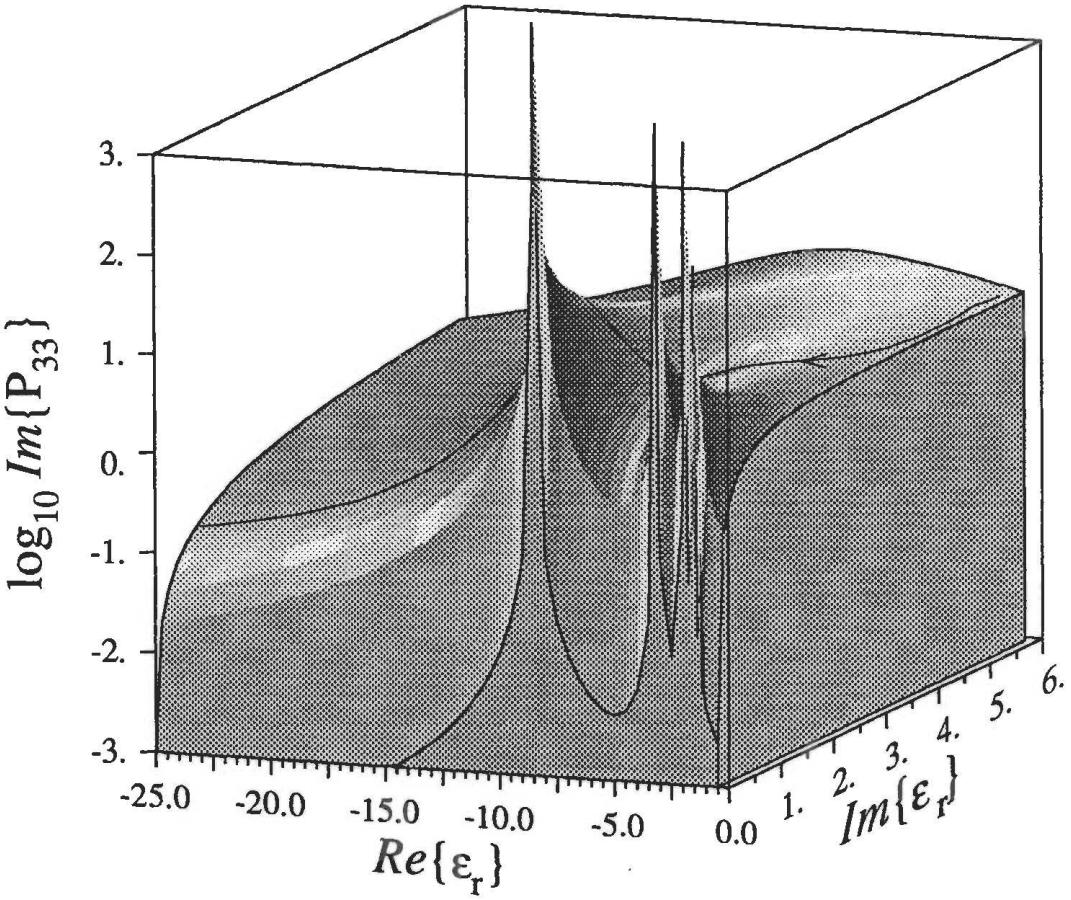

Figure 3.27 — $\hat{z}$–incident, $Im\{$Polarizability$\}$, sep=0.8.

ϵ(freq) for gold is superimposed.

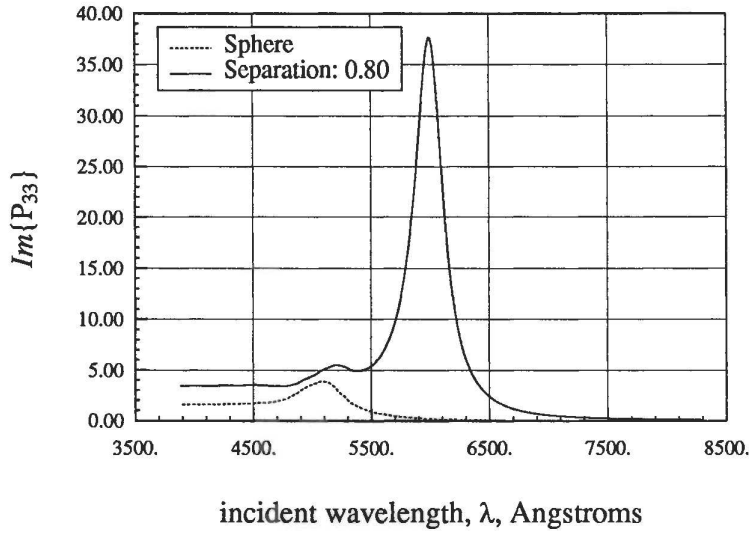

Figure 3.28 — $\hat{z}$–incident absorption spectrum of coagulated gold spheres, sep=0.8.

field for coagulated gold spheres as a function of separation. This data is a good fit to the computer–generated numbers; we use a fit to generate this plot in order to save time. The features in this figure are the same as those noted for figures 3.14, 3.16, 3.18, 3.20, and 3.22: the absorption spectra for the $\hat{\mathbf{z}}$–directed incident electric field. In this figure however, the continuous variation in the absorption peak's position and magnitude gives a better picture of their variability. As the separation increases toward 1 (from 0), and hence from a single sphere, through two coagulated spheres, and on to two just–touching spheres, we see that the single–sphere absorption peak "spawns" other peaks as the geometry becomes more cusp-like. The first, and by far the strongest, extra peak begins to form at a separation of 0.4 or so. This peak then moves to progressively larger wavelengths, and increases in magnitude sharply after a separation of about 0.9. Another, smaller, peak begins to form at a separation of 0.8 or so, and is also spawned by the persistent single–sphere absorption peak. It moves toward longer wavelengths and increases slightly in magnitude by the time the two spheres are just touching.

3.4.4 Comparison with Experiment

Comparison of the results presented previously for coagulated gold spheres to experimental work is essential for confidence in these results. While there have been many studies on gold colloids and their spectra for differing levels of coagulation, to date there have been no experimental results presented in the literature that characterize the coagulation in the colloid sufficiently to accurately compare with the coagulated-spheres model that is presented here. We present here some typical experimental results from Turkevitch, *et al.* (1954). Figure 3.30 shows the absorption spectra of two different gold colloids: one that is very nearly uniform size spheres, while the other has been induced to coagulate to a degree that was not measured, but was assumed to be relatively small. That is, one curve is for

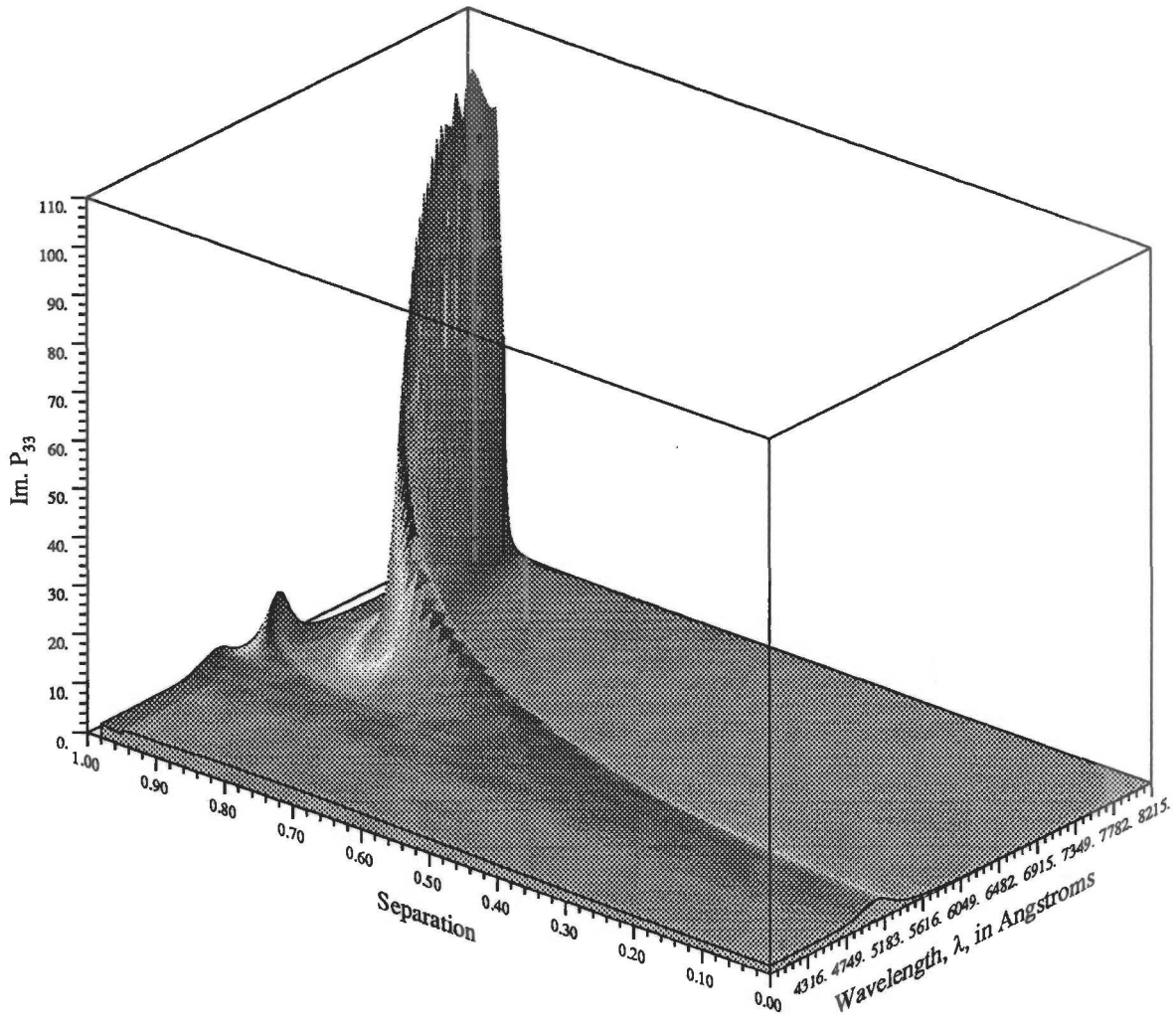

Figure 3.29 — $\hat{z}$–incident absorption spectrum as function of geometry, for gold.

Note that the high-frequency structure seen in the largest resonance is an artifact of the sampling process used to generate this plot. The variation is really smooth and continuous.

gold spheres, while the other is for a combination of mostly gold spheres and some coagulated gold spheres. A direct numerical comparison with our calculations is not possible because many critical parameters are unknown, i.e. the permittivity of the suspending liquid, the number fractions of spheres and coagulated spheres, and the typical geometries for coagulated spheres, but in spite this, a comparison of the general trends in the data can be made. In particular, the non-coagulated gold spheres show the same general behavior:

1. Small-wavelength absorption much higher than that at high wavelengths.
2. Large, narrow peak slighly above 500 nm, with roughly twice the absorption of the low-wavelength absorption.

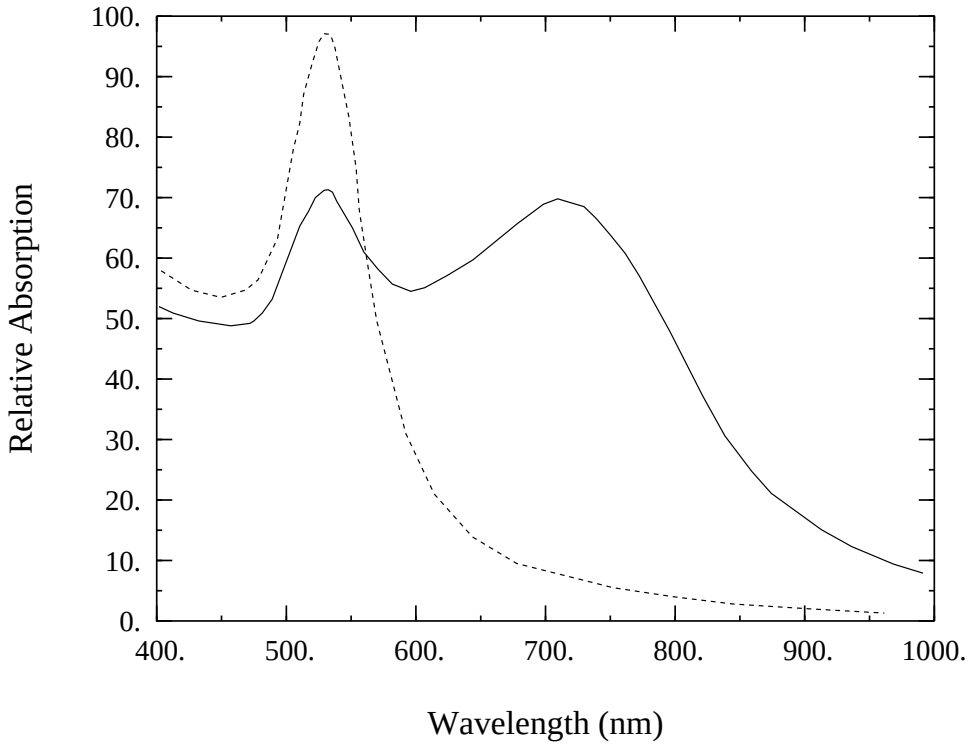

Figure 3.30 — Absorption spectra of 40 nm diameter colloidal gold, from Turkevitch *et al.* (1954).
(- - - - Spheres only; —— Spheres and Aggregated Spheres.)

The mixed non-coagulated/coagulated spheres are also very similar overall, but many details are quite different. First, a direct comparison with figures 3.15 through 3.18 is inappropriate because those figures are for the absorption due to coagulated spheres **only,** while the Turkevitch measurements are on a mixture of spheres and coagulated spheres. Next, the broad absorption peak centered at 700 nm in the measurements does not look like the narrow absorption bands in our calculations. This is most probably due to variations in the coagulation geometries, (especially since the coagulation is not limited to sets of two merged spheres) giving a wide spread of many narrow absorption bands. Despite this, it is obvious from the measurements that coagulation causes a new absorption band at higher wavelengths (between 650 nm and 800 nm) just as predicted by the calculations given here.

Hence, at least qualitatively, the calculations presented here for coagulated spheres are consistent with the measured data.

3.5 Results for Different Coagulation Geometries

The absorption spectra presented in sec. 3.4 (figs. 3.13 - 3.22) have an intriguing aspect about them: the absorption peak that one sees for a single sphere is evident in each of the spectra for the coagulated spheres cases. This leads to the idea that there are aspects about the absorption that are dependent on local shape rather than global, because the two coagulated spheres were made of pieces of spheres. The idea is that the absorption could be decomposed into pieces with some absorption due to the spherical character of each particle and some due to the cleft produced between them by the coagulation process.

The problem is explored in somewhat more generality than stated above in that which follows. Note that a similar study was carried out at this lab by Czerwinski (1984), where the interest focussed on surface bumps and pits (both rotationally-symmetric) in cylinders.

3.5.1 Cases Studied

Continuing the coagulation theme, this section closely investigates a particular cleft and places it in coagulated spheres of differing overall shape, as well as altering the cleft shape slightly. In this way some idea as to the importance of global/local shape effects on the scattering can be discerned. The variations made in the cleft shape are as follows:

a. circular arcs only,

b. straight lines only, and

c. straight lines with arcs to round the top corners.

The variation in the overall shape consisted of having two hemispheres of varying radii attached at the coagulation point by the clefts. The basic idea is to see just how sensitive the resonances and their strengths are to changes in a feature on a particle of the same overall shape and likewise to see how sensitive these are to an altered overall shape.

The clefts are shown in cross-section in fig. 3.31. The canonical coagulated shape is shown in cross-section in fig. 3.32.

3.5.2 Resonance Variations

This part discusses the effect on the shape resonances of varying the radius of two coagulated spheres, with the three different choices of clefts. After that, the variability due to the slightly-different clefts is investigated. For the first cleft, that made with two circular arcs, the results are presented in figs. 3.33 and 3.34. Note that in every figure in this section contiguous resonances are drawn with lines, and the major resonance is indicated by circular marks. Ignoring the change in strength of the major $\hat{\mathbf{x}}$-incidence resonance for the moment, the most dramatic change is seen in the most negative resonance for $\hat{\mathbf{z}}$-incidence: varying from about -8.5 at the smallest radius of 0.5 (where it is the major resonance), to about -3.7 at a radius of 2.0 (where it is now a minor resonance). Using the smaller of the resonances as

Cleft 1:
(complete
shape shown)

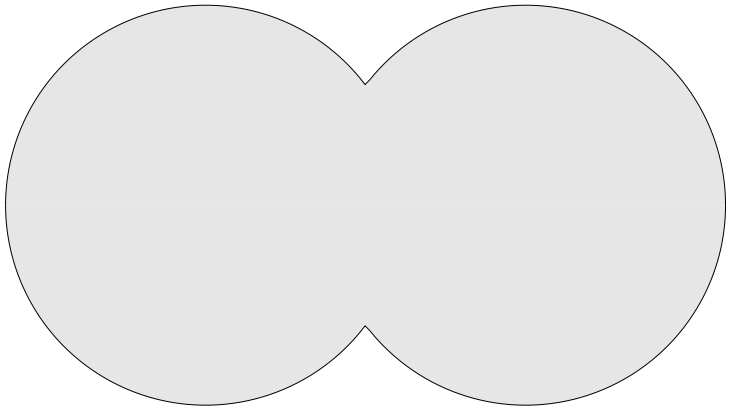

Cleft 2:
(close-up)

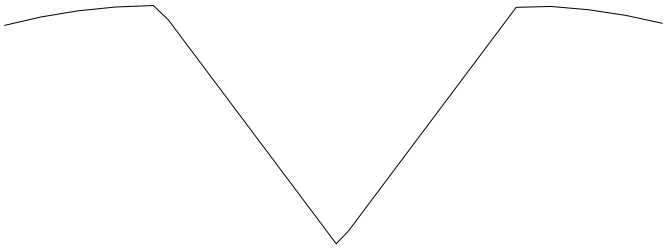

Cleft 3:
(close-up)

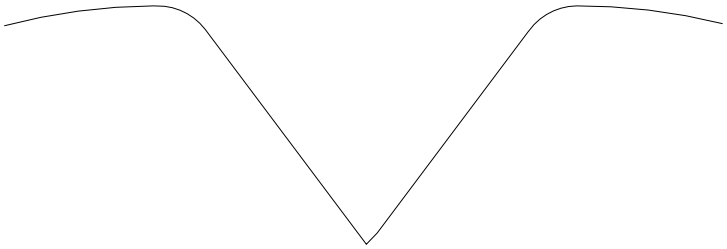

Figure 3.31 — The three cleft shapes that were used.

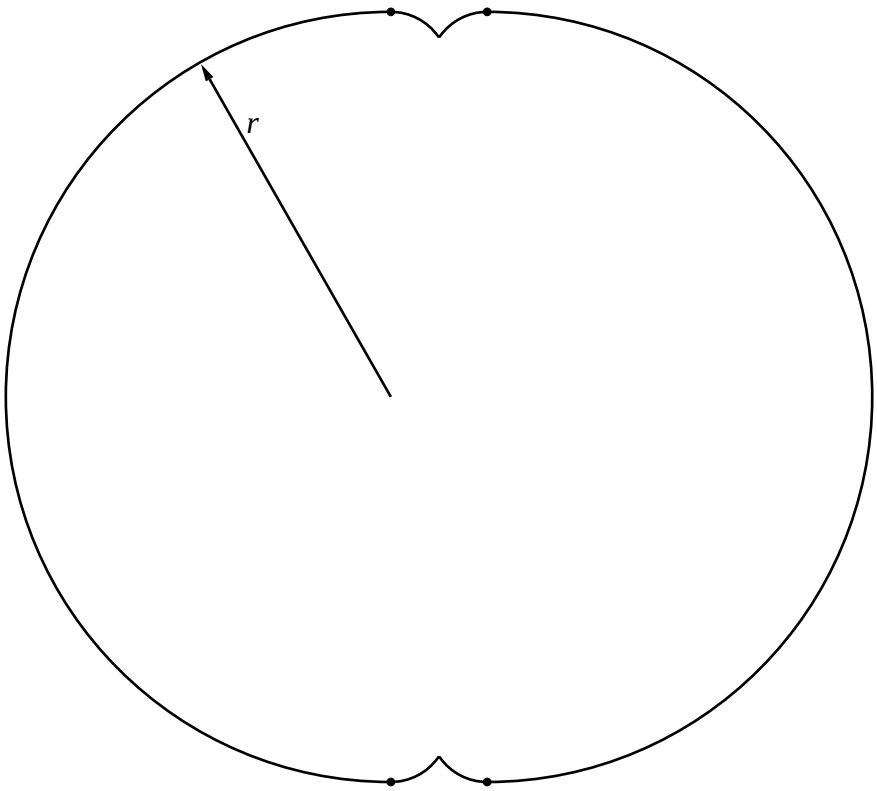

Figure 3.32 — The overall coagulated shape: hemispheres joined with clefts.

The radius of the hemispheres is varied to produce a family of shapes representing the different coagulation geometries. The cleft dimensions are constant.

---

the reference, this is a change of about 130%, hence, this resonance is a sensitive function of the hemisphere radius.

In contrast, the major resonance in the $\hat{\mathbf{x}}$-incidence case only varies between -1.76 and -1.84 over the same range, a difference of only 5%. In general, the resonanaces for $\hat{\mathbf{x}}$-incidence are usually very slowly-varying functions of the geometry.

Returning to the $\hat{\mathbf{z}}$-incidence case, the other resonances shown are seen to be far less variable than the major one. The resonance with the second largest strengths varies from -2.64 (at large radius) to -3.24 over the range, an increase from the larger

geometry of 23%. This is still a significant variability over the range of shapes. The third largest resonances vary from -1.92 (at large radius) to -2.0, the isolated sphere resonance. This is an increase of 4%. In general, the weaker a resonance is, the less it varies numerically, though not necessarily in percentage error. The minor $\hat{\mathbf{x}}$-incidence resonance varies very little (2%).

Lastly, mention should be made of the variability in the strengths of the $\hat{\mathbf{z}}$-incidence resonances. As the shape becomes more nearly a sphere, with increasing radius, the resonance with the greatest strength approaches that of the single sphere, as it should. The other resonances become weaker as this happens, and so the changes in the strengths of the resonances are believable.

The second cleft is presented in figs. 3.35 and 3.36. Ignoring the change in strength of the major $\hat{\mathbf{x}}$-incidence resonance for the moment, again, the most negative $\hat{\mathbf{z}}$-incidence resonance varies the most: from -7.88 at the smallest radius of 0.5 (where it is the major resonance) to -4.09 at a radius of 2.0 (where it is now a minor resonance). Using the smaller of the resonances as the reference, this is an increase of 93%, so again, the major $\hat{\mathbf{z}}$-incidence resonance is a sensitive function of hemisphere radius.

The major $\hat{\mathbf{x}}$-incidence resonance varies over the range from -2.03 to -1.94, a variation of 5%. This is not significantly different than for the previous cleft.

The $\hat{\mathbf{z}}$-incidence resonances again show an interesting shift in strength: but now the shift occurs even earlier than previously, starting to shift at about a radius of 0.9, where previously it shifted at a radius of 1.4 or so. The variability of the minor $\hat{\mathbf{z}}$-incidence resonance values (ignoring their strength ranking for the moment) is as follows: -1.86 to -2.03, a 9% increase; and -2.99 to -2.60, a 15% increase. This is no more variable than with the first cleft, despite the extra slope discontinuity in this cleft compared to the previous one.

The other $\hat{\mathbf{x}}$-incidence resonances vary on the order of 20% from about -1.47 to -1.75, which is a much larger variation than for the first cleft.

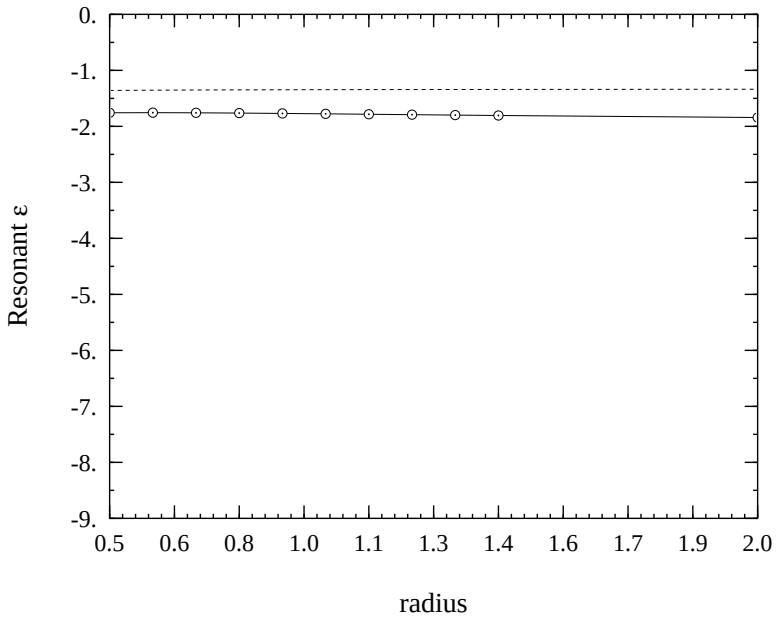

Figure 3.33 — Resonances for first cleft in spheres: $\hat{x}$-incidence .

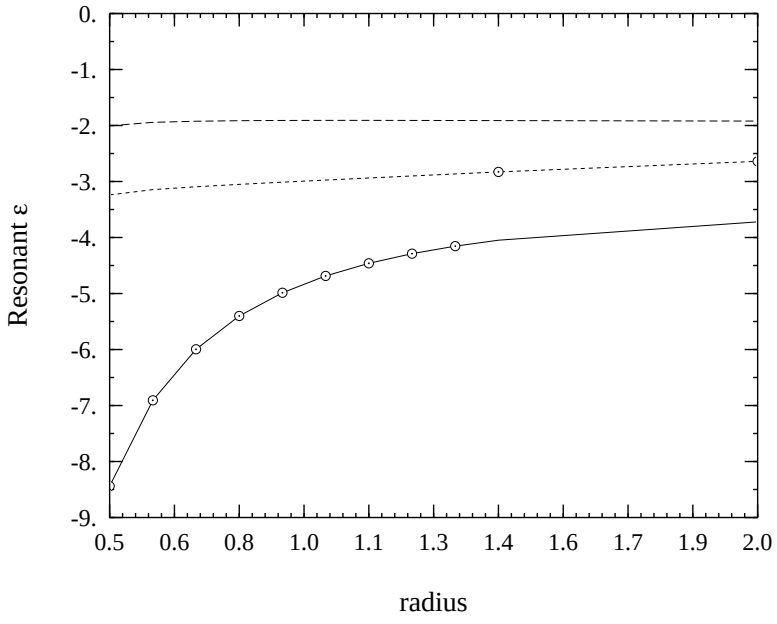

Figure 3.34 — Resonances for first cleft in spheres: $\hat{z}$-incidence .

The third cleft is presented in figs. 3.37 and 3.38. There is very little difference between the $\hat{\mathbf{z}}$-incidence results here and previously. The only difference is that the strength shift takes place later: at about a radius of 1.0 rather than 0.8, as compared to the second cleft. The $\hat{\mathbf{x}}$-incidence resonances are slightly different than in the previous cases, but not significantly.

A comparison of these results to the known resonances of the sphere provides very little information, unfortunately. The sphere has only one resonance at -2, no others (for plane wave incidence). Hence, the most that can be said about the comparison to the sphere is that as the radius of the spheres with the clefts gets bigger they geometrically approach a sphere, and their resonances also approach that of a sphere.

The following table summarizes the results. In table 3.1 the differences are taken over the range in radii from 0.5 to 2. The first number is the absolute difference, while the second number is the percentage difference over the range, using the smaller number as the reference.

Table 3.1 — Variability of resonances in coagulated spheres

	cleft 1	cleft 2	cleft 3
major z	4.8, 130%	3.8, 93%	3.91, 96%
other z	0.6, 23%	0.17, 9%	0.2, 11%
other z	0.08, 4%	0.40, 15%	0.4, 15%
major x	0.08, 5%	0.09, 5%	0.04, 2%
other x	2%	0.3, 20%	0.17, 13%

3.6 Conclusions and Suggestions for Future Work

Coagulation can have an enormous impact on the absorption characteristics of spherical particles. The major requirement is that the real part of the dielectric constant at the frequency of interest be negative, and, even better, be quite close,

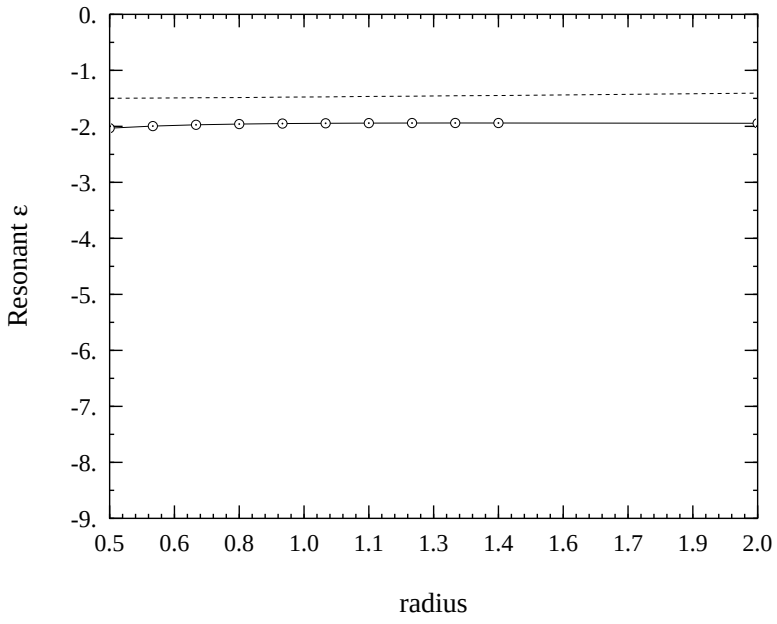

Figure 3.35 — Resonances for second cleft in spheres: $\hat{x}$-incidence .

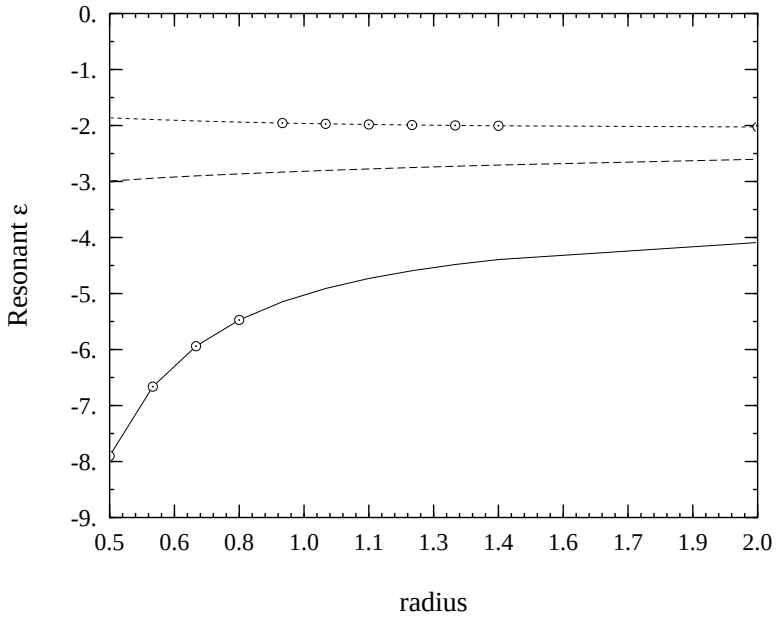

Figure 3.36 — Resonances for second cleft in spheres: $\hat{z}$-incidence .

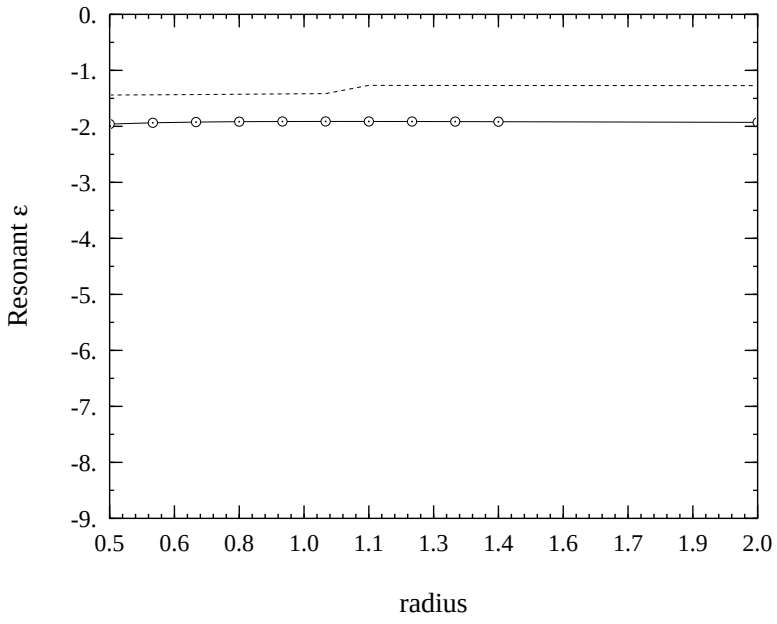

Figure 3.37 — Resonances for third cleft in spheres: $\hat{x}$-incidence .

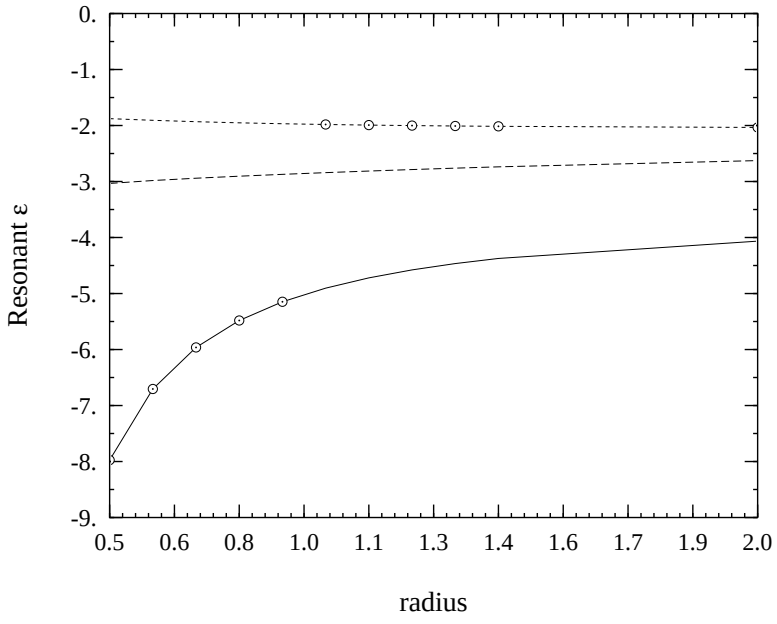

Figure 3.38 — Resonances for third cleft in spheres: $\hat{z}$-incidence .

in the complex plane, to a shape resonance. The final shape of a coagulated sphere pair is dependent on mechanical and material properties, including that of the ambient medium, not to mention the effects of the heating from the absorption of the incident electromagnetic field. Hence, a final coagulated-spheres shape was specified by simply intersecting two spheres, rather than attempting any kind of detailed modeling of the ensemble of shapes that occurs in nature. That this theory agrees, at least qualitatively, with experimental evidence available from work in gold colloids is gratifying.

A great deal can be learned about small particle absorption with the use of calculated near fields and polarizability tensor elements (as a function of ϵ_r) for different shapes. The shape effects can be quite striking for materials that have bulk permittivities with negative real parts and small (< 3 or so) imaginary parts. Gold in the visible is one such material and it was used extensively in the calculations presented here.

The model of the polarizability tensor elements given in sec. 3.3 is very simple and has intuitively-pleasing physical interpretations for its parameters (resonance positions and strength), while representing our numerically–generated data quite well.

The studies shown in sec. 3.5, though limited to but a few shapes, indicate that the resonance positions (values of ϵ_r) are strongly coupled to the existence of a cleft, at least for the coagulated spheres family of shapes. The minor resonances show far less sensitivity to the presence of the cleft and may be the source of the "conserved" absorption peak, on which the global shape effects hypothesis was based.

CHAPTER IV

COAGULATION DYNAMICS OF TWO DIELECTRIC SPHERES

4.1 Motivation

This chapter presents work done to better understand the dynamical process of coagulation of spherical particles in the atmosphere. In particular, the particles considered are small both electromagnetically and aerodynamically (see eqs. 4.1–4.3). Many researchers have addressed the problem of small coagulating spheres in the atmosphere (*e.g.,* Hocking (1959)) and others have added electric forces to the fluid dynamics to try to account for charged particles (for perfectly conducting spheres) and for an external static electric field (Krasnogorskaya (1965a, 1965b)). In particular, Krasnogorskaya gave trajectories for charged and uncharged perfectly conducting spheres either with or without an external static electric field. From this analysis one gets collision efficiencies under each condition which can be used to infer the importance of these conditions to the coagulation process.

This work of Krasnogorskaya has not been built upon since. In this chapter her work is extended to the case of dielectric spheres, with the external force due to an incident plane wave. The solution is intended to show the effect of another external force in the coagulation picture, and as such does not include the other previously-included static charge forces as in Krasnogorskaya's work. The possible contribution of this force is all that is intended, not a complete characterization

of the actual coagulation process with full accounting for every possible external force. The intent is to explore the possibilities with the application to atmospheric aerosols in mind, but without actually applying the formulation to any particular problem. The variety of responses obtained in this way is richer, and may allow application to other areas where some of the parameters may be closer in magnitude to those used here (*e.g.,* colloid coagulation).

The important parameters (Hidy and Brock (1970)) and their values in this context are as follows:

$$\text{Reynolds number} \equiv \mathcal{R}e = \frac{\rho V R}{\mu} \ll 1 \quad \text{(viscous flow)} \tag{4.1}$$

$$\text{Knudsen number} \equiv Kn = \frac{\lambda_G}{R} \ll 1 \quad \text{(continuum)} \tag{4.2}$$

$$\text{electrical size} = \frac{\Delta X |\epsilon_r|}{\lambda} \ll 1 \quad \text{(quasi-static)} \tag{4.3}$$

where λ_G is the mean-free path of the air molecules, ΔX is the total size of the system of particles, and ϵ_r is the complex relative dielectric constant of the particles with respect to the air. We also have μ as the viscosity of the fluid medium, V the relative velocity of the fluid medium and the particles, and R a characteristic radius of the particle.

Both the magnitude and wavelength of the incident electric field are unrestricted. Unphysical values will be avoided, and the particle radius will be kept less than 50μm, but greater than 19μm, where the formulation of Hocking (1959), which we use, is known to be valid (Hidy and Brock (1970)). The size of the entire system of particles, ΔX, will be limited to about $50R \approx 1$ mm. This limits the wavelength of the incident radiation, λ, to be greater than 50 mm, for R_{max}, where the relative permittivity, ϵ_r, is limited to a reasonable magnitude of about 5. Note that for simulations where ΔX is smaller (say $10R$) then λ_{min} is also smaller (2 mm).

4.2 Fluid Forces

The formulation of Hocking, including the extensions of Krasnogorskaya, is made up of the differential equations of motion for two spheres, 1 and 2, of different radii (within limits). The variables have been normalized as follows: all lengths normalized by the diameter of the largest sphere (d_1), and time normalized by the quantity $d_1/(2u_\infty)$, where $u_\infty = d_1^2\rho_d g/(18\eta)$ is the terminal velocity of the particle. Here, ρ_d is the density of the particle, g is the acceleration due to gravity, and η is the viscosity of the medium (air). Note that the terminal velocity is the fastest a particle can fall under the influence of gravity with the compensating force due to friction with the air.

The resultant equations are referred to a $\rho - z$ coordinate system, as shown:

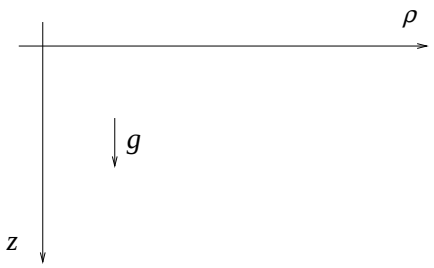

Figure 4.1 — Coordinate system used for two spheres settling in the atmosphere.

Note that this coordinate system is not to be confused with the $\rho - z$ coordinates that are referenced to the particles. The context makes clear which system is being used. The equations of motion are:

$$I\frac{dv_{1z}}{dt} = 1 \; - \frac{l_1 z - t_1 \rho}{r} + b_1 F_{1z} \tag{4.4}$$

$$I\frac{dv_{1\rho}}{dt} = \quad - \frac{l_1 \rho + t_1 z}{r} + b_1 F_{1\rho} \tag{4.5}$$

$$a^2 I\frac{dv_{2z}}{dt} = a^2 - \frac{l_2 z - t_2 \rho}{r} + b_2 F_{2z} \tag{4.6}$$

$$a^2 I \frac{dv_{2\rho}}{dt} = \quad -\frac{l_2\rho + t_2 z}{r} + b_2 F_{2\rho} \tag{4.7}$$

and

$$\frac{dz_1}{dt} = v_{1z}, \qquad \frac{d\rho_1}{dt} = v_{1\rho} \tag{4.8}$$

$$\frac{dz_2}{dt} = v_{2z}, \qquad \frac{d\rho_2}{dt} = v_{2\rho} \tag{4.9}$$

$$z = z_2 - z_1, \qquad \rho = \rho_2 - \rho_1 \tag{4.10}$$

$$r = \sqrt{z^2 + \rho^2}, \qquad a = d_2/d_1, \qquad I = \frac{\rho_d d_1 u_\infty}{9\eta} \tag{4.11}$$

$$b_1 = \frac{1}{3\pi d_1 \eta u_\infty} \qquad b_2 = \frac{1}{3\pi d_2 \eta u_\infty} \tag{4.12}$$

where the parameters l_1, l_2, t_1, and t_2 are complicated expressions taken from the work of Hocking (1959).

Hence, given the initial positions and velocities of each of the two particles, these equations can be integrated numerically to give the trajectories of the spherical particles falling through a viscous liquid under the influence of gravity (initially falling at their terminal velocities in our case) and also due to the influence of some, as yet unspecified, external force, $\mathbf{F}$, in Newtons. In our case, when this force is evaluated at particle number two it is found to be equal and opposite to the force evaluated at particle one. This is due to the attraction and repulsion between the particles due to the disturbing influence of the other particle on the total electric field. Hence $\mathbf{F}_1 = -\mathbf{F}_2$. Also in our case we use equal-sized spheres, $a = 1$, to minimize the effects of coagulation due to fluid forces. In this case, inertia and fluid forces are still operable, but the main cause of coagulation is the electromagnetic force.

The trajectories one gets from this can be quite complex, but what overall parameters are important for characterizing the coagulation process? The most important one that is used by many practitioners, including Hocking and Krasnogorskaya, is the collision efficiency. Let $\rho_{grazing}$ be the initial value of ρ for which

the trajectory is such that the particles just graze one another; any larger and they would not collide. This must be evaluated for an initial z separation large enough so that $\rho_{grazing}$ is independent of this initial z separation. The definition of the collision efficiency then reads:

$$\text{Eff}_{collision} = \left(\frac{\rho_{grazing}}{2R}\right)^2 = \left(\frac{\rho_{grazing}}{d_1}\right)^2 \tag{4.13}$$

This definition gives an efficiency of unity when the collisions are such that the particles start with a lateral (ρ) separation equal to the sum of their radii. A comparison of this efficiency with that when there is no applied field gives an idea of how effective the field is in influencing the coagulation process.

But the collision efficiency is not the only important parameter. In what follows, performance parameters will be introduced as needed for specific applications.

4.3 Vibration and Turbulence

4.3.1 Vibration

The electromagnetic force between the particles is really time dependent. In fact, it is harmonic, at a frequency 2ω for an incident field at ω. For very high frequencies and very small particles one might think that the particle vibration so caused can be ignored in computing the trajectories – and in certain cases this is indeed so. To develop this idea in detail, some things to consider are:

1. the effect of vibration on particle trajectories, and
2. the effect of vibration on fluid flow.

The first of these may be analyzed by an approximation using a straightforward application of Newton's law:

$$\mathbf{F} = m\mathbf{a} = m\frac{d^2x}{dt^2} \tag{4.14}$$

with the force given by:

$$\mathbf{F} = m\hat{\mathbf{x}}\cos^2(\omega t) \tag{4.15}$$

After two integrations this yields:

$$x(t) = C_1 + C_2 t + \frac{1}{4}t^2 - \frac{1}{8\omega^2}\cos(2\omega t) \tag{4.16}$$

$(t \geq 0)$ for the particle trajectory.

To assess the importance of the cosine term to the motion we compare both $x(t)$ and $v(t)$ to their approximations which have the harmonic term removed.

Let x_N be the trajectory of the particle with the cosine term removed. Then the error in using x_N as an approximation to x is:

$$\%\text{error}(t) = \frac{x_N(t) - x(t)}{x(t)} 100 \tag{4.17}$$

If we assume that $C_1 = C_2 = 0$, for the worst-case error, we get:

$$\%\text{error}\,|_{max}\,(t) = \frac{\frac{1}{8\omega^2}\cos(2\omega t)}{\frac{1}{4}t^2 - \frac{1}{8\omega^2}\cos(2\omega t)} 100 \tag{4.18}$$

A cursory inspection of this equation yields a misleading and somewhat imprecise conclusion: the t^2–term in the denominator causes the error to approach zero as the time increases to infinity. Looking more closely, the worst error occurs at times such that $2\omega t = n\pi$ for $n = 0, 2, \ldots$ This gives:

$$\%\text{error}\,|_{max}\,(n) = \frac{200}{\pi^2 n^2 - 2} \tag{4.19}$$

the magnitude of which is shown in fig. 4.2. So when using $x_N(t)$ as an approximation to $x(t)$ with better than 1% accuracy in the trajectories, one would have to ignore the results for the first five half-periods or for $t < \frac{5\pi}{2\omega}$.

The velocity is:

$$v(t) = C_1 + \frac{t}{2} + \frac{1}{4\omega}\sin(2\omega t) \tag{4.20}$$

$$v_N(t) = C_1 + \frac{t}{2} \tag{4.21}$$

With $C_1 = 0$ for the worst case, this gives:

$$\%\text{error}\,|_{max}\,(t) = \frac{v_N(t) - v(t)}{v(t)} 100 \tag{4.22}$$

$$= \frac{-\frac{1}{4\omega}\sin(2\omega t)}{\frac{t}{2} + \frac{1}{4\omega}\sin(2\omega t)} 100 \tag{4.23}$$

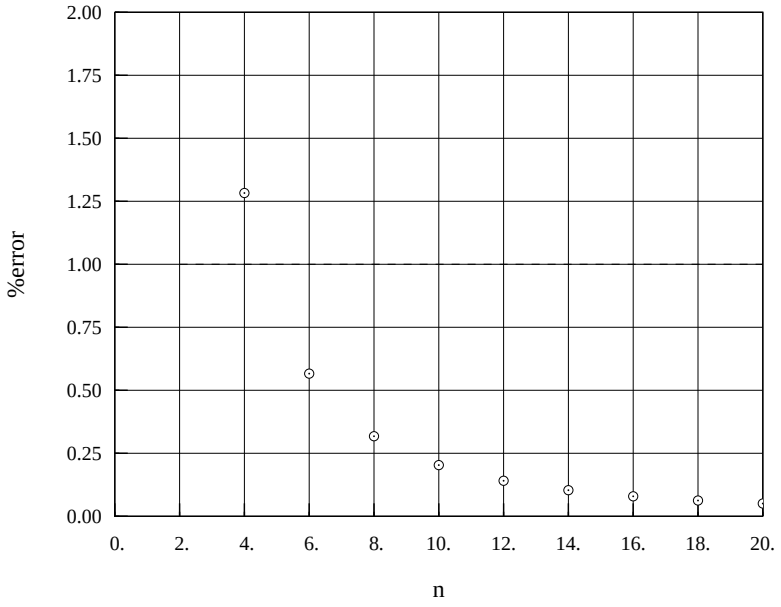

Figure 4.2 — Maximum percentage error as a function of the number of cycles since the start of the force. Error is for x_N used to approximate x.

The maximum error is seen to occur at times such that $2\omega t = \pi(\frac{1}{2} + n)$, n even, giving:

$$\%\text{error}\,|_{max}\,(n) = -\frac{100}{\pi(n + \frac{1}{2}) + 1} \tag{4.24}$$

the magnitude of which is shown in fig. 4.3. So when using $v_N(t)$ as an approximation to $v(t)$ with better than 1% accuracy in the velocity, one would have to ignore the results for the first 30 half-periods or for $t < \frac{30\frac{1}{2}\pi}{2\omega}$.

All this works well when the gradient in the force field is small, and when the particles are far apart. In our case both of these assumptions need more scrutiny when the particles get close enough so that a vibration amplitude could cause them to collide. From the previous analysis, both particles vibrate with an amplitude of $F/(8m\omega^2)$, hence the maximum relative displacement from their approximated values is $2F/(8m\omega^2)$, because the two particles are shaken 180 degrees out of phase.

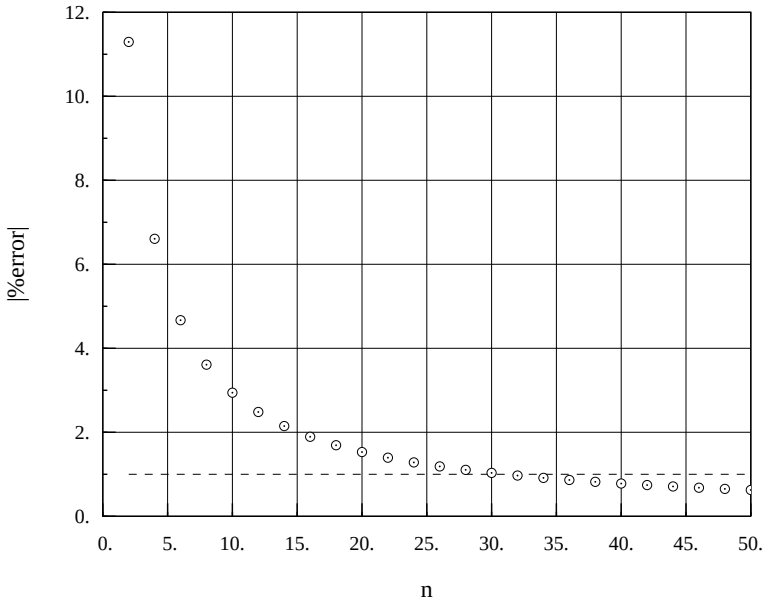

Figure 4.3 — Maximum percentage error as a function of the number of cycles since the start of the force. Error is for v_N used to approximate v.

This means that when the particles are closer, the vibration will cause them to collide within at least one period of oscillation.

The data presented here uses the $x(t)$ criterion, *i.e.,* the trajectories are presented for $t > \frac{5\pi}{2\omega}$, and *until* they are approximately $\frac{2F}{8m\omega^2}$ apart, or until they stop moving for other reasons.

4.3.2 Turbulence

The turbulence of the atmosphere is ignored almost completely in this analysis. The only place it appears is when analyzing the slow-moving trajectories. Then, turbulence is expected to make a noticeable difference, and hence invalidate any kind of predictive quality from the results. Consequently, assuming a turbulent atmosphere that would make a positional difference of one particle radius in 10 seconds or so, the slow-moving trajectories will be ignored and are not shown here.

4.4 Electromagnetic Forces

The static and quasi-static electromagnetic forces between two spheres is discussed in this section. There are three main subdivisions:

1. static force between charged particles,
2. static force due to total field when in the presence of a uniform static field,
3. quasi-static force due to total field when illuminated with a plane wave.

The first two have been treated thoroughly by Davis (1962, 1964a, 1964b) for perfectly conducting spheres, and used by Krasnogorskaya in her analysis. The third is the subject of this chapter, and is for dielectric spheres.

Briefly, when two perfectly conducting charged spheres approach each other the charges rearrange along the surface. The force due to nonuniform distribution of these charges causes relative movement between the spheres. Further details can be found in the cited papers of Davis and in Lindblad and Semonin (1963).

For the plane wave case a quasi-static approximation is used for the field, and hence for the force as well. This means that the problem is solved as in statics, except with a finite complex ϵ_r, giving a complex field, $\mathbf{E}$.

To find the force on one sphere due to the presence of the other, start with the assumption of an arbitrary rotationally-symmetric particle. The total electric field is known for uniform incident fields directed along the symmetry axis (z-axis) or along a line perpendicular to the symmetry axis (x-axis). There are more particles in the system than the one that is being focussed on, but the interest here is only in the forces on this one particle in the known total field of the system of particles.

Choose a cylindrical coordinate system (ρ, ϕ, z). For $\hat{\mathbf{z}}$-incident fields we have:

$$\mathbf{E}_3^{inc} = E_o \hat{\mathbf{z}}, \tag{4.25}$$

$$\Phi_3^{inc} = -E_o z. \tag{4.26}$$

Because the body is rotationally symmetric about the z-axis, the total potential is a function of ρ and z. Hence, with s representing the distance along the perimeter

of the body in the $\phi = 0$ plane (x-z plane),

$$\Phi_3^{tot} = V_3(s), \tag{4.27}$$

and

$$\mathbf{E}_3^{tot} = -\nabla\Phi_3^{tot} = -\nabla V_3(s) \tag{4.28}$$

$$= -\left[\hat{\boldsymbol{\rho}}\frac{\partial}{\partial\rho}V_3(s) + \hat{\boldsymbol{\phi}}\frac{1}{\rho}\frac{\partial}{\partial\phi}V_3(s) + \hat{\mathbf{z}}\frac{\partial}{\partial z}V_3(s)\right] \tag{4.29}$$

$$\mathbf{E}_3^{tot} = -\left[\hat{\boldsymbol{\rho}}\frac{\partial}{\partial\rho}V_3(s) + \hat{\mathbf{z}}\frac{\partial}{\partial z}V_3(s)\right]. \tag{4.30}$$

For $\hat{\mathbf{x}}$-incident fields:

$$\mathbf{E}_1^{inc} = E_o\hat{\mathbf{x}}, \tag{4.31}$$

$$\Phi_1^{inc} = -E_o x = -E_o\rho\cos\phi. \tag{4.32}$$

Symmetry gives:

$$\Phi_1^{tot} = V_1(s)\cos\phi, \tag{4.33}$$

and hence

$$\mathbf{E}_1^{tot} = -\nabla\Phi_1^{tot} = -\nabla[V_1(s)\cos\phi] \tag{4.34}$$

$$= -\left\{\hat{\boldsymbol{\rho}}\cos\phi\frac{\partial}{\partial\rho}V_1(s) + \hat{\boldsymbol{\phi}}\frac{1}{\rho}V_1(s)\frac{\partial}{\partial\phi}\cos\phi + \hat{\mathbf{z}}\cos\phi\frac{\partial}{\partial z}V_1(s)\right\} \tag{4.35}$$

$$\mathbf{E}_1^{tot} = -\left\{\left[\hat{\boldsymbol{\rho}}\frac{\partial}{\partial\rho}V_1(s) + \hat{\mathbf{z}}\frac{\partial}{\partial z}V_3(s)\right]\cos\phi - \hat{\boldsymbol{\phi}}\frac{1}{\rho}V_1(s)\sin\phi\right\}. \tag{4.36}$$

The geometry of the problem is given in fig. 4.4, where $\mathbf{E}^{inc} = E_o[\hat{\mathbf{z}}\cos\beta + \hat{\mathbf{x}}\sin\beta]$, with $\mathbf{E}^{inc}$ in the $x-z$ plane. Hence:

$$\mathbf{E}^{tot} = \mathbf{E}_3^{tot}\cos\beta + \mathbf{E}_1^{tot}\sin\beta. \tag{4.37}$$

where $\mathbf{E}_3^{tot}$ represents the total field with a $\hat{\mathbf{z}}$-incident field, and $\mathbf{E}_1^{tot}$ similarly for a $\hat{\mathbf{x}}$-incident field. Since all of the numerical calculations are done in the x-z plane,

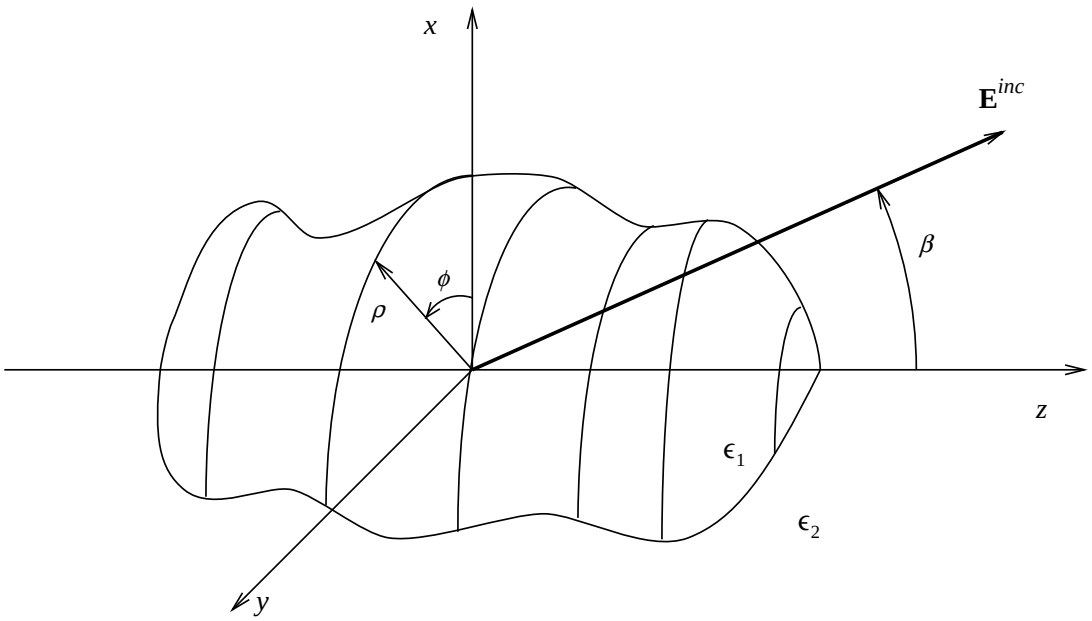

Figure 4.4 — Rotationally-symmetric geometry showing the incident electric field vector in the x-z plane at an angle β to the z-axis.

the following is calculated in our program:

$$E_{3z} = -\frac{\partial}{\partial z}V_3(s) \qquad E_{3x} = -\frac{\partial}{\partial \rho}V_3(s) = -\frac{\partial}{\partial x}V_3(s)\,\Big|_{\phi=0} \tag{4.38}$$

$$E_{1z} = -\frac{\partial}{\partial z}V_1(s) \qquad E_{1x} = -\frac{\partial}{\partial \rho}V_1(s) = -\frac{\partial}{\partial x}V_1(s)\,\Big|_{\phi=0} \tag{4.39}$$

$$E_{1\phi} = -\frac{1}{\rho}V_1(s) \tag{4.40}$$

giving the total electric field as:

$$\mathbf{E}^{tot} = (\hat{\mathbf{z}}E_{3z} + \hat{\boldsymbol{\rho}}E_{3x})\cos\beta + \left\{[\hat{\mathbf{z}}E_{1z} + \hat{\boldsymbol{\rho}}E_{1x}]\cos\phi + \hat{\boldsymbol{\phi}}E_{1\phi}\sin\phi\right\}\sin\beta \tag{4.41}$$

Generalize the force formula for static fields found in Stratton (1946), page 152, to the case where the field is time-varying, while the force can still be calculated at every instant t, as if the fields were static:

$$\mathbf{F}(t) = \epsilon_0 \int_S \left\{\boldsymbol{\mathcal{E}}(\mathbf{r},t)\left[\boldsymbol{\mathcal{E}}(\mathbf{r},t)\cdot\hat{\mathbf{n}}'\right] - \frac{1}{2}\left|\boldsymbol{\mathcal{E}}(\mathbf{r},t)\right|^2\hat{\mathbf{n}}'\right\} dS' \tag{4.42}$$

where $\boldsymbol{\mathcal{E}}(\mathbf{r},t)$ denotes the real time-varying static field such that

$$\boldsymbol{\mathcal{E}}(\mathbf{r},t) = \mathrm{Re}\left\{\mathbf{E}^{tot}e^{-i\omega t}\right\} \tag{4.43}$$

and the outward normal of the surface is:

$$\hat{\mathbf{n}}' = (\hat{\mathbf{x}}\cos\phi' + \hat{\mathbf{y}}\sin\phi')\cos\alpha' - \hat{\mathbf{z}}\sin\alpha' = \hat{\boldsymbol{\rho}}\cos\alpha' - \hat{\mathbf{z}}\sin\alpha' \tag{4.44}$$

where α' has been defined previously (see sec. 2.2). Also note that $dS' = \rho'\,d\phi'\,ds'$, with s' along the perimeter of the body. Rewrite $\hat{\boldsymbol{\rho}} = \hat{\mathbf{x}}\cos\phi' + \hat{\mathbf{y}}\sin\phi'$ in the expressions for $\mathbf{E}^{tot}$. This must also be written as an explicit function of time so that it can be separated out before the integration. The result is:

$$\begin{aligned}\boldsymbol{\mathcal{E}}(\mathbf{r},t) = \quad & \{\hat{\mathbf{z}}(E_{3zr}\cos\omega t - E_{3zi}\sin\omega t) \\ & + (\hat{\mathbf{x}}\cos\phi' + \hat{\mathbf{y}}\sin\phi')(E_{3xr}\cos\omega t - E_{3xi}\sin\omega t)\}\cos\beta \\ + \Big\{ & [\hat{\mathbf{z}}(E_{1zr}\cos\omega t - E_{1zi}\sin\omega t) \\ & + (\hat{\mathbf{x}}\cos\phi' + \hat{\mathbf{y}}\sin\phi')(E_{1xr}\cos\omega t - E_{1xi}\sin\omega t)]\cos\phi' \\ & + \hat{\boldsymbol{\phi}}(E_{1\phi r}\cos\omega t - E_{1\phi i}\sin\omega t)\sin\phi'\Big\}\sin\beta\end{aligned} \tag{4.45}$$

with the added r-subscripts meaning the real part and the i-subscripts the imaginary part.

Due to symmetry it is expected that there will be no net force in the $\hat{\boldsymbol{\phi}}$-direction (no rotation) and no net force in the $\hat{\mathbf{y}}$-direction, which is out of the plane of the incident electric field direction. Hence it is expected that:

$$\mathbf{F} = F_x\hat{\mathbf{x}} + F_z\hat{\mathbf{z}}. \tag{4.46}$$

To finish the specification of the force it is necessary to find each component. First the z-component:

$$\mathbf{F}\cdot\hat{\mathbf{z}} = \epsilon_0\int_S \left\{(\boldsymbol{\mathcal{E}}\cdot\hat{\mathbf{z}})(\boldsymbol{\mathcal{E}}\cdot\hat{\mathbf{n}}') - \frac{1}{2}\mathcal{E}^2\hat{\mathbf{n}}'\cdot\hat{\mathbf{z}}\right\}\,dS' \tag{4.47}$$

The integral becomes:

$$F_z = \epsilon_0 \pi \left\{ \int_s f_a \rho' \, ds' \cos^2 \omega t + \int_s f_b \rho' \, ds' \sin^2 \omega t + \int_s f_c \rho' \, ds' \sin \omega t \cos \omega t \right\} \quad (4.48)$$

where:

$$\begin{aligned} f_a = & \cos^2 \beta \left\{ 2a'e' \cos \alpha' - a'^2 \sin \alpha' + e'^2 \sin \alpha' \right\} \\ & + \sin^2 \beta \left\{ c'g' \cos \alpha' - 1/2 c'^2 \sin \alpha' + 1/2 g'^2 \sin \alpha' + 1/2 a_1'^2 \sin \alpha' \right\} \quad (4.49) \\ f_b = & \cos^2 \beta \left\{ 2b'f' \cos \alpha' - b'^2 \sin \alpha' + f'^2 \sin \alpha' \right\} \\ & + \sin^2 \beta \left\{ d'h' \cos \alpha' - 1/2 d'^2 \sin \alpha' + 1/2 h'^2 \sin \alpha' + 1/2 b_1'^2 \sin \alpha' \right\} \quad (4.50) \\ f_c = & \, 2 \cos^2 \beta \left\{ -a'f' \cos \alpha' + a'b' \sin \alpha' - b'e' \cos \alpha' - e'f' \sin \alpha' \right\} \\ & + \sin^2 \beta \left\{ -c'h' \cos \alpha' + c'd' \sin \alpha' - d'g' \cos \alpha' - g'h' \sin \alpha' - a_1' b_1' \sin \alpha' \right\} \\ & \quad (4.51) \end{aligned}$$

and

$$a' = E_{3zr} \qquad c' = E_{1zr} \quad (4.52)$$

$$b' = E_{3zi} \qquad d' = E_{1zi} \quad (4.53)$$

$$e' = E_{3xr} \qquad g' = E_{1xr} \quad (4.54)$$

$$f' = E_{3xi} \qquad h' = E_{1xi} \quad (4.55)$$

$$a_1' = E_{1\phi r} \qquad b_1' = E_{1\phi i} \quad (4.56)$$

Repeating this analysis for F_x gives:

$$\mathbf{F} \cdot \hat{\mathbf{x}} = \epsilon_0 \int_S \left\{ (\boldsymbol{\mathcal{E}} \cdot \hat{\mathbf{x}})(\boldsymbol{\mathcal{E}} \cdot \hat{\mathbf{n}}') - \frac{1}{2} \mathcal{E}^2 (\hat{\mathbf{n}}' \cdot \hat{\mathbf{x}}) \right\} dS' \quad (4.57)$$

The integral can be simplified to:

$$F_x = \pi \epsilon_0 \sin \beta \cos \beta \left[\int_s g_a \rho' \, ds' \cos^2 \omega t + \int_s g_b \rho' \, ds' \sin^2 \omega t + \int_s g_c \rho' \, ds' \sin \omega t \cos \omega t \right] \quad (4.58)$$

where:

$$g_a = \cos\alpha'[e'g' - a'c' - a'_1 e] + \sin\alpha'[-a'g' - c'e' + a'a'_1] \tag{4.59}$$

$$g_b = \cos\alpha'[f'h' - b'd' - b'_1 d'] + \sin\alpha'[-d'f' - b'h' + b'b'_1] \tag{4.60}$$

$$g_c = \cos\alpha'[a'd' + a'_1 f + b'c' + b'_1 e' - e'h' - f'g'] + \sin\alpha'[-a'b'_1 + a'h' - a'_1 b' + b'g' + c'f' + d'e'] \tag{4.61}$$

4.5 Results

The physical situation that was investigated is that of two spherical particles each with a diameter of 38μm falling in the atmosphere at their terminal velocity (0.046 m/sec or 0.129 mi/hr). The initial relative positions of these particles in a plane was the only geometrical difference between the different simulations. The incident EM field was assumed to have a wavelength longer than the total size of the 2-particle system but was otherwise unspecified. The field strength of the incident EM plane wave was a parameter, varied between about 0.2 V/m and 700 V/m. A typical number for the field strength of solar radiation in the upper atmosphere is 726 V/m, or 1.4 KW/m^2, (Howell and Bereny (1979), p. 25). Other authors have used numbers of similar magnitudes (Schlamp, *et al.,* (1976)). Lastly, the (complex) dielectric constant of the particles was chosen to be either near a resonance ($\epsilon_r = -2.01 + j0.01$) or off-resonance ($\epsilon_r = 2.0 + j0.1$).

Note that without the EM force component the two particles would remain separated and there would be no change in their relative positions. This is so because (1) the particles' initial separation is so large that the fluid forces are negligible, and (2) because the particles are the same size and mass: hence their terminal velocities are the same (recall that the initial conditions specify the two particles are falling at their terminal velocities), and (3) the particles carry no net charge or intrinsic dipole moment.

The relative trajectory of one particle with respect to the other was the raw data that was produced here. Essentially, the governing differential equations were integrated numerically and the resulting trajectory plotted. The numerical package DEPISODE was used for the integration (Byrne and Hindmarsh (1975)).

The total force on one particle in the presence of the other is critical in obtaining the trajectories. At each time step the force is evaluated anew and Newton's first law is integrated to obtain the next position in the trajectory. This is a computationally-intensive process.

An intuitive feel for the likely trajectories can be gleaned from a knowledge of this force vector as a function of relative position (and dielectric constant). The incident field strength would mostly provide only an arbitrary scale factor and so is ignored here. Figures 4.5 and 4.6 show the total force fields on one particle when near one (and only one) other particle in an ambient vertical **E** field. The axes are marked in units of sphere diameters. Each arrow starts at the relative position of the particle in question and points in the direction of the force on that particle assuming that there is another particle located at the origin. The length of the arrows indicates the relative strength of the force. **The two figures have different scaling for the arrows and so cannot be compared as far as the force magnitudes are concerned.** (Were they to have the same scaling as the resonant case, most of the nonresonant arrows would be invisible.) Notice that the force field is quite different for the two cases shown: non-resonant *vs.* resonant. This qualitative difference alone is enough to generate interest in this, but as will be shown later, there is a quantitative difference as well, with the resonant case having much larger forces. This, too, is a good reason for this investigation.

A qualitative understanding of a large part of these force fields (the regions where the separation is large) is possible through the use of the non-interacting approximation. In this case this approximation yields the force between two parallel

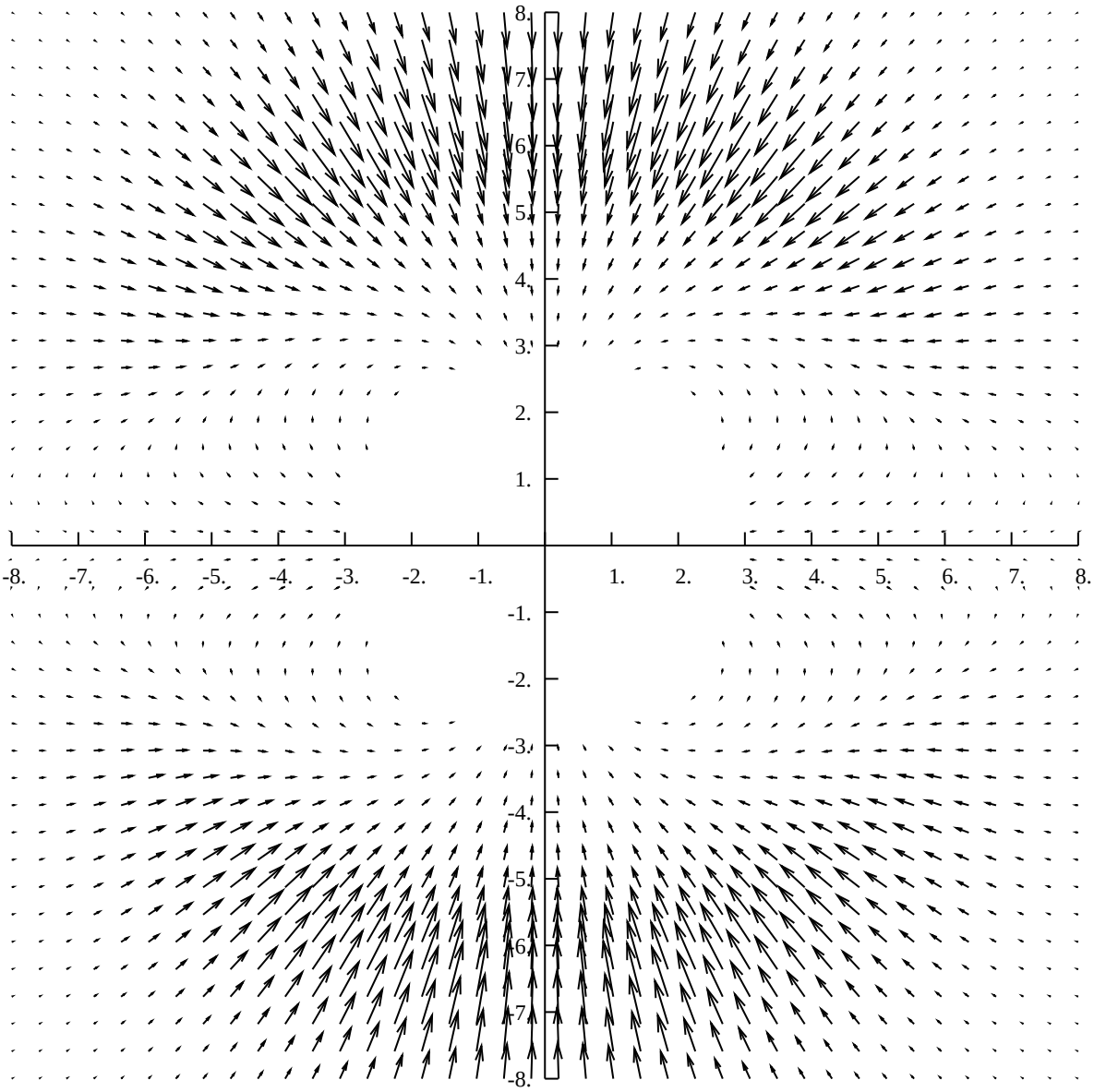

Figure 4.5 — Force between two spheres, resonant case.

Region shown is ±8 units from reference sphere. Note that the arrows are not to scale between this figure and the next. Axes are marked in units of sphere diameters.

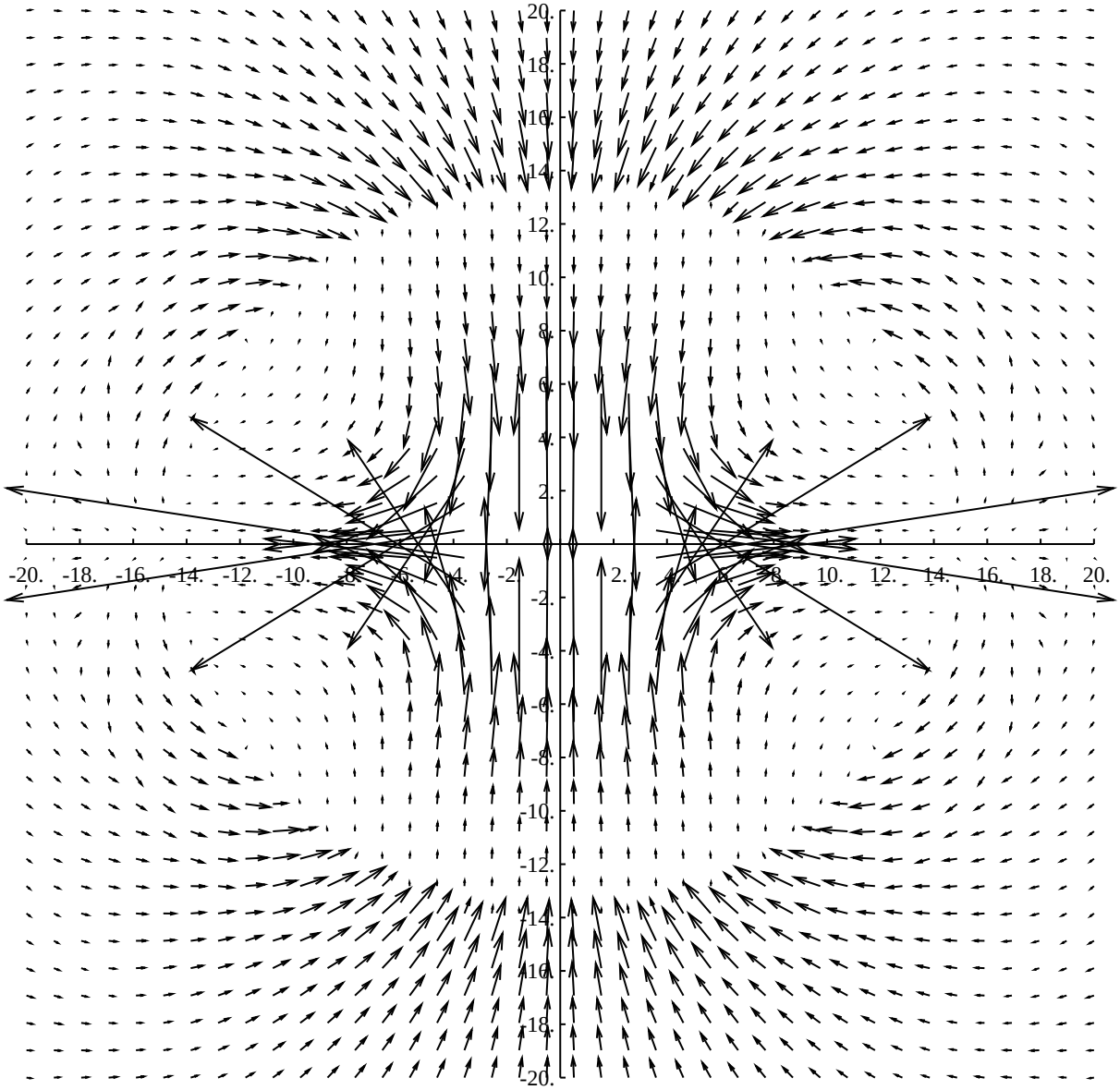

Figure 4.6 — Force between two spheres, non-resonant case.

Region shown is ±20 units from reference sphere. Note that the arrows are not to scale between this figure and the previous one. Axes are marked in units of sphere diameters.

(vertical) dipoles, since the external field of a sphere in a uniform static electric field is that of a dipole at the center of the sphere.

The electric field of a dipole with dipole moment, $\mathbf{p_2}$, in a spherical coordinate system (r', θ', ϕ') (aligned with the dipole) is:

$$\mathbf{E}_{dipole}(\mathbf{r}) = \frac{p_2}{4\pi\epsilon_0 r'^3}\left[\hat{\mathbf{r}}'\, 2\cos\theta' + \hat{\boldsymbol{\theta}}'\sin\theta'\right] \tag{4.62}$$

See fig. 4.7 for the definitions of the symbols. Note that the dipole was chosen to be centered at the origin and oriented at some angle in the x-z plane.

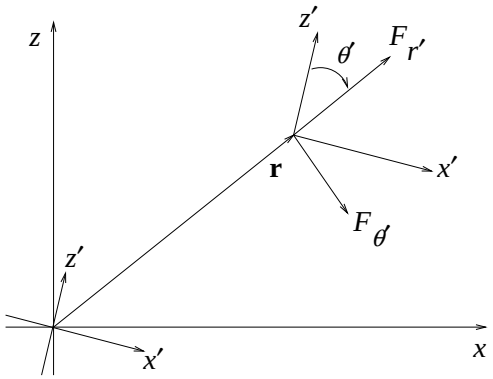

Figure 4.7 — Dipole at origin and associated force vectors at a distant point.

The next step is to find the force on another dipole, due to the field of this one. From Stratton (1941), p. 176:

$$\mathbf{F} = \nabla(\mathbf{p}\cdot\mathbf{E}) \tag{4.63}$$

where $\mathbf{E}$ is the external field within which the dipole is immersed. Specializing to parallel dipoles:

$$\mathbf{p} = p_1\hat{\mathbf{z}}' = p_1(\hat{\mathbf{r}}'\cos\theta' - \hat{\boldsymbol{\theta}}'\sin\theta') \tag{4.64}$$

Hence:

$$\mathbf{F} = \frac{-3p_1p_2}{4\pi\epsilon_0 r'^4}\left[\hat{\mathbf{r}}'(2\cos^2\theta' - \sin^2\theta') + \hat{\boldsymbol{\theta}}'(2\cos\theta'\sin\theta')\right] \tag{4.65}$$

Decomposition to the x'-z' axes yields

$$F_{x'} = F_{r'} \sin\theta' + F_{\theta'} \cos\theta' \tag{4.66}$$

$$F_{z'} = F_{r'} \cos\theta' - F_{\theta'} \sin\theta', \tag{4.67}$$

giving:

$$F_{x'} = \frac{-3p_1p_2}{4\pi\epsilon_0 r'^4} \sin\theta' \left[\sin^2\theta' - 4cos^2\theta'\right] \tag{4.68}$$

$$F_{z'} = \frac{-3p_1p_2}{4\pi\epsilon_0 r'^4} \cos\theta' \left[-3 + \cos^2\theta'\right] \tag{4.69}$$

Lastly, transformation to the x-z coordinates is necessary. (See fig. 4.8.)

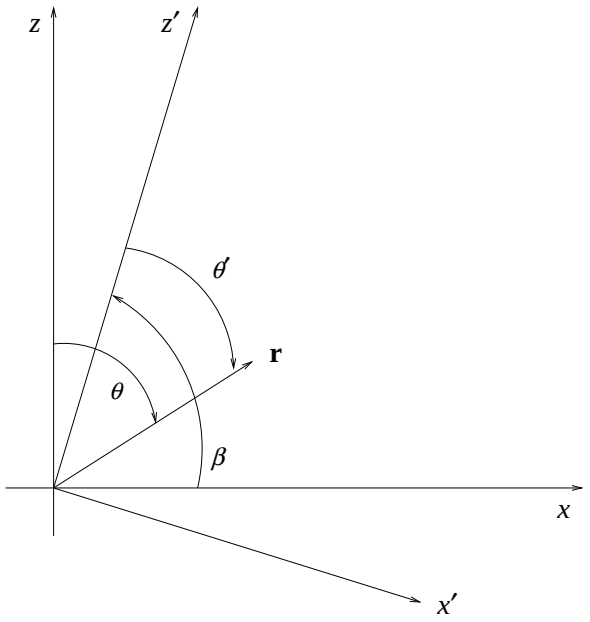

Figure 4.8 — Coordinate transformation for parallel dipoles polarized at an angle β with respect to the x-axis.

We have:

$$\theta' = \theta - (\pi/2 - \beta) = \theta + \beta - \pi/2 \tag{4.70}$$

and also

$$F_x = F_{x'} \sin\beta + F_{z'} \cos\beta \tag{4.71}$$

$$F_z = -F_{x'} \cos\beta + F_{z'} \sin\beta \tag{4.72}$$

This dipole-dipole force field is shown in fig. 4.9. The similarity between this and much of the force field in figs. 4.5 and 4.6 is obvious and can safely be assumed to be mostly due to the the same mechanism.

This leaves us with the forces when the spheres are nearly-touching. It is there where the qualitative differences are so dramatic. No attempt will be made to understand the forces here quantitatively. Qualitatively, however, it is apparent that when near an absorption resonance the fields are large and favor coagulation over separation, while for the off-resonance case the fields are much smaller and favor coagulation only when the particles are initially nearly vertically-aligned.

With this intuitive picture built up, the trajectories are presented next.

4.5.1 Resonant Trajectories

A typical result for a trajectory starting far away, but still close enough to be attracted is seen in fig. 4.10. In all the other figures, there are many trajectories shown on each plot. This is for convenience only, as each trajectory is the result of a separate run with two particles falling in the atmosphere. Note that the smaller of the two circles shown in the figures represents the sphere at the origin. All trajectories are *relative* to the center of this sphere. The larger of the circles represents the closest possible approach of a trajectory to the reference sphere, as the trajectories track the *center* of the second sphere relative to the first. The axes are marked in units of sphere diameters. The trajectory lasts for $37,530$ scaled time units (15.5 sec.) and the last half of the distance to the particle is covered in the last 30 time units (12.4 msec.), or, the last half of the total distance is covered in

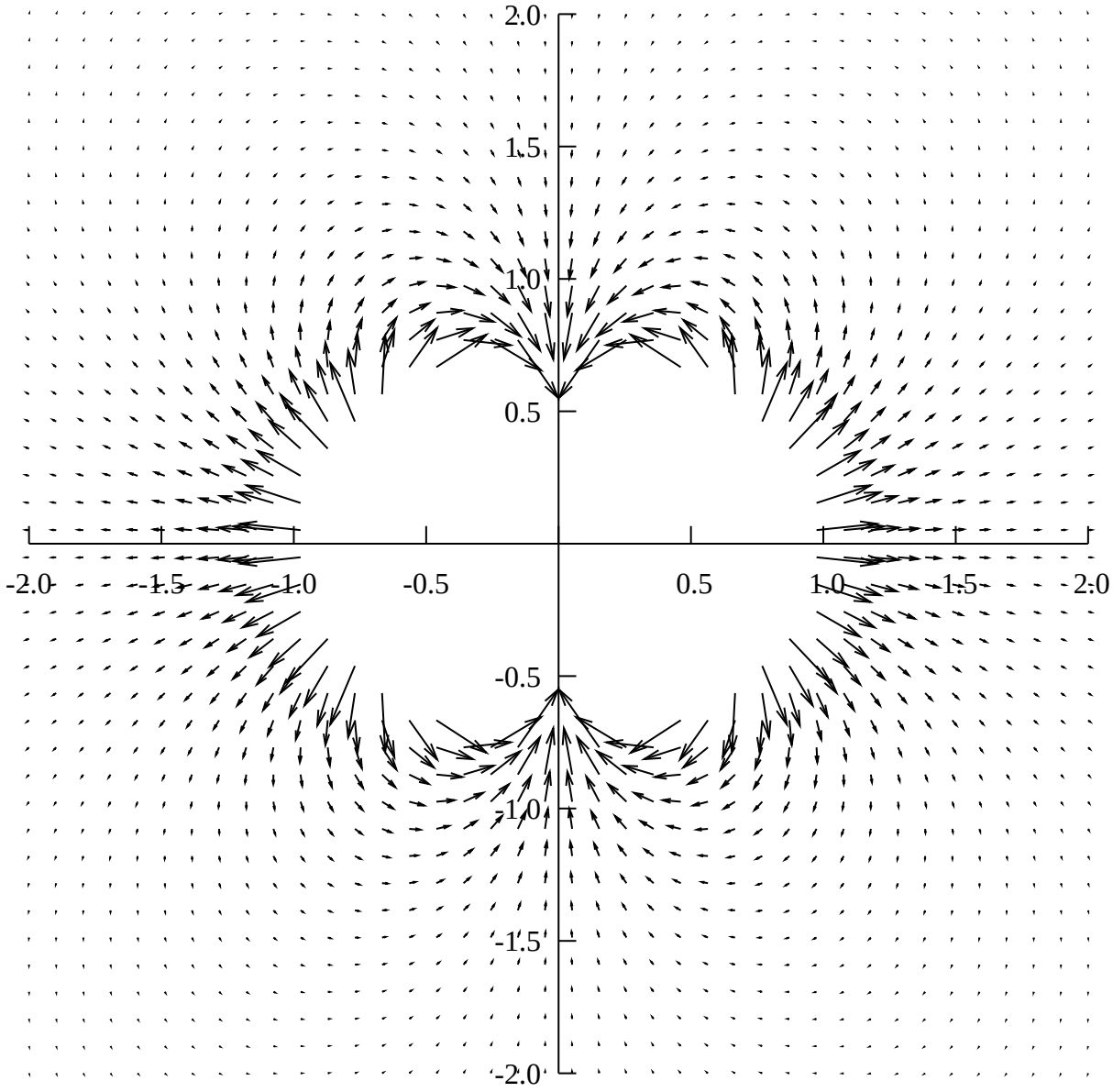

Figure 4.9 — Force vectors between two parallel vertical dipoles.

Note that the arrows are not to scale between this figure and figs. 4.5 and 4.6. Force vectors that were too long were omitted.

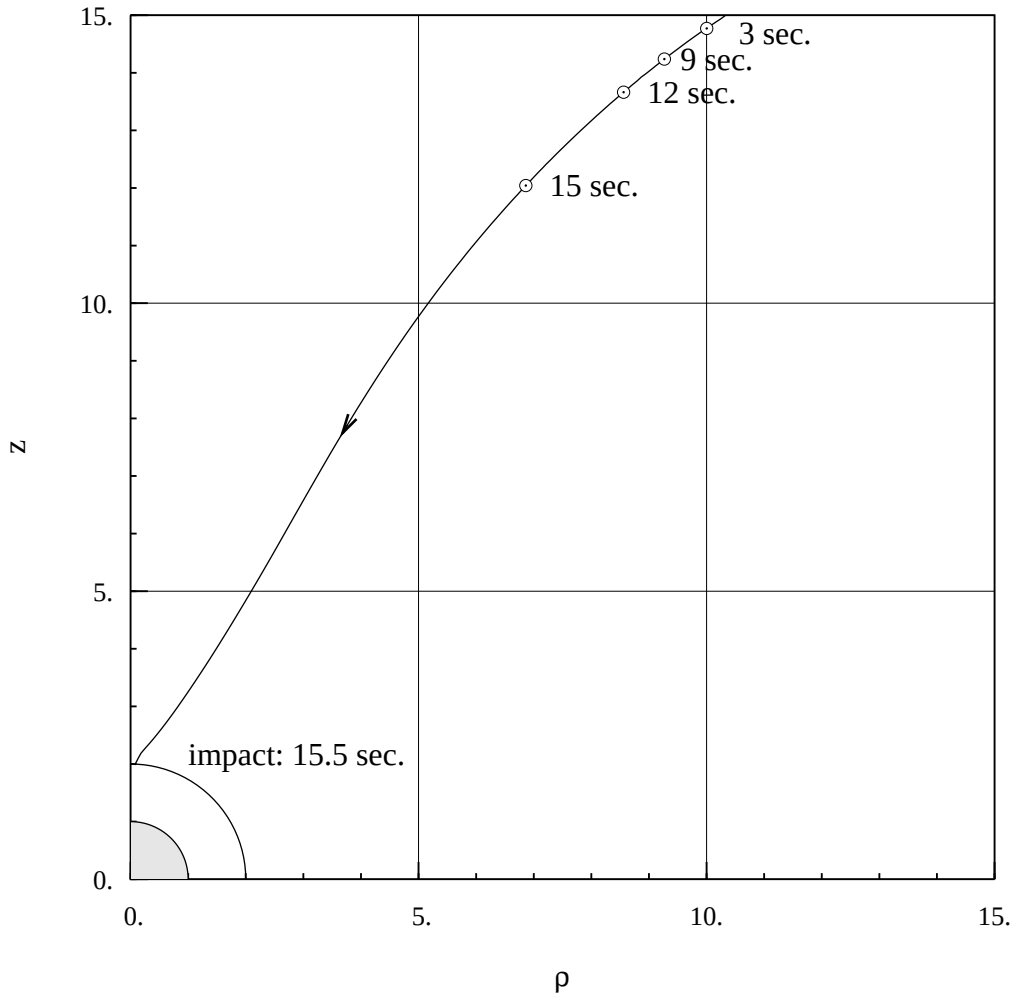

Figure 4.10 — Typical trajectory for resonant case.

The marks show the time elapsed since the start of the simulation. Axes are marked in units of sphere diameters.

0.08% of the total time. This shows the typical acceleration for the resonant case as the particles approach each other more closely.

Figures 4.11 and 4.12 show families of trajectories for incident field strengths of 2.24 V/m and 0.224 V/m respectively. Not shown are those trajectories that were never affected by the electromagnetic force and so did not show any relative movement. Also, recall that those trajectories that moved less than one diameter

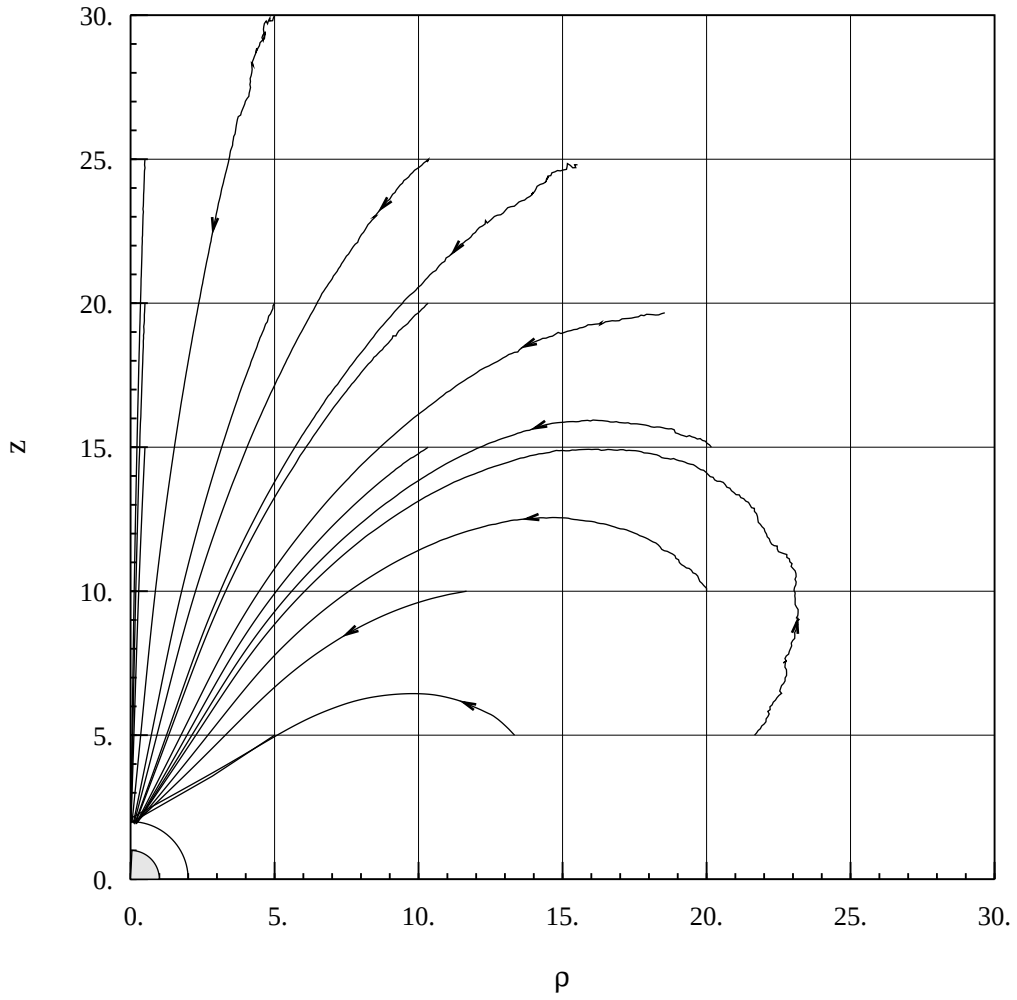

Figure 4.11 — Trajectories for resonant case, $E_0 = 2.24$ V/m.

Each trajectory is a separate simulation run. Axes are marked in units of sphere diameters.

---

in 10 minutes of real time were not shown for the same reason, the idea being that atmospheric turbulence would be far more powerful. Consequently, an "interaction region" can be delimited about each particle to specify the pairwise interaction region, where attraction occurs. This region is sketched for each case in figs. 4.13 and 4.14. Because of the minimal differential affect of the fluid forces and gravity in this case, the regions are symmetric vertically.

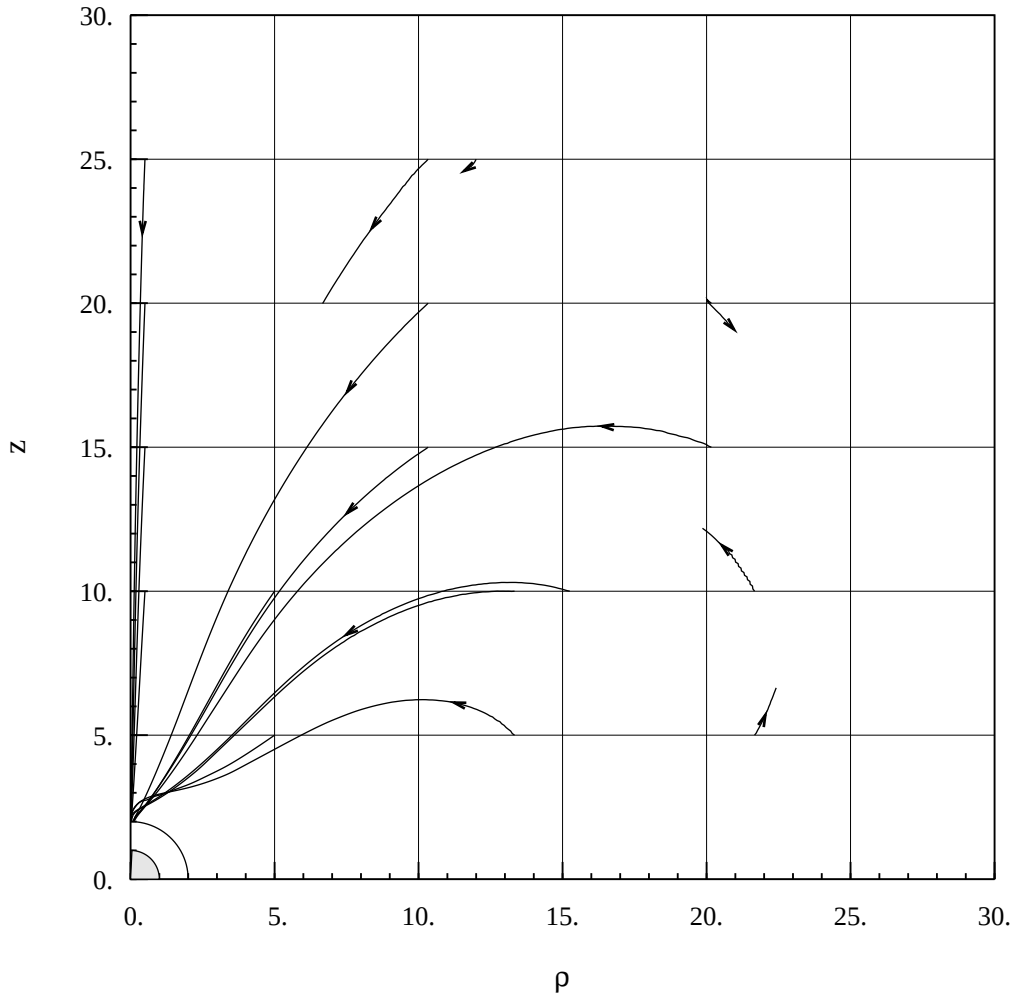

Figure 4.12 — Trajectories for resonant case, $E_0 = 0.224$ V/m.

Each trajectory is a separate simulation run. Axes are marked in units of sphere diameters.

The trajectories show that almost all particles that interact will collide. The exceptions are those that start close to, but horizontal, to each other. In that case, the repulsion is dominant and the particles quickly diverge from each other. The converging trajectories also show another interesting feature: the final geometry of the coagulated pair lines up with the vertical. Since the major force here is electromagnetic, the particles are lining up with the incident electric field, which in this

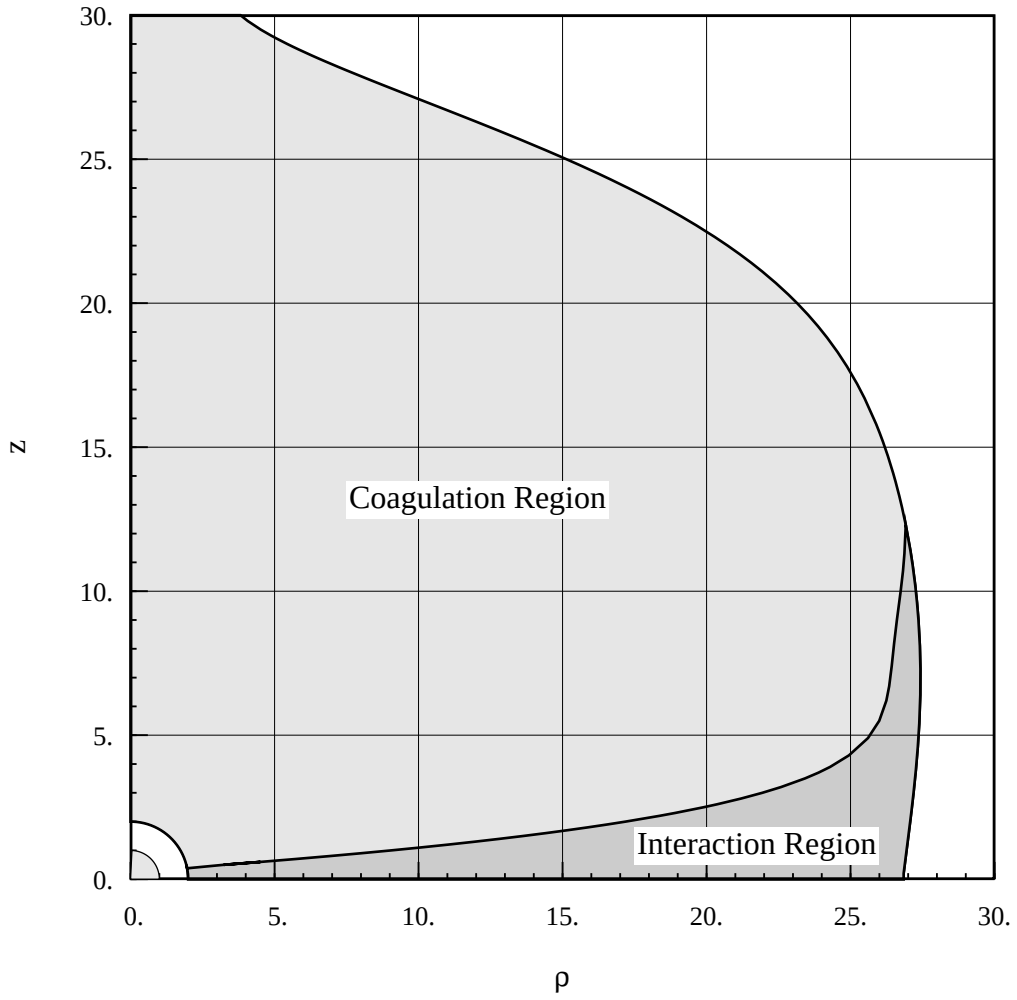

Figure 4.13 — Interaction and coagulation regions for the resonant case, $E_0 = 2.24$ V/m.

Axes are marked in units of sphere diameters.

---

case is vertical. This phenomenon has been observed experimentally (Krasny-Ergen (1936)). Besides the obvious difference in the paths of the trajectories between the two figures, the biggest difference is that the extent of the region of starting points from which the particles contact each other is different. The case with the *higher* incident field strength, and hence stronger force field, shows a *larger*, or more spread

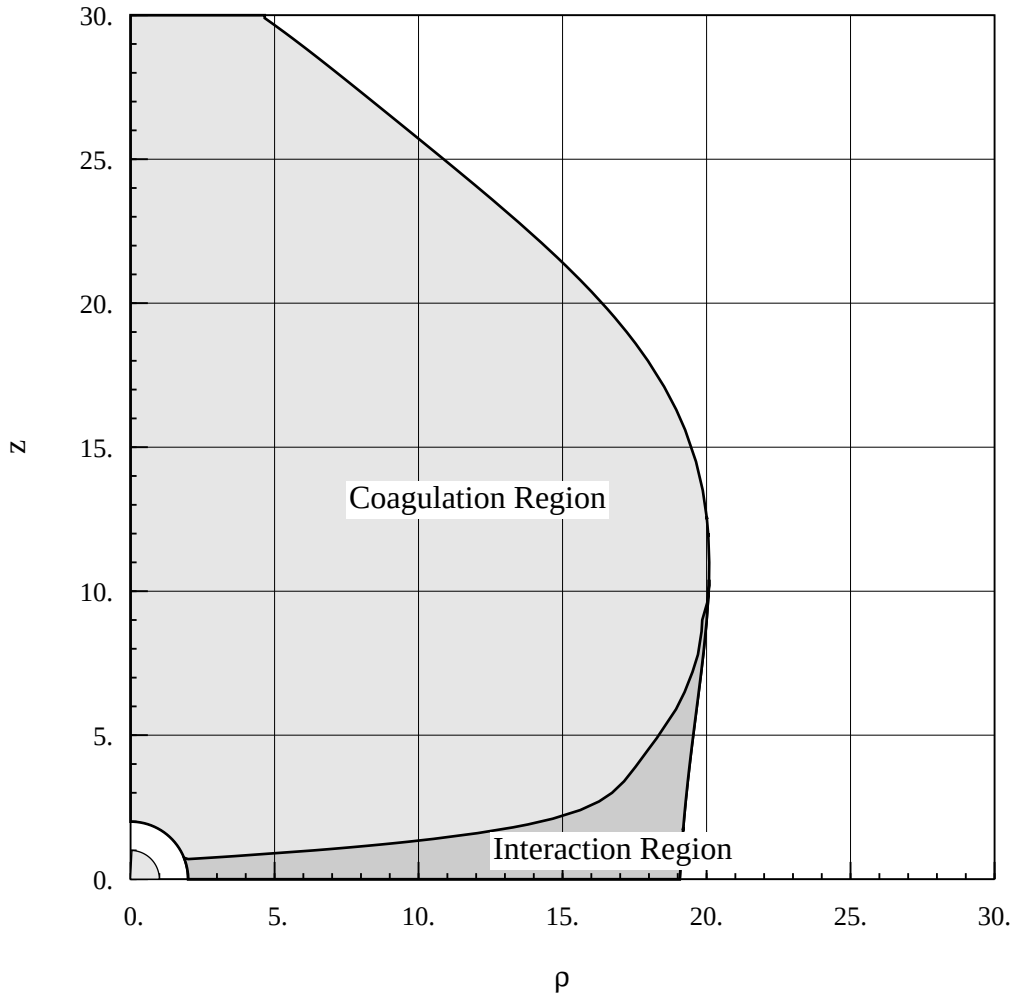

Figure 4.14 — Interaction and coagulation regions for the resonant case, $E_0 = 0.224$ V/m.

Axes are marked in units of sphere diameters.

---

out, contact region. This is possibly due to inertia.

The coagulation regions are vague at best. These are presented to give a feel for the interactions and a convenient method for comparison between the different cases. The region extends much farther from the reference particle in the vertical direction, as the dipole attraction is greatest there. The minimum, when they are

next to each other horizontally, can be thought of as due to the repulsion of two parallel dipoles. The extent of this region is largely dependent on the incident field strength.

The interaction region is significantly larger than the coagulation region in the region next to the reference particle, where the dipole repulsion is large.

4.5.2 Non-Resonant Trajectories

Figures 4.15 and 4.16 show families of trajectories for incident field strengths of 2.24 V/m and 22.4 V/m respectively. Again, an "interaction region" can be delimited about each particle, but also the "coagulation region" in the non-resonant cases is much smaller than the interaction region, and much smaller than the coagulation region in the resonant case. Both of these regions are sketched for each case in figs. 4.17 and 4.18.

The trajectories show that only those particles that are nearly vertically aligned at the outset will collide. The remainder of the trajectories show that the force becomes repulsive and that the particles are ejected horizontally from the reference sphere. Another new phenomenon here is that there is a "backwater" region at which the particles that are ejected tend to cluster, and here their relative velocities become quite small. So many particles will tend to "cluster" without coagulating, remaining in the backwater region of another particle. The converging trajectories show another difference from that of the resonant trajectories, in that the contact region here is quite large, covering most of the particle. Hence, the particles cannot be said to be lining up with the incident electric field (vertical), as in the resonant case.

Again, the coagulation regions are vague at best. The region extends much farther from the reference particle in the vertical direction, as the dipole attraction is greatest there. The minimum, when they are next to each other horizontally, can

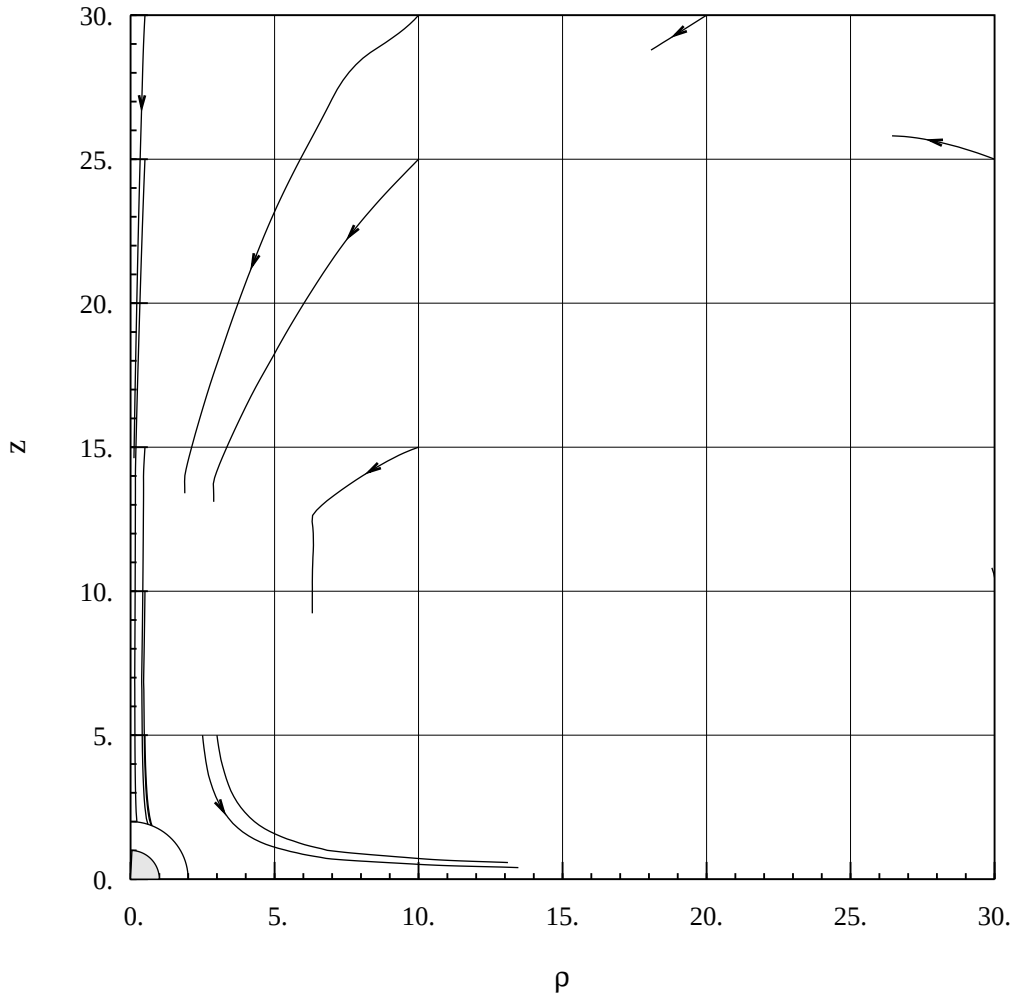

Figure 4.15 — Trajectories for non-resonant case, $E_0 = 2.24$ V/m.

Each trajectory is a separate simulation run. Axes are marked in units of sphere diameters.

---

be thought of as due to the repulsion of two parallel dipoles. The extent of this region is largely dependent on the incident field strength.

The interaction region is far bigger than the coagulation region for the non-resonant case. Most of the interaction here results only in loosely bound particles without coagulation. No similar effect is seen in the resonant case.

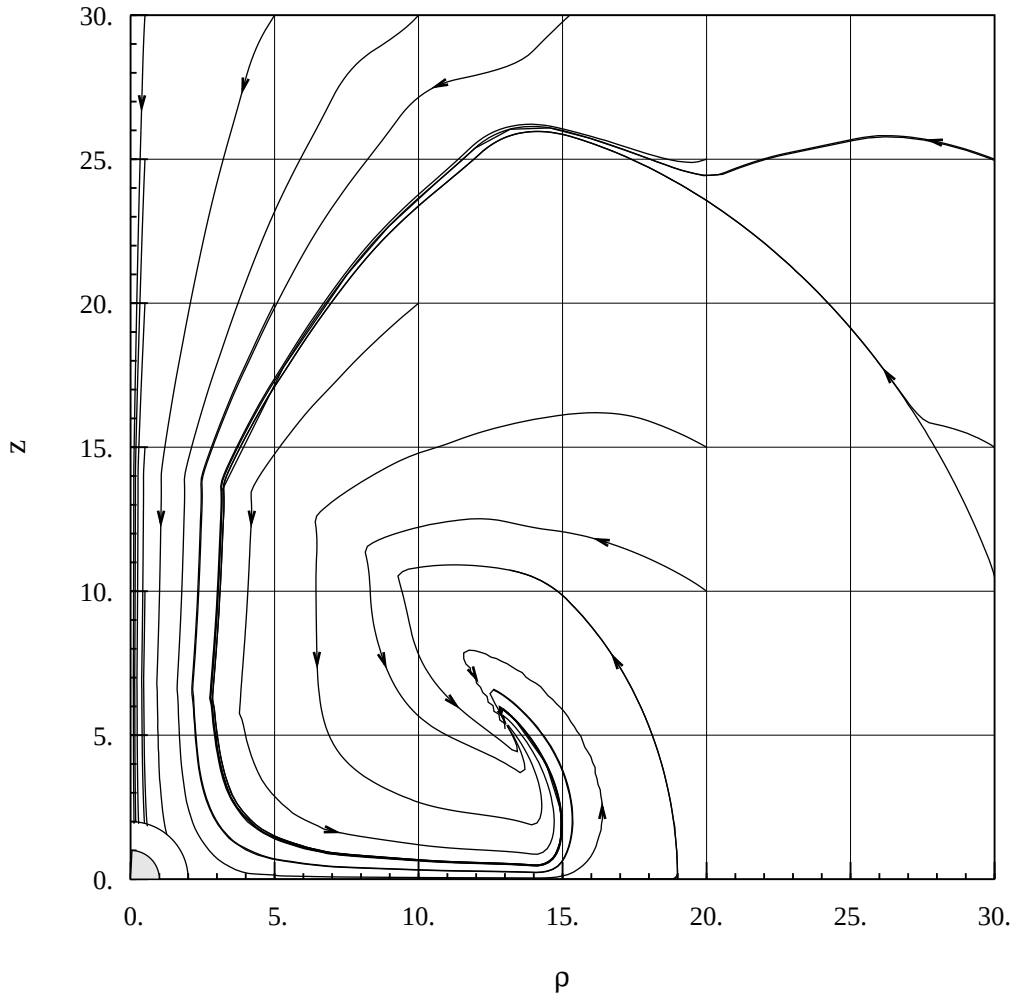

Figure 4.16 — Trajectories for non-resonant case, $E_0 = 22.4$ V/m.

Each trajectory is a separate simulation run. Axes are marked in units of sphere diameters.

4.6 Conclusions and Future Work

This chapter has shown that coagulation of small particles can be greatly affected by the kind of resonance phenomenon that has been explored in this thesis. Specifically, coagulation can be induced between particles when irradiated at a frequency near a resonance. When not near a resonance the coagulation is driven by other forces which are not of concern here. In addition, when the electromagnetic

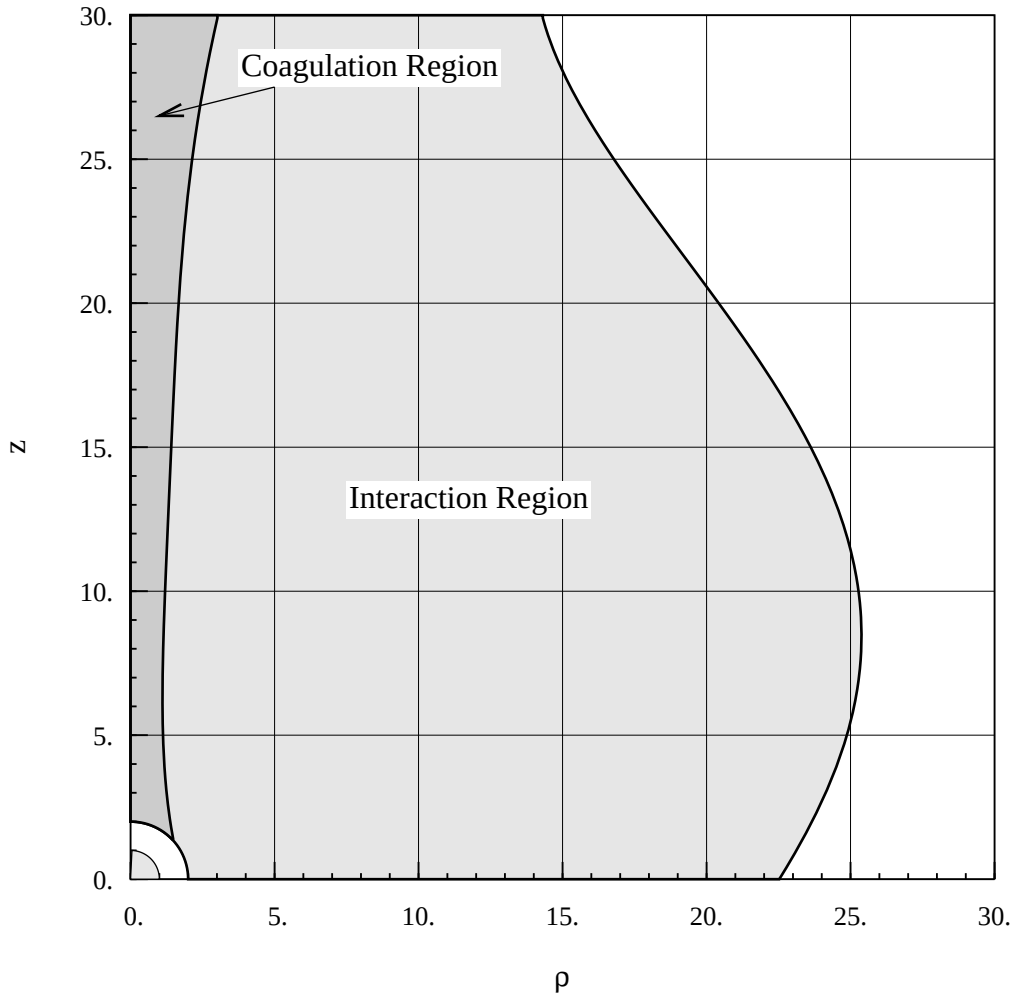

Figure 4.17 — Interaction and coagulation regions for the non-resonant case, $E_0 = 2.24$ V/m.

Axes are marked in units of sphere diameters.

---

force is dominant, as it is here, the coagulated particles are aligned along the applied electric field vector.

One use of this could be to help determine the effect of sunlight on aerosols in the upper atmosphere. For example, determining such properties as size and shape of particles formed could be important to atmospheric chemistry where many reactions

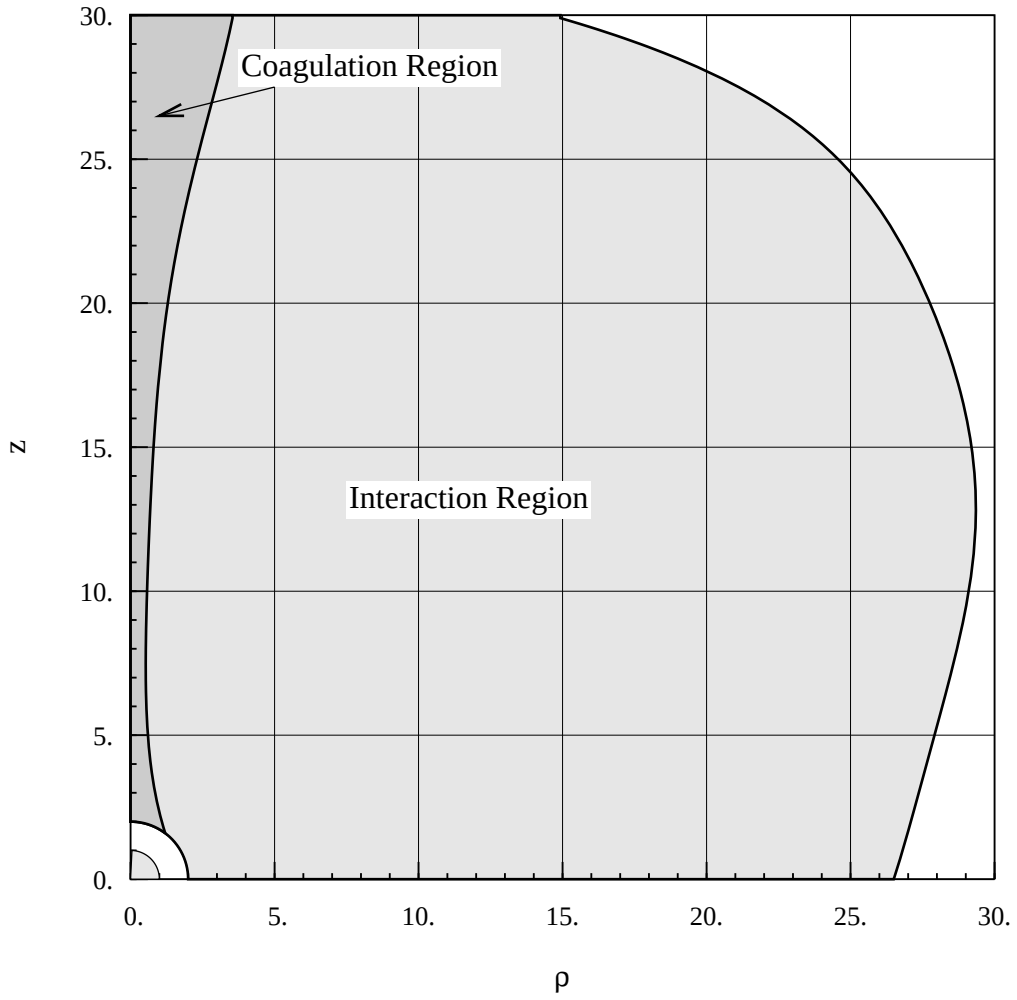

Figure 4.18 — Interaction and coagulation regions for the non-resonant case, $E_0 = 22.4$ V/m.

Axes are marked in units of sphere diameters.

---

are catalyzed on particle surfaces. Also, the possible catalytic effects of the surface resonance itself could be explored, e.g., in the context of the recent stratospheric ozone depletion problems.

One extension to this work would be to explore the effects of the fluid-electromagnetic interaction. This would involve two spheres of *different sizes,* thereby

changing the importance of electromagnetic *vs.* fluid forces in a controlled way. Through this sort of study one could see under what conditions the electromagnetic force becomes swamped by the fluid force (and gravity), as well as the effect on the coagulation times and trajectories. It is expected that the fluid force will easily exceed the electromagnetic force for cases where the particles are very different in size, and where there is no electromagnetic resonance. In cases where there **is** a resonance, however, close approaches to the resonant geometry could overcome the fluid force and cause coagulation. This sort of behavior is also expected for arbitrary non-spherical particles, with the added complication of a dependence on the orientation angles of each particle. This is important, but the main ideas presented above will not change. That is, electromagnetic resonances can still play a large part in the coagulation process, with the relative particle sizes modulating the relative importance of fluid and electromagnetic forces. The above study might also provide a model of the coagulation of a single particle to an already-agglomerated mass represented by the larger sphere.

A further extension to the present theory would include using the approximate dipole-dipole force field between arbitrary-shaped particles, but only when they are far apart. Then, as they approach more closely, the solution of the non-rotationally-symmetric problem should be used, including the fluid forces that are involved as well. This is an order of magnitude more complex than the study done here.

Another possible extension would involve accounting for the relative phase of the electromagnetic field between different particles, while ignoring it within the same particle. The idea would be to still use the Rayleigh approximation, but to include the known phase term on top of the static formulation. This would allow simulations of small particles with larger separations, and would be only slightly more complicated than the work presented here.

CHAPTER V

APPLICATION TO PHOTOSYNTHESIS: STACKED THIN DISKS

5.1 Motivation

The previous chapters of this thesis describe work in resonant absorption by particles of various shapes. When thinking of real-life applications for this topic, photosynthesis naturally suggested itself. Since light gathering in plants is done by molecules embedded in the surface of stacked thin disks, it is apparent that resonant absorption could play a major role in photosynthetic light absorption. Light gathering in algae is not associated with closely-spaced stacked disks, and hence it is likely that this stacking was an improvement during evolution. From the previous work in this thesis, some idea as to what kinds of shapes produce what kinds of characteristic resonant epsilons has been developed. Hence, it is reasonable to believe that shapes so different from spheres, and with such a dense stacking arrangement, would have large, negative resonant epsilons. That the chlorophyll molecules reside on the outside of the membrane is also highly suggestive, since in resonant absorption *that* is where the total field is enhanced. Naturally, to investigate this idea quantitatively required detailed modeling and calculations, which are presented in this chapter.

This chapter presents the change in resonance positions as a function of both stacking geometry and size and investigates the implications to absorption at the

frequencies relevant to photosynthesis. The results suggest that resonant absorption occurs for a class of plants that are adapted to bright sunlight in semi-arid conditions, called C4 plants.

5.2 Background

This section details the relevant biological knowledge needed to understand the rest of this chapter. Two terms that are used quite often in the biological literature are *in vivo* and *in vitro*. The term *in vivo* refers to a process in a living system in its natural state. The term *in vitro* refers to an experiment that is done on some system in a controlled laboratory environment, often thought of as a "test-tube" experiment. Most experiments in photosynthesis research have been done *in vitro,* with some arguments concerning the correlation to the actual system *in vivo.*

Photosynthesis in plants is carried out in sub-cellular structures called chloroplasts. A single plant cell can have many chloroplasts, depending on the cell's function. Within each chloroplast is the molecular machinery that carries out the light harvesting, and conversion of the energy into energy-storage molecules, such as glucose. (Note that light harvesting means that the light is *permanently* absorbed rather than just temporarily absorbed to be re-emitted later.) The structures internal to the chloroplast where the light harvesting is carried out are called thylakoid membranes. These are highly-folded membranes with chlorophyll pigments embedded in them. Each chloroplast contains many thylakoid membranes, as well as a large vacuole (storage sac) to contain the produced energy-storage molecules.

A comparison of the small, stacked disk-shaped thylakoid membranes of sugar cane mesophyll cells with the larger and more widely-spaced thylakoids of sugar cane bundle sheath cells is shown in fig. 5.1. Note that the width of a larger disk is on the order of ten times that of the smaller disk, with a similar increase in the average disk spacing. Usually, plants that exhibit both types of thylakoid shapes are termed C4 plants and have unique properties. The mesophyll cells are responsible

for the majority of the light harvesting and are the major constituent of the leaves in these plants. However, near the "veins" of the leaves the other types of cells are abundant and are responsible for the terminal reactions of the conversion of light energy into starch-like molecules for transport to the rest of the plant. Corn, as well as the sugar cane shown here, possesses such an anatomy, as discussed in more detail later.

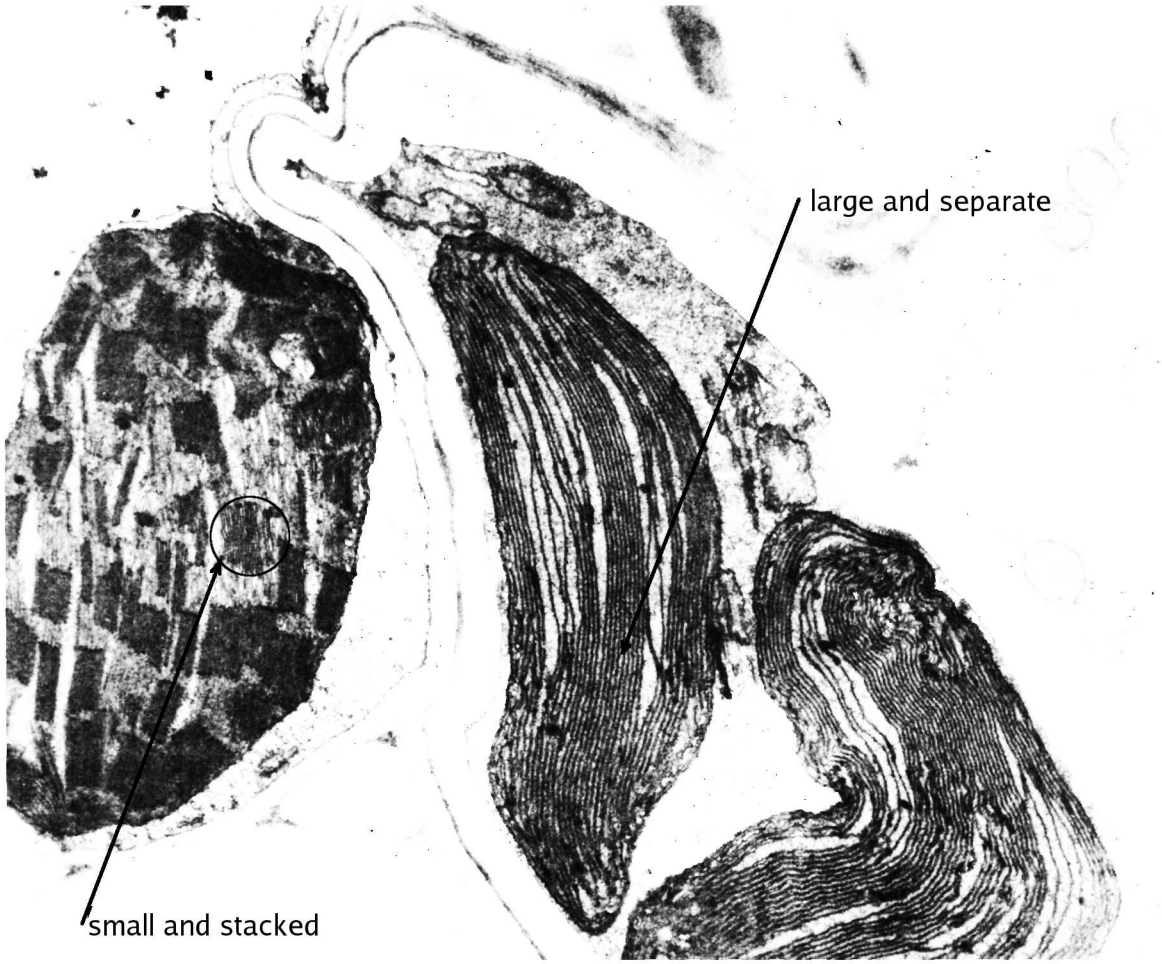

Figure 5.1 — Thylakoid size and shape variation: small and stacked *vs.* large and separate.

Section of sugar cane leaf showing bundle sheath chloroplast (right) and mesophyll cell chloroplast (left). In mesophyll chloroplast note abundance of small, closely-stacked thylakoids. (From fig. 14-7 of Devlin and Witham (1983))

5.2.1 Detailed Thylakoid Structure

The structure of one thylakoid membrane complex is depicted in fig. 5.2. This shows how the thylakoids in higher plants tend to associate into stacks of closely-separated thin disks. There are also portions that are not stacked. Each complex is one closed membrane that is highly folded to produce this structure.

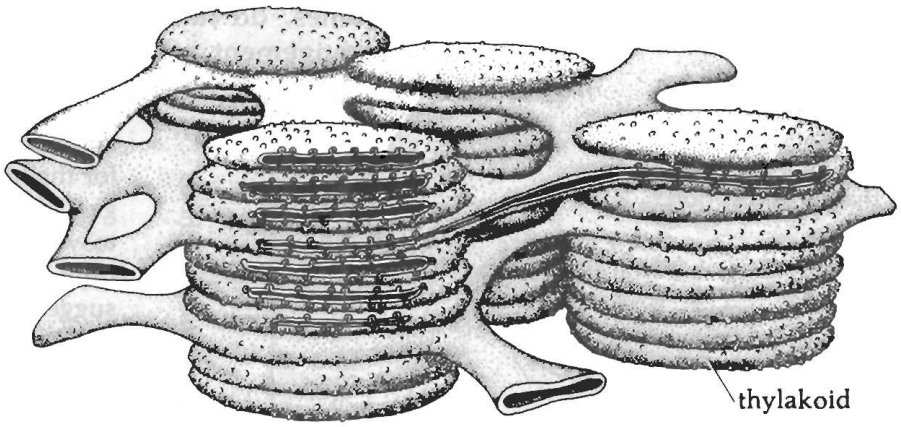

Figure 5.2 — Stacked thylakoid membranes with membrane-bound pigment complexes indicated. (From fig. 12-8 of Devlin and Witham (1983))

It has been determined that these membranes contain the chlorophyll and other molecules that are associated with light harvesting. There is a complex organization of these molecules, with two different complexes that are responsible for the terminal absorption event in photosynthesis. Briefly, a specialized chlorophyll molecular complex is surrounded by several hundred chlorophyll molecules that are termed antennae chlorophyll. There are many such complexes on the surface of each thylakoid disk. These chlorophyll are responsible for the primary absorption of photons, with the energy being transferred from molecule-to-molecule by resonance transfer until being absorbed by the terminal complex. (See fig. 5.3.)

Each terminal complex then catalyzes a charge separation which fixes the energy absorbed into chemical energy. From there, the charge separation drives other reac-

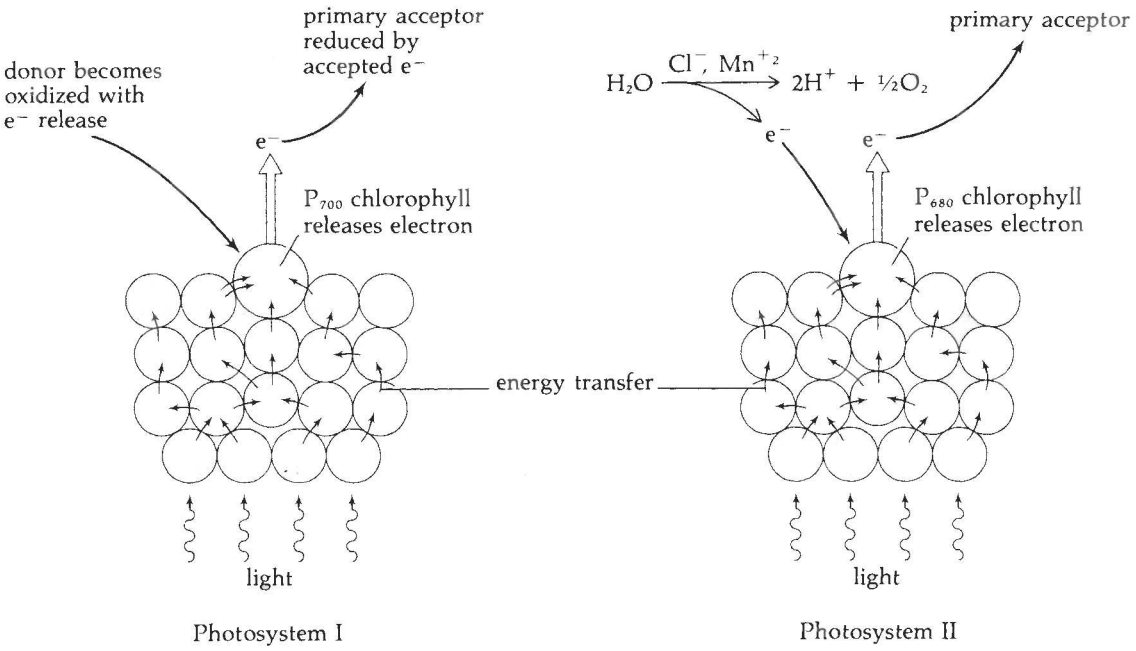

Figure 5.3 — Antennae chlorophyll, resonance energy transfer between them, and associated photosystems of the primary light-harvesting reactions. (From fig. 13-7 of Devlin and Witham (1983))

Each photosystem complex is one of hundreds embedded in each thylakoid membrane disk.

---

tions with the final product being energized molecules such as ATP and NADPH. These molecules are used throughout the rest of the chloroplast to synthesize complex sugars, such as glucose, for energy storage.

The terminal complexes of chlorophyll come in two varieties, called PSI and PSII, for PhotoSystem I and II. Each has a different absorption peak, and so absorbs photons from a different frequency band. Each also has different catalytic reactions associated with it for the production of the molecules with high-energy phosphate bonds. In particular, PSI is associated with the production of NADPH and PSII with the production of ATP. (See fig. 5.4.)

Recently, the reason for *two* photosystems was discovered and much detail is

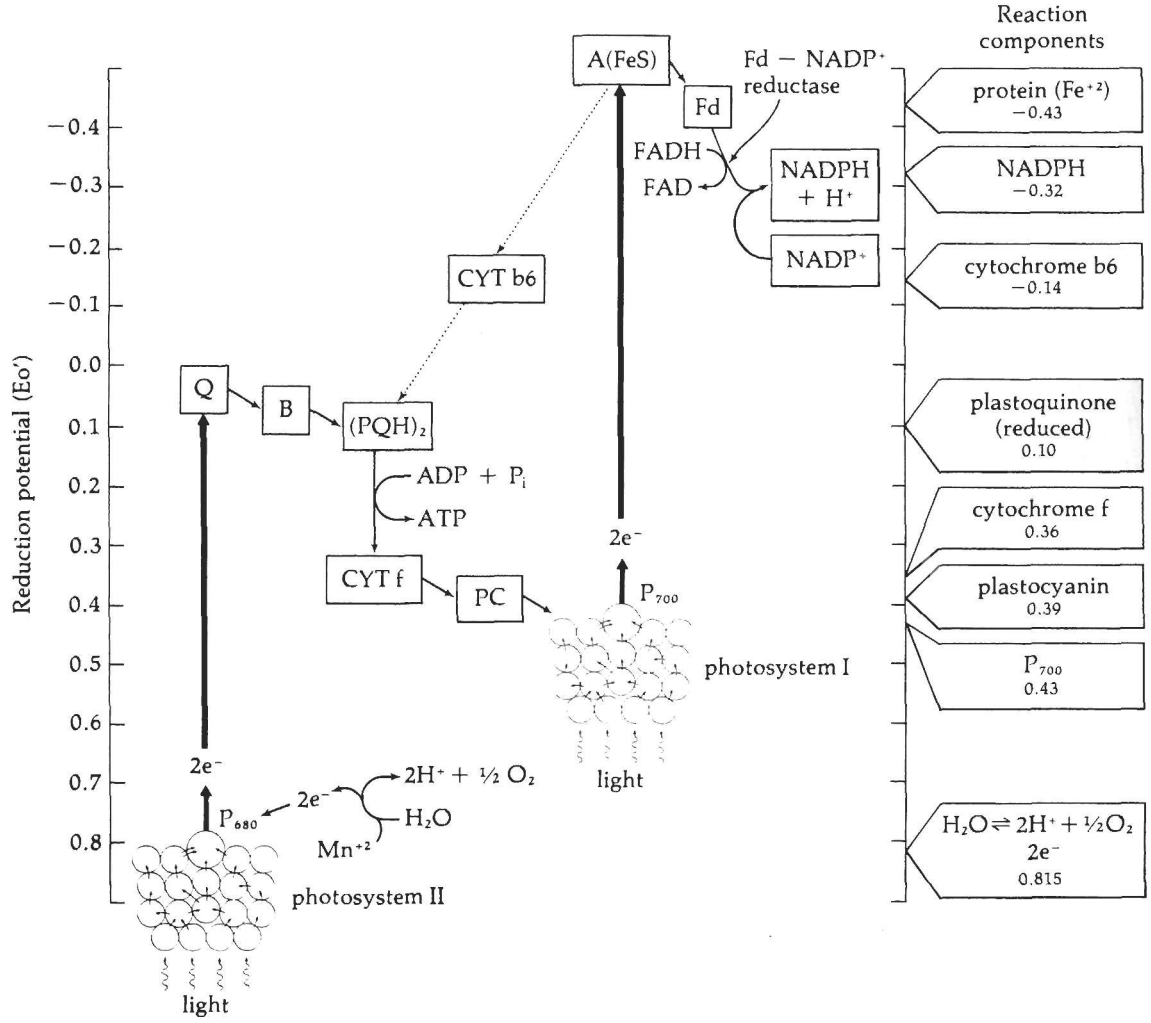

Figure 5.4 — Detailed reaction scheme of molecules associated with the primary light-harvesting reactions. (From fig. 13-12 of Devlin and Witham (1983))

now known. The photosystems are linked, as seen in fig. 5.4, and so through the differential regulation of each the entire process can be controlled. Specifically, plants can regulate the amount of photons being channeled to each photosytem on a time scale of minutes, and so control the absorption spectrum of the leaf as a whole. This rapid control mechanism allows plants to adapt to constantly changing conditions of lighting without sacrificing efficiency.

One major function of the stacking of the thylakoids has been determined to be this regulation of input photon energy to the two systems. By shuffling the

photosystem molecules around, and hence unstacking slightly, this balance can be altered dramatically. In particular, the PSI molecules are in the majority in regions of the thylakoid membranes that are exposed directly to the internal fluid of the chloroplast. In contrast, the PSII molecules are almost exclusively associated with membrane regions that are adjacent to one another. Since this chapter is concerned with the stacked membranes, PSII will be the focus of interest here.

5.2.2 The Variety of Plant Metabolisms

Another major variation among plants is that of the primary plant metabolism. The molecules associated with carbon dioxide fixation are different and, ultimately, the reactions involved are different. Three main categories exist, termed C3, C4, and CAM metabolisms. Most house plants are a common example of C3 plants, which need lots of water and varying amounts of light. Corn is representative of C4 plants, growing in semi-arid conditions, and bright light. A well-known CAM plant is a cactus, which is adapted to life with very little water and high-intensity light. In fact, CAM plants close their stomata during the daylight hours to conserve water. This leads to different cycles during the night and day: C4 at night, and C3 during the day.

Besides these macroscopic differences, there are differences in microscopic architecture as well. In particular, C4 plants tend to have thylakoids with large stacks and small disk-widths, while C3 plants have more thylakoid stacks, with much wider disks. In relation to the work here, it appears that C4 plants have stacks that can be approximated as Rayleigh, while C3 plants have larger disks that are too wide to be treated with the Rayleigh approximation.

5.2.3 Pertinent Unknowns

1. Detailed chemical makeup of fluids inside and outside the thylakoids is unknown.

[C.F. Yocum, personal communication] * Hence: no optical properties available.

2. Optical properties of chlorophyll are known, but only *in vitro,* in artificial solvents. How close to *in vivo* is it?
3. There are no appropriate absorption measurements on bare thylakoids that could verify this theory. [C.F. Yocum, personal communication]
4. There is no detailed survey of thylakoid size and shape across C3/C4/CAM plants.

5.3 Modeling

The true state of the absorption process *in vivo* is far too complicated to simulate here. This section presents an overview of all the major attributes involved in the real situation, and describes the approximations used to make the problem tractable by the present methods.

There is a tremendous amount of variability in nature. The photosynthetic apparatus is no exception. The size, shape, and chemical makeup of the chloroplasts and thylakoid membranes is highly variable from species-to-species and even from cell-to-cell within the same plant.

5.3.1 Size

The characteristic size of stacked thylakoids is determined by the diameter of the individual disks of the thylakoid membrane complex. (Because the stack is not usually taller than the disk diameter.) The size used here is assumed to be less than about 100 nm, the typical size of a thylakoid from a corn mesophyll chloroplast. This is not typical, as there is no "typical," but was chosen because it was small enough to apply Rayleigh theory.

---

* C. F. Yokum: Professor and Dept. Head, Dept. of Biological Sciences, University of Michigan, Ann Arbor.

5.3.2 Shape

One shape of thylakoid membrane is used in this model. It is an "average" of corn, spinach, and tobacco thylakoids found in the literature.

5.3.3 Chemistry

The chemical makeup is quite heterogeneous. Only one absorption spectrum was chosen here (chlorophyll *a,* in ether) because chlorophyll *a* is common and gives an approximate behavior that is typical. The detailed spectrum is quite complicated and it was felt that such detail was unnecessary to demonstrate the enhanced absorption idea. The *in vivo* absorption spectrum of chlorophyll is expected to be different, but has not been measured accurately. Hence, due to lack of alternative data, this complication will be ignored here.

The chemical makeup of the fluids that are interior and exterior to the thylakoid membranes is largely unknown. Hence, there is no way to accurately account for it. The assumption is that in the visible region the main interaction of light is carried out by the chlorophyll molecules. (This is justified in sec. 5.3.4 where the absorption in a significant region of the visible spectrum is very large.) Hence, the importance of the remaining material may be minimal. If the dielectric model is accurate this is a very good approximation, since the chlorophyll model gives very large (and negative) dielectric constants throughout a significant portion of the visible region. This kind of behavior minimizes the medium effects because of the tremendous absorption by the chlorophyll dielectric layer.

5.3.4 Approximate Dielectric Constant

This part presents the model used to simulate the effects of chlorophyll on the absorption. The numerical simulation uses thin disks of uniform dielectric constant throughout. The model presented here gives the dielectric constant of the layer of chlorophyll within each thylakoid membrane, based on the measured absorption

spectra of a chlorophyll suspension in ether. Hence, the validity of using a disk of uniform composition to simulate each of the real disks which are non-uniform is based on the plausible assumption that this outer layer absorbs most of the radiation, and each disk therefore appears impenetrable, similar to a conductor. This assumption is plausible because within the visible range the chlorophyll is a strong absorber and is likely to be responsible for the majority of the absorption. That the dielectric constant so calculated does indeed show the expected behavior over a significant portion of the visible spectrum justifies this assumption.

The model is based on the idea that the dielectric constant is largely due to the induced dipole moment for each molecule, as a function of frequency. The strength of the dipole is used along with the number density of the molecule in question to give an induced polarization field, which is directly related to the dielectric constant. This is essentially the Lorentz model presented in sec. 3.1. The only difference here is the determination of the induced dipole in the molecule. This is the critical step.

Given an absorption spectrum of chlorophyll *a,* appropriate parameters may be measured and then used in a general formula derived in Jackson (1975) (eqn 17.70), for the total (scattering plus absorption) cross section of a molecular dipole:

$$\sigma_t(\omega) = 6\pi\lambda\!\!\!^{-2}_0 \frac{\omega^2\Gamma\Gamma_t}{(\omega_0^2-\omega^2)^2+\omega^2\Gamma_t^2} \tag{5.1}$$

where $\lambda\!\!\!^{-}_0 = \lambda_0/2\pi$; λ_0, ω_0 are the center of the absorption peak; Γ_t is the total width (rad/sec) at half maximum of the peak; and Γ is related to the re-radiation lifetime, with $\Gamma \ll \Gamma_t$ for a good absorber.

All parameters are easily obtained from an absorption curve. Because chlorophyll *a* has two major absorption peaks in the visible region, the simulation required the addition of two terms, one for each peak.

The numbers so determined are shown in table 5.1. The comparison of the modeled absorption spectrum with that measured for Chlorophyll *a* in ether is

shown in fig. 5.5. Note that in this figure the extinction coefficient, ε, is defined by:

$$\log_{10}\left(\frac{I_0}{I}\right) = \varepsilon C \ell \tag{5.2}$$

where I_0 is the intensity incident on the sample, I is the intensity measured by the spectrometer after passing through the sample, C is the concentration of chlorophyll molecules in the liquid, and ℓ is the path length of the light beam through the sample. The relationship between σ_t and ε is obtained using the idea that σ_t represents the portion of a light beam that is occluded by the presence of one molecule. This gives:

$$\log_{10}\left(\frac{I_0}{I_0\left\{1 - 1.602 \times 10^{23} \text{ molecules/mole } C(\text{moles/liter}) \; \ell \; \sigma_t\right\}}\right) = \varepsilon C \ell \tag{5.3}$$

Table 5.1 — Model parameters for Chlorophyll *a* absorption spectrum in ether

	ω_0	Γ_t	Γ
low-λ peak	4.373×10^{15} rad/sec	1.8×10^{14} sec^{-1}	2.403×10^{10} sec^{-1}
hi-λ peak	2.839×10^{15} rad/sec	6.45×10^{13} sec^{-1}	2.836×10^{9} sec^{-1}

The determination of the dielectric constant from this absorption spectrum is carried out next. From Jackson (1975), the absorption due to a dipole, $\mathbf{p}$,

$$\mathbf{p} = \alpha(\omega)\mathbf{E}_0 e^{-i\omega t} \tag{5.4}$$

is

$$\sigma_t(\omega) = 4\pi\frac{\omega}{c}\text{Im.}\alpha(\omega) \tag{5.5}$$

Equating this and the model for absorption yields:

$$\text{Im.}\alpha(\omega) = \frac{3}{2}c^3\sum_{i=1}^{2}\frac{\omega}{\omega_{0i}^2}\frac{\Gamma_i\Gamma_{ti}}{(\omega_{0i}^2 - \omega^2)^2 + \omega^2\Gamma_{ti}^2} \tag{5.6}$$

where $i = 1, 2$ corresponds to the two different peaks in the absorption spectrum of chlorophyll *a*. As in chapter 3, this leads to the imaginary part of the dielectric constant:

$$\epsilon_r'' = 4\pi N\text{Im.}\alpha(\omega) \tag{5.7}$$

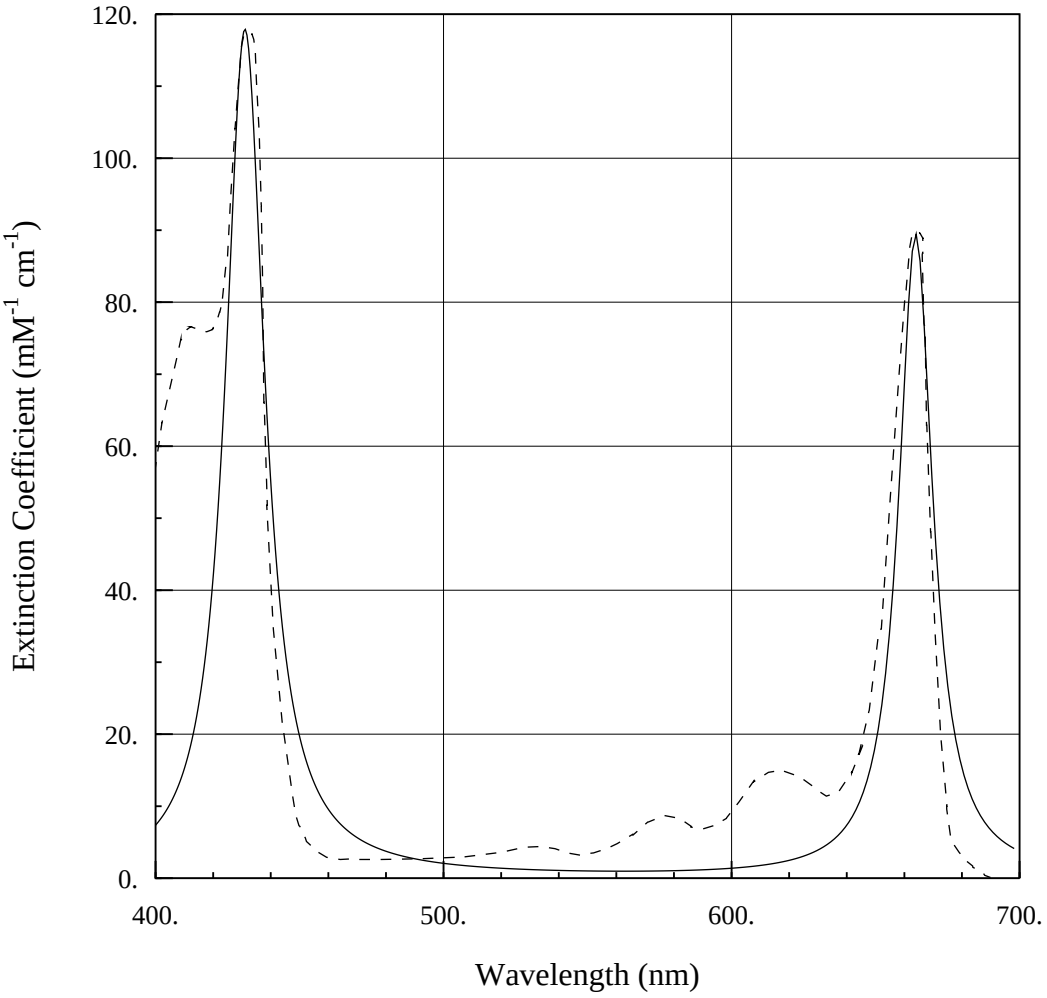

Figure 5.5 — Comparison of measured (– –) and modeled (——) absorption for chlorophyll *a* in ether. Measured data from Clayton (1965).

where N is the number density of chlorophyll molecules in the thylakoid membranes. Note that this is in the same form as the Lorentz model result (eqs 3.4–3.6). Hence it immediately follows that

$$\epsilon_r'' = \sum_{i=1}^{2} \frac{\omega_{pi}^2 \, \Gamma_{ti} \, \omega}{(\omega_{0i}^2 - \omega^2)^2 + \omega^2 \, \Gamma_{ti}^2} \tag{5.8}$$

giving the real part:

$$\epsilon_r' = 1 + \sum_{i=1}^{2} \frac{\omega_{pi}^2(\omega_{0i}^2 - \omega^2)}{(\omega_{0i}^2 - \omega^2)^2 + \omega^2\Gamma_{ti}^2} \tag{5.9}$$

where

$$\omega_{pi}^2 = \frac{6\pi N c^3 \Gamma_i}{\omega_{0i}^2} \tag{5.10}$$

The only new parameter to determine here is the number density of the chlorophyll molecules. In particular, the density on the internal faces of the thylakoid membrane stacks is the parameter of interest, as that is where the PSII complexes appear. The density was estimated as follows: the number of particles on a stacked thylakoid membrane surface (seen using freeze-fracture techniques as in fig. 2b, Giddings, *et al.* (1980)) was counted in a small region. The identity of these particles is still debatable. The number density of these particles is approximately 2.87×10^{25} particles/m^3. If they are assumed to be PSII complexes, with about 300 chlorophyll molecules per particle (Hipkins and Baker (1986), sec. 1.3.1), then a density of

$$N = 8.6 \times 10^{27} \text{chlorophyll molecules/m}^3 \tag{5.11}$$

is obtained, since the thickness of the membrane is on the order of 1 Å. If these particles are not PSII complexes, there is a different number of chlorophyll molecules per particle. However, at the present time, the best guess is that they are PSII complexes (Staehelin (1983)).

However, because of this imprecise value for N, it is best to allow for a large variation from the value given here. Hence, a variation of an order of magnitude was allowed for, each way.

The real part of the modeled dielectric constant is shown in figure 5.6. The different curves are for different values of N. Note that there are regions where the real part of the dielectric constant is negative. The imaginary part of the modeled dielectric constant is shown in figure 5.7. The portion of the spectrum where the real part is negative and the imaginary part is small is where resonant absorption

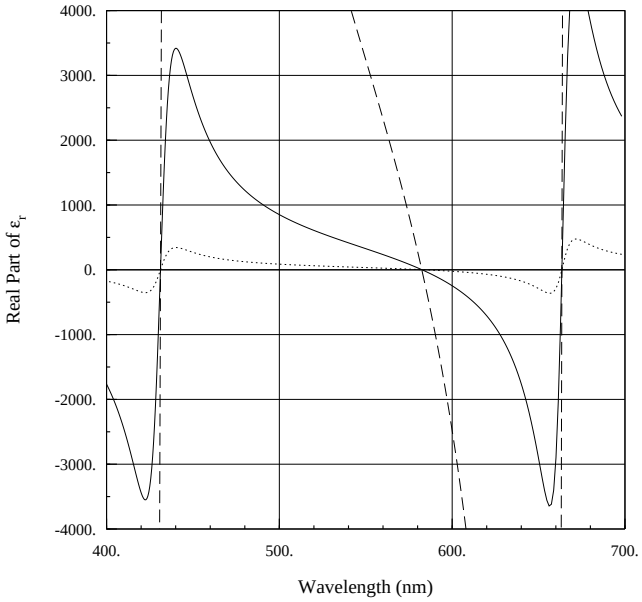

Figure 5.6 — Calculated real part of dielectric constant for a layer of chlorophyll molecules on a stacked thylakoid membrane.

(——— $N = 8.6 \times 10^{27}$; — — — $N \times 10$; · · · $N/10$.)

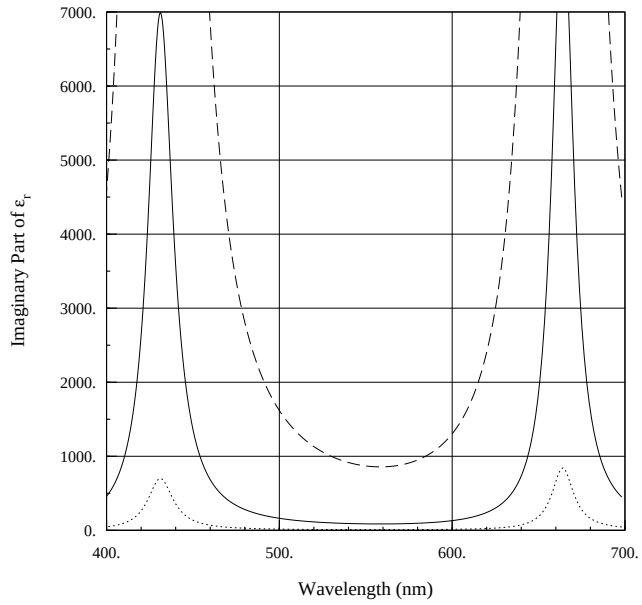

Figure 5.7 — Calculated imaginary part of dielectric constant for a layer of chlorophyll molecules on a stacked thylakoid membrane.

(——— $N = 8.6 \times 10^{27}$; — — — $N \times 10$; · · · $N/10$.)

could occur. It is possible that an accurate dielectric model is best given with the smaller N value. In that case, the losses in the absorption band (580–620 nm) are much smaller and so the resonance would be much more pronounced than for the value of N given here.

5.4 Numerical Results

5.4.1 The Numerical Procedure

The numerical procedure described in sections 2.1 through 2.4 of this thesis was used here. Note that the resonant epsilons were the desired results, rather than the absorption spectra. This was to see if the resonances occured at large negative values, as was thought, and if so, just how large. The strength of the resonances was used as an indicator of their importance to the overall response of the particle, as has been done throughout the rest of this thesis. This is analogous to a coupling coefficient.

5.4.2 The Cases Studied

The cases studied here include thin disks with an aspect ratio of 23:1, that are not stacked, or are stacked in 3, 5 or 7 layers, with a layer spacing of one-tenth of the disk thickness. This geometry was selected as an accurate model of the stacked portion of an "average" thylakoid membrane. As mentioned before, the membrane thickness is ignored since the actual thickness is less than 1 Å, much less than the disk thickness. The number of membranes in a stack varies from species-to-species, ranging from 1 for some algae up to 100 for many plants.

Since the interest is in the resonance positions, ϵ_r, no fixed relative permittivity need be provided to the program. (Recall that this is the eigenvalue problem, and the eigenvalues are related to the resonant epsilons.) For the numerical integration, the number of segments that the membrane is divided into is 100 along the flat part, and 30 along the circular end-cap. A semicircular end-cap was chosen as a good

approximation to a real membrane as well as to avoid any resonances that could be introduced by using a square-cut end-cap. Figure 5.8 sketches the geometry used. The major resonances and their strengths are determined as a function of geometry in the next section.

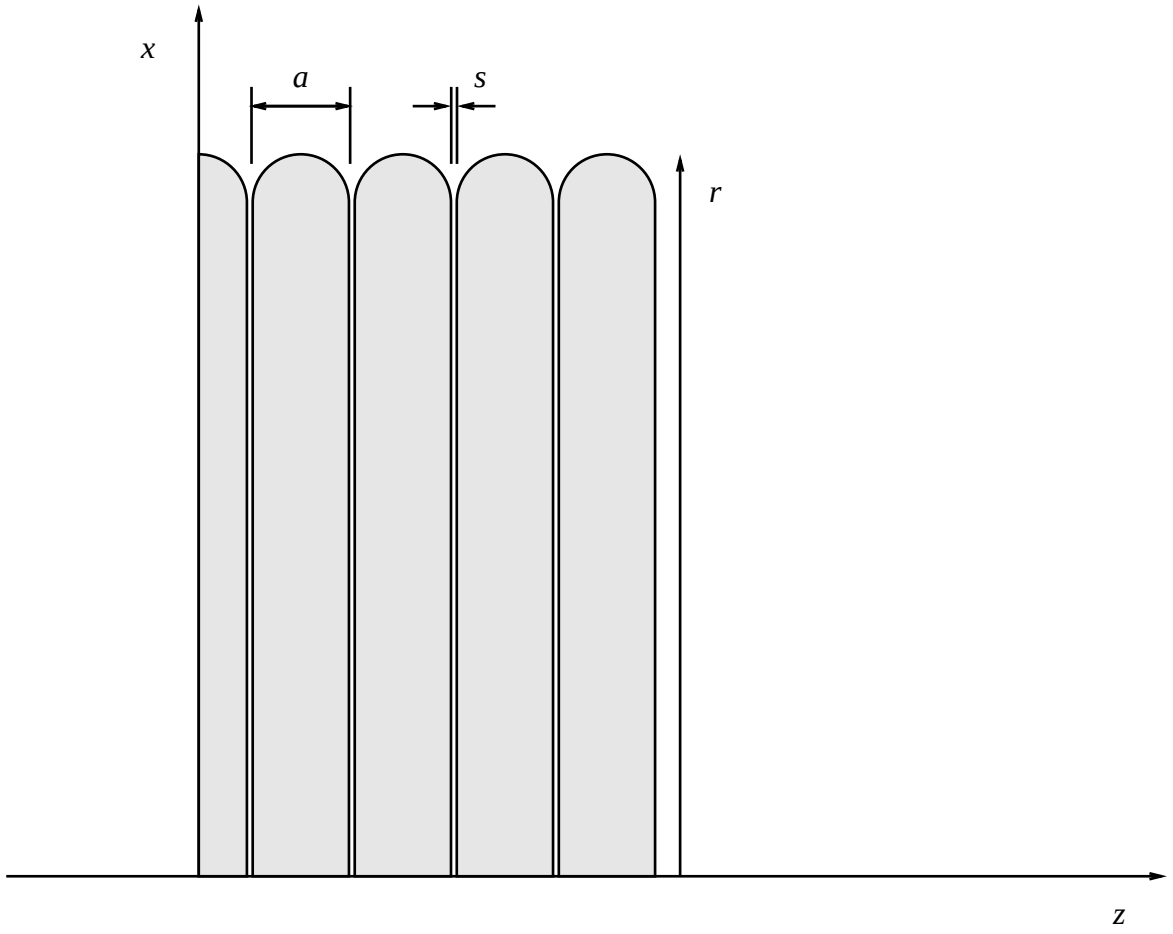

Figure 5.8 — Schematic diagram of Thylakoid membrane geometry simulated with thin disks.

Dimensions for the "average" corn thylakoids were determined to be: $a = 7.25$ nm, $s = 0.75$ nm, and $r = 50$ nm. The simulation done here used: $a = 1$, $s = 0.1$, and $r = 11.5$.

5.4.3 Results

Figure 5.9 shows a detailed picture of the stacked-disk geometry in relation to the incident fields.

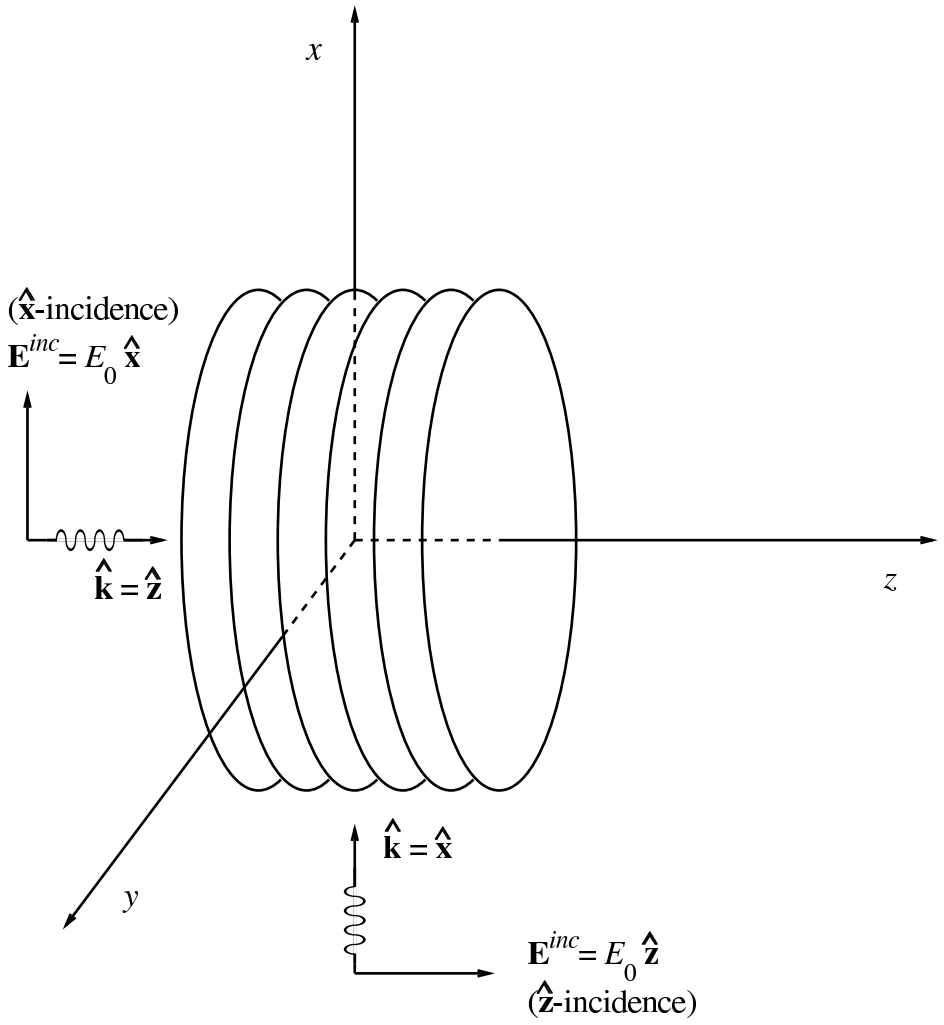

Figure 5.9 — Incident fields in relation to the stacked disks.

The major resonances and their strengths are shown in the following 4 tables. The strengths are listed to show which resonances make the greatest contribution to the total field for a particular incident field. The single disk is shown in table 5.2. Tables 5.3 through 5.5 show the resonances for various stacking configurations:

1, 3, 5, and 7 disks, respectively. The strength is the magnitude of the imaginary part of the appropriate polarizability tensor element. (As in the other chapters of this thesis, for $\hat{\mathbf{x}}$-incidence use P_{11}, and for $\hat{\mathbf{z}}$-incidence use P_{33}.) The change in the major resonances as more disks are stacked is shown in fig. 5.10.

The results show that the $\hat{\mathbf{x}}$-incidence resonances for stacked disks are far larger in their effect on the total field because their strengths are 10–100 times that of the most resonant $\hat{\mathbf{z}}$-incidence resonance. This disparity tends to increase as more disks are added: from 113 times with 3 stacked disks, to 63 times with 5 stacked disks, to 175 times with 7 stacked disks. The positions of the resonances, while not monotonic, still show a distinct and dramatic rise to values in the negative 100's when the disks are stacked.

Table 5.2 — Resonances for single disk.

(Values of $Re.\{\epsilon_r\}$, with $Im.\{\epsilon_r\} = 0$, at which the absorption is infinite.)

$\hat{\mathbf{x}}$-inc	$\hat{\mathbf{z}}$-inc	strength
-1.989		1018
	-2.074	250
	-0.848	107
	-0.997	102

Table 5.3 — Resonances for 3 stacked disks.

(Values of $Re.\{\epsilon_r\}$, with $Im.\{\epsilon_r\} = 0$, at which the absorption is infinite.)

$\hat{\mathbf{x}}$-inc	$\hat{\mathbf{z}}$-inc	strength
-370.25		177648
-68.6		3513
	-118.5	1582
	-45.4	216

Table 5.4 — Resonances for 5 stacked disks.

(Values of $Re.\{\epsilon_r\}$, with $Im.\{\epsilon_r\} = 0$, at which the absorption is infinite.)

$\hat{\mathbf{x}}$-inc	$\hat{\mathbf{z}}$-inc	strength
-161.8		56542
-127.75		2641
-37.4		1170
	-59.5	892
	-243.6	142

Table 5.5 — Resonances for 7 stacked disks.

(Values of $Re.\{\epsilon_r\}$, with $Im.\{\epsilon_r\} = 0$, at which the absorption is infinite.)

$\hat{\mathbf{x}}$-inc	$\hat{\mathbf{z}}$-inc	strength
-97.8		28275
-82.2		3601
	-294.8	163
	-153.0	122

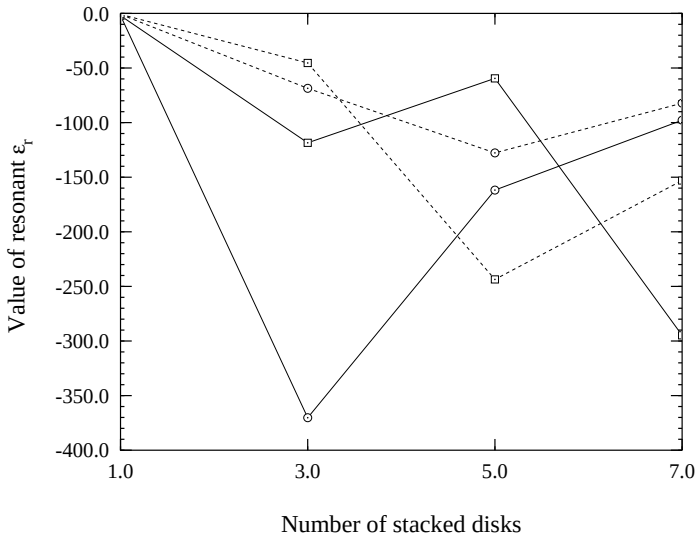

Figure 5.10 — Variation of major resonances for stacked disks.

Major resonances (——) and minor resonances (– –) are shown for both $\hat{\mathbf{x}}$-incidence (⊙) and for $\hat{\mathbf{z}}$-incidence (⊡).

To compare the absorption characteristics of the stacked and unstacked disks it is sufficient to compare the polarizability tensor elements, suitably scaled. In fig. 5.10 the absorption of three stacked disks is compared to that of a single disk, with the absorption scaled to be on a per chlorophyll molecule basis, which is the same as a per unit area of thylakoid membrane, since we are assuming a uniform distribution of chlorophyll molecules. As expected from the resonance positions and strengths, the $\hat{\mathbf{x}}$-incident absorption enhancement is much larger than in the $\hat{\mathbf{z}}$-incident case. Note the absorption enhancement in the two absorption bands: $\hat{\mathbf{z}}$-incidence enhancement of 250 at about 430 nm, and $\hat{\mathbf{x}}$-incidence enhancement of 2000 at about 610 nm. Also note the $\hat{\mathbf{z}}$-incidence enhancement of 500 at about 670 nm. This is *not* at an expected absorption band.

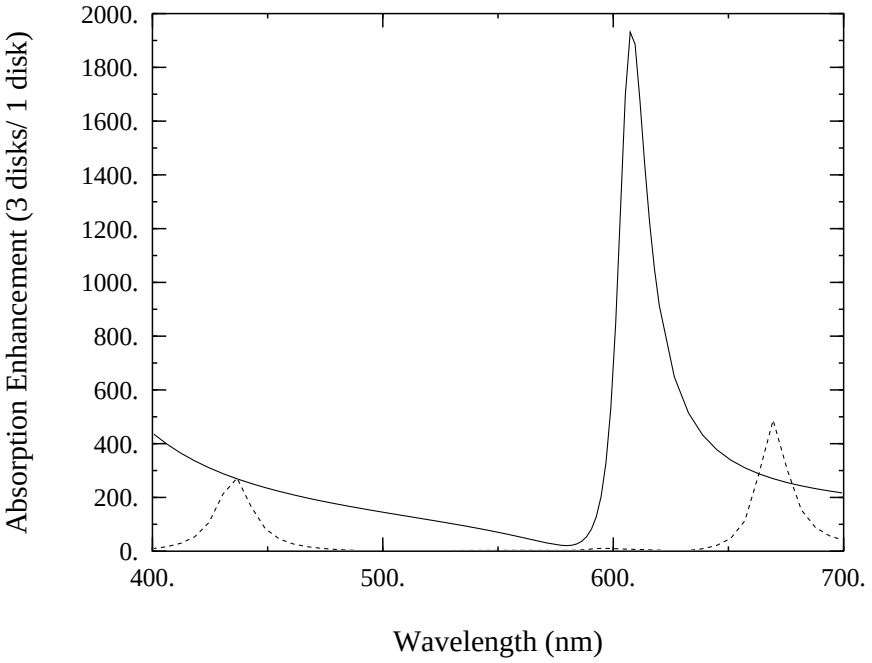

Figure 5.11 — Calculated absorption enhancement of 3 stacked disks over that of 1 disk, normalized to thylakoid surface area. (——– $\hat{\mathbf{x}}$-inc.; – – – $\hat{\mathbf{z}}$-inc.)

5.5 Interpretation

The results presented in the previous section show that the electromagnetic behavior of the stacked thin disks is drastically different than that for the single thin disks. In particular, the values for the most influential resonant epsilons (those with the largest influence on the total field) are on the order of 100 times larger for stacked disks than for single disks. Applied to photosynthesis, via the dielectric model presented in sec. 5.3, this means that in the spectral band where the modeled dielectric constant has a large negative real part and a small imaginary part (approx. 580 nm to 620 nm in figs. 5.6 and 5.7) the absorption is expected to be much larger for the stacked thylakoids than for the unstacked ones. Hence, if this enhanced absorption can be utilized by the cell, then this would be a worthwhile adaptation, one that would likely be conserved through the evolutionary process. That is the hypothesis put forward here.

Note that the absorption spectra of actual stacked disks of chlorophyll have not been presented in fig. 5.11, only the enhancement due to stacking. The main reason for this is that the calculated absorption spectra would be misleading, especially if thought of as something one could expect to measure. There are a number of reasons for this. One reason is that because there is such a great variety of pigments on a plant thylakoid, other than chlorophyll *a,* the true absorption spectrum for the thylakoid would have to account for these as well. Another reason is that the calculated ϵ_r'' in the region where $\epsilon_r' < 0$, near 600 nm, is quite large, on the order of 50–100. This is so large that resonance absorportion would be very small there, because the resonance is effectively damped by the losses. If the actual ϵ_r'' is as large as that calculated here, then resonant absorption is probably not happening in thylakoids. However, the calculation of ϵ_r was approximate at best, and so it it is still quite possible that a resonance absorption occurs. The main result of my estimation of ϵ_r is that the real part goes negative, and does so at a higher frequency

(energy) than the PSII trap, hence allowing the absorbed photons to feed energy to the PSII complex.

A note concerning the incident field polarization is in order here. Because the $\hat{\mathbf{x}}$-incident resonances are on the order of $100\times$ the strength of the $\hat{\mathbf{z}}$-incident resonances, one would expect that the thylakoids could make better use of the partially-polarized sunlight by orienting their stacked thylakoids appropriately. A reorientation effect has in fact been observed in some algae when exposed to bright light: they present their thylakoids edge-on to the propagation direction of the light. This is probably a simple "intercept less light" approach, however it makes the concept of thylakoids rotating to better capture (or avoid) light much more plausible. Which leads to the next idea. It is not unreasonable to suspect that the direction-specific resonance is taken advantage of by plants, by light-intensity-induced rotation of thylakoids. This has proved difficult to measure in plants [C.F. Yocum, personal communication]. However, Kiss, *et al.* (1986) show that corn mesophyll chloroplasts (*in vitro*) are very easily reoriented (a smaller applied field for same amount of reorienting) in a magnetic field compared to other species. While this shows nothing about what happens *in vivo,* the implication is clear, especially knowing that natural sunlight is slightly polarized, that plants could take advantage of this and reorient their stacked thylakoids in response to variable natural lighting conditions.

One implication of this is that the resonant absorption may be used as a method to *increase* the absorption when there is little light and to *decrease* the absorption when there is too much. This could be thought of as a replacement for what the algae can do with their single disk (avoiding intercepting the sunlight (edge-on), or intercepting all of it (face-on)), but which the plants cannot do with their stacked disks. The stacked architecture of plant thylakoids means that there is no edge-on because even when one disk of the stack is edge-on, the stack as a whole does not

really have an edge, and so the absorption cannot be affected significantly by such geometrical considerations alone. That some plants (in particular corn) can use this resonance to enhance or attenuate their light absorption could explain why they do better in bright light. It is therefore likely that the resonance is used to increase the dynamic range of illumination levels that are both bearable and useable to the plant. This would quite effectively widen its niche in the environment and so would tend to be conserved by evolution.

However, despite the fact that most plants have stacked thylakoids, there is still tremendous variety in the details of their arrangement, size, and metabolism between different species. This is not the place for an exhaustive survey of this, but as an example consider corn and spinach. Corn has thick, tough leaves while spinach has thin delicate ones. Corn uses C4 metabolism while spinach uses C3. Corn has 100 nm-wide disks in the thylakoids of its leaf mesophyll cells, while spinach leaf cell thylakoids have 300 nm-wide disks. Hence, corn thylakoid stacks are Rayleigh for incident wavelengths greater than 500 nm or so (yellow and red light), while spinach thylakoids aren't Rayleigh in the visible; they are too big.

The implication is that corn has evolved to use this enhanced absorption feature, whereas spinach has not. An inference one could draw from this, yet to be confirmed, is that C4 plants, like corn, have evolved in their different niches and taken advantage of this feature of stacked thylakoids. In support of this is the fact that the efficiency of photosynthesis in bright-light C4 plants is monotonically increasing with brightness up to the brightest possible light from the sun, while that of C3 (average light) plants falls off before that and they suffer from other ailments at such high light levels (Devlin and Witham(1983)). The task of confirming this hypothesis would be more appropriate for a biochemist or a botanist already familiar with these plants and their variations.

5.6 Needed Biological Work

Because of the speculative nature of this chapter, this section on future validation experiments is included. The hope is that these suggested experiments give the biological researcher a solid base with which to validate the claims in this chapter. The most basic experiment which concerns the fundamental idea of this chapter is to determine if the stacked thylakoids absorb more than unstacked ones. Obtaining "free" thylakoids is a solved problem, and so will not be treated in any detail here. See Hipkins and Baker (1986) for an excellent treatment of the standard techniques used in photosynthesis research. Once free thylakoids are obtained, there is a known mixture whose addition to the thylakoid suspension is known to induce unstacking (Staehelin (1980)). Also, the spectroscopy is relatively straightforward, other than the constraint that the solution be illuminated with real or simulated sunlight, as the process of photosynthesis can work in quite a different manner when illuminated with different spectra. The absorption spectra obtained must be generated using a bandpass filter at the detector. Lastly, to avoid multiple scattering, the solution must be relatively dilute. Just how dilute would be for the experimenter to determine. The experiment would proceed as follows:

1. Separate the chloroplasts from maize mesophyll cells.
2. Rupture the chloroplasts. Remove the thylakoids and the intercellular fluid (cytoplasm), and put into the test cells used for spectroscopy. Since the cytoplasm should be used for dilution, extra portions of it should be gathered.
3. With white light illumination, measure absorption spectra of the thylakoid/cytoplasm mixture at various concentrations. Find a concentration where multiple scattering is minimal by continually diluting with cytoplasm and remeasuring the spectrum until the *shape* of the absorption spectrum ceases to change appreciably. This is where the nearest-neighbor interactions (between different groups of stacked thylakoids) have ceased to play a role in the absorption process.

4. Next add the "unstacking" mixture so that the resultant concentration of thylakoids is known. Measure the absorption spectrum as before, as a function of elapsed time since initiating the unstacking reaction. When it stops changing, it is probably unstacked as far as possible.
5. Make sure the solutions in 3 and 4 were what was wanted: use portions of each and perform other tests to observe the number density and percent stacked vs. unstacked, and the like. Some iteration through the above steps may be necessary to get pure samples of stacked and unstacked membranes with few impurities such as broken thylakoids, broken chloroplast envelopes, stacked thylakoids in the unstacked solution, etc.
6. Compare absorption spectra normalized to the concentration of chlorophyll, of stacked disks vs. unstacked disks. Hopefully there is enhanced absorption in the stacked thylakoids in some band near 600 nm.

A complication to the above experiment is that the distribution of PSI and PSII complexes over the membranes changes when they are unstacked. This causes a change in the absorption spectrum all by itself, but the extent of this change is not known quantitatively. A possible way to avoid this redistribution of photosystems is to freeze the membranes from the very start (just after step 2, above). Then the unstacking may not result in photosystem redistribution if the experiment is carried out quickly. This is because the redistribution is enabled by diffusion, which is highly temperature-dependent. But only the experiment will be able to verify this; apparently no one has yet done unstacking without the concomitant photosystem redistribution.

If this fundamental experiment shows enhanced absorption for stacked thylakoids at all, then more detailed experiments can be done to further quantify the effect:

1. Find the optical dielectric constants of fluid media inside and outside thylakoids.

2. With one unstacked thylakoid, try to get it to be flat. This may require charging the outside of the membrane to inhibit folding by causing repulsion between different parts of itself. Find the apparent optical dielectric constant of the thin disk so formed by modeling it as a coated thin disk.
3. Explore the effect of PSI/PSII distribution on apparent optical dielectric constant. Freeze the stacked thylakoids, if that has been shown to work in the past. Possibly experiment with adding other large molecules to the solution which could mimic the interactions that cause the PSI/PSII segregation *in vivo*.
4. Try to orient the stacks and look at absorption as a function of incident polarization.
5. Explore the effect of the incident spectrum on the apparent optical dielectric constant. This would apply to leaves shaded by other leaves in a canopy.
6. Try all this with spinach leaves, and see if there is any kind of enhancement.
7. Try all sorts of other plants, in particular a CAM plant, and see what happens.
8. Figure out an easy way to monitor the amount of stacking and the width of the disks. Vary amount and spectrum of incident light and see how these two very important parameters vary with time. Since other changes can vary on time scales of days, hours, or minutes, this may vary on any of those time scales, hence the need for a convenient assay. Possibly, the resonant epsilons could play a part here, using a low intensity tunable laser to probe for shape, but only as long as the particles remained small enough to be approximated with Rayleigh theory.

5.7 Conclusions

This chapter has shown that the resonances of thin stacked disks probably play a role in the absorption of light by plants with small thylakoid disks, very likely the C4 plants. An hypothesis for this role has been put forward, but there may be more involved than has been accounted for here, and more detailed measurements

are in order, some of which have been mentioned in the previous section. Besides the experiments, the modeling performed in this chapter could be improved in the future. In particular:

1. Refine the dielectric model to include the measured optical properties from the suggested experiments in sec. 5.6.
2. Include the effects of the thin shell in the numerical code.
3. Add a comparison with the absorption of very large thylakoid disks that cannot be approximated by Rayleigh theory. This would require a specialized code to be written.
4. Include the effects of the fluids that surround the thylakoid membranes. (Their dielectric constants.)
5. Refine the dielectric model to include contributions from other pigments in the thylakoids. Account more precisely for the variety of states that a single pigment may occupy, and hence alter its absorption characteristics.
6. Add a dynamic model to the system, so that the geometry and distribution of particles, and amount of unstacked thylakoid, etc. are accounted for by models of how they change with changing conditions, such as brightness, moisture, and incident spectrum. Track as a function of time, and compare to experiments. Are the simple models accurate?

This may be a fruitful new method to use to understand the entire process of photosynthesis. As long as the biochemical events can be modeled with macroscopic changes, then those things can be accounted for this way. The detailed biochemistry would not be an appropriate topic for this modeling, of course, but the large-scale effects would be.

In summary, an analysis new to phosynthesis research has been applied to the primary absorption event with the result that a new regulation mechanism has been postulated for stacked thylakoids of C4 plants to allow them to control the amount

of light absorbed on a short time scale, in response to changing light-intensity conditions. Whether this regulation hypothesis is correct or not, the stacked thylakoids of the C4 plants generally appear to be small enough that the absorption resonances found here should be occurring in some form. Although the ultimate use to which the plant puts this may be different than that postulated here, its occurrence is very likely. Lastly, a series of experimental steps have been outlined which could lead to confirmation of the computed resonance effects and validation of the regulation hypothesis.

CHAPTER VI

CONCLUSIONS AND FUTURE WORK

This thesis has shown several exploratory researches into the effects of the resonance absorption phenomenon in small particles. First, a computer program was written for the simulation work. The program solves the electrostatics problem, but with a complex dielectric constant corresponding to the electromagnetic wave phase propagation. This required reworking of an already-existing program; generalizing and augmenting it for irregularly-shaped particles and far more accurate integral evaluations. The program works with arbitrary rotationally-symmetric particles and groups of particles whose trace in a meridian plane can be made up of arcs and straight lines. Their maximum dimensions must also be small sompared to the free space wavelength. The program output consists of the surface potentials as well as the near and internal potentials. Another program calculates the electric field using finite differences of the potential. The polarizability tensor elements are also calculated, as well as the values of the resonances which occur in absorption regions of the bulk materials from which the particles are composed. The resonances are shape-dependent (and incidence-dependent) only, and so do not depend on the choice of a dielectric constant. The program was exhaustively checked against available theoretical formulations for special cases and was verified to within 1% of accuracy for the situations where it is used in this thesis. The results also compared well with available experimental results. This gives us confidence in our non-spherical results.

Based on the above work, a model was developed to explain the behavior of the polarizability tensor elements. The model is quite simple and does a very good job modeling the results of the research presented here. This model was published in Pierce and Weil (1990).

The absorption phenomena associated with coagulated spheres was explored in the context of explaining the dramatic color changes seen in gold colloids upon coagulation. The results of our simulations show qualitative agreement with those experimental studies. Quantitative agreement will have to wait for more extensive efforts, experimental as well as theoretical, aimed just at that. The changes in the total potential field surrounding the particle were presented in a graphic comparison of a resonant and a non-resonant case. This showed a dramatic difference in the shapes of the real part of the fields, with a major increase in the magnitude of the imaginary part of the fields, where the increased absorption is apparent. Possible fruitful future work in this area includes:

(1) Finding better ways of choosing the "major" resonances of a particle from the set of possible resonances.

(2) Understanding the near and internal electric field structure near a resonance, and subsequently exploiting that knowledge for a practical end. (For example, see the patent of L. Brus and A. Nitzan: "Chemical Processing using Electromagnetic Field Enhancement," U.S. Patent $4,481,091$.)

A study of the resoanances as a function of coagulation geometry was also undertaken. These resonances are the values of the dielectric constant that produced very large local fields. This showed that, within this family of shapes, a surface perturbation can be noted separately from the change in shape across that family. This was done with clefts in ever-wider spheres, but the suspicion is that it generalizes to other families of shapes. This observation is based on the fact that a major resonance can be dramatically affected by the clefts presence, while the change in

overall shape has a greater affect on the minor resonances, within a family of shapes. This research certainly requires more study if one wishes to apply it to real-world particles which can be quite irregular.

The study of coagulation dynamics carried out here shows a major difference in the electromagnetic-induced coagulation of small particles depending on whether or not they exhibit a resonance and if it is excited. The non-resonant particle pairs shown here rarely coagulate, merely approaching each other closely at most, while the resonant particle pairs usually coagulate, and coagulate lined up with the electric field. This aligning capability of the impressed field has been long known (Krasny-Ergen (1936)), but this is the first study of dielectric particles to show it in some detail.

Lastly, photosynthesis appears to take advantage of these resonances in the context of allowing some plants to regulate the amount of sunlight that is absorbed. Some plants do this with large disks that fall into the physical optics regime. They can either orient the large face of the disk towards the light, or not, to regulate their light absorption. Other plants, however, use many small closely-stacked disks. These plants cannot use the above mechanism of control, but since they are small the resonance phenomenon comes into play. Since the strength of the resonance depends strongly on the orientation of the disks to the incident field, perhaps these plants use this to regulate their light absorption. Much future work is necessary in this area to verify and further understand this phenomenon.

APPENDICES

APPENDIX A

DETAILS OF ROTATIONALLY-SYMMETRIC FORMULATION

This appendix gives the details for the derivation of equations (2.37) and (2.43) in section 2.2. It was felt that these details should be presented to provide more completeness to the formulation.

1. The outward normal

It is relatively straightforward to derive the general expression:

$$\hat{\mathbf{n}}' = \pm\Big(-\hat{\mathbf{z}}\sin\alpha' + \cos\alpha'[\hat{\mathbf{x}}\cos\phi' + \hat{\mathbf{y}}\sin\phi']\Big) \tag{A.1}$$

The sign, however, is not so straightforward. It is known that $\hat{\mathbf{n}}'$ must be an outward normal: from the body into the medium. But information about outside/inside is not necessarily contained in a simple $\rho(z)$ for a body. Hence $\rho(z)$ must be constrained so that this information is available from it. This is done by requiring that the body be entered as directed line segments (or arcs), such that the inside of the body is on the **right** as we trace that line segment from start to finish. This definition is a standard one in several branches of mathematics.

Hence the definition of α' is really:

$$\alpha' = \left[\tan^{-1}\left(\frac{\partial\rho'}{\partial z'}\right)\right]\,\text{sign}\left(\frac{ds}{dz}\right) \tag{A.2}$$

with the choice of the positive sign for $\hat{\mathbf{n}}'$:

$$\hat{\mathbf{n}}' = \cos\alpha'(\hat{\mathbf{x}}\cos\phi' + \hat{\mathbf{y}}\sin\phi') - \hat{\mathbf{z}}\sin\alpha' \tag{A.3}$$

2. $\nabla'\left(\frac{1}{R}\right)$:

It is known that

$$R^2 = (\rho - \rho')^2 + (z - z')^2 + 2\rho\rho'[1 - \cos(\phi - \phi')]. \tag{A.4}$$

hence:

$$\nabla'\left(\frac{1}{R}\right) = -\frac{1}{R^2}\nabla'(R) = -\frac{1}{2R^3}\nabla'(R^2) \tag{A.5}$$

$$\nabla'(R^2) = \hat{\boldsymbol{\rho}}\left[-2(\rho - \rho') + 2\rho[1 - \cos(\phi - \phi')]\right] + \frac{\hat{\boldsymbol{\phi}}}{\rho'}\left[-2\rho\rho'\sin(\phi - \phi')\right] + \hat{\mathbf{z}}\left[-2(z - z')\right] \tag{A.6}$$

3. $\cos\phi \int \cos(\gamma)\frac{\partial}{\partial n'}\left(\frac{1}{R}\right)d\gamma$

The expression for the derivative term gives:

$$\cos\phi \int_0^{2\pi} \cos(\gamma)\frac{\partial}{\partial n'}\left(\frac{1}{R}\right)d\gamma = -\cos\phi \int_0^{2\pi} \frac{a\cos\gamma - b\cos^2\gamma}{R^3}d\gamma \tag{A.7}$$

where $a = \rho'\cos\alpha' - (z' - z)\sin\alpha'$, and $b = \rho\cos\alpha'$.

Hence:

$$\cos\phi \int_0^{2\pi} \cos(\gamma)\frac{\partial}{\partial n'}\left(\frac{1}{R}\right)d\gamma = -\cos\phi\left\{a\int_0^{2\pi}\frac{\cos\gamma}{R^3}d\gamma - b\int_0^{2\pi}\frac{\cos^2\gamma}{R^3}d\gamma\right\} \tag{A.8}$$

$$= -2\cos\phi\left\{a\int_0^{\pi}\frac{\cos\gamma}{R^3}d\gamma - b\int_0^{\pi}\frac{\cos^2\gamma}{R^3}d\gamma\right\} \tag{A.9}$$

$$= +2\cos\phi\left\{[(z' - z)\sin\alpha' - \rho'\cos\alpha']\Omega_1 + \rho\cos\alpha'\Omega_2\right\} \tag{A.10}$$

as desired.

4. $\int_0^{2\pi}\frac{\partial}{\partial n'}\left(\frac{1}{R}\right)d\phi' = 2\left\{\rho\cos\alpha'\Omega_1 + [(z' - z)\sin\alpha' - \rho'\cos\alpha']\Omega_0\right\}$

It is known that:

$$\int_0^{2\pi} \frac{\partial}{\partial n'}\left(\frac{1}{R}\right) d\phi' = -\int_{\phi-0}^{\phi-2\pi} \frac{-(a - b\cos\gamma)}{R^3} d\gamma \tag{A.11}$$

with $\gamma = \phi - \phi'$ and where a and b are as given previously.

Hence

$$= -a\int_{\phi-2\pi}^{\phi} \frac{d\gamma}{R^3} + b\int_{\phi-2\pi}^{\phi} \frac{\cos\gamma}{R^3} d\gamma \tag{A.12}$$

$$= -2a\int_0^{\pi} \frac{d\gamma}{R^3} + 2b\int_0^{\pi} \frac{\cos\gamma}{R^3} d\gamma \tag{A.13}$$

and with the definitions for a and b

$$= 2\Big\{[(z' - z)\sin\alpha' - \rho'\cos\alpha']\Omega_0 + \rho\cos\alpha'\Omega_1\Big\} \tag{A.14}$$

as desired.

5. Re-express Ω_i's in terms of the complete elliptic integrals.

The definitions of the complete elliptic integrals are as follows (see Abramowitz and Stegun, 1964).

1. Complete elliptic integral of the first kind:

$$K(m) = \int_0^{\pi/2} (1 - m\sin^2\theta)^{-1/2} d\theta \tag{A.15}$$

2. Complete elliptic integral of the second kind:

$$E(m) = \int_0^{\pi/2} (1 - m\sin^2\theta)^{+1/2} d\theta \tag{A.16}$$

3. $dK(m)/dm$:

$$\frac{dK(m)}{dm} = \frac{1}{2}\int_0^{\pi/2} \frac{\sin^2\theta}{(1 - m\sin^2\theta)^{3/2}} d\theta \tag{A.17}$$

The definition for Ω_0 is

$$\Omega_0 \equiv \int_0^{\pi} \frac{1}{R^3} d\gamma \tag{A.18}$$

where

$$R^2 = \left[(\rho+\rho')^2+(z-z')^2\right]\left[1-\frac{4\rho\rho'}{(\rho+\rho')^2+(z-z')^2}\sin^2\left[\frac{1}{2}(\pi-\gamma)\right]\right] \tag{A.19}$$

Make the substitutions

$$m = \frac{4\rho\rho'}{(\rho+\rho')^2+(z-z')^2} \tag{A.20}$$

$$\theta = \frac{1}{2}(\pi-\gamma), \qquad d\theta = -d\gamma/2, \quad d\gamma = -2d\theta \tag{A.21}$$

Then

$$R^2 = \frac{4\rho\rho'}{m}(1-m\sin^2\theta) \tag{A.22}$$

and Ω_0 simplifies to the form

$$\Omega_0 = \int_0^\pi \frac{1}{R^3}d\gamma = \int_{\pi/2}^0 \frac{-2d\theta}{\left[\frac{4\rho\rho'}{m}(1-m\sin^2\theta)\right]^{3/2}} \tag{A.23}$$

$$= \frac{1}{4}\left(\frac{m}{\rho\rho'}\right)^{3/2}\int_0^{\pi/2}\frac{d\theta}{\left[(1-m\sin^2\theta)\right]^{3/2}} \tag{A.24}$$

From their definitions, form:

$$K(m)+2m\frac{dK(m)}{dm} = \int_0^{\pi/2}\left(\frac{1-m\sin^2\theta}{(1-m\sin^2\theta)^{3/2}}+\frac{m\sin^2\theta}{(1-m\sin^2\theta)^{3/2}}\right)d\theta \tag{A.25}$$

$$= \int_0^{\pi/2}\frac{d\theta}{(1-m\sin^2\theta)^{3/2}} \tag{A.26}$$

which is a scaled version of the previous expression for Ω_0, hence

$$\Omega_0 = \frac{1}{4}\left(\frac{m}{\rho\rho'}\right)^{3/2}\left[K(m)+2m\frac{dK(m)}{dm}\right] \tag{A.27}$$

The definition for Ω_1 is

$$\Omega_1 = \int_0^\pi \frac{\cos\gamma}{R^3}\,d\gamma \tag{A.28}$$

From previous derivations, recall that

$$\cos\gamma = 2\sin^2\theta - 1 \tag{A.29}$$

$$R^2 = \frac{4\rho\rho'}{m}(1-m\sin^2\theta) \tag{A.30}$$

$$\theta = \frac{1}{2}(\pi-\gamma) \tag{A.31}$$

$$d\gamma = -2\,d\theta \tag{A.32}$$

Combining all of these gives

$$\Omega_1 = \int_0^{\pi/2} \frac{2(2\sin^2\theta - 1)}{\left(\frac{4\rho\rho'}{m}\right)^{3/2}(1 - m\sin^2\theta)^{3/2}} d\theta \tag{A.33}$$

$$= \left(\frac{m}{\rho\rho'}\right)^{3/2} \int_0^{\pi/2} \frac{4\sin^2\theta - 2}{8(1 - m\sin^2\theta)^{3/2}} d\theta \tag{A.34}$$

From their definitions, form:

$$(1 - m/2)\frac{dK(m)}{dm} - \frac{1}{4}K(m) = \int_0^{\pi/2} \frac{(1 - m/2)\frac{1}{2}\sin^2\theta - \frac{1}{4}(1 - m\sin^2\theta)}{(1 - m\sin^2\theta)^{3/2}} d\theta \tag{A.35}$$

$$= \int_0^{\pi/2} \frac{4\sin^2\theta - 2}{8(1 - m\sin^2\theta)^{3/2}} d\theta \tag{A.36}$$

which is a scaled version of the previous expression for Ω_1, hence

$$\Omega_1 = \left(\frac{m}{\rho\rho'}\right)^{3/2} \left[(1 - m/2)\frac{dK(m)}{dm} - \frac{1}{4}K(m)\right] \tag{A.37}$$

The definition for Ω_2 is

$$\Omega_2 = \int_0^{\pi} \frac{\cos^2\gamma}{R^3} d\gamma \tag{A.38}$$

As before, simplify this expression to

$$\Omega_2 = \int_0^{\pi/2} \frac{2(2\sin^2\theta - 1)^2}{\left(\frac{4\rho\rho'}{m}\right)^{3/2}(1 - m\sin^2\theta)^{3/2}} d\theta \tag{A.39}$$

$$\Omega_2 = \left(\frac{m}{\rho\rho'}\right)^{3/2} \int_0^{\pi/2} \frac{2(2\sin^2\theta - 1)^2}{8(1 - m\sin^2\theta)^{3/2}} d\theta \tag{A.40}$$

From their definitions, form:

$$\frac{2}{m}(1 - m/2)^2 \frac{dK(m)}{dm} - \frac{1}{m^2}(1 - m^2/4)K(m) + \frac{1}{m^2}E(m) =$$

$$\int_0^{\pi/2} \left(\frac{8}{8}\right) \frac{\frac{1}{m}(1 - m/2)^2\sin^2\theta - \frac{1}{m^2}(1 - m^2/4)(1 - m\sin^2\theta) + \frac{1}{m^2}(1 - m\sin^2\theta)^2}{(1 - m\sin^2\theta)^{3/2}} d\theta \tag{A.41}$$

The numerator becomes: $= 2\left[2\sin^2\theta - 1\right]^2$ hence

$$\Omega_2 = \frac{1}{m^2}\left(\frac{m}{\rho\rho'}\right)^{3/2}\left\{2m(1-m/2)^2\,\frac{dK(m)}{dm} - (1-m^2/4)K(m) + E(m)\right\} \quad \text{(A.42)}$$

as desired.

6. Series expressions for elliptic integrals.

Since

$$m = \frac{4\rho\rho'}{(\rho+\rho')^2 + (z-z')^2} \quad \text{(A.43)}$$

and ρ, ρ' are both non-negative, the minimum of m (being the minimum of the numerator with a finite denominator) is zero. The maximum of m occurs at the minimum of the denominator, with a finite numerator. This occurs for $z = z'$ and $\rho = \rho'$, giving the maximum of m being one.

There are series expressions for the elliptic integrals in Abramowitz and Stegun (1964), pages 591–2. There it is required that $m \in [0,1]$, which is satisfied in this case. The expression for $K(m)$ given there is:

$$K(m) = (a_0 + a_1 m_1 + \ldots + a_4 m_1^4) + (b_0 + b_1 m_1 + \ldots + b_4 m_1^4)\ln(1/m_1) + \varepsilon(m) \quad \text{(A.44)}$$

with $|\varepsilon(m)| \leq 2 \times 10^{-8}$, and

$$\begin{array}{ll} a_0 = 1.38629\ 436112 & b_0 = 0.5 \\ a_1 = 0.09666\ 344259 & b_1 = 0.12498\ 593597 \\ a_2 = 0.03590\ 092383 & b_2 = 0.06880\ 248576 \\ a_3 = 0.03742\ 563713 & b_3 = 0.03328\ 355346 \\ a_4 = 0.01451\ 196212 & b_4 = 0.00441\ 787012 \end{array} \quad \text{(A.45)}$$

with $m_1 = 1 - m$. Next, the expression for $E(m)$ is given as:

$$E(m) = (1 + a_1' m_1 + \ldots + a_4' m_1^4) + (b_1' m_1 + \ldots + b_4' m_1^4)\ln(1/m_1) + \varepsilon(m) \quad \text{(A.46)}$$

with $|\varepsilon(m)| \leq 2 \times 10^{-8}$, and

$$\begin{array}{ll} a_1' = 0.44325\ 141463 & b_1' = 0.24998\ 368310 \\ a_2' = 0.06260\ 601220 & b_2' = 0.09200\ 180037 \\ a_3' = 0.04757\ 383546 & b_3' = 0.04069\ 697526 \\ a_4' = 0.01736\ 506451 & b_4' = 0.00526\ 449639 \end{array} \quad \text{(A.47)}$$

with $m_1 = 1 - m$.

For $dK(m)/dm$, the term-by-term derivative of the appropriate series, given above, gives:

$$\frac{dK(m)}{dm} = -\frac{dK(m)}{dm_1} = -\left[\begin{array}{l} (a_1 + 2a_2 m_1 + 3a_3 m_1^2 + 4a_4 m_1^3) \\ +(b_1 + 2b_2 m_1 + 3b_3 m_1^2 + 4b_4 m_1^3)\ln(1/m_1) \\ +(b_0 + b_1 m_1 + b_2 m_1^2 + b_3 m_1^3 + b_4 m_1^4) m_1 (-m_1^{-2}) \end{array}\right] \tag{A.48}$$

$$= -\left[\begin{array}{l} (a_1 + 2a_2 m_1 + 3a_3 m_1^2 + 4a_4 m_1^3) \\ +(b_1 + 2b_2 m_1 + 3b_3 m_1^2 + 4b_4 m_1^3)\ln(1/m_1) \\ +(b_0 + b_1 m_1 + b_2 m_1^2 + b_3 m_1^3 + b_4 m_1^4)(1/m_1) \end{array}\right] \tag{A.49}$$

Hence:

$$\begin{aligned} \frac{dK(m)}{dm} = {} & b_0(1/m_1) - (a_1 - b_1) - (2a_2 - b_2)m_1 - (3a_3 - b_3)m_1^2 - (4a_4 - b_4)m_1^3) \\ & - (b_1 + 2b_2 m_1 + 3b_3 m_1^2 + 4b_4 m_1^3)\ln(1/m_1) \end{aligned} \tag{A.50}$$

This series is first given in Senior and Ahlgren (1972), however no error estimate was given for it.

APPENDIX B

DETAILS OF SINGULARITY EXTRACTION AND INTEGRATION

This appendix fills in some of the steps in the derivation of the singularity integration formulas detailed in section 2.4.

1. $1/m_1$ Term

At $\phi = 0$, and $\hat{\mathbf{x}}$-excitation, (2.71) and (2.72) give:

$$\left.\begin{array}{ll} \text{outside:} & -2\Phi_1(\mathbf{r}) \\ \text{bndry:} & -(1+\epsilon)\Phi_1(\mathbf{r}) \\ \text{inside:} & -2\epsilon\Phi_1(\mathbf{r}) \end{array}\right\} = 2\rho + \frac{1}{\pi}\int_S W_1(s')\Big\{\rho\cos\alpha'\,\Omega_2 + [(z'-z)\sin\alpha' - \rho'\cos\alpha']\,\Omega_1\Big\}\rho'\mathrm{d}s' \tag{B.1}$$

where

$$\Phi_1(\mathbf{r}) = -\frac{1}{1-\epsilon}W_1(s)\cos\phi \tag{B.2}$$

and where Ω_1 and Ω_2 are elliptic integrals, where the troublesome singularities occur.

Following Senior (1983), write:

$$\Omega_1 = \widetilde{\Omega_1} + (1 - m/2)\ \left(\frac{m}{\rho\rho'}\right)^{3/2}\frac{1/2}{1-m} \tag{B.3}$$

$$\Omega_2 = \widetilde{\Omega_2} + \frac{2}{m}(1 - m/2)^2\left(\frac{m}{\rho\rho'}\right)^{3/2}\frac{1/2}{1-m} \tag{B.4}$$

where $\widetilde{\Omega_i}$ is the 'non-singular' part, leftover after the removal of the $\frac{1}{1-m}$ singularity term. Now to analytically integrate this $\frac{1}{1-m}$ singularity term.

A transfer to $s-t$ coordinates is convenient (fig. 2.6). Note that this is redefining the s variable from global to local.

Simplify the Ω_i 's so that the only s'–dependence will be in the $\frac{1}{1-m}$ term, and set $s' = 0$ in the coefficients, that multiply the kernel, under the assumption that their variation with respect to s' is small compared to that of the singularity term. The kernel term is

$$K_1 = \{\rho \cos\alpha' \, \Omega_2 + [(z' - z)\sin\alpha' - \rho' \cos\alpha'] \, \Omega_1\}\rho' \tag{B.5}$$

$$= \Big\{(s\sin\alpha' + t\cos\alpha')\cos\alpha' \, \Omega_2 + \Big[\,[(s'-s)\cos\alpha' - (t'-t)\sin\alpha']\sin\alpha' - (s'\sin\alpha' + t'\cos\alpha')\cos\alpha'\Big] \, \Omega_1\Big\}(s'\sin\alpha' + t'\cos\alpha') \tag{B.6}$$

In this case the s' – terms inside cancel, leaving the outermost s' – term. This must remain, as neglecting it will cause errors when $s'\sin\alpha' \geq t'\cos\alpha'$, *i.e.,* near vertical portions of the boundary. Hence write:

$$K_1 = \widetilde{K_1} + K_{11}\left[\frac{1}{1-m}\right] + K_{12}\left[\frac{s'}{1-m}\right] \tag{B.7}$$

Analytically integrating the $\frac{1}{1-m}$ – and the $\frac{s'}{1-m}$ – terms gives:.

$$\int_{-\frac{\Delta}{2}}^{+\frac{\Delta}{2}} \frac{1}{1-m}\, ds' = 2\sin\alpha'(s\sin\alpha' + t\cos\alpha')\ln\left|\frac{\Delta^2/4 - s\Delta + s^2 + (t'-t)^2}{\Delta^2/4 + s\Delta + s^2 + (t'-t)^2}\right| + \Delta$$

$$+ \frac{4s^2\sin^2\alpha' + 4tt'\cos^2\alpha' + 4s(t+t')\sin\alpha'\cos\alpha'}{t'-t}\left\{\tan^{-1}\left(\frac{\Delta - 2s}{2(t'-t)}\right) + \tan^{-1}\left(\frac{\Delta + 2s}{2(t'-t)}\right)\right\} \tag{B.8}$$

and:

$$\int_{-\frac{\Delta}{2}}^{+\frac{\Delta}{2}} \frac{s'}{1-m}\,ds' = (s\sin\alpha' + t\cos\alpha')\Bigg\{4\sin\alpha'\Delta + (4s\sin\alpha' + 2t'\cos\alpha')\ln\left|\frac{X(+\Delta/2)}{X(-\Delta/2)}\right|$$
$$+ \frac{4[s(s\sin\alpha' + t'\cos\alpha') - \sin\alpha'(t'-t)^2]}{t'-t}\left[\tan^{-1}\left(\frac{\Delta-2s}{2(t'-t)}\right) + \tan^{-1}\left(\frac{\Delta+2s}{2(t'-t)}\right)\right]\Bigg\} \tag{B.9}$$

Now expressions for the Ω_i 's are required. Here treat the coefficients of the kernels as **constants** during the integration, and so in these constants let $s' = 0$. This gives:

$$m = \frac{4t'\cos\alpha'[s\sin\alpha' + t\cos\alpha']}{s^2 + (t+t')^2 + 4t'\sin\alpha'(s\cos\alpha' - t\sin\alpha')} \tag{B.10}$$

$$1 - m/2 = \frac{s^2 + (t+t')^2 + 2t'\sin\alpha'(s\cos\alpha' - t\sin\alpha')}{s^2 + (t+t')^2 + 4t'\sin\alpha'(s\cos\alpha' - t\sin\alpha')} \tag{B.11}$$

$$\left(\frac{m}{\rho\rho'}\right)^{3/2} = \frac{8}{[s^2 + (t+t')^2 + 4t'\sin\alpha'(s\cos\alpha' - t\sin\alpha')]^{3/2}} \tag{B.12}$$

Using these in the expressions for the Ω_i's :

$$\Omega_0 = \widetilde{\Omega_0} + \frac{8t'\cos\alpha'(s\sin\alpha' + t\cos\alpha')}{\{s^2 + (t+t')^2 + 4t'\sin\alpha'(s\cos\alpha' - t\sin\alpha')\}^{5/2}}\left[\frac{1}{1-m}\right] \tag{B.13}$$

$$\Omega_1 = \widetilde{\Omega_1} + \frac{4[s^2 + t^2 + t'^2 + 2t'\sin\alpha'(s\cos\alpha' - t\sin\alpha')]}{\{s^2 + (t+t')^2 + 4t'\sin\alpha'(s\cos\alpha' - t\sin\alpha')\}^{5/2}}\left[\frac{1}{1-m}\right] \tag{B.14}$$

$$\Omega_2 = \widetilde{\Omega_2} +$$
$$\frac{2[s^2 + t^2 + t'^2 + 2t'\sin\alpha'(s\cos\alpha' - t\sin\alpha')]^2}{t'\cos\alpha'(s\sin\alpha' + t\cos\alpha')\{s^2 + (t+t')^2 + 4t'\sin\alpha'(s\cos\alpha' - t\sin\alpha')\}^{5/2}}\left[\frac{1}{1-m}\right] \tag{B.15}$$

Use these to find IK_1 and IK_3, the integrated kernels, which are used to find the potential inside and outside the body for each incidence angle. As with the Ω_i's , the IK_i's are separated into singular and non-singular pieces. Hence:

$$IK_1 = \int \{\rho \cos\alpha' \, \Omega_2 + [(z' - z)\sin\alpha' - \rho' \cos\alpha'] \, \Omega_1\} \rho' \, ds' \tag{B.16}$$

$$IK_3 = \int \{\rho \cos\alpha' \, \Omega_1 + [(z' - z)\sin\alpha' - \rho' \cos\alpha'] \, \Omega_0\} \rho' \, ds' \tag{B.17}$$

For notational purposes use:

$$IK_i = \widetilde{IK}_i + IK_{i,extra} \tag{B.18}$$

Doing IK_1 first:

$$IK_{1,extra} = K_{11} \int \left[\frac{1}{1-m}\right] + K_{12} \int \left[\frac{s'}{1-m}\right] \tag{B.19}$$

Solve for K_{11}:

$$K_{11} = \frac{2\cos\alpha'[s^2 + t^2 + t'^2 + 2t'\sin\alpha'(s\cos\alpha' - t\sin\alpha')]}{\{s^2 + (t+t')^2 + 4t'\sin\alpha'(s\cos\alpha' - t\sin\alpha')\}^{5/2}}(s^2 + t^2 - t'^2) \tag{B.20}$$

After a little bit of thought it will be obvious that:

$$K_{12} = \frac{K_{11}\sin\alpha'}{t'\cos\alpha'} \tag{B.21}$$

Giving:

$$IK_1 = \widetilde{IK}_1 + \frac{2[s^2+t^2+t'^2+2t'\sin\alpha'(s\cos\alpha'-t\sin\alpha')](s^2+t^2-t'^2)}{\{s^2 + (t+t')^2 + 4t'\sin\alpha'(s\cos\alpha' - t\sin\alpha')\}^{5/2}} \cdot\left\{\cos\alpha' \int \left[\frac{1}{1-m}\right] + \frac{\sin\alpha'}{t'} \int \left[\frac{s'}{1-m}\right]\right\} \tag{B.22}$$

And after simplifying the $\{\cdots\}$ term:

$$IK_1 = \widetilde{IK_1} + \frac{2[s^2+t^2+t'^2+2t'\sin\alpha'(s\cos\alpha'-t\sin\alpha')](s^2+t^2-t'^2)}{\{s^2+(t+t')^2+4t'\sin\alpha'(s\cos\alpha'-t\sin\alpha')\}^{5/2}}\cdot$$

$$\Big[\Big(\cos\alpha'+\frac{4\sin^2\alpha'}{t'}(s\sin\alpha'+t\cos\alpha')\Big)\Delta$$

$$+4\sin\alpha'(s\sin\alpha'+t\cos\alpha')\Big(\cos\alpha'+\frac{s\sin\alpha'}{t'}\Big)\ln\left|\frac{\frac{\Delta^2}{4}-s\Delta+s^2+(t'-t)^2}{\frac{\Delta^2}{4}+s\Delta+s^2+(t'-t)^2}\right|$$

$$+\frac{4(s\sin\alpha'+t\cos\alpha')}{t'-t}[2\sin\alpha'(s\sin\alpha'+t\cos\alpha')+t'(\cos^2\alpha'-\sin^2\alpha')+\frac{\sin^2\alpha'}{t'}(s^2-t^2)]$$

$$\cdot\left[\tan^{-1}\left(\frac{\Delta-2s}{2(t'-t)}\right)+\tan^{-1}\left(\frac{\Delta+2s}{2(t'-t)}\right)\right]\Big] \tag{B.23}$$

Similarly for $\hat{\mathbf{z}}$ – excitation. At $\phi=0$, (2.71) and (2.72) give:

$$\left.\begin{array}{ll}\text{outside:} & -2\Phi_3(\mathbf{r})\\ \text{bndry:} & -(1+\epsilon)\Phi_3(\mathbf{r})\\ \text{inside:} & -2\epsilon\Phi_3(\mathbf{r})\end{array}\right\} = 2z+\frac{1}{\pi}\int_S W_3(s')\Big\{\rho\cos\alpha'\,\Omega_1+[(z'-z)\sin\alpha'-\rho'\cos\alpha']\,\Omega_0\Big\}\rho'\mathrm{d}s' \tag{B.24}$$

where

$$\Phi_3(\mathbf{r}) = -\frac{1}{1-\epsilon}W_3(s) \tag{B.25}$$

and where Ω_0 and Ω_1 are elliptic integrals, where the troublesome singularities occur. The Ω_i's were evaluated during our solution for K_1. As with the kernel term for $\hat{\mathbf{x}}$–incidence, write:

$$K_3 = \widetilde{K_3} + K_{31}\Big[\frac{1}{1-m}\Big] + K_{32}\Big[\frac{s'}{1-m}\Big] \tag{B.26}$$

The integrations done for IK_1 are the same ones needed for IK_3 and so do not need to be repeated. Hence:

$$IK_{3,extra} = K_{31} \int \left[\frac{1}{1-m}\right] + \mathrm{K}_{32} \int \left[\frac{s'}{1-m}\right] \tag{B.27}$$

where:

$$K_{31} = \frac{4t' \cos^3\alpha'(s\sin\alpha' + t\cos\alpha')(s^2 + t^2 - t'^2)}{\{s^2 + (t+t')^2 + 4t'\sin\alpha'(s\cos\alpha' - t\sin\alpha')\}^{5/2}} \tag{B.28}$$

So:

$$IK_3 = \widetilde{IK_3} + \frac{4t' \cos^2\alpha'(s\sin\alpha' + t\cos\alpha')(s^2 + t^2 - t'^2)}{\{s^2 + (t+t')^2 + 4t'\sin\alpha'(s\cos\alpha' - t\sin\alpha')\}^{5/2}} \cdot\left\{ \cos\alpha' \int \left[\frac{1}{1-m}\right] + \frac{\sin\alpha'}{t'} \int \left[\frac{s'}{1-m}\right]\right\} \tag{B.29}$$

The term with the integrals in it is the same as in IK_1, hence:

$$\begin{aligned} IK_3 = \widetilde{IK_3} &+ \frac{4t' \cos^2\alpha'(s\sin\alpha' + t\cos\alpha')(s^2 + t^2 - t'^2)}{\{s^2 + (t+t')^2 + 4t'\sin\alpha'(s\cos\alpha' - t\sin\alpha')\}^{5/2}} \\ \Big[\Big[&(\cos\alpha' + \frac{4\sin^2\alpha'}{t'}(s\sin\alpha' + t\cos\alpha'))\Delta \\ &+ 4\sin\alpha'(s\sin\alpha' + t\cos\alpha')(\cos\alpha' + \frac{s\sin\alpha'}{t'}) \ln\left|\frac{\frac{\Delta^2}{4} - s\Delta + s^2 + (t'-t)^2}{\frac{\Delta^2}{4} + s\Delta + s^2 + (t'-t)^2}\right| \\ &+ \frac{4(s\sin\alpha' + t\cos\alpha')}{t'-t}[2\sin\alpha'(s\sin\alpha' + t\cos\alpha') + t'(\cos^2\alpha' - \sin^2\alpha') + \frac{\sin^2\alpha'}{t'}(s^2 - t^2)] \\ &\Big[\tan^{-1}\left(\frac{\Delta - 2s}{2(t'-t)}\right) + \tan^{-1}\left(\frac{\Delta + 2s}{2(t'-t)}\right)\Big]\Big]\Big] \end{aligned} \tag{B.30}$$

2. $\ln\left|\frac{1}{m_1}\right|$ Term

Here repeat the same analysis as for the $\frac{1}{1-m}$ term, but now extract a different singular term: the $\ln|1-m|$ term.

The two integrals below will be needed:

$$\mathrm{I} = \int_{-\frac{\Delta}{2}}^{+\frac{\Delta}{2}} \ln|1-m|\, ds' \tag{B.31}$$

$$\mathrm{II} = \int_{-\frac{\Delta}{2}}^{+\frac{\Delta}{2}} s' \ln|1-m|\, ds' \tag{B.32}$$

Our expression for I becomes:

$$\begin{aligned}
\mathrm{I} = & \left[\ln|\eta_1^+| - 2\right]\left(\frac{\Delta}{2} - s\right) - \left[\ln|\eta_1^-| - 2\right]\left(-\frac{\Delta}{2} - s\right) \\
& + 2(t'-t)\left\{\tan^{-1}\left(\frac{\frac{\Delta}{2}-s}{(t'-t)}\right) - \tan^{-1}\left(\frac{-\frac{\Delta}{2}-s}{(t'-t)}\right)\right\} \\
& - \left[\ln|\eta_2^+| - 2\right]\left(s[\sin^2\alpha' - \cos^2\alpha'] + 2t\sin\alpha'\cos\alpha' + \frac{\Delta}{2}\right) \\
& + \left[\ln|\eta_2^-| - 2\right]\left(s[\sin^2\alpha' - \cos^2\alpha'] + 2t\sin\alpha'\cos\alpha' - \frac{\Delta}{2}\right) \\
& - 2[t(\sin^2\alpha' - \cos^2\alpha') - t' - 2s\sin\alpha'\cos\alpha']\cdot \\
& \left\{\tan^{-1}\left(\frac{s[\sin^2\alpha' - \cos^2\alpha'] + 2t\sin\alpha'\cos\alpha' + \frac{\Delta}{2}}{t(\sin^2\alpha' - \cos^2\alpha') - 2s\sin\alpha'\cos\alpha' - t'}\right)\right. \\
& \left. - \tan^{-1}\left(\frac{s[\sin^2\alpha' - \cos^2\alpha'] + 2t\sin\alpha'\cos\alpha' - \frac{\Delta}{2}}{t(\sin^2\alpha' - \cos^2\alpha') - 2s\sin\alpha'\cos\alpha' - t'}\right)\right\}
\end{aligned} \tag{B.33}$$

And for II:

$$\begin{aligned}
\mathrm{II} = & \frac{1}{2}\left[\frac{\Delta^2}{4} - s^2 + (t'-t)^2\right]\ln\left|\frac{\eta_1^+}{\eta_1^-}\right| - s\Delta \\
& + 2s(t'-t)\left[\tan^{-1}\left(\frac{\frac{\Delta}{2}-s}{(t'-t)}\right) - \tan^{-1}\left(\frac{+\frac{\Delta}{2}+s}{(t'-t)}\right)\right] \\
& - \frac{1}{2}\left\{\begin{array}{l} \dfrac{\Delta^2}{4} - 2\left[s(\sin^2\alpha' - \cos^2\alpha') + 2t\sin\alpha'\cos\alpha'\right]^2 \\ \\ + \left[s^2 + (t'-t)^2 + 4t'\cos\alpha'(s\sin\alpha' + t\cos\alpha')\right] \end{array}\right\}\ln\left|\frac{\eta_2^+}{\eta_2^-}\right| \\
& - \left[s(\sin^2\alpha' - \cos^2\alpha') + 2t\sin\alpha'\cos\alpha'\right]\Delta \\
& + 2\left[s(\sin^2\alpha' - \cos^2\alpha') + 2t\sin\alpha'\cos\alpha'\right]\left[t(\sin^2\alpha' - \cos^2\alpha') - t' - 2s\sin\alpha'\cos\alpha'\right]
\end{aligned}$$

$$\cdot \left[\tan^{-1} \left(\frac{s(\sin^2\alpha' - \cos^2\alpha') + 2t \sin\alpha' \cos\alpha' + \left(\frac{\Delta}{2}\right)}{\left[t(\sin^2\alpha' - \cos^2\alpha') - t' - 2s \sin\alpha' \cos\alpha'\right]} \right) \right.$$
$$\left. - \tan^{-1} \left(\frac{s(\sin^2\alpha' - \cos^2\alpha') + 2t \sin\alpha' \cos\alpha' - \left(\frac{\Delta}{2}\right)}{\left[t(\sin^2\alpha' - \cos^2\alpha') - t' - 2s \sin\alpha' \cos\alpha'\right]} \right) \right] \tag{B.34}$$

Now look at Ω_i's. Extracting the ln-terms from the elliptic integrals:

$$\mathrm{K}\Big|_{extra} = b_0 \ln\left|\frac{1}{m_1}\right| = -b_0 \ln|m_1| = -\frac{1}{2}\ln|m_1| \tag{B.35}$$

$$\frac{\mathrm{dK}}{dm}\Big|_{extra} = -b_1 \ln\left|\frac{1}{m_1}\right| = b_1 \ln|m_1| \tag{B.36}$$

and $b_1 = 0.12498593597$ from Abramowitz and Stegun (1964).

Now substitute into the expressions for Ω_i, to get:

$$\Omega_{0,extra} = \frac{1}{4}\left(\frac{m}{\rho\rho'}\right)^{3/2} \left\{2mb_1 - \frac{1}{2}\right\} \ln|m_1| \tag{B.37}$$

$$\Omega_{1,extra} = \left(\frac{m}{\rho\rho'}\right)^{3/2} \left\{\left(1 - \frac{m}{2}\right) b_1 + \frac{1}{8}\right\} \ln|m_1| \tag{B.38}$$

$$\Omega_{2,extra} = \frac{1}{m^2}\left(\frac{m}{\rho\rho'}\right)^{3/2} (1 - m/2)\left\{2mb_1(1-m/2) + \frac{1}{2}(1+m/2)\right\} \ln|m_1| \tag{B.39}$$

The expressions for m, $\left(\frac{m}{\rho\rho'}\right)^{3/2}$, and $(1-m/2)$ are already known, but $(1+m/2)$ is still needed:

$$1 + \frac{m}{2} = \frac{s^2 + (t-t')^2 + 6t' \cos\alpha'(s\sin\alpha' + t\cos\alpha')}{s^2 + (t+t')^2 + 4t' \sin\alpha'[s\cos\alpha' - t\sin\alpha']} \tag{B.40}$$

For conciseness let $\mathrm{Y} = s^2 + (t+t')^2 + 4t' \sin\alpha'(s\cos\alpha' - t\sin\alpha')$.

Also let $\mathrm{X} = 4t' \cos\alpha'(s\sin\alpha' + t\cos\alpha')$. This gives:

$$\Omega_{0,extra} = \frac{1}{(\mathrm{Y})^{5/2}} \left\{(4b_1 - 1)\mathrm{X} - s^2 - (t-t')^2\right\} \ln|m_1| \tag{B.41}$$

Now let $\mathrm{Z} = s^2 + t^2 + t'^2 + 2t' \sin\alpha'(s\cos\alpha' - t\sin\alpha')$. Note that $\mathrm{Y} = \mathrm{Z} + \mathrm{X}/2$.

Hence:

$$\Omega_{1,extra} = \frac{1}{(\mathrm{Y})^{5/2}} \left\{ 8b_1\mathrm{Z} + \frac{1}{2}\mathrm{X} \right\} \ln|m_1| \tag{B.42}$$

$$\Omega_{2,extra} = \frac{8\mathrm{Z}}{\mathrm{X}^2\mathrm{Y}^{3/2}} \left\{ \begin{array}{c} 2b_1\mathrm{X}\cdot\mathrm{Z}+ \\ \\ \frac{1}{2}\mathrm{Y}\left[s^2 + (t'-t)^2 + 6t'\cos\alpha'(s\sin\alpha' + t\cos\alpha')\right] \end{array} \right\} \ln|m_1| \tag{B.43}$$

Now given all these expressions write:

$$IK_1 = \int_{-\frac{\Delta}{2}}^{+\frac{\Delta}{2}} \left\{ \begin{array}{l} (s\sin\alpha' + t\cos\alpha')\cos\alpha'\,\Omega_{2,extra} \\ \\ -\left(s\cos\alpha'\sin\alpha' + (t'-t)\sin^2\alpha' + t'\cos^2\alpha'\right)\Omega_{1,extra} \end{array} \right\} (s'\sin\alpha' + t'\cos\alpha')\,ds' \tag{B.44}$$

$$IK_3 = \int_{-\frac{\Delta}{2}}^{+\frac{\Delta}{2}} \left\{ \begin{array}{l} (s\sin\alpha' + t\cos\alpha')\cos\alpha'\,\Omega_{1,extra} \\ \\ -\left(s\cos\alpha'\sin\alpha' + (t'-t)\sin^2\alpha' + t'\cos^2\alpha'\right)\Omega_{0,extra} \end{array} \right\} (s'\sin\alpha' + t'\cos\alpha')\,ds' \tag{B.45}$$

hence:

$$IK_{1,extra} = \overline{IK_1}\left[t'\cos\alpha'\cdot\mathrm{I} + \sin\alpha'\cdot\mathrm{II}\right] \tag{B.46}$$

$$IK_{3,extra} = \overline{IK_3}\left[t'\cos\alpha'\cdot\mathrm{I} + \sin\alpha'\cdot\mathrm{II}\right] \tag{B.47}$$

where:

$$\overline{IK_1} = (s\sin\alpha' + t\cos\alpha')\cos\alpha' \frac{8\mathrm{Z}}{\mathrm{X}^2\mathrm{Y}^{3/2}} \left\{ \begin{array}{l} 2b_1\mathrm{X}\cdot\mathrm{Z} + \frac{1}{2}\mathrm{Y}\left[s^2 + (t'-t)^2\right. \\ \left. +6t'\cos\alpha'(s\sin\alpha' + t\cos\alpha')\right] \end{array} \right\}$$
$$-\left(s\cos\alpha'\sin\alpha' + (t'-t)\sin^2\alpha' + t'\cos^2\alpha'\right)\frac{1}{(\mathrm{Y})^{5/2}}\left\{8b_1\mathrm{Z} + \frac{1}{2}\mathrm{X}\right\} \tag{B.48}$$

$$\overline{IK_3} = (s\sin\alpha' + t\cos\alpha')\cos\alpha' \frac{1}{(\mathrm{Y})^{5/2}}\left\{8b_1\mathrm{Z} + \frac{1}{2}\mathrm{X}\right\}$$
$$-\left(s\cos\alpha'\sin\alpha' + (t'-t)\sin^2\alpha' + t'\cos^2\alpha'\right)\frac{1}{(\mathrm{Y})^{5/2}}\left\{(4b_1-1)\mathrm{X} - s^2 - (t-t')^2\right\} \tag{B.49}$$

The two expressions for $IK_{1,extra}$ and $IK_{3,extra}$ are used to replace some of the numerical integration over one segment of the surface boundary. The numbers so calculated are more accurate than those from the purely numerical procedure, and should give accurate results when the point is very close to the boundary of the body.

BIBLIOGRAPHY

BIBLIOGRAPHY

Abramowitz, M. and I. A. Stegun, 1964. *Handbook of Mathematical Functions.* National Bureau of Standards.

Arfken, G. 1985. *Mathematical Methods for Physicists,* 3rd edition, Academic Press.

Arvas, E., R. F. Harrington, and J. R. Mautz, 1986. Radiation and Scattering from Electrically Small Conducting Bodies of Arbitrary Shape. *IEEE Trans Ant Prop,* **34,** 66.

Aravind, P. K., A. Nitzan, and H. Metiu, 1981. The Interaction Between Electromagnetic Resonances and its Role in Spectroscopic Studies of Molecules Adsorbed on Colloidal Particles or Metal Spheres. *Surf Sci,* **110,** 189.

Asano, S. and G. Yamamoto, 1975. Light Scattering by a Spheroidal Particle. *Appl Opt,* **14,** 29.

Berry, M. V. and I. C. Percival, 1986. Optics of Fractal Clusters such as Smoke. *Optica Acta,* **33,** 577.

Bickel, W. S. and M. E. Stafford, 1980. Biological Particles as Irregularly Shaped Scatterers. *in* Schuerman, D., ed. "Light Scattering by Irregularly Shaped Particles," Plenum, NY. p 299.

Bohren, C. F. and D. R. Huffman, 1983. *Absorption and Scattering of Light by Small Particles,* Wiley, NY.

Borghese, F., P. Denti, R. Saija, and G. Toscano, 1987a. Extinction Coefficients for a Random Dispersion of Small Stratified Spheres and a Random Dispersion of their Binary Aggregates. *J Opt Soc Am,* **4,** p. 1984.

Borghese, F., P. Denti, R. Saija, G. Toscano, and O. I. Sindoni, 1987b. Optical Absorption Coefficient of a Dispersion of Clusters Composed of a Large Number of Spheres. *Aerosol Sci Technol,* **6,** 173.

Born, M. and E. Wolf, 1980. *Principles of Optics, 6th ed.* (esp p. 657) Pergamon, Oxford.

Bottiger, J. R., E. S. Fry, and R. C. Thompson, 1980. Phase Matrix Measurements for Electromagnetic Scattering by Sphere Aggregates. *in* Schuerman, D., ed. "Light Scattering by Irregularly Shaped Particles," Plenum, NY. p 283.

G. D. Byrne and A. C. Hindmarsh, 1975. A Polyalgorithm for the Numerical Solution of Ordinary Differential Equations, *ACM Trans. on Mathematical Software,* **1,** 71–96.

Czerwinski, P. 1984. Shift of Resonances due to Surface Perturbations. *Radiation Laboratory Memo,* **109955–510–M.**

Davis, M. H., 1962. The forces between conducting spheres in a uniform electric field. *RAND Memo,* **RM–2607–1–PR.**

Davis, M. H., 1964a. Two charged spherical conductors in a uniform electric field: Forces and field strength. *Quart. Journ. Mech. and Applied Math.,* **17,** 499.

Davis, M. H., 1964b. Two charged spherical conductors in a uniform electric field: Forces and field strength. *RAND Memo,* **RM–3860–PR.**

Devlin, Robert M., and Witham, Francis H., 1983. *Plant Physiology, 4th ed.,* Willard Grant Press, Boston.

Embury, J. 1980. Absorption by Small Regular Non–Spherical Particles in the Rayleigh Region. *in* Schuerman, D., ed. "Light Scattering by Irregularly Shaped Particles," Plenum, NY. p 97.

Fahlen, T. S. and Bryant, H. C. 1966. Direct Observation of Surface Waves on Water Droplets. *J Opt Soc Am,* **56,** 1635.

Féat, G. R. and Levine, S. 1975. The Double–Layer Interaction of Two Charged Colloidal Spherical Particles of a Concentrated Dispersion in a Medium of Low Dielectric Constant: II A Cell Model. *Chem Soc Lon J: Faraday Trans II,* **71,** 102.

Féat, G. R. and Levine, S. 1976a. The Double–Layer Interaction of Two Charged Colloidal Spherical Particles of a Concentrated Dispersion in a Medium of Low Dielectric Constant: III Approximation of Perfectly Conducting Particles. *J Coll & Intfc Sci,* **54,** 34.

Féat, G. R. and Levine, S. 1976b. The Double–Layer Interaction of Two Charged Colloidal Spherical Particles of a Concentrated Dispersion in a Medium of Low Dielectric Constant: IV Conducting Particles in Contact. *Chem Soc Lon J: Faraday Trans II,* **72,** 501.

Fuchs, R. 1975. Theory of the Optical Properties of Ionic Crystal Cubes. *Phys Rev B,* **11,** 1732.

Fuchs, R. 1978. Infrared Absorption in MgO Microcrystals. *Phys Rev B,* **18,** 7160.

Fuller, K. A., Kattawar, G. W., Wang, R. T. 1986. Electromagnetic Scattering from Two Dielectric Spheres: Further Comparisons Between Theory and Experiment. *Appl Opt,* **25,** 2521.

Giddings, T. H. Jr., N. W. Withers, and L. A. Staehelin, 1980. Supramolecular Structure of Stacked and Unstacked Regions of Photosynthetic Membranes. *Proc. Natl. Acad. Sci. USA* **77,** 352.

Goyette, A. and Navon, A. 1976. Two Dielectric Spheres in an Electric Field. *Phys Rev B,* **13,** 4320.

Grams, G. W. 1980. *In–situ* Light Scattering Techniques for Determining Aerosol Size Distributions and Optical Constants. *in* Schuerman, D., ed. "Light Scattering by Irregularly Shaped Particles," Plenum, NY. p 243.

Herrick, D. F. and Senior, T. B. A. 1977. Low–Frequency Scattering by Rectangular Dielectric Particles. *Appl Phys,* **13,** 175.

Hidy, G. M., and J. R. Brock, 1970. *The Dynamics of Aerocolloidal Systems,* Pergamon Press, Oxford.

Hipkins, M. F., and Baker, N. R., 1986. *Photosynthesis energy transduction: a practical approach,* IRL Press, London.

Hocking, L. M., 1959. The collision efficiency of small drops. *Quart. J. Royal Meteorol. Soc.,* **85,** 44.

Holland, A. C., and Gagne, G. 1970. The Scattering of Polarized Light by Polydisperse Systems of Irregular Particles. *Appl Opt,* **9,** 1113.

Howell Y. and J. A. Bereny, 1979. *Engineer's Guide to Solar Energy,* Solar Energy Information Services, San Mateo, CA.

Huffman, D. R. and Bohren, C. F. 1980. Infrared Absorption Spectra of Non–Spherical Particles Treated in the Rayleigh–Ellipsoid Approximation. *in* Schuerman, D., ed. "Light Scattering by Irregularly Shaped Particles," Plenum, NY. p 103.

Jackson, J. D. 1975. *Classical Electrodynamics,* John Wiley and Sons, New York.

Jeffrey, D. J. and Van Dyke, M. 1978. The Temperature Field or Electric Potential Around Two Almost Touching Spheres. *J Inst Maths Applics,* **22,** 337.

Jeffrey, D. J. and Onishi, Y. 1980. Electrostatics of Two Unequal Adhering Spheres. *J Phys A,* **13,** 2847.

Jones, D. S. 1964. *The Theory of Electromagnetism,* Pergamon, Oxford.

Kattawar, G. W. and Humphreys, T. J. 1980. Electromagnetic Scattering from Two Identical Pseudospheres. *in* Schuerman, D., ed. "Light Scattering by Irregularly Shaped Particles," Plenum, NY. p 177.

Kattawar, G. W. and Dean, C. E. 1983. Electromagnetic Scattering from Two Dielectric Spheres: Comparison Between Theory and Experiment. *Opt Letts,* **8,** 48.

Keller, J. B., Kleinman, R. E., and Senior, T. B. A. 1972. Dipole Moments in Rayleigh Scattering. *J Inst Maths Applics,* **9,** 14.

Kellogg, O. D. 1953. *Foundations of Potential Theory,* Dover, NY.

Kiehl, J. T., Ko, M. W., Mugnai, A., and Chýlek, P. 1980. Perturbation Approach to Light Scattering by Non-Spherical Particles. *in* Schuerman, D., ed. "Light Scattering by Irregularly Shaped Particles," Plenum, NY. p 135.

Kiss, J. G., GY. I. Garab, Zs. M. Tóth, and Á. Faludi–Dániel, 1986. The light-Harvesting Chlorophyll a/b Protein acts as a Torque Aligning Chloroplasts in a Magnetic Field. *Photosynthesis Research* **10,** 217.

Kittel, C., 1976. *Introduction to Solid state Physics,* 5th edition, John Wiley and Sons, NY. (esp. p. 410.)

Kleinman, R. E. 1965. The Rayleigh Region. *Proc IEEE,* **53,** 848.

Kleinman, R. E. 1967. Far Field Scattering at Low Frequencies. *Appl Sci Res,* **18,** 1.

Kleinman, R. E. 1973. Dipole Moments and Near Field Potentials. *Appl Sci Res,* **27,** 335.

Kleinman, R. E. and Senior, T. B. A. 1972. Rayleigh Scattering Cross Sections. *Radio Sci,* **7,** 937.

Kleinman, R. E. and Senior, T. B. A. 1986. Rayleigh Scattering. in *Low and High Frequency Asymptotics,* V. K. Varadan, and V. V. Varadan, eds., Elsevier.

Krasnogorskaya, N. V., 1965a. Effect of Electrical Forces on the Coalescence of Perticles of Comparable Sizes. *Izv., Atmospheric and Oceanic Physics Series,* Vol. 1, No. 3, pp. 339–345. Translated by J. S. Sweet.

Krasnogorskaya, N. V., 1965b. The eefect of Electric Forces on Formation of Precipitation. *Izv., Atmospheric and Oceanic Physics Series,* Vol. 1, No. 4, pp. 402–412. Translated by D. G. Fry.

Krasny-Ergen, W., 1936. Zwei lietende, isolierte Kugeln im homogenen elektrischen Feld. *Ann d. Physik,* **27,** 459.

Lindblad, N. R., and R. G. Semonin, 1963. Collision Efficiency of Cloud Droplets in Electric Fields. *J. Geophys. Rsch.,* **68,** 1051.

Love, J. D. 1975. Dielectric Sphere–Sphere and Sphere–Plane Problems in Electrostatics. [*Q J*] *Mech Appl Math,* **28,** 449.

Macdonald, H. M. 1895. The Electrical Distribution on a Conductor Bounded by Two Spherical Surfaces Cutting at any Angle. *Proc Lond Math Soc (1),* **XXVI,** 156.

Mei, K. K. and Van Bladel, J. 1963. Low–Frequency Scattering by Rectangular Cylinders. *IEEE Trans Ant Prop,* **11,** 52.

Mie, G. 1908. Beiträge zur optik trüber Medien, Speziell kolloidaler Mettalösungen. *Ann. d. Physik,* **25,** 377–442.

Nelson, D. F. 1979. *Electric, Optic, and Acoustic Interactions in Dielectrics,* (esp. Ch. 9) John Wiley and Sons, New York.

Olaofe, G. O. 1970. Scattering by two Rayleigh–Debye Spheres. *Appl Opt,* **9,** 429.

O'Meara, D. J. Jr. and Savile, D. A. 1980. The Electrical Forces on Two Touching Spheres in a Uniform Field. [*Q J*] *Mech Appl Math,* **34,** 9.

Phillips, H. B. 1934. Effect of Surface Discontinuity on the Distribution of Potential. *J Math & Phys,* **13,** 261.

Physik Daten, Part II, 1981, Fachinformationzentrum Energie, Physik, Mathematik, GMBH, Karlsruhe.

Pierce, L. E., 1987. Improved Method for Computation of Near Fields of Dielectric Bodies of Arbitrary Profile, *Radiation Laboratory Memo,* **023618–1–1.**

Pierce, L. E. and Weil, H., 1987. Absorption by Spheres and Aggregates of Spheres. *Proceedings of the 1987 Scientific Conference on Obscuration and Aerosol Research,* 1988.

Pierce, L. E. and Weil, H., 1988. Resonances and Near and Internal Fields of Spheres with Cavities and Coagulated Spheres. *Proceedings of the 1988 Scientific Conference on Obscuration and Aerosol Research,* to be published.

Pierce, L. E. and Weil, H., 1990. Electromagnetic Scattering from Nonspherical Particles: A new Polarisability Model with Application to Agglomerating Spheres. *Electronics Letts.,* **26,** 180.

Pinnick, R. G. , Carroll, D. E., and Hofmann, D. J. 1976. Polarized Light Scattered from Monodisperse Randomly Oriented Nonspherical Aerosol Particles: Measurements. *Appl Opt,* **15,** 384.

Ramm, A. G. 1982. *Iterative Methods for Calculating Static Fields and Wave Scattering by Small Bodies,* Springer–Verlag, NY.

Rayleigh, 1897. On the Incidence of Aerial and Electric Waves upon Small Obstacles in the form of Ellipsoids or Elliptic Cylinders, and on the passage of Electric

Waves through a circular Aperture in a Conducting Screen. *Phil Mag,* **XLIV,** 28.

Ross, D. K. 1975. The Interaction Energy, Field Strength and Force Acting on a Pair of Dielectric Spheres Embedded in a Dielectric Medium. *SIAM J Appl Math,* **29,** 699.

Ross, D. K. 1976. The Interaction of Two Charged Dielectric Spheres – A Note on the Applications to Water Droplets and Ion Pairs. *Acta Phys Polon,* **A50,** 423.

Ruppin, R. 1982. Surface modes of two spheres. *Phys Rev B,* **26,** 3440.

Sarkar, T. K., Siarkiewicz, K. R., and Stratton, R.F. 1981. Survey of Numerical Methods for Solution of Large Systems of Linear Equations for Electromagnetic Field Problems. *IEEE Tran Ant Prop,* **29,** 847.

Saunders, M. J. 1970. Near–Field Backscattering Measurements from a Microscopic Water Droplet. *J Opt Soc Am,* **60,** 1359.

Saunders, M.J. 1980. The Effect of the Electric Field on the Backscattered Radiance of a Single Water Droplet. *in* Schuerman, D., ed. "Light Scattering by Irregularly Shaped Particles," Plenum, NY. p 237.

Schlamp, R. J., S. N. Grover, H. R. Pruppacher, and A. E. Hamielec, 1976. A numerical Investigation of the Effect of Electric Charges and Vertical External Electrci Fields on the Collision Efficiency of Cloud Drops. *Journ. of the Atmospheric Sciences,* **33,** 1747.

Senior, T. B. A. 1976. Low–Frequency Scattering by a Dielectric Body. *Radio Sci,* **11,** 477.

Senior, T. B. A. 1980. Effect of Particle Shape on Low Frequency Absorption. *Appl Opt,* **19,** 2483.

Senior, T. B. A. 1982. Low–Frequency Scattering by a Perfectly Conducting Body. *Radio Sci,* **17,** 741.

Senior, T. B. A., 1983. Computation of the Near Fields of a Dielectric Body, *Radiation Laboratory Memo,* **019955–508–M.**

Senior, T. B. A. and Ahlgren, D. J. 1972. The Numerical Solution of Low Frequency Scattering Problems. *Radiation Laboratory Report,* **103630–9–T.**

Senior, T. B. A. and Willis, T. M. III 1982. Rayleigh Scattering by Dielectric Bodies. (Program Description) *IEEE Trans Ant Prop,* **30,** 1271.

Siegel, K. M. 1959a. Far Field Scattering From Bodies of Revolution. *Appl Sci Res B,* **7,** 293.

Smith, G. S. and Barakat, R. 1975. Electrostatics of Two Conducting Spheres in Contact. *Appl Sci Res,* **30,** 418.

Snow, S. 1949. Potential Problems and Capacitance for a Conductor Bounded by Two Intersecting Spheres. *J Res of Ntl Bur Stds,* **43,** 377.

Srivastava, M. and Brownlee, D. E. 1980. Reflectivity of Single Micron–Sized Irregularly Shaped Dust Grains. *in* Schuerman, D., ed. "Light Scattering by Irregularly Shaped Particles," Plenum, NY. p 291.

Staehelin, L. A., D. P. Carter, and A. McDonald, 1980. Adhesion between Chloroplast Membranes: Experimental Manipulation and Incorporation of the Adhesion Factor into Artificial Membranes. *in* Membrane-Membrane Interactions, N. B. Gilula, ed., Raven Press, New York.

Staehelin, L. A., 1983. Control and Regulation of the Spatial Organization of Membrane Components by Membrane–Membrane INteractions. *Modern Cell Biology,* **2,** 73.

Stevenson, A. F. 1953a. Solution of Electromagnetic Scattering Problems as Power Series in the Ratio (Dimension of Scatterer)/Wavelength. *J Appl Phys,* **24,** 1134.

Stevenson, A. F. 1953b. Electromagnetic Scattering by an Ellipsoid in the Third Approximation. *J Appl Phys,* **24,** 1143.

Stratton, J. A. 1941. *Electromagnetic Theory,* McGraw–Hill, NY.

Turkevitch, J., Garton, G., and Stevenson, P. C. 1954. The color of colloidal gold. *J Colloid Sci,* **9,** (Suppl. 1), 26.

van de Hulst, H. C. 1957. *Light Scattering by Small Particles,* Dover, NY.

Wang, R. T. 1980. Extinction Signatures of Non–Spherical/Non–Isotropic Particles. *in* Schuerman, D., ed. "Light Scattering by Irregularly Shaped Particles," Plenum, NY. p 255.

Wang, R. T., Greenburg, J. M., and Schuerman, D. W. 1981. Experimental Results of Dependent Light Scattering by Two Spheres. *Opt Letts,* **6,** 543.

Weil, H., and Willis, T. M. 1987. Disk Scattering and Absorption by an Improved Computational Method. *Applied Optics,* **26,** 3987.

Weil, H. 1986. Surface Roughness, Clustering and Material Effects in Absorption and Scattering by Electrically Small Particles. *Proceedings of the 1985 Scientific Conference on Obscuration and Aerosol Research,* CRDEC-SP-86019, p. 547. and *Radiation Laboratory Memo,* **RL 803.**

Weil, H., Senior, T. B. A., Willis, T. M. III 1985. Internal and Near Fields of Small Particles Irradiated in Spectral Absorption Bands. *J. Opt. Soc. Am A,* **2,** 989.

Weitz, D. A., Lin, M. Y., and Sandroff, C. J. 1985. Colloidal Aggregation Revisited: New Insights Based on Fractal Structure and Surface Enhanced Raman Scattering. *Surf Sci,* **158,** 147.

Willis, T. M. III. 1982. Low Frequency Scattering by a Thin Dielectric Plate. *Radiation Laboratory Memo,* **019955–502–M.**

Willis, T. M., 1984. Improved Computation of Near Fields of a Dielectric Body, *Radiation Laboratory Memo,* **019955–509–M.**

Willis, T. M., H. Weil, and D. M. LeVine, 1988. Applicability of Physical Optics Thin Plate Scattering Formulas for Remote Sensing. *IEEE Trans. Geosci. Remote Sensing,* **26,** March 1988, p. 153.

Wiscombe, W. and Mugnai, A. 1980. Exact Calculations of Scattering from Moderately–Nonspherical T_n–Particles: Comparisons with Equivalent Spheres. *in* Schuerman, D., ed. "Light Scattering by Irregularly Shaped Particles," Plenum, NY. p 141.

Zerull, R. H. and Giese, R. H. 1974. Microwave Analogue Studies. *in* Gehrels, T., ed. "Planets, stars and nebulae; studied with photopolarimetry," Univ. of Arizona Press, p 307.

Zerull, R. H., Giese, R. H., Schwill, S., and Weiss, K. 1980. Scattering by Particles of Non–Spherical Shape. *in* Schuerman, D., ed. "Light Scattering by Irregularly Shaped Particles," Plenum, NY. p 273.